

UNIVERSIDAD AUTÓNOMA DE NUEVO LEÓN
FACULTAD DE INGENIERÍA MECÁNICA Y ELÉCTRICA



**“SYNTHESIS AND CHARACTERIZATION OF Cu-Sn-S THIN FILMS
FOR PHOTOVOLTAIC AND PHOTODETECTION APPLICATIONS”**

POR

ALBERT PAUL

2032354

**COMO REQUISITO PARA OBTENER EL GRADO DE
DOCTORADO EN INGENIERÍA DE MATERIALES**

Julio 2023

UNIVERSIDAD AUTÓNOMA DE NUEVO LEÓN
FACULTAD DE INGENIERÍA MECÁNICA Y ELÉCTRICA



**“SYNTHESIS AND CHARACTERIZATION OF Cu-Sn-S THIN FILMS
FOR PHOTOVOLTAIC AND PHOTODETECTION APPLICATIONS”**

POR

ALBERT PAUL

2032354

**COMO REQUISITO PARA OBTENER EL GRADO DE
DOCTORADO EN INGENIERÍA DE MATERIALES**

Julio 2023

CERTIFICATE

UNIVERSIDAD AUTÓNOMA DE NUEVO LEÓN Facultad de Ingeniería Mecánica y Eléctrica Posgrado

Los miembros del Comité de Evaluación de Tesis recomendamos que la Tesis "Synthesis and characterization of Cu-Sn-S thin films for photovoltaic and photodetection applications", realizada por el estudiante Albert Paul, con número de matrícula 2032354, sea aceptada para su defensa como requisito parcial para obtener el grado de Doctor en Ingeniería de Materiales.

El Comité de Evaluación de Tesis

Dr. David Avellaneda Avellaneda
Director

Dr. Sadasivan Shaji
Revisor

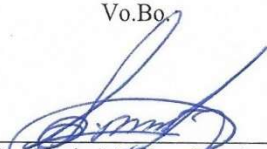
Dr. Domingo Ixcóatl García Gutiérrez
Revisor

Dr. Manuel García Méndez
Revisor

Dra. Shadai Lugo Loredo
Revisor

Dr. Jorge Oswaldo González Garza
Revisor

Vo.Bo.


Dr. Simón Martínez Martínez
Subdirector de Estudios de Posgrado

Institución 190001

Programa 122608

Acta Núm. 331

Ciudad Universitaria, a 8 de septiembre de 2023.

Dedicated to my dear father, who could not witness this adventure

Late. Mr. K.O Paulose

And

My beloved mother

Mrs. Moly Paulose

Thank you for allowing me to pursue my dreams and also for being my greatest strength, biggest supporter, and truest believer of all time.

ACKNOWLEDGEMENTS

First of all, I am grateful to the Lord Almighty for filling my life journey with uncountable blessings and love.

I would like to express my deepest gratitude to Facultad de Ingeniería Mecánica y Eléctrica (FIME) of Universidad Autónoma de Nuevo León (UANL) for accepting me as a research scholar and for providing all the necessary facilities to carry out my investigation. I am extremely indebted to Consejo Nacional de Humanidades, Ciencias, y Tecnologías (CONAHCYT), México for supporting me with the doctoral scholarship throughout this journey. I want to express my profound gratitude to Centro de Investigación y Desarrollo Tecnológico (CIDET), Centro de Innovación, Investigación y Desarrollo en Ingeniería y Tecnología (CIIDIT), Centro de Investigación e Innovación en Ingeniería Aeronáutica (CIIA), Centro de Investigación en Materiales Avanzados (CIMAV) for the laboratory and characterization facilities provided.

Words cannot express my gratitude towards Dr. David Avellaneda Avellaneda for accepting me as a doctoral student. I am extremely grateful for his helpful advice, constant support, and patience during my Ph.D. research. His great knowledge and peaceful conversations have encouraged me to push myself and made me a better version of myself. This endeavor would not have been possible without his support throughout this memorable journey.

I would like to extend my thanks to Dr. Sadasivan Shaji and Dra. Bindu Krishnan for their guidance and insightful advice throughout this part of life.

I would also like to thank Dr. Azael Martínez de la Cruz and Dr. Simón Martínez Martínez for their support in the administrative processes.

I would like to acknowledge Dra. Selene Sepulveda Guzman, Dra. Shadai Lugo Loreda, Dr. Sanal K.C, Dr. Josué Amílcar Aguilar Martínez, Dr. Edgar O. Garcia Sanchez, Dra. Maria Isabel Mendivil Palma, Ing. Jesus Alejandro Arizpe Zapata and, for helping and providing the facilities for Raman spectroscopy, XRD, SEM, EDX, and XPS analysis. I greatly appreciate Dr. Manju Thankamoni for her encouraging words and for introducing me to this research opportunity.

I might not have completed this voyage without the help of my colleagues Paulosutty, Tijin, Aiswarya, Akshana, Sebin, Vineetha, Surya, Sreed, Anjali, Jacob, Katia, Joseph, Pooja, Ashly, Varshika, Wilfred, Shilpa, and Jithin.

A special thanks to all my friends from Mexico and India for their help and support throughout my Ph.D. expedition. Words cannot express my gratitude to Anila Treesa Paul, Rinto Rapheal, Criza Mariyam Rinto, and all my family and friends.

Finally, I truly thank everyone who has influenced and inspired me to become who I am today.

CONTENTS

ABSTRACT	XI
RESUMEN	XII
LIST OF FIGURES	XIII
LIST OF TABLES	XIX
ABBREVIATIONS	XX
CHAPTER 1	1
INTRODUCTION TO THIN FILM PHOTOVOLTAICS	1
1.1 Photovoltaic energy: the world is trooping to a sustainable future	1
1.2 Fundamentals of photovoltaic devices	2
1.3 Thin film photovoltaics - present scenario and outlook	5
1.3.1 Silicon solar cell	7
1.3.2 Cadmium telluride - CdTe.....	8
1.3.3 Copper indium gallium selenide/sulfide - CIGS	9
1.3.4 Perovskites	9
1.3.5 Copper zinc tin sulfide/selenide - CZT(S,Se).....	10
1.4 Copper tin sulfide thin films - $Cu_xSn_yS_z$	12
1.4.1 Cu_2SnS_3	12
1.4.2 Cu_4SnS_4	13
1.5 Photodetector applications using Cu-Sn-S thin films	14
1.6 Hypothesis	17
1.7 General objective	17
1.8 Specific objectives	18
1.9 Justification	18
CHAPTER 2	20
EXPERIMENTAL METHODOLOGY AND CHARACTERIZATION METHODS	20
2.1 Cu-Sn-S thin films deposition	20
2.1.1 SnS precursor films using chemical bath	20
2.1.2 Thermal evaporation of Cu precursor film on SnS films.	23
2.1.3 Annealing of the stacked precursor layers in the sulfur atmosphere (sulfurization)	24
2.2 Characterization techniques	26

2.2.1 X-ray diffraction (XRD).....	26
2.2.2 Raman spectroscopy.....	27
2.2.3 Scanning electron microscope (SEM).....	27
2.2.4 Atomic force microscope (AFM).....	28
2.2.5 X-ray photoelectron spectroscopy (XPS).....	28
2.2.6 Energy dispersive X-ray spectroscopy (EDX).....	29
2.2.7 UV-Vis-NIR spectroscopy.....	29
2.2.8 Photoconductivity measurements.....	30
CHAPTER 3	32
SYNTHESIS AND CHARACTERIZATION OF SnS and Cu₄SnS₄ THIN FILMS	32
3.1 Synthesis and characterization of SnS precursor thin films	32
3.1.1 Structure analysis - XRD and Raman spectroscopy.....	33
3.1.2 Chemical composition- XPS.....	34
3.1.3 Elemental composition- EDX.....	35
3.1.4 Surface morphology- SEM and AFM.....	35
3.1.5 Optical characterization.....	36
3.1.6 Electrical characterization.....	37
3.2 Role of Cu precursor layer thickness on the formation and the properties of Cu₄SnS₄ thin films	39
3.2.1 X-ray diffraction analysis.....	39
3.2.2 Raman analysis.....	41
3.2.3 Compositional analysis - XPS.....	42
3.2.4 EDX analysis.....	44
3.2.5 Surface morphology-SEM.....	44
3.2.6 Surface topography - AFM.....	45
3.2.7 Optical characterization.....	46
3.2.8 Electrical characterization.....	49
3.2.9 Photovoltaic device.....	50
CHAPTER 4	52
INFLUENCE OF SULFURIZATION PARAMETERS ON THE SYNTHESIS AND PROPERTIES OF Cu₂SnS₃ THIN FILMS	52
4.1 Influence of sulfur quantity on the deposition and properties of Cu-Sn-S thin films	52
4.1.1 X-ray diffraction analysis.....	52

4.1.2 Raman Analysis.....	54
4.1.3 Chemical composition -XPS	55
4.1.4 Elemental composition-EDX	57
4.1.5 Surface morphology-SEM.....	58
4.1.6 Optical characterization.....	60
4.1.7 Electrical characterization	61
4.2 Influence of sulfurization time on the properties of Cu₂SnS₃ thin films	62
4.2.1 X-ray diffraction analysis.....	62
4.2.2 Raman analysis.....	63
4.2.3 Chemical composition -XPS	64
4.2.4 Elemental composition-EDX	66
4.2.5 Surface morphology - SEM.....	68
4.2.6 Optical characterization.....	69
4.2.7 Electrical characterization	70
4.3 Effect of sulfurization temperature on the properties of Cu₂SnS₃ thin films.....	71
4.3.1 X-ray diffraction analysis.....	72
4.3.2 Rietveld refinement	74
4.3.3 Raman analysis.....	75
4.3.4 Chemical composition - XPS	76
4.3.5 Elemental composition - EDX	78
4.3.6 Surface morphology- SEM.....	81
4.3.7 Surface topography -AFM.....	83
4.3.8 Optical characterization.....	84
4.3.9 Electrical characterization	86
CHAPTER 5	88
PHOTOVOLTAIC AND PHOTODETECTION APPLICATIONS USING OPTIMIZED	
Cu₂SnS₃ THIN FILMS.....	88
5.1 CdS/CTS photovoltaic device	88
5.1.1 CdS/CTS thin film solar cell	88
5.1.2 Effect of vacuum annealing on CdS/CTS thin film solar cell	90
5.1.3 Self powered CTS/CdS photodetector	92
5.2 CdS/SnS/CTS photovoltaic structure	99
5.2.1 SCAPS 1D simulation.....	99

5.2.2 CdS/SnS/CTS thin film solar cell.....	103
5.2.3 Self powered CdS/SnS/CTS photodetector	105
CHAPTER 6	114
CONCLUSIONS AND OUTLOOK	114
REFERENCES	116
ANNEXURE	138
Annexure A	138
Novel low-cost synthesis of crystalline SnI₄ thin films via anionic replacement: Effect of iodization time on properties.....	138
LIST OF PUBLICATIONS.....	146

ABSTRACT

Earth-abundant and non-toxic copper-tin-sulfide (CTS) thin films attracted great research interest due to their suitable optoelectronic properties like p-type electrical conductivity, bandgap ranging from 0.80 to 1.7 eV, and high optical absorption coefficient ($\alpha > 10^5 \text{ cm}^{-1}$). Cu_2SnS_3 and Cu_4SnS_4 have been found as interesting candidates for absorber layers in photovoltaic systems within the Cu-Sn-S group. In this work, Cu_4SnS_4 and Cu_2SnS_3 thin films were synthesized via sulfurization of stacked layers of chemically deposited SnS and thermally evaporated Cu. The influence of the thickness of Cu precursor and sulfurization parameters on the properties of Cu-Sn-S thin films was studied. Thin films with optimized properties were incorporated into photovoltaic structures and evaluated their photovoltaic and photodetection parameters. Photovoltaic structure of FTO/n-CdS/p-SnS/p- Cu_2SnS_3 /Ag resulted in photovoltaic parameters: $V_{oc} = 415 \text{ mV}$, $J_{sc} = 17.2 \text{ mAcm}^{-2}$, $\text{FF} = 30 \%$, and $\text{PCE} = 2.12 \%$. This study demonstrates the first Cu_2SnS_3 thin film based self-powered photodetector with a high responsivity and specific detectivity of 15.56 mA W^{-1} and $1.41 \times 10^{11} \text{ Jones}$ in the NIR region. This photovoltaic structure (CdS/SnS/CTS) displayed a rapid response time of 10.2 milliseconds for UV-Vis-NIR detection. Higher photovoltaic performance and enhanced photodetection parameters can be attained by further iterations of the deposition parameters. In summary, this work emphasizes the scope of this material and encourages the scientific community to explore earth-abundant, environmentally benign, and low-cost materials to produce high-performance photovoltaic and photodetection devices.

RESUMEN

Las distintas fases de las películas delgadas de cobre-estaño-sulfuro (CTS), las cuáles no son tóxicas y además son abundantes en la tierra, atrajeron un gran interés de investigación debido a sus propiedades optoelectrónicas adecuadas, como conductividad eléctrica de tipo p, banda prohibida ajustable (0.8 a 1.7 eV) y altos valores de coeficientes de absorción ópticos ($\alpha > 10^5 \text{ cm}^{-1}$). Particularmente, las fases Cu_2SnS_3 y Cu_4SnS_4 se han encontrado como candidatos interesantes para funcionar como capas absorbentes en sistemas fotovoltaicos dentro del grupo Cu-Sn-S. En este trabajo, sintetizamos películas delgadas de Cu_4SnS_4 y Cu_2SnS_3 mediante sulfuración de capas apiladas de SnS depositadas químicamente y Cu evaporado térmicamente. Se estudió la influencia del espesor del precursor de Cu y los parámetros de sulfuración sobre las propiedades de las películas delgadas de Cu-Sn-S. Películas delgadas de la fase Cu_2SnS_3 con sus propiedades optimizadas, fueron incorporadas en estructuras fotovoltaicas y se realizó la evaluación de sus parámetros fotovoltaicos, además de sus propiedades de foto-detección. La estructura fotovoltaica con una capa absorbidora de Cu_2SnS_3 además de una capa adicional de SnS (tipo-p) y CdS como material tipo ventana, resultó en parámetros fotovoltaicos: $V_{oc} = 415 \text{ mV}$, $J_{sc} = 17.2 \text{ mAcm}^{-2}$, $FF = 30 \%$, y $PCE = 2.12 \%$. Fabricamos el primer fotodetector auto-impulsado basado en película delgada de Cu_2SnS_3 con alta capacidad de respuesta y detectividad de 15.56 mA W^{-1} y 1.41×10^{11} Jones en la región NIR. Esta nueva estructura mostró un tiempo de respuesta extremadamente rápido del orden de 10 milisegundos para tiempos de subida y bajada (*rise, decay*), para la detección UV-Vis-NIR. Se proponen iteraciones adicionales de los parámetros de deposición y la optimización de las fases para lograr valores de eficiencia de conversión más altos. En resumen, nuestra investigación enfatiza el alcance de estos compuestos y anima a la comunidad científica a explorar este tipo de materiales con componentes abundantes en la corteza terrestre, no tóxicos y de bajo costo para producir dispositivos fotovoltaicos y de fotodetección de alto rendimiento.

LIST OF FIGURES

Figure 1.1 (a) Typical photovoltaic structure (b) solar cell equivalent circuit (c) output I-V plot of a solar cell under illumination.....	3
Figure 1.2 Verified conversion efficiencies chart from the National Renewable Energy Laboratory (NREL, USA) showing the greatest research cells across a variety of solar systems, https://www.nrel.gov/pv/assets/images/best-research-cell-efficiencies.jpg (accessed on 15 June 2023).....	6
Figure 1.3 Photovoltaic structure of CdTe solar cell.....	8
Figure 1.4 Photovoltaic structure of a CIGS-based solar cell.	9
Figure 1.5 Photovoltaic structure of a perovskite solar cell.	10
Figure 1.6 Photovoltaic structure of a CZTSSe solar cell.	11
Figure 2.1 (a) Experimental setup for chemical bath deposition, (b) chemical solution after 17 h deposition.....	21
Figure 2.2 Intercovamex TE12P Thermal evaporator equipment (left) and schematic diagram of thermal evaporation (right).....	23
Figure 2.3 Lindberg/Blue M™ Mini-Mite Tube Furnace equipment (left) and schematic representation of sulfurization process (right).....	24
Figure 2.4 Substrate and superstrate photovoltaic structures of thin film solar cells.....	25
Figure 2.5 The Keithley Pico ammeter (model 6487) and data acquisition computer for I-V measurements.	31
Figure 3.1 SnS chemical bath after 17 hours and obtained SnS thin films	32
Figure 3.2 a) XRD pattern of SnS thin film with a standard pattern of orthorhombic SnS and, b) Raman spectrum of SnS thin film.	33
Figure 3.3 XPS (a) survey and (b) core level spectra of Sn and S from SnS thin film.	34
Figure 3.4 EDX elemental mapping of (a) Sn, and (b) S of SnS thin film.....	35
Figure 3.5 (a,b) SEM images, (c) 3D AFM image, and (d) 2D AFM image of SnS thin film.	36
Figure 3.6 (a) Transmittance and specular reflectance (b) Tauc plot of SnS thin film.	37
Figure 3.7 Cyclic photoresponse of SnS thin films under a bias voltage of 10 V.....	38

This SnS precursor layer deposited via chemical bath deposition was used to synthesize Cu-Sn-S thin films.....	38
Figure 3.8 XRD patterns (relative intensity) of Cu ₄ SnS ₄ samples with copper thicknesses of 150, 175, 185, and 200 nm sulfurized at 500 °C for 1 h.....	40
Figure 3.9 XRD patterns of Cu ₄ SnS ₄ samples of Cu thicknesses of 150,175,185 and 200 nm sulfurized at 550 °C for 1 h along with Cu ₄ SnS ₄ (JCPDS #029-0584) standard pattern.	41
Figure 3.10 Raman spectra of the 150, 175, 185, and 200 nm samples.	42
Figure 3.11 XPS (a) survey scan, and core level spectra of (b) Cu, (c) Sn, and (d) S of 185 nm sample.....	43
Figure 3.12 SEM images (a) 150, (b) 175, (c) 185, and (d) 200 nm samples, respectively.	45
Figure 3.13 AFM images of (a) 150, (b) 175, (c) 185, and (d) 200 nm thin films.....	46
Figure 3.14 Absorbance spectra of Cu ₄ SnS ₄ samples with copper thickness 150 to 200 nm sulfurized at 550 °C for 1 h.	47
Figure 3.15 (a) Transmittance and (b) reflectance spectra of Cu ₄ SnS ₄ samples with copper thickness 150 to 200 nm sulfurized at 550 °C for 1 h.	47
Figure 3.16 Tauc plots of Cu ₄ SnS ₄ thin films with different copper thickness sulfurized at 550 °C for 1 h.	48
Figure 3.17 Photoconductive response of Cu ₄ SnS ₄ thin films with a bias voltage of 1 V... ..	50
Figure 3.18 Current density vs voltage curves of FTO/Cu ₄ SnS ₄ /CdS/C/Ag.....	51
Figure 4.1 XRD patterns of Cu-Sn-S films sulfurized using 10, 100, 200, and 300 mg of sulfur powder along with standard JCPDS patterns of Cu ₂ SnS ₃ and Cu ₄ SnS ₄	54
Figure 4.2 Raman spectra of Cu-Sn-S samples sulfurized using 10, 100, 200, and 300 mg of sulfur.....	55
Figure 4.3 XPS spectra of Cu, Sn, and S for samples sulfurized using 10, 100, 200, and 300 mg of sulfur.	56
Figure 4.4 EDX spectra of samples sulfurized using 10, 100, 200, and 300 mg of sulfur... ..	58
Figure 4.5 SEM images of Cu-Sn-S samples sulfurized using 10, 100, 200, and 300 mg of sulfur powder.....	59
Figure 4.6 a) Transmittance b) reflectance and c) Tauc plots (bandgap) of Cu-Sn-S films sulfurized using different quantities of sulfur powder.....	60

Figure 4.7 Photoconductive response of Cu-Sn-S films sulfurized using different quantities of sulfur powder.....	61
Figure 4.8 XRD patterns of Cu ₂ SnS ₃ samples sulfurized for 30, 60, 90, and 120 min with monoclinic Cu ₂ SnS ₃ (JCPDS#98-005-8702) pattern.	63
Figure 4.9 Raman spectra of Cu ₂ SnS ₃ samples sulfurized for 30, 60, 90, and 120 min.	64
Figure 4.10 XPS core electron spectra of (a) Cu, (b) Sn, and (c) S of samples sulfurized for different durations. Deconvoluted core electron spectra of (d) Cu, (e) Sn, and (f) S of 60 min sample.....	65
Figure 4.11 EDX elemental mapping of Cu, Sn, and S for different sulfurization durations.	67
Figure 4.12 SEM images of samples sulfurized for 30, 60, 90, and 120 min.	68
Figure 4.13 (a) Transmittance and (b) reflectance of samples sulfurized for 30, 60, 90, and 120 min.	69
Figure 4.14 Tauc plots of films sulfurized for 30, 60, 90, and 120 min.....	70
Figure 4.15 Current-voltage curve of films sulfurized for 30, 60, 90, and 120 min.	71
Figure 4.16 (a) XRD patterns of Cu ₂ SnS ₃ samples sulfurized at 350 to 500 °C along with standard monoclinic Cu ₂ SnS ₃ pattern and (b) magnified principal peak of XRD patterns along with the standard pattern of monoclinic, cubic, and tetragonal Cu ₂ SnS ₃	72
Figure 4.17 XRD pattern of sample sulfurized at 550 °C along with sample photo as inset.	73
Figure 4.18 Rietveld refinement results of 500 °C sample with a graphical representation of refined unit cell as inset.	74
Figure 4.19 Raman spectra of Cu ₂ SnS ₃ samples sulfurized at 350, 400, 450, and 500 °C...	76
Figure 4.20 XPS a) survey, core electron spectrum of b) Cu, c) Sn, and d) S of sample sulfurized at 500 °C.	77
Figure 4.21 XPS depth profile analysis of 500 °C sample.	78
Figure 4.22 EDX spectra of Cu ₂ SnS ₃ films sulfurized at 350 to 500 °C.....	79
Figure 4.23 EDX elemental mapping of Cu ₂ SnS ₃ samples sulfurized at 350 to 500 °C.....	80
Figure 4.24 SEM images of Cu ₂ SnS ₃ samples sulfurized at 350 to 500 °C.	82
Figure 4.25 AFM 2D and 3D images of samples sulfurized at 350 to 500 °C.....	83

Figure 4.26 Optical (a) transmittance and (b) reflectance of Cu_2SnS_3 thin films sulfurized at 350, 400, 450, and 500 °C.	84
Figure 4.27 Tauc plots of Cu_2SnS_3 films sulfurized at 350, 400, 450, and 500 °C.....	85
Figure 4.28 Photoresponse measurements of samples sulfurized at 400, 450, and 500 °C.	87
Figure 5.1 Current density vs voltage characteristics of the CdS/CTS photovoltaic cell. ...	89
Figure 5.2 Current density vs voltage plot of CdS/CTS device annealed at different temperatures (100 - 400 °C)	91
Figure 5.3 a) Photovoltaic device structure of CdS/CTS photodetector, b) photoresponse for 20 cyclic illuminations under 50 W halogen source illumination, c) photoresponse for one cycle of illumination for rise/decay time evaluation (data interval of 12 ms).....	93
Figure 5.4 Cyclic photoresponse of the device illuminated with LEDs of different wavelengths.	94
Figure 5.5 Cyclic photoresponse under illumination using different laser sources of wavelengths (532, 785, 840, and 1064 nm) and halogen 50 W lamp (bias voltage = 0 V). 95	95
Figure 5.6 Power density vs photocurrent (a-c) and power density vs responsivity (d-f) for 532, 785, and 1064 nm lasers at zero bias of CdS/CTS device.....	96
Figure 5.7 Power law fitting of photocurrent vs incident power density for different lasers (532, 785, and 1064 nm).....	97
Figure 5.8 Variation of a) detectivity and b) responsivity vs wavelength of CdS/CTS photodetector under illumination using different laser sources.....	98
Figure 5.9. Simulated current density vs voltage curve of FTO/CdS/CTS/Ag and FTO/CdS/SnS/CTS/Ag photovoltaic structures using SCAPS-1D software.	102
Figure 5.10 Maximum simulated current density vs voltage curve of FTO/n-CdS/p-SnS/p-CTS/Ag photovoltaic structures using SCAPS-1D software	103
Figure 5.11 Current density vs voltage curve of FTO/CdS/SnS/ Cu_2SnS_3 /Ag photovoltaic structure (schematic structure and image of cell in the inset).	104
Figure 5.12 a) Photovoltaic device structure of FTO/CdS/SnS/ Cu_2SnS_3 photodetector, b) photoresponse for 20 cyclic illuminations under 50 W halogen source illumination, and c) photoresponse for one cycle of illumination for rise/decay time evaluation (data interval of 12 ms).	106

Figure 5.13 Cyclic photoresponse under illumination using 30 W LED sources of different wavelengths.	107
Figure 5.14 Cyclic photoresponse under illumination using different laser sources of wavelengths (532, 785, 840, 980, and 1064 nm) and solar AM 1.5G simulator illumination (bias voltage = 0 V).	108
Figure 5.15 Power density vs photocurrent (a-c) and power density vs responsivity (d-f) for 532, 785, and 1064 nm lasers at zero bias.	110
Figure 5.16 Power law fitting of photogenerated current vs incident power density for different lasers (532, 785, and 1064 nm).	111
Figure 5.17 Variation of a) detectivity and b) responsivity vs wavelength of CdS/SnS/CTS photodetector under illumination using different laser sources.	113
Figure 7.1 Experimental procedure of the two-stage deposition of SnI ₄ thin films using anionic replacement mechanism.	139
Figure 7.2 XRD patterns of the S1 (30 s), S2 (60 s), S3 (90 s), and S4 (120 s) SnI ₄ thin films along with the standard pattern of SnI ₄ (JCPDS 01-077-0139).	139
Figure 7.3 Rietveld refinement result of S3 SnI ₄ sample and graphical representation of refined unit cell.	140
Figure 7.4 Raman spectra of the S1, S2, S3, and S4 SnI ₄ samples.	140
Figure 7.5 XPS (a) survey spectrum (b) core level spectrum of Sn and I (c) depth profile of S3 SnI ₄ (90 s iodinated) sample showing Sn and I core level spectrum.	141
Figure 7.6 Elemental mapping of as prepared SnS and S3 SnI ₄ thin films.	141
Figure 7.7 SEM images of (a) SnS, (b) S1, (c) S2, (d) S3, and (e) S4 SnI ₄ thin films, respectively.	142
Figure 7.8 AFM images of (a) as prepared SnS, (b) S1, (c) S2, (d) S3, and (e) S4 SnI ₄ thin films, respectively.	142
Figure 7.9 (a) Absorbance, (b) transmittance, (c) reflectance spectra, and (d) Urbach energy plots for different SnI ₄ samples.	143
Figure 7.10 Tauc plots of (a) S1, (b) S2, (c) S3, and (d) S4 SnI ₄ thin films along with photographs of film in the inset.	143
Figure 7.11 Photoluminescence spectra of SnI ₄ samples excited with a wavelength of 227 nm.	144

Figure 7.12 Variation of the real and imaginary part of complex refractive index with wavelength..... 145

Figure 7.13 I-V characteristics of SnI₄ thin films iodinated for different time durations. . 145

LIST OF TABLES

Table 1.1 Self-powered heterojunction photodetection devices and parameters	16
Table 3.1 Elemental composition from EDX analysis and Cu/Sn ratio of Cu_4SnS_4 films with different copper layer thicknesses.	44
Table 3.2 Bandgap and conductivity values of samples with different copper layer thicknesses.	49
Table 4.1 EDX elemental composition of samples sulfurized using 10, 100, 200, and 300 mg of sulfur.....	57
Table 4.2 Elemental composition of Cu_2SnS_3 thin films sulfurized for 30, 60, 90, and 120 min duration.....	66
Table 4.3 Elemental composition of samples sulfurized at 350 to 500 °C.....	79
Table 5.1 V_{oc} , J_{sc} , FF, and efficiency of CdS/CTS device annealed at different temperatures (100 - 400 °C).....	92
Table 5.2 Material parameters used for various materials for the SCAPS-1D program	99
Table 5.3 Parameters used for defects at interfaces of the layers.....	100
Table 5.4 Photovoltaic devices reported using monoclinic Cu_2SnS_3 thin films.....	105

ABBREVIATIONS

V_{oc} – open circuit voltage

J_{sc} – Short circuit current

FF – Fill factor

PCE- Power conversion efficiency

CTS- Cu_2SnS_3

CBD- Chemical bath deposition

SEM- Scanning electron microscopy

XRD- X-ray diffraction

EDS/EDX - Energy dispersive spectroscopy

AFM- Atomic force microscopy

XPS- X-ray photoelectron spectroscopy

PR- photoresponse

CHAPTER 1

INTRODUCTION TO THIN FILM PHOTOVOLTAICS

This chapter describes the importance of harvesting solar energy along with some fundamentals of solar cells and photovoltaic parameters. Some of the commercially proven and notable emerging thin film solar cell technologies and their current situation are discussed. These technologies are encountering some difficulties in long-term use and large-scale industrialization. On this context, earth-abundant, nontoxic, and cost-effective Cu-Sn-S thin films are proposed for photovoltaic applications and photodetection.

1.1 Photovoltaic energy: the world is trooping to a sustainable future

Solar energy is envisioned as a building stone for a sustainable future that relies on eco-friendly renewable energy sources. Alexander Becquerel discovered the photovoltaic effect in 1839, which is the transformation of light energy into electrical output. While working on a solid-state device made of selenium, a similar effect was also detected by Adams and Day [1]. Solar cells use p-n semiconductor junctions to transform sunlight into electrical energy. The development of silicon solar cells in 1950 resulted in a huge advancement in solar energy harvesting. Chapin, Fuller, and Pearson reported a Si-photovoltaic structure with an efficiency of 6 % in 1954 [2]. There on, solar photovoltaics has emerged as one of the prominent future sources of green energy. Silicon solar cells have reached a maximum efficiency of around 25 % [3]. They are commercially available worldwide and dominate the photovoltaic market [4]. Interestingly, thin film technologies like CIGS and CdTe have also achieved maximum power conversion efficiencies of 23.3 and 21.0 %, respectively [3]. Researchers around the globe have been working extensively to substitute these materials due to their disadvantages like high production cost, material scarcity, and toxicity. Currently, solar energy contributes a significant amount of renewable energy share in a handful of nations around the world. Many countries including China, United States, Germany, India, and Japan are focusing on electricity generation from photovoltaics. Solar energy provides 4 % of average grid electricity in EU countries and it is more than 7 % in the

case of Germany and Italy [5]. Worldwide electricity production from photovoltaics staggered around 1.8 % by the end of 2017 [4]. Through the strategic movement across the world, energy share from photovoltaics is expected to reach 21.8 % by 2030 [6]. On this occasion, enormous investigations on earth-abundant, non-toxic, cost-effective, and easily producible materials are necessary for a sustainable future.

1.2 Fundamentals of photovoltaic devices

Semiconductors are materials that exhibit electrical conductivity between conductors and insulators. The electrical characteristics of these materials are very sensitive to temperature changes or impurity levels. The electronic band (range of energy levels that electrons may have within it) which consists of valence electrons is called the valence band and higher energy electrons are contained in the conduction band. Bandgap of a material refers to the energy difference between the valence band maximum and conduction band minimum of that material. The energy distance between the vacuum level to the lowest point of the conduction band is termed as electron affinity [7]. Semiconductors are classified according to electrical behavior based on inherent electronic structure and impurity atoms as intrinsic or extrinsic semiconductors. Extrinsic semiconductors are further classified into n-type and p-type according to the impurity present in the material (p-acceptor impurities and n-donor impurities). A photovoltaic device usually consists of a p-n junction that functions according to the photovoltaic effect. A p-n junction is formed when p and n-type semiconductors join and produce an internal electric field (V_{bi} - built-in voltage) within the structure. This electric field acts as a basic force behind the photovoltaic effect.

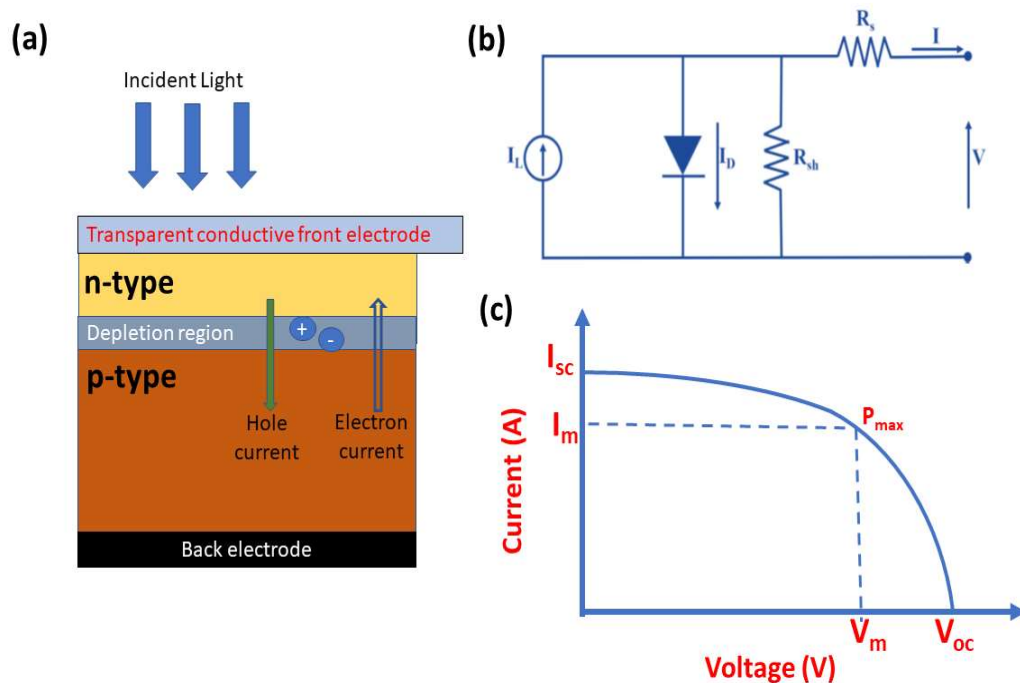


Figure 1.1 (a) Typical photovoltaic structure (b) solar cell equivalent circuit (c) output I-V plot of a solar cell under illumination.

The typical photovoltaic structure of a thin film solar cell is given in Figure 1.1a. The transparent conductive layer of the structure allows incoming light radiation to penetrate into window layer. This layer will transmit photons with energies up to the bandgap of the window layer material and enter into the absorber material. These photons generate electron-hole pairs inside the absorber material. All holes produced in the n-type region (minority charge carriers) that reach near depletion region will flow towards the p-type region under the influence of the built-in electric field that is already present across the p-n junction interface. Similar to holes, all minority charge carriers generated (electrons) in the p-type region move towards the n-type. Before they are gathered in the front or back electrodes, some of the electrons and holes will be recombined via a variety of recombination mechanisms, including Auger, radiative, and Shockley-Read Hall recombination [8]. Those accumulations cause a potential difference between n and p-type layers and this voltage can yield a current through an external circuit [9].

A solar cell behaves exactly like a normal diode (p-n junction) under dark conditions. From this perspective, a solar cell can easily be explained with an electric equivalent circuit, as

depicted in figure 1.1(b). Current and voltage inside the circuit without light are related by the Shockley equation.

$$I_D = I_0 \left[\exp\left(\frac{eV}{kT}\right) - 1 \right] \quad (\text{equation 1.1})$$

Where k - Boltzmann constant, e - fundamental unit charge of an electron, I_0 - inverse saturation current, T - the temperature in the unit of K. The term $\frac{kT}{e}$ is related to thermal voltage V_t [10].

Under light illumination, due to the presence of photogenerated current I_{ph} , this relation turns into:

$$I = I_{ph} - I_0 \left[\exp\left(\frac{eV}{nkT}\right) - 1 \right] \quad (\text{equation 1.2})$$

Where n is the ideality measure which indicates how closely a diode follows the ideal diode equation. The shunt resistance (R_{sh}) indicates the current losses around the cell due to mechanical defects and material dislocations [11]. Series resistance results from ohmic voltage loss either at connections or different layers of material. It relates maximum power generation of cells with open circuit voltage and varies under different illuminations [12]. Shunt resistance R_{sh} is related to the reduction of the maximum output voltage V_{oc} whereas series resistance R_s is primarily related to the reduction of the maximum output current I_{sc} [10]. For the ideal case, shunt resistance must be infinity ($R_{sh}=\infty$) and series resistance as low as possible ($R_s=0$).

The current-voltage relation of a real solar cell (considering R_{sh} and R_s) is expressed below:

$$I = I_{ph} - I_0 \left[\exp\left(\frac{e}{nkT}(V + IR_s)\right) - 1 \right] - \frac{V + IR_s}{R_{sh}} \quad (\text{equation 1.3})$$

k - Boltzmann constant, e - charge of an electron, I_0 - inverse saturation current, T - the temperature in K, n - ideality factor, R_{sh} - shunt resistance, and R_s - series resistance.

Figure 1.1(c) represents the I-V characteristics of a solar cell under illumination. When a solar cell is short-circuited, the circuit has no voltage between the terminals. The maximum current that could pass through the circuit when the endpoints are shorted is known as the short circuit current (I_{sc}). Short circuit current per area is termed as current density (J_{sc}) which is represented in terms of mAcm^{-2} . The open circuit voltage V_{oc} is defined as the maximum voltage that can be extracted from the cell when external circuit is in open condition [13]. The ratio of electrical power output to illumination input power (P_{in}), is known as the efficiency (η) of a photovoltaic cell, as follows:

$$\eta = \frac{V_{oc} I_{sc} FF}{P_{in}} \quad (\text{equation 1.4})$$

where the fill factor (FF) is the ratio of output power to the ideal power of the solar cell. The fill factor is determined by the equation as follows:

$$FF = \frac{V_m I_m}{V_{oc} I_{sc}} \quad (\text{equation 1.5})$$

These are the important parameters for the evaluation of solar cell performance.

1.3 Thin film photovoltaics - present scenario and outlook

Thin films include a considerable thickness range, varying from a few nanometers to some micrometers. The structural, chemical, and physical characteristics of thin films depend on the various synthesis methods and their deposition conditions. The atomic level random nucleation and growth processes are responsible for the attractive properties of thin-film materials. The reproducibility and possibility of tuning these properties by varying deposition parameters give an extra edge to this technology. Thin film solar cells provide a variety of design and manufacturing choices, making them a viable technology for photovoltaics on Earth and in space. Thin film solar cells require only a thin layer of absorber material compared to conventional solar cells due to their high absorption coefficient [14]. Various layers (contact, window, intrinsic, absorber, etc.) of thin film solar cells can be deposited using a variety of methods (thermal evaporation, sputtering, spin coating, etc.) on different types of substrates [15]. Due to their adaptability, these layers can be modified and engineered to enhance photovoltaic efficiency. Production of large-area devices creates more challenges to the thin film device fabrication process and necessitates proper control over the

whole deposition process. Invention of novel, low-cost, and innovative materials and a complete understanding of thin-film deposition techniques can help in the production of highly efficient devices. The material must meet specific requirements to be used as an absorber material in a photovoltaic structure. Absorber materials are desirable consisting of earth-abundant, non-toxic materials with high absorption coefficient and optical bandgap between 1.0 to 1.7 eV. Longer stability, good photovoltaic conversion efficiency, high carrier lifetime, and easy large-scale production are also considered as essential qualities for an absorber material [16]. Figure 1.2 represents the verified conversion efficiencies chart from the National Renewable Energy Laboratory (NREL, USA) showing the greatest research cells across a variety of solar technologies.

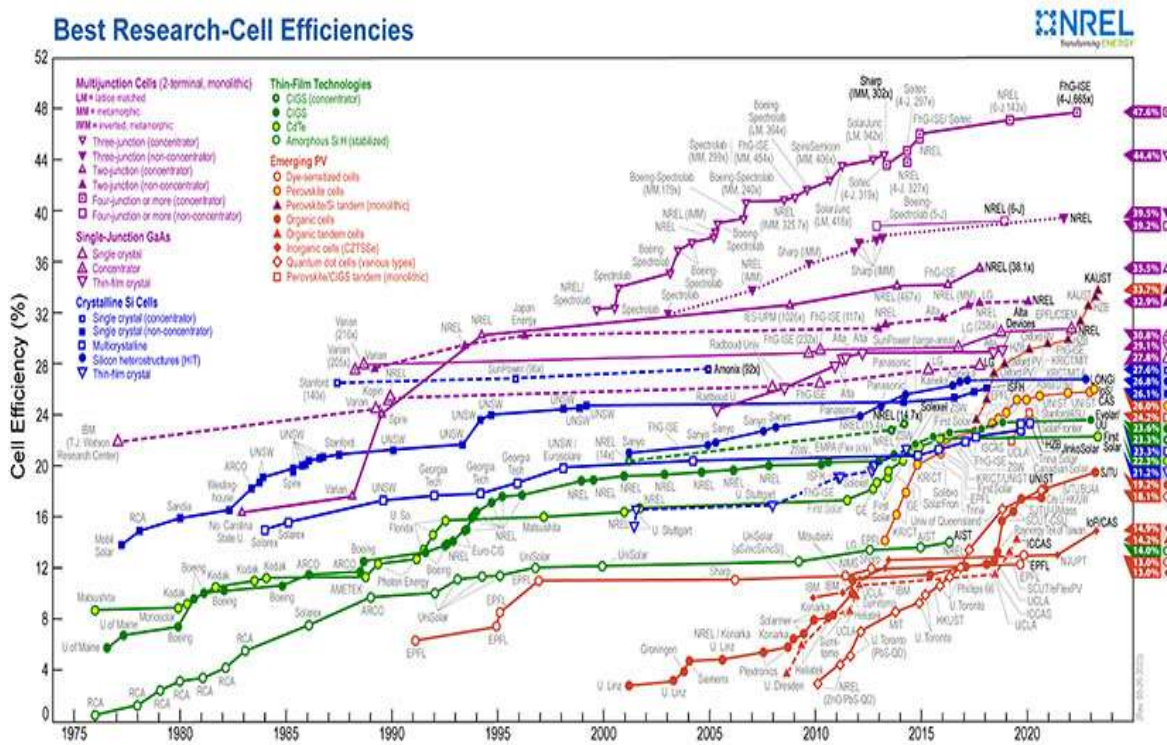


Figure 1.2 Verified conversion efficiencies chart from the National Renewable Energy Laboratory (NREL, USA) showing the greatest research cells across a variety of solar systems, <https://www.nrel.gov/pv/assets/images/best-research-cell-efficiencies.jpg> (accessed on 15 June 2023).

The worldwide solar-cell market involves various types of solar cells, but silicon solar cells rule the market. Regardless of the benefits of high performance, easy fabrication, and stability of silicon solar cells, they also have some drawbacks. The need for structurally high-quality silicon substrates, lack of flexibility, comparatively higher production cost, and poor optical absorption which necessitates tens of micrometers thick active device material are the main issues for crystalline silicon photovoltaic technology [17]. Thin film photovoltaics is an affordable alternative to conventional solar cell modules for their efficient productivity, facile deposition process, availability of different types of substrates, material reduction, flexibility, and high-performance stability [18]. Proper optimization of deposition techniques and material properties is anticipated to produce economical and efficient thin film photovoltaics. Currently, single-junction solar cells are classified into various classes based on absorber material and development: (1) crystalline Si solar cells; (2) thin-film photovoltaic technologies, primarily comprising cadmium telluride (CdTe), copper indium gallium selenide (CIGS), and gallium arsenide (GaAs); (3) emerging technologies, such as organic/inorganic perovskite solar cells, dye-sensitized solar cells, and quantum dot solar cells [19]. Some of those well-established solar cell technologies are discussed below along with their present and future outlooks.

1.3.1 Silicon solar cell

The first crystalline silicon solar cell was reported by Bell Labs in 1954 [2]. Currently, the laboratory scale efficiency of Si-based solar cells reached up to 26 % [20] and more than 80 % of photovoltaic devices in the market are based on silicon. The very first p-i-n configuration Si solar cell was created by Carlson and Wronski with a power conversion efficiency (PCE) of 2.4 %, and they forecasted a maximum efficiency of 14-15 % [21]. Subsequently, the development of multi-junction cells and modules led to the efficient absorption of a wide spectrum and Guha et. al. demonstrated a multijunction photovoltaic structure with an efficiency of 11 % [22]. Recently, silicon-based solar cells touched a world record efficiency of 26.81 % with photovoltaic parameters: $V_{oc}= 751$ mV, $J_{sc}= 41.45$ mAcm⁻², and FF= 86.07 % by electrically optimizing the nanocrystalline silicon hole contact layers [23]. Incorporating high-bandgap tandem material with Si is a potential strategy for achieving

conversion efficiencies higher than 30 % by enhancing solar spectrum absorption [24]. Even though Si solar cells give higher efficiencies, they have some drawbacks such as complicated manufacturing processes, indirect bandgap nature, susceptibility to temperature changes, and high production costs [25].

1.3.2 Cadmium telluride - CdTe

The first photovoltaic structure based on CdTe thin film was developed by Bonnet and Rabenhorst in 1972 which delivered an efficiency of 6 % [26]. The Shockley-Queisser theory suggests that CdTe can deliver superior V_{oc} values around 1 V and short circuit current densities around 30 mAcm^{-2} . Consequently, CdTe thin film solar cells can give maximum efficiency values of 32 %. Figure 1.3 represents the schematic diagram of a CdTe thin film solar cell structure. The typical bandgap for CdTe is 1.5 eV, and it could be produced using a huge spectrum of chemical and physical deposition techniques [27]. Recently, CdTe-based solar cells attained a power conversion efficiency of 20.8 % with a J_{sc} of 30.5 mAcm^{-2} , V_{oc} of 856 mV, and a fill factor of 79.8 % [28]. By utilizing different strategies such as band gap grading, copper embedding, and novel n-type layers, CdTe thin film solar cells achieved a laboratory-scale efficiency of 22.1 % [20]. The low availability of Te is the main limitation of CdTe-based solar cells. Also, the toxicity of Cd can cause numerous environmental problems in the future due to the complicated recycling and disposal of this material.

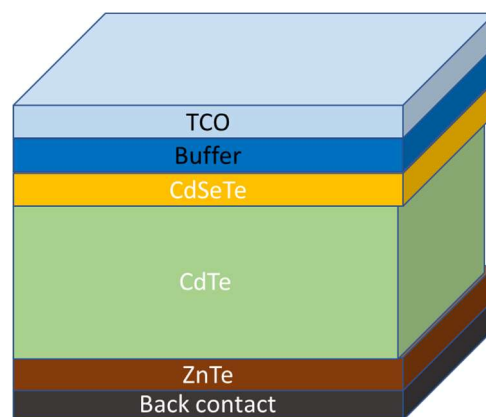


Figure 1.3 Photovoltaic structure of CdTe solar cell.

1.3.3 Copper indium gallium selenide/sulfide - CIGS

CIGS belongs to the I–III–VI₂ family which crystallizes in a tetragonal chalcopyrite structure of CuXY₂ (X = In, Ga and Y = Se, S) [29]. Thin film solar cells with CIGS absorber layers have achieved efficiencies of around 23 % [30]. The stability and efficiency of CIGS solar cells are comparable to that of Si solar cells. Lately, the concentration of Ga has varied to provide an appropriate bandgap and conduction band profile that yields higher open circuit voltages and power conversion efficiencies. Figure 1.4 represents the typical photovoltaic structure of CIGS-based thin film solar cells. Recent investigations demonstrated flexible and lightweight CIGS modules with photovoltaic efficiency values greater than 18 % [9]. The durability and performance of CIGS devices are encouraging; however, several aspects make the industrial-scale fabrication of CIGS devices less likely. The production requires intelligent processes to control the composition of elements during the deposition of this quaternary compound. Due to the utilization of costly and scarce metals like In and Ga, the cost of manufacture is escalated [9]. Replacement of these elements with earth-abundant Zn and Sn resulted in the development of non-toxic CZTS material.

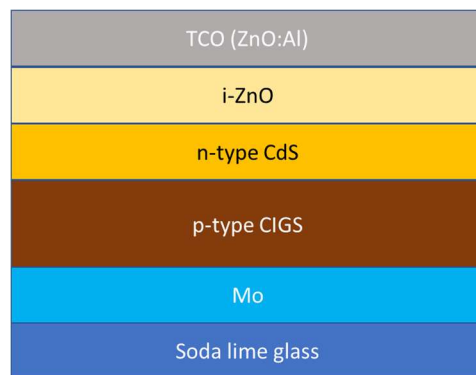


Figure 1.4 Photovoltaic structure of a CIGS-based solar cell.

1.3.4 Perovskites

Organic/inorganic halide perovskite thin film photovoltaic technology has demonstrated great improvement in photovoltaic conversion during the last decade. A perovskite material displays a general formula of ABX₃, where A, B, and X represent a monovalent cation,

divalent cation, and an anion, respectively [31]. Perovskite thin films possess suitable properties for photovoltaic applications such as high optical absorption coefficient, prolonged carrier lifetime, longer carrier diffusion length, and tunable band gap [32]. Figure 1.5 represents the standard photovoltaic structure of a perovskite solar cell. Significant improvement in the optoelectronic properties of perovskite material and optimization of device architecture resulted in an excellent power conversion efficiency of 25.7 % [3]. Lately, FAPbI₃ perovskite layers treated with volatile alkylammonium chlorides delivered a power conversion efficiency of 26.08 %. This approach could produce controlled crystallization of FAPbI₃ perovskite thin films and they exhibit photovoltaic parameters of $V_{oc}= 1.18 \text{ V}$, $J_{sc}= 25.7 \text{ mAcm}^{-2}$, and $FF= 86.15 \%$ [33]. Perovskite layers are suitable candidates for photovoltaic devices due to their simplicity of fabrication using solution procedures and other non-vacuum deposition techniques. However, most of the high-performing perovskite materials are composed of highly toxic Pb and others face instability and poor lifetime. These difficulties make perovskite materials vulnerable to commercialization.

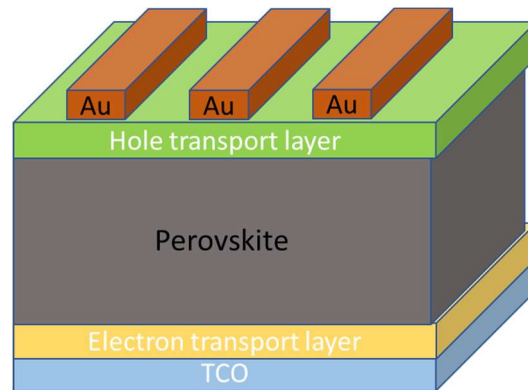


Figure 1.5 Photovoltaic structure of a perovskite solar cell.

1.3.5 Copper zinc tin sulfide/selenide - CZT(S,Se)

Kesterite (CZTSSe) solar cells are anticipated as a viable material for sustainable energy harvesting due to earth-abundant elements, appropriate bandgap, strong absorption, and lower production cost [34]. Figure 1.6 represents the photovoltaic structure of a CZTSSe thin film solar cell. Recently, they have attained a power efficiency of 13.4 % with photovoltaic parameters of $J_{sc}= 34.2 \text{ mAcm}^{-2}$, $V_{oc}= 532 \text{ mV}$, and $FF= 73.4 \%$ [35]. Even though those

have shown considerable advancement in photovoltaic performance, the practical industrial application requires further improvements in power conversion efficiencies and manufacturing techniques. CZT(S,Se) possesses high defect density due to a higher number of elements which causes charge recombination and band tail formation [36]. The complex four-element phase diagram of CZT(S,Se) produces different binary phases and intrinsic defects in the fabrication process and these are found to be vulnerable to non-radiative recombination in the bulk and at interfaces, which needs to be addressed for future development. Various tactics have been suggested in recent years to overcome these obstacles to produce highly efficient Kesterite solar cells. Various strategies such as doping/alloying, defects control, thermal treatment, crystallization path manipulation, interface passivation, and bandgap modification have helped to improve its photovoltaic performance [37]. Extensive studies are required on growth processes, its chemical composition, transport properties, and recombination mechanisms to realize the commercialization of Kesterite solar cells.

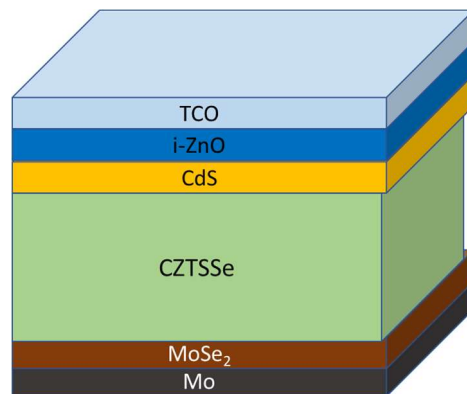


Figure 1.6 Photovoltaic structure of a CZTSSe solar cell.

Thin film technologies are facing many challenges to meet the simultaneous necessities of higher power conversion efficiencies, cost-effectiveness, easy material availability, higher stability, and non-toxicity. Systematic in-depth research is necessary to achieve these qualities which can greatly influence the pavement for a sustainable future. This study explores the photovoltaic and photodetection performance of Cu-Sn-S thin films deposited via a three-step process.

1.4 Copper tin sulfide thin films - $\text{Cu}_x\text{Sn}_y\text{S}_z$

The augmented necessity for natural energy caused numerous investigations for earth-abundant, non-toxic, and affordably priced solar cells. Cu-Sn-S thin films have been greatly explored around the globe owing to their excellent optoelectronic properties and excellent stability in atmospheric conditions. Cu-Sn-S shows numerous stoichiometries such as Cu_2SnS_3 , $\text{Cu}_2\text{Sn}_3\text{S}_7$, Cu_3SnS_4 , Cu_4SnS_4 , $\text{Cu}_5\text{Sn}_2\text{S}_7$, and $\text{Cu}_{10}\text{Sn}_2\text{S}_{13}$. Among all these phases, Cu_2SnS_3 , Cu_3SnS_4 , and Cu_4SnS_4 are found to be the most stable phases in the system. Cu_3SnS_4 phase can be found in three different crystalline structures: tetragonal, cubic, and orthorhombic [38,39]. Cu_3SnS_4 is electronically as well as structurally similar to CuS and highly conductive. Cu exhibits a dual oxidation state of +1 and +2 states and becomes the reason for the metallic behavior of Cu_3SnS_4 with a high hole carrier concentration of $\sim 10^{22} \text{ cm}^{-3}$. This metallic nature of the Cu_3SnS_4 phase makes it unsuitable for photovoltaic applications. Whereas Cu_2SnS_3 and Cu_4SnS_4 phases exhibit suitable properties for photovoltaic applications [40,41].

1.4.1 Cu_2SnS_3

Cu_2SnS_3 exhibits p-type conductivity, a direct bandgap between 0.8 to 1.7 eV, and a large absorption coefficient ($\alpha > 10^5 \text{ cm}^{-1}$) [42]. It can be synthesized via different deposition techniques: chemical bath deposition, sputtering, spray pyrolysis, pulsed laser deposition, doctor blade, atomic layer deposition, sol-gel technique, and thermal evaporation [43–50]. Different crystal structures such as cubic, tetragonal, triclinic, and monoclinic were reported for this particular phase [51–53]. The suitable optoelectronic properties of Cu_2SnS_3 attracted numerous investigations on this phase. The maximum efficiency values estimated for Cu_2SnS_3 thin film solar cells are in the range of 20-30 % however experimentally reported values are still inferior [54]. Even though Cu_2SnS_3 thin films are predicted as potential candidates for photovoltaics, researchers are only able to achieve a maximum power conversion efficiency of 4.3 % [55]. Whereas the incorporation of silver (Ag), sodium (Na), and germanium (Ge) in Cu_2SnS_3 thin film have resulted in power conversion efficiencies of 3.9, 5.1, and 6.7 %, respectively [56–58].

Titilayo demonstrated the first solar cell based on Cu_2SnS_3 in 1987 with a power conversion efficiency of 0.11 % [59]. Later, Berg et. al. reported the device structure of Glass/Mo/ Cu_2SnS_3 /CdS/AZO/Al with photovoltaic parameters V_{oc} = 104 mV, J_{sc} = 17.1 mAcm^{-2} , FF= 30.4 %, and an efficiency= 0.54 % [60]. Researchers paid more attention to the development of Cu_2SnS_3 -based solar cells after 2012, till then the efficiency values achieved by Cu_2SnS_3 solar cells were not appreciable. Chino et. al. improved the power conversion efficiency to 2.54 % with photovoltaic parameters: V_{oc} = 211 mV, J_{sc} = 28.0 mAcm^{-2} , and FF = 43 %. A device architecture of Glass/Mo/ Cu_2SnS_3 /CdS/AZO/Al was adapted in which the Cu_2SnS_3 absorber layer was synthesized by sulfurizing the precursor layers at 580 °C for a couple of hours [61]. Kanai et. al. further enhanced the photovoltaic performance using the Cu_2SnS_3 absorber layer produced by thermally treating co-evaporated Cu, Sn, and S layers at 570 °C. They achieved V_{oc} = 248 mV, J_{sc} = 33.5 mAcm^{-2} , FF = 44 %, and an efficiency of 3.66 % using the same device structure [62]. They reported a PCE of 4.29 % for copper-deficient Cu_2SnS_3 -based solar cells which exhibited a V_{oc} = 258 mV, J_{sc} = 35.6 mAcm^{-2} , and FF= 46 % [55]. Recently, Zhang et. al. implemented a photovoltaic structure of Mo/ Cu_2SnS_3 /CdS/i-ZnO/AZO/Ag and obtained an efficiency of 3.05 % [63]. The deposition method, growth conditions, and annealing conditions do have a significant impact on the photovoltaic performance of Cu_2SnS_3 thin film solar cells. Polymorphic nature, poor microstructure morphology, presence of impurities or unreacted binary phases, and crystal imperfections of Cu_2SnS_3 thin films are the main reasons behind relatively lower photovoltaic parameters. Extensive investigations and innovative device structures are necessary for the further advancement of Cu_2SnS_3 solar cells. This study investigates the effect of sulfurization parameters on the crystal structure, surface morphology, elemental composition, and optoelectrical properties of Cu_2SnS_3 thin films produced by sulfurization of chemically deposited SnS and thermally evaporated Cu layers.

1.4.2 Cu_4SnS_4

Cu_4SnS_4 thin film is proposed as a potential candidate for absorber material in thin film solar cells. Even though it shows good optoelectronic properties, the Cu_4SnS_4 phase is not much explored for photovoltaic applications in contrast with Cu_2SnS_3 . Cu_4SnS_4 crystallizes in the

orthorhombic system in the *Pnma* space group, which was first reported by S. Jaulmes in 1977 [64]. It also crystallizes in a monoclinic structure of space group $P2_{1/c}$ at lower temperatures which are isostructural with Cu_4GeS_4 [65,66]. Cu_4SnS_4 goes through a phase transition from an arranged monoclinic phase to a disordered orthorhombic phase at a temperature of $-43\text{ }^\circ\text{C}$. At higher temperatures, facile movement of the Cu ions was responsible for the transition of the monoclinic to a relatively disordered orthorhombic structure [66,67]. Cu_4SnS_4 is polycrystalline in nature and requires an optimum amount of Cu for the complete conversion of binary phases (CuS , SnS , Cu_2S , Sn_2S_3 , SnS_2) into the ternary phase. Cu_4SnS_4 thin films have been deposited using different methods such as chemical bath deposition [54,68,69], thermal co-evaporation [70], doctor blade process [71], and SILAR [72]. Cu_4SnS_4 shows high electrical conductivity due to large sub-gap absorption and high defect density. Extensive optimization of deposition parameters and post-deposition treatments are necessary for the improvement in optoelectronic properties.

Nair et. al. fabricated Cu_4SnS_4 thin films by annealing stacked CuS/SnS thin films deposited by chemical bath deposition and found them to be suitable for photovoltaic applications [68]. Chen et. al. studied the photovoltaic properties of Cu_4SnS_4 thin films deposited via a combination of mechanochemical and doctor blade methods [71]. They fabricated a photovoltaic structure of $\text{Mo}/\text{CTS}/\text{In}_2\text{S}_3/\text{TiO}_2/\text{FTO}$ glass that yielded photovoltaic parameters: $V_{oc}= 300\text{ mV}$, $J_{sc}= 29.24\text{ mAcm}^{-2}$, $\text{FF} = 26\%$, and $\text{PCE}= 2.34\%$. Chalapathi et. al. reported enhanced hole mobility for Cu_4SnS_4 thin films by annealing stacked layers of chemical bath-deposited CuS and SnS thin films. All films exhibited p-type electrical conductivity and high hole mobilities up to $150\text{ cm}^2\text{V}^{-1}\text{s}^{-1}$ after high-temperature annealing [73]. Additionally, they studied the effect of nitrogen and sulfur pressures during the thermal treatment on the deposition and properties of the Cu_4SnS_4 thin films. Increasing total (N_2+S_2) pressure from 1.3 to 66.7 kPa resulted in bigger grains [69]. In this work, the Cu_4SnS_4 phase was synthesized by sulfurization of stacked layers of SnS and Cu (different thicknesses).

1.5 Photodetector applications using Cu-Sn-S thin films

A photodetector is an optoelectronic device that generates electrical signals from optical input. Photodetectors are used for video imaging, biomedical imaging, gas sensing, optical

communications, security/surveillance, night vision, and motion detection applications. The photodetection process in semiconducting materials is based on the creation of electron-hole pairs under light irradiation. Incoming photons will be absorbed by the material if they have energy higher than or equal to the bandgap of that semiconducting material. As a consequence, electrons will excite from the valence band to the conduction band which results in the formation of photogenerated electron-hole pairs. These generated charge carriers can be separated by an external electric field to produce a photocurrent. This phenomenon is used to detect light by producing equivalent electrical signals [74].

The heterojunction self-powered photodetectors have emerged as key optoelectronic devices owing to the conversion of optical signals to electrical signals without any applied bias voltage [75]. The built-in field at the p-n heterojunction aids the efficient separation of charge carriers and suppression of the carrier recombination and also facilitates self-powered operation [76]. Much beyond, Cu₂SnS₃-based self-powered photodetectors consisting of earth-abundant and low-cost materials can contribute greatly to sustainable and stable photodetection.

The three important photodetection parameters such as responsivity (R), detectivity (D*), and linear dynamic range (LDR) of a photodetector are calculated in this study [75,77].

Output photocurrent under unit incident light power is the measure of responsivity, which gives a measure of the sensitivity of a photodetector to incident light signals. This parameter directly reflects the conversion of the photoelectric signal of the device under illumination. Responsivity represents the strength of the electrical signal output by the device and it is calculated using the formula below

$$R = \frac{I_{\text{Light}} - I_{\text{dark}}}{P_{\text{inc}} S} \quad (\text{equation 1.6})$$

Where P_{inc} is the power density of incoming radiation on the actual area and S is the electrode area.

Detectivity (D*) implies the ability of a photodetector to detect weak signals from the noise signal environment and is determined by equation 1.7.

$$D^* = R_{\lambda} \sqrt{\frac{S}{2 e I_{\text{dark}}}} \quad (\text{equation 1.7})$$

where R_λ is the responsivity at the wavelength λ , S is the effective area of illumination, and e is the absolute value of electron charge.

The linear dynamic range (LDR) of the photodetector can be evaluated to determine the signal-to-noise ratio of the photodetection structure. It is defined as the relative ratio of photocurrent to dark current which is typically expressed in decibels (dB).

$$LDR(D) = 20 \log \frac{I_{\text{photocurrent}}}{I_{\text{dark}}} \quad (\text{equation 1.8})$$

Rise and decay times are important factors that demonstrate the detection capabilities of a photodetector. Rise time is defined as the time needed to increase the photocurrent from 10 to 90 % of its maximum value while decay time is the time taken to decrease photocurrent from 90 to 10 % of its maximum value [78].

Table 1.1 Self-powered heterojunction photodetection devices and parameters

Detection range	Device structure	Responsivity (mA W ⁻¹)	Detectivity (Jones)	Rise time (ms)	Decay time (ms)	Reference
UV-Vis	MAPbI ₃ /CdS	430	2.3×10 ¹¹	14	-	[76]
UV	β-Ga ₂ O ₃ /4HSiC	10.35	8.8×10 ⁹	11	19	[79]
UV-NIR	SnS ₂ /ZnO _{1-x} S _x	8.28	5.1×10 ¹⁰	49	26	[80]
UV-NIR	NiO/Si	13.08	1.0×10 ¹¹	85	85	[81]
UV	CuSCN/Ga ₂ O ₃	5.5	3.8×10 ¹¹	450	260	[82]
UV	NiO/ZnO	13.01	5.6×10 ¹¹	197	537	[83]
Vis	SnS/CdS	10.4	2.1×10 ¹⁰	30	30	[84]

Even though Cu₂SnS₃ thin films show good photovoltaic properties, photodetection abilities are not well studied yet. Recent reports suggest widening the application of Cu₂SnS₃ thin films to broadband photodetection [42]. Dias et. al. demonstrated Vis-IR photodetection properties of Cu₂SnS₃ thin films prepared by spin coating. They presented a responsivity and detectivity of 16.32 mA W⁻¹ and 5.1×10¹⁰ Jones under IR illumination of 477.7 mWcm⁻².

Moreover, IR photodetectors based on Cu_2SnS_3 quantum dots were synthesized by a solution heat-up method which exhibited a responsivity and detectivity of 200 mA W^{-1} and 3.47×10^{10} Jones under IR illumination (750 - 1150 nm) of 480 mW cm^{-2} [85]. They also synthesized Cu_2SnS_3 quantum dots by solvothermal method and the corresponding device displayed a responsivity and detectivity of 7.66 mA W^{-1} and 2.1×10^{10} Jones under IR illumination of 480 mW cm^{-2} [86]. Even though all these devices exhibited high detectivity values, the longer response time (> 4 seconds) and transient photoresponse profile persisted as a serious concern. To overcome these drawbacks and improve the photodetection abilities, Cu_2SnS_3 was integrated into a heterojunction device. Many researchers have fabricated heterojunction photodetectors and investigated their detection abilities using different sources (Table 1.1). Interestingly, various research groups have demonstrated the potential capability of chalcogenide materials for self-powered photodetection [80,87,88]. Recently, Chang et. al. reported an SnS/CdS heterojunction self-powered photodetector with the highest responsivity and specific detectivity of 10.4 mA W^{-1} and 3.56×10^{11} Jones, respectively [84]. Therefore, heterojunction photodetectors based on Cu_2SnS_3 are expected to produce self-driven, air-stable, broadband, and high-performance photodetection due to the broad absorption and stability of this material.

1.6 Hypothesis

Cu-Sn-S thin films with p-type conductivity, suitable band gap (1 to 1.5 eV), and high absorption coefficient ($\sim 10^5 \text{ cm}^{-1}$) can be obtained through the optimization of parameters of three-stage deposition including chemical bath deposition, thermal evaporation, and sulfurization for optoelectronic applications.

1.7 General objective

To optimize the deposition parameters of the three-stage deposition method (chemical bath deposition, thermal evaporation, and sulfurization) for Cu-Sn-S thin films and incorporation of optimized phases with suitable optoelectronic properties such as optimum bandgap (1-1.5 eV) and high absorption coefficient $\sim 10^5 \text{ cm}^{-1}$ into photovoltaic and photodetection devices.

1.8 Specific objectives

- 1) To synthesize and characterize SnS thin films deposited via chemical bath deposition
- 2) To deposit Cu layers (varied thickness) by thermal evaporation on the SnS thin films.
- 3) To anneal these films under a sulfur atmosphere (sulfurization) to obtain different ternary phases of the Cu-Sn-S system
- 4) To optimize the deposition conditions: the thickness of precursor layers, sulfurization temperature/time, and quantity of sulfur powder to obtain different Cu-Sn-S phases
- 5) To evaluate structure, composition, microstructure, optical, and electrical properties utilizing a variety of characterization techniques
- 6) To incorporate suitable phases into photovoltaic structures or photodetection devices (thin film solar cells or photodetectors)
- 7) To evaluate the impact of post-deposition vacuum thermal treatments on the photovoltaic performance
- 8) To evaluate the photovoltaic performance of different phases of Cu-Sn-S thin films by assessing principal solar cell parameters (V_{oc} , J_{sc} , fill factor, efficiency)
- 9) To fabricate heterojunction photodetectors and evaluate principal photodetection parameters such as responsivity, response time, and detectivity.

1.9 Justification

Optimization of earth-abundant, non-toxic materials is extremely important for reducing production costs and environmental issues that arise from toxic materials for futuristic optoelectronic devices. Cu-Sn-S thin films are considered to be suitable candidates for photovoltaic applications. Unfortunately, the experimentally achieved power conversion efficiencies of the Cu-Sn-S thin films are lower than their theoretically predicted values (Cu_2SnS_3 -30 % and Cu_4SnS_4 -25 %) [54]. The deposition method, annealing process, and annealing conditions are the key factors affecting the properties of Cu-Sn-S thin films, also they have a huge impact on the photovoltaic performance [49]. Extensive exploration of different deposition techniques is essential to achieve better photovoltaic parameters for this

material. The incorporation of the copper layer by thermal evaporation on SnS deposited via chemical bath deposition and following sulfurization of these stacked layers is an effective route to the synthesis of Cu-Sn-S ternary thin films. In this study, deposition parameters for a three-step deposition method that combines physical and chemical deposition methods (chemical bath deposition, thermal evaporation, and sulfurization) are optimized to achieve the desired surface morphology, bandgap, absorption coefficient, and electrical conductivity. Optimized phases with suitable optoelectronic properties such as p-type conductivity, appropriate bandgap, and high absorption coefficient are incorporated into photovoltaic structures. Photovoltaic performance and photodetection abilities of $\text{Cu}_x\text{Sn}_y\text{S}_z$ thin films synthesized by a three-step method (chemical bath deposition, thermal evaporation, and sulfurization) are discussed in the following chapters of this thesis.

CHAPTER 2

EXPERIMENTAL METHODOLOGY AND CHARACTERIZATION METHODS

This chapter describes the experimental methodology adapted to synthesize Cu-Sn-S thin films and the details about the deposition techniques used. Specific experimental parameters are mentioned individually in the introduction part of different sections. Also, the characterization techniques used to study the material properties are discussed in detail.

2.1 Cu-Sn-S thin films deposition

A wide variety of microstructures and subsequent properties of the films can be obtained by simply modifying the deposition conditions during the growth of the film. The properties of Cu-Sn-S thin films depend on the synthesizing method, substrate material, substrate temperature, deposition rate, annealing conditions, precursor layers, etc. For the synthesis of Cu-Sn-S thin films, a combination of chemical and physical deposition methods was utilized in this study. Cu-Sn-S thin films were synthesized via sulfurization of stacked layers of SnS and Cu deposited via chemical bath deposition and thermal evaporation, respectively.

2.1.1 SnS precursor films using chemical bath

Chemical bath deposition (CBD) is a facile and low-cost deposition technique for the synthesis of homogeneous thin films. Chemical bath deposition is the controlled precipitation of a substance on the substrate from a chemical solution. Figure 2.1(a,b) represents the experimental setup for the chemical bath deposition and the chemical solution after 17 h deposition (reaction). To produce uniform and compact thin films with this approach, the rate of chemical reaction must be strictly regulated. Both the availability of nucleation sites and the supersaturation of the chemical solution affect the final thickness of the film. The growth of a thin film inside a chemical bath depends upon various factors. The most important parameters are the complexing agent, pH of the chemical bath, temperature of the chemical

bath, and nature of the substrate. Therefore, it is necessary to understand the influence of different deposition parameters on the growth mechanism of the film to optimize them. These are discussed in detail below.

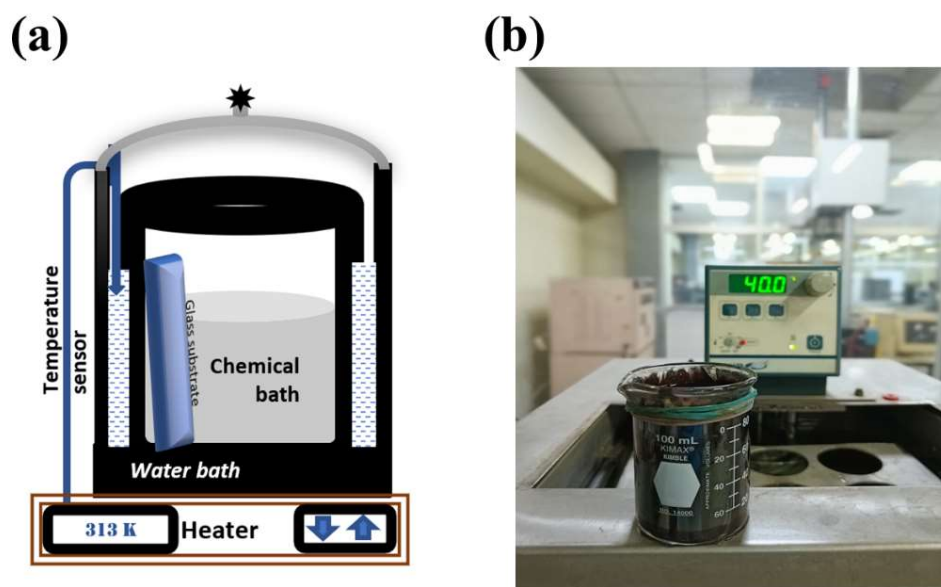


Figure 2.1 (a) Experimental setup for chemical bath deposition, (b) chemical solution after 17 h deposition.

- Complexing agent- In most cases, an alkaline solution is used for chemical bath depositions and a complexing agent is introduced to inhibit the metal complex from precipitating. They aid in slowing down the release of metal complexes in chemical baths and quick bulk formation of the final product can be avoided by varying concentrations of complexing agents. Subsequently, the rate of reaction will be reduced which can result in controlled deposition.
- pH of the solution- The supersaturation condition regulates both the speed of chemical reaction and the pace of deposition. The metal complex typically becomes more stable by decreasing the number of available metal ions as the pH of the chemical bath is raised. As a result, the reaction rate will decrease, and deposition on the substrate will be reduced.
- Temperature of the solution - Another important factor that affects the speed of the reaction is the temperature of the solution. The dissociation of the complex becomes faster with the increasing temperature of the solution. This leads to greater interaction

between ions due to the increased kinetic energy of the molecules. This can result in the alteration of the final thickness depending on the limit of supersaturation of the chemical bath.

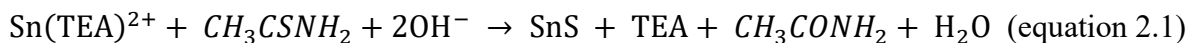
- Nature of substrate- The adherence of the compound and the kinetics of the reaction are both greatly influenced by the nature of the substrate. Therefore, the first crucial step in the thin film deposition process is substrate cleaning. When the lattice characteristics of substrates and depositing material are well matched, a higher deposition rate and final thickness are expected.

The CBD approach has the following important advantages over other methods.

- A facile method for thin film deposition
- No need for a high vacuum for execution
- Reproducible, consistent, and well-adhered thin films
- Optimum material consumption
- Cost-effective for large-scale production.

SnS chemical bath was prepared by mixing chemicals as follows: 1 g of $\text{SnCl}_2 \cdot 2\text{H}_2\text{O}$ was dissolved in 5 mL of acetone (CH_3COCH_3) in a 100 mL beaker. To this solution, 12 mL of 3.7 M triethanolamine ($\text{N}[\text{CH}_2\text{CH}_2\text{OH}]_3$, TEA) was added with continuous stirring, followed by 10 mL of 4 M ammonia ($\text{NH}_3(\text{aq})$), 8 mL of 1 M thioacetamide (CH_3CSNH_2), and 65 mL of deionized water to obtain a total volume of 100 mL [89]. Premium glass substrates were dipped in soap solution and subjected to ultrasonication for 10 minutes. These glass slides were thoroughly rinsed with water after being gently cleaned with a soap solution. Finally, the cleaned substrates were treated with distilled water and deionized water in the ultrasonicating bath. Cleaned premium microscope glass substrates were dried under hot air flow and placed vertically with a slight inclination in the chemical bath.

The SnS deposition is caused by an overall chemical reaction as follows [90,91]:



Increased duration of the chemical bath or multiple depositions using newly produced baths can help to improve the thickness of the films.

2.1.2 Thermal evaporation of Cu precursor film on SnS films.

Thermal evaporation is a high vacuum physical vapor deposition technique to deposit different materials on different substrates. Figure 2.2 represents the Intercovamex model - TE12P thermal evaporator equipment (left) and a schematic diagram of thermal evaporation (right). The material was kept on a resistive boat and evaporated by resistive heating, by passing a high current through that resistive boat usually made of W, Ta, or Mo, depending on the material to be evaporated. Commonly, thermal evaporation is employed for applications requiring electrical connections where single metals are deposited. By carefully regulating the temperature of different crucibles, more complicated applications such as the co-deposition of multiple materials, can also be accomplished.

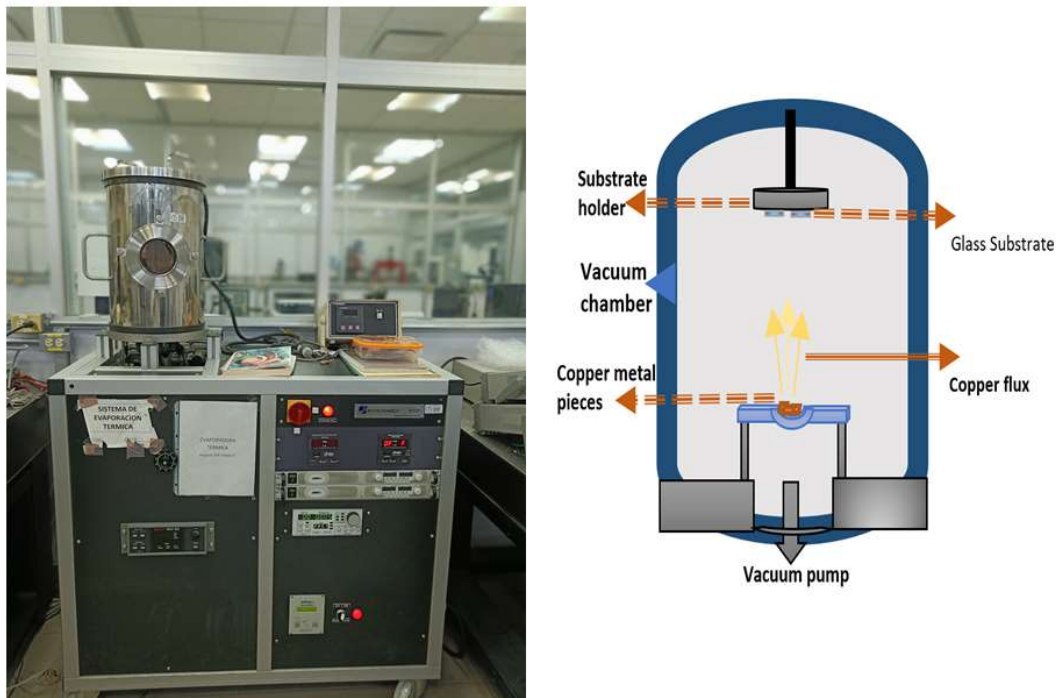


Figure 2.2 Intercovamex TE12P Thermal evaporator equipment (left) and schematic diagram of thermal evaporation (right).

Cu layers of different thicknesses were deposited on SnS thin films using a Thermal evaporator. Cu metal pieces with a purity of 99.99 % were used as the evaporation material. The initial pressure of the thermal evaporation chamber was kept at 4×10^{-5} Torr for all depositions. A high current (~ 190 A) was applied between the ends of the tungsten boat with

metal pieces. An inbuilt quartz crystal thickness monitor (sigma instruments model SQM-160) of the evaporation system was used to estimate the thickness of formed copper layers, which was confirmed by a Stylus profilometer (KLA Tencor model Alpha Step D-100) afterward.

2.1.3 Annealing of the stacked precursor layers in the sulfur atmosphere (sulfurization)

Stacked layers of Cu/SnS thin films were cut into small pieces (2.5 x 2 cm) and annealed in a sulfur atmosphere. Figure 2.3 represents Lindberg/Blue M™ Mini-Mite tube furnace equipment (left) and a schematic representation of the sulfurization process (right). The sulfur powder was taken inside a semi-cylindrical glass vessel (12 x 2.5 cm) above which samples were placed. The samples and the glass vessel were wrapped with aluminum foil and loaded inside the quartz tube furnace. To avoid sample contamination, high-purity nitrogen gas was circulated into the tube furnace throughout the experiment at extremely low pressure. The tube furnace was heated to the desired temperature and kept there for the required duration using an inbuilt temperature-controlling program of the equipment. The samples were allowed to cool down naturally to room temperature.

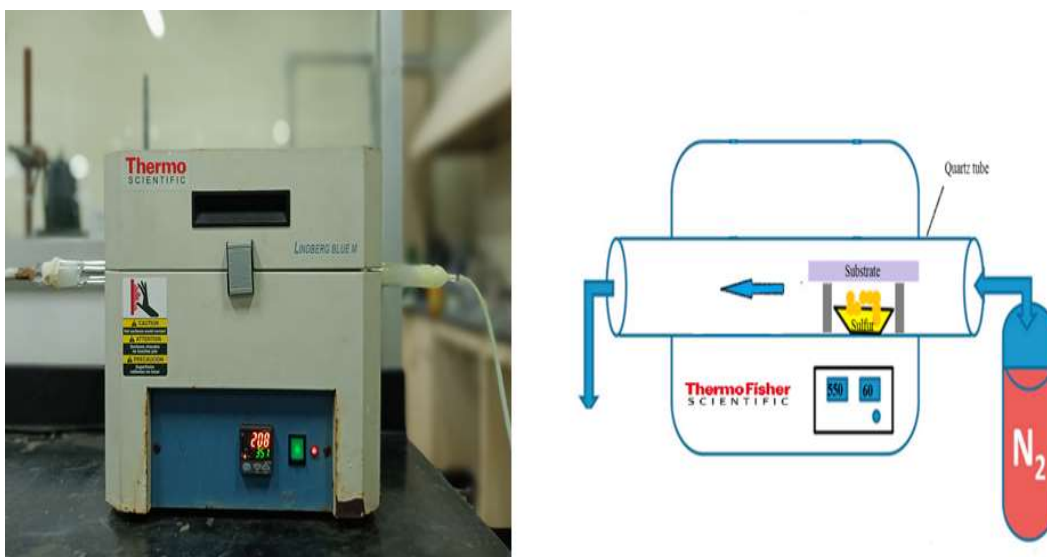


Figure 2.3 Lindberg/Blue M™ Mini-Mite Tube Furnace equipment (left) and schematic representation of sulfurization process (right).

2.1.4 Photovoltaic device and heterojunction photodetector

Photovoltaic architectures of FTO/CdS/Cu_xSn_yS_z/Ag or FTO/Cu_xSn_yS_z/CdS/Ag were fabricated using Cu_xSn_yS_z thin films deposited by the three-stage process mentioned above (section 2.1.1 to 2.1.3). CdS thin film deposited by chemical bath deposition at 70 °C for 40 minutes, was used as the n-type layer. 100 ml of CdS chemical bath was prepared by sequentially mixing 10 ml of 0.1 M cadmium chloride (CdCl₂), 5 ml of 3.7 M triethanolamine (N[CH₂CH₂OH]₃), 10 ml of 15 M ammonium hydroxide (NH₄OH), 10 ml of 1 M thiourea (CH₄N₂S) and 65 ml of preheated deionized water (at 70 °C) [92]. Cu₂SnS₃ thin films were deposited on FTO or FTO/CdS stack according to the device configuration described above (Figure 2.4). Conductive silver paint was used for contact electrodes.

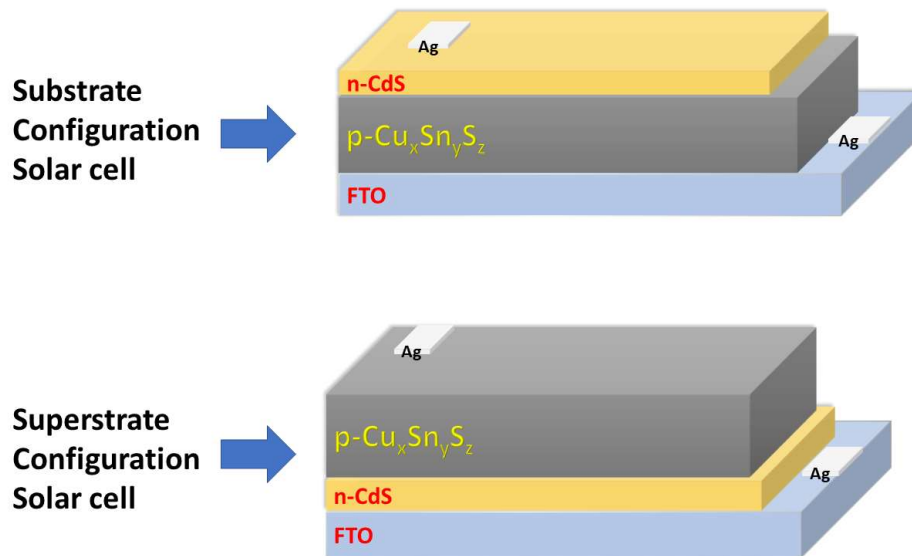


Figure 2.4 Substrate and superstrate photovoltaic structures of thin film solar cells.

The same device structure was used in a photoconductive mode for self-powered photodetector applications by painting electrodes on the top. Laser sources of different wavelengths (532, 785, 840, 980, and 1064 nm) and 30 W LEDs were used in this study to evaluate the detection capabilities of the photodetection device.

2.2 Characterization techniques

The crystal structure, chemical composition, surface morphology, and optical and electrical characteristics of synthesized samples were studied using XRD, Raman spectroscopy, XPS, SEM, EDX, AFM, UV-Vis-NIR spectroscopy, and I-V measurements. A detailed discussion of the characterization techniques is described in this part.

2.2.1 X-ray diffraction (XRD)

XRD technique was employed to gain information on the crystal structure, phases, preferred crystal orientations (texture), average grain size, strain, and crystal defects. The X-rays produced by the source get diffracted by the sample and enter the detector. When the sample has a repetitive arrangement of atoms, the scattered X-ray waves will experience constructive interference in some particular directions that obey Bragg's law. A Malvern PANalytical Empyrean XRD instrument equipped with Cu K α radiation ($\lambda=1.5406 \text{ \AA}$) in Bragg-Brentano reflection configuration was used to measure the diffraction patterns of samples. XRD patterns were measured in normal incidence mode (scan range 5 to 80°) and compared with JCPDS/PDF files to identify the structures and phases present in the sample. The average crystallite size of the films was computed using the Debye Scherrer formula (equation 2.2) [93].

$$D = \frac{k \lambda}{\beta \cos \theta} \quad (\text{equation 2.2})$$

where β is the broadening of the diffraction line measured at half maximum intensity (radians), $\lambda = 1.5406 \text{ \AA}$ (wavelength of the X-ray source radiation) and θ is the Bragg's angle. Where k is the shape factor of the crystallites which is assumed to be 0.9 for spherical. The dislocation density (δ) was computed using the relation (equation 2.3) [94].

$$\delta = \frac{1}{D^2} \quad (\text{equation 2.3})$$

where D is the average crystallite size calculated from the Debye-Scherrer formula.

2.2.2 Raman spectroscopy

Raman spectroscopy is a light scattering technique based on the interaction of light with the chemical bonds within a material. Since the different bonds in molecules vibrate at different frequencies, different molecules will absorb unique frequencies of light and get excited to different vibrational levels. Most of the light will be elastically scattered (Rayleigh scattering) whereas a fraction of light ends up in characteristic inelastic scattering (Raman scattering). Raman spectrum will give knowledge about chemical bonding, properties of molecular structures, chemical environment, and amorphous impurities. It is used to distinguish between different crystal structures of Cu-Sn-S thin films due to its similitude in X-ray diffraction peaks.

A Thermo-Scientific DXRTM3 microscope with a 532 nm monochromatic laser was employed for the Raman spectroscopy experiments. The Raman spectrum between 50 and 3000 cm^{-1} was captured for the analysis.

2.2.3 Scanning electron microscope (SEM)

Scanning electron microscopy is used to study the surface morphology of the samples. It applies a focused beam of high-energy electrons to the surface and generates a variety of signals from the sample. Interaction of the electron beam with the sample will produce several signals containing secondary electrons, back-scattered electrons, and unique X-rays depending on the depth of interacted atoms. The signals produced from interactions between electrons and specimens provide details on the exterior morphological features, chemical content, and grain growth of the sample. Secondary electrons aid to generate surface images while backscattered electrons help to demonstrate the different phases present [95]. Uniform and compact bigger grains are essential for photovoltaic applications which are imaged with the help of this technique.

In this study, a Hitachi SU8020 SEM with cold cathode field emission source was utilized for the imaging of the samples. An acceleration voltage between 0.5 and 4 kV and current between 1 and 25 μA were applied.

2.2.4 Atomic force microscope (AFM)

With the help of AFM, it is possible to acquire 3D images of samples without any complicated sample preparation procedures. An atomic force microscope can give a field view extending from atomic scales to several micrometers. AFM 3D images give nano-scale information on surface roughness, defects, and nucleation/growth modes. It can be operated in different modes such as contact mode and semi-contact mode. The primary element of AFM consists of a microcantilever with a pointed tip and a laser beam that falls on the tip. The irradiated laser is reflected into a set of photodiodes that gives an electric signal relative to the deviation of beam power impacting the photodiodes [96].

In this study, the NT-MDT AFM SOLVER PRO device was employed in contact/semi-contact mode and NT-MDT image analysis software was used for image acquisition and analysis.

2.2.5 X-ray photoelectron spectroscopy (XPS)

X-ray photoelectron spectroscopy is a surface-sensitive technique to assess the chemical state, bonding structure, and composition of surfaces and interfaces. The basic principle behind X-ray photoelectron spectroscopy is the emission of electrons from the surfaces when irradiated by suitable electromagnetic radiation. This phenomenon is termed the photoelectric effect and was explained by Einstein in 1905. The energy of the emitted electrons depends on the energy of the incident photon and electrons are ejected only if the energy of photons has a minimum energy to eject electrons from the atom which is called the work function. The kinetic energy of these ejected electrons will be measured by a detector and then translated into binding energies [97].

In this work, a Thermo Scientific K α X-ray photoelectron spectrometer system capable of depth profiling was used to analyze various samples of interest. XPS survey scan was employed to find elements present on the surface of the sample and a high-resolution scan aided to study the oxidation state of elements. Analyses were done for the samples after a surface etching for 30 s (\sim 20–30 nm) by Ar⁺ ions of 2 keV to remove the surface

contaminants. The binding energies of different elements were determined utilizing the C1 peak at 284.6 eV as a reference for charge correction.

2.2.6 Energy dispersive X-ray spectroscopy (EDX)

The basic principle of energy dispersive X-ray spectroscopy is the generation of characteristic X-rays from a specimen when an electron beam is incident on the sample. EDX is a fast, semi-quantitative, and non-destructive characterization technique with a lateral resolution of micron range. Electrons from the atoms on the sample are expelled when an electron hits the surface. Subsequently, an electron from a higher shell fills the gap left by the expelled electron to maintain equilibrium. These energy differences between those levels will be released as characteristic X-rays and the detector counts the X-rays and determine their energies. When electron beams are incident on the samples, characteristic X-rays are produced according to the nature of the elements present in the sample [98].

In this work, the elemental composition of the samples was studied using an APEX octane detector (acceleration voltage ~ 15 kV, working distance ~ 15 cm) integrated with scanning electron microscopy (SEM, Hitachi SU8020).

2.2.7 UV-Vis-NIR spectroscopy

UV-Vis-NIR spectroscopy operates by passing a beam of light through the sample and measuring the light of a specific wavelength reaching a detector. It measures transmittance and reflectance from the UV range (250 nm) to the near IR range (2500 nm).

The equation below was used to determine the absorption coefficient.

$$\alpha = \frac{1}{d} \ln \left[\frac{(1-R)^2 + \sqrt{(1-R)^4 + (2R)^2}}{2T} \right] \quad (\text{equation 2.4})$$

where d, T, and R are the thickness, transmittance, and reflectance of the film, respectively. The Tauc relation was used to determine the bandgap from the absorption coefficient [99].

$$(\alpha h\nu)^n = C(h\nu - E_g) \quad (\text{equation 2.5})$$

where E_g is the bandgap, C is a constant, and ν is the frequency of incoming radiation. The value of the exponent (n) is related to the electronic nature of the band gap, with values of $\frac{1}{3}$, $\frac{1}{2}$, $\frac{2}{3}$, and 2 corresponding to indirect forbidden, indirect allowed, direct forbidden, and direct allowed transitions, respectively [100]. The bandgap values are estimated by extrapolating the linear portion of the $(\alpha h\nu)^2$ vs $(h\nu)$ curve to the x-axis; intercept at $y=0$ indicates the bandgap.

In this study, a JASCO V-770 spectrophotometer was used to measure the specular reflectance and transmittance of the thin films. Cleaned glass slides were used as a standard for baseline measurements in transmittance measurements and a mirror attachment for the same in reflectance measurements.

2.2.8 Photoconductivity measurements

The photocurrent response of the films was analyzed using I-V and photocurrent measurements under dark and light conditions. By measuring the photoconductive response, the electrical characteristics of the films were probed. To determine the electrical properties (I-V characteristics), two planar electrodes (5×5 mm) were coated on top of the samples utilizing a conductive Ag paint (SPI® supplies). Resistivity was measured using the equation as follows:

$$\rho = \frac{V(L_1 \times d)}{L_2 I} \quad (\text{equation 2.6})$$

where ρ is the sample resistivity (Ωcm), L_1 , L_2 length and separation of the silver electrodes (cm), d is the film thickness (cm), I is the current (A), and V is the applied voltage (V).

To evaluate the photodetection abilities, cyclic photoresponse measurements were done under the illumination of a halogen source, 30 W LEDs of different wavelengths, 532, 785, and 1064 nm lasers with variable power densities, and 840 and 980 nm diode lasers with fixed power. A voltage was applied, and the corresponding current was measured using a Keithley Pico ammeter (model 6487), which is connected to a computer for data acquisition (Figure 2.5). The rise and decay time of the photodetection device for different wavelengths were measured and values were determined by fitting using origin software.



Figure 2.5 The Keithley Pico ammeter (model 6487) and data acquisition computer for I-V measurements.

Cu-Sn-S thin films were fabricated utilizing a three-stage process that includes chemical bath deposition, thermal evaporation, and sulfurization. Various characterization methods have been used for the evaluation of the properties of Cu-Sn-S films. Furthermore, thin films with optimized properties were used to fabricate thin film solar cells and photodetection devices.

CHAPTER 3

SYNTHESIS AND CHARACTERIZATION OF SnS and Cu₄SnS₄ THIN FILMS

This chapter demonstrates the synthesis and characterization of the SnS thin film precursor layer and Cu₄SnS₄ thin films. SnS precursor layer was deposited using chemical bath deposition and the formation of SnS was confirmed using different characterization techniques. Phase pure Cu₄SnS₄ remains one of the least explored phases in the Cu-Sn-S family. The effect of the copper precursor layer on the synthesis and properties of Cu₄SnS₄ thin films were studied.

3.1 Synthesis and characterization of SnS precursor thin films

SnS thin films were deposited using CBD as described in the general experimental methodology (section 2.1.1). Chemical bath deposition for 17 h at 40 °C resulted in dark brown thin films of thickness 450 nm and the surface was found to be uniform. Figure 3.1 represents the chemical bath after 17 h of reaction and resulting films.

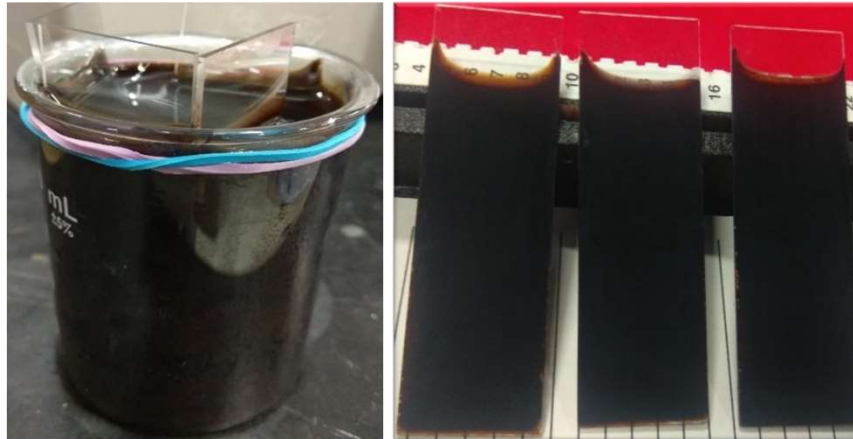


Figure 3.1 SnS chemical bath after 17 hours and obtained SnS thin films

3.1.1 Structure analysis - XRD and Raman spectroscopy

XRD analysis was employed to determine the crystal structure of synthesized SnS thin films. Figure 3.2(a) depicts the diffraction pattern (normal incidence) along with the standard pattern of orthorhombic SnS (JCPDS # 01-073-1859). The diffraction pattern reveals the formation of orthorhombic SnS with prominent peaks at 30.7, 31.6, 31.7, and 38.8° which corresponds to (0 1 1), (1 1 1), (3 0 1), and (3 1 1) reflection planes, respectively. The formation of SnS is further confirmed by analyzing the vibrational modes present in the Raman spectrum. Figure 3.2(b) represents the Raman spectrum of the synthesized SnS film. Raman spectrum of SnS thin film exhibits peaks at 44, 95, 160, 173, 223, and 307 cm^{-1} . Intense peaks at 95 and 223 cm^{-1} are associated with the first order single phonon A_g modes reported for SnS [101]. Intense peaks at 44 and 160 cm^{-1} are also consistent with the A_g and B_{3g} vibration modes of SnS. These peak positions are also in agreement with previous reports [102,103]. The peak at 307 cm^{-1} indicates the presence of the Sn_2S_3 phase in the films [104]. Mahdi et. al. also reported Sn_2S_3 peaks along with SnS vibrational peaks while using the chemical bath deposition technique [105]. The formation of SnS was confirmed by combining the outcomes of XRD and Raman analysis.

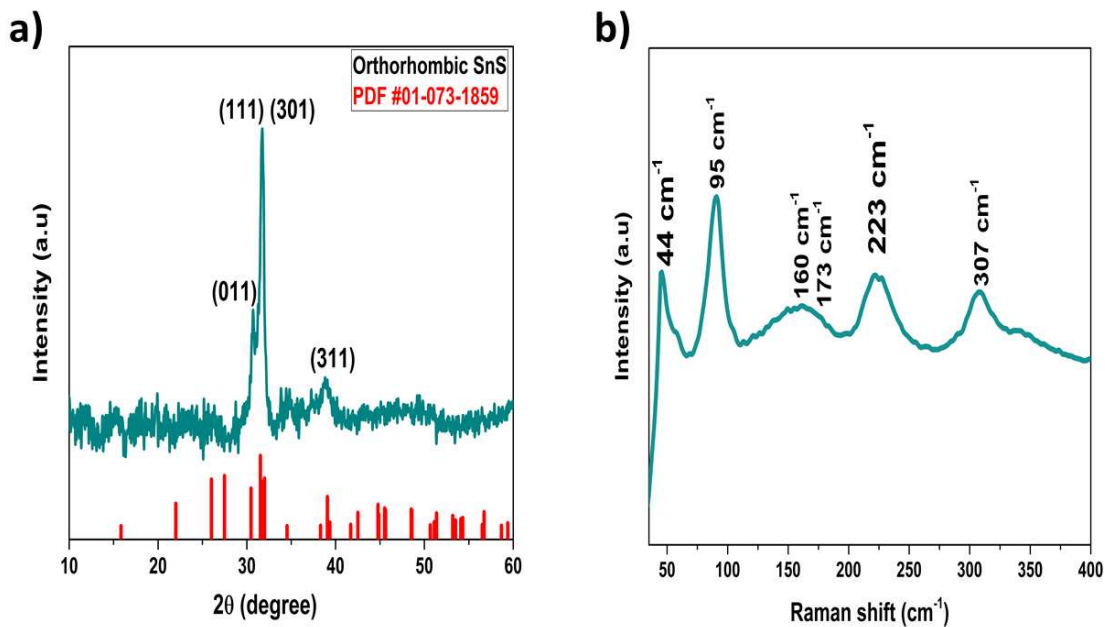


Figure 3.2 a) XRD pattern of SnS thin film with a standard pattern of orthorhombic SnS and, b) Raman spectrum of SnS thin film.

3.1.2 Chemical composition- XPS

The chemical composition of SnS thin film was studied using XPS analysis. Figure 3.3(a) shows survey scan of SnS thin film and figure 3.3(b) represents the core electron high-resolution spectrum of tin and sulfur. The background of peaks was determined using a Shirley function, and the binding energy of C1s (284.6 eV) was utilized for the binding energy correction. Characteristic peaks from the XPS survey spectrum confirmed the presence of Sn and S elements. The core level spectrum of Sn consists of doublets at 485.5 and 493.9 eV with an energy difference of 8.4 eV. These peaks are associated with Sn 3d_{5/2} and Sn 3d_{3/2} states and confirm the presence of the Sn⁴⁺ state [106]. The deconvoluted core level spectrum of sulfur shows two peaks at 161.28 and 162.48 eV with an energy separation of 1.2 eV. These values are accounted for S p_{3/2} and S p_{1/2} doublet peaks and confirm the presence of S²⁻ [107].

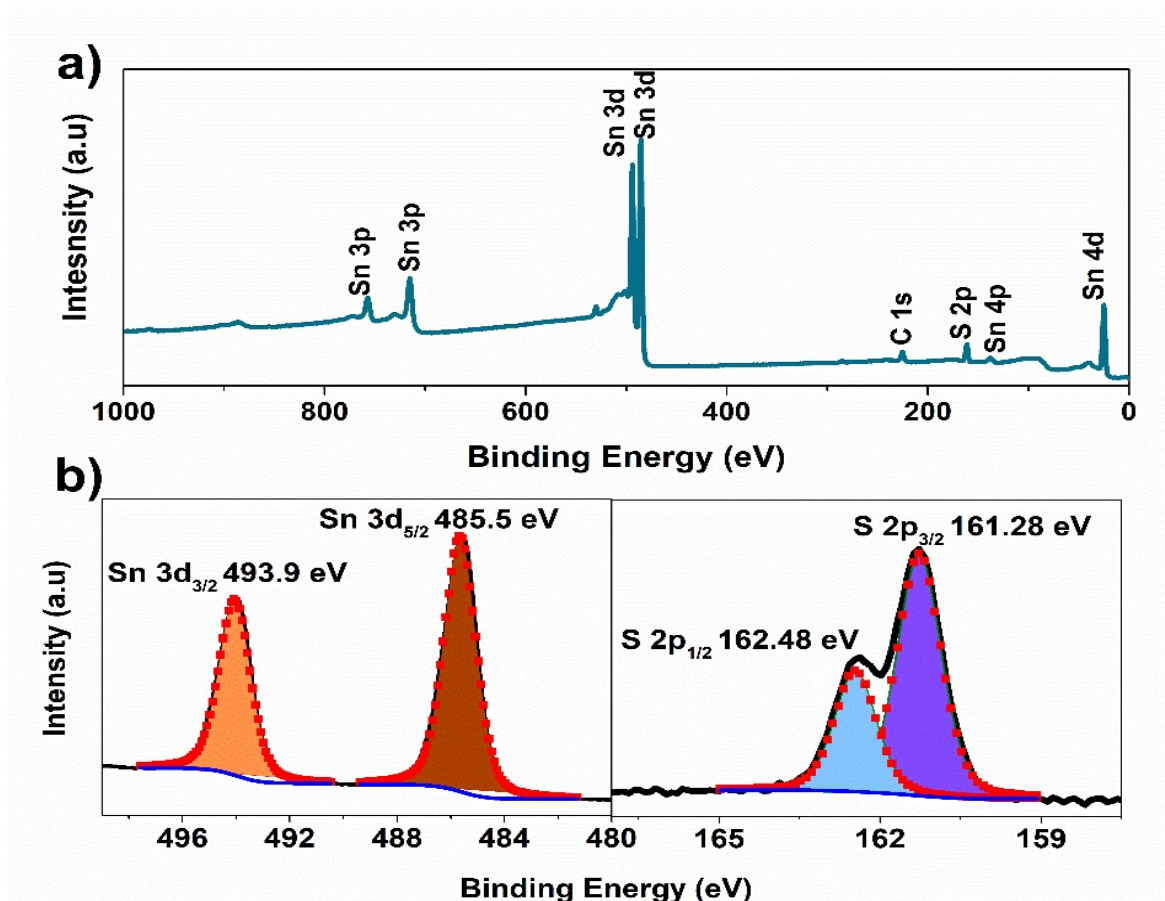


Figure 3.3 XPS (a) survey and (b) core level spectra of Sn and S from SnS thin film.

3.1.3 Elemental composition- EDX

The elemental composition of SnS thin film was studied using EDX analysis and the elemental mapping of Sn and S are given in Figure 3.4(a-b). SnS thin films show a slightly tin-rich composition with an elemental composition of Sn= 57.3 % and S= 42.7 %. EDX elemental mapping reveals the uniform distribution of Sn and S throughout the SnS thin film.

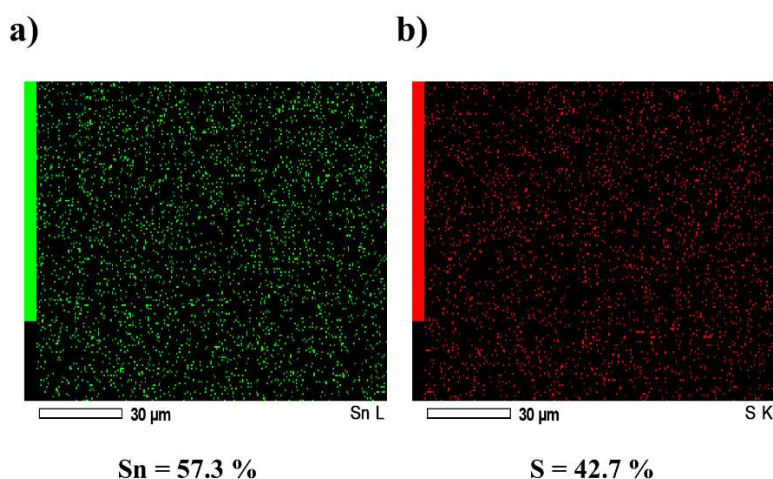


Figure 3.4 EDX elemental mapping of (a) Sn, and (b) S of SnS thin film.

3.1.4 Surface morphology- SEM and AFM

The surface morphology of SnS thin film was studied using scanning electron microscopy (SEM) and the corresponding SEM image is given in Figure 3.5(a). The surface morphology of SnS shows uniformly distributed clusters of petals like grains. Flower-like surface morphology of SnS is also evident from the magnified SEM image (Figure 3.5(b)). The surface morphology of SnS was also studied using 3D and 2D AFM imaging given in Figure 3.5(c-d). Three-dimensional images of SnS film give a better understanding of the height variations of the grains on the surface. The average roughness value of SnS film was found to be 24 nm from image analysis. AFM images are consistent with SEM images and exhibit a uniform distribution of grains throughout the surface.

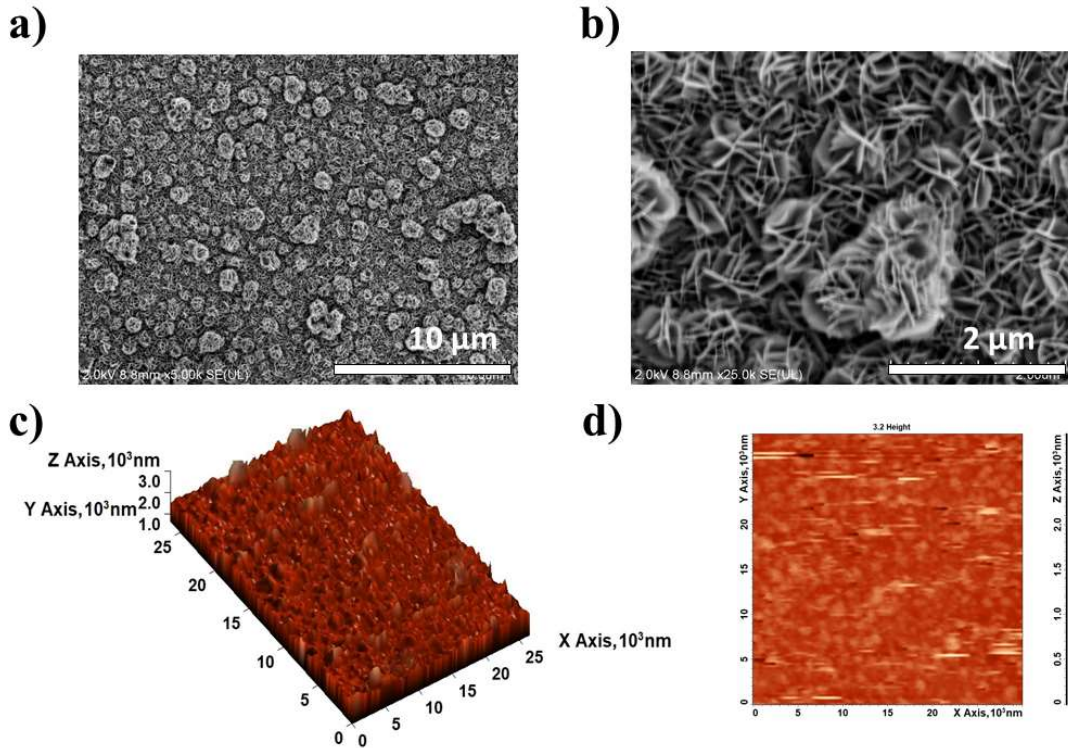


Figure 3.5 (a,b) SEM images, (c) 3D AFM image, and (d) 2D AFM image of SnS thin film.

3.1.5 Optical characterization

Figure 3.6(a) represents the transmittance and specular reflectance of the SnS thin film. SnS film shows high transmittance and low reflectance values in the NIR region whereas complete absorption in the UV region. The absorption coefficient of SnS thin film was calculated using measured values of transmittance and reflectance using equation 2.4: Calculation shows a high absorption coefficient $>10^4 \text{ cm}^{-1}$ for SnS thin film in the UV-Vis region. The optical bandgap of deposited SnS film is 1.46 eV with a direct transition, (figure 3.6(b)) which makes it suitable for photovoltaic applications.

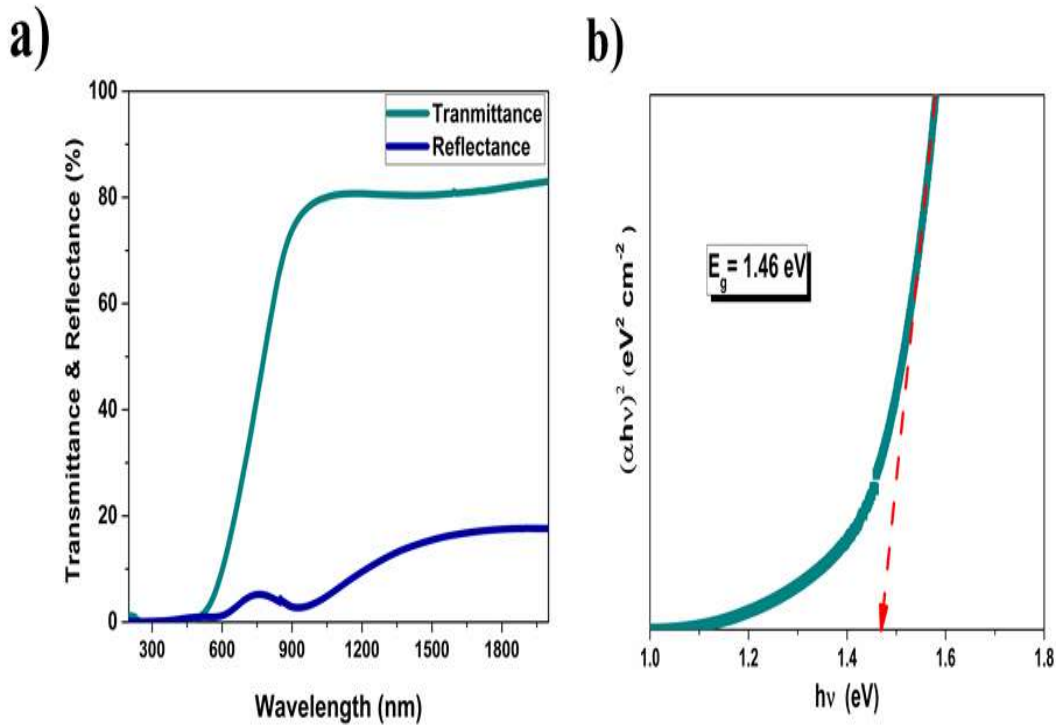


Figure 3.6 (a) Transmittance and specular reflectance (b) Tauc plot of SnS thin film.

3.1.6 Electrical characterization

Electrical properties of SnS thin film were evaluated using photoresponse measurements by painting two planar electrodes (7 x 7 mm), with a separation of 7 mm on the surface of the sample, and electrical conductivity (σ) obtained were 2.11×10^{-4} and $5.4 \times 10^{-4} (\Omega \cdot \text{m})^{-1}$ in dark and light conditions, respectively. Figure 3.7 represents the cyclic photoresponse of SnS thin films (20 s dark- 20 s light- 20 s dark) under a bias voltage of 10 V. SnS thin film exhibits a transient photoconductive response due to the presence of charge carrier trap levels inside the material [108]. The thicknesses of SnS film deposited via chemical bath deposition (40 °C) are 150, 200, and 450 nm for 5, 6, and 17 h depositions, respectively.

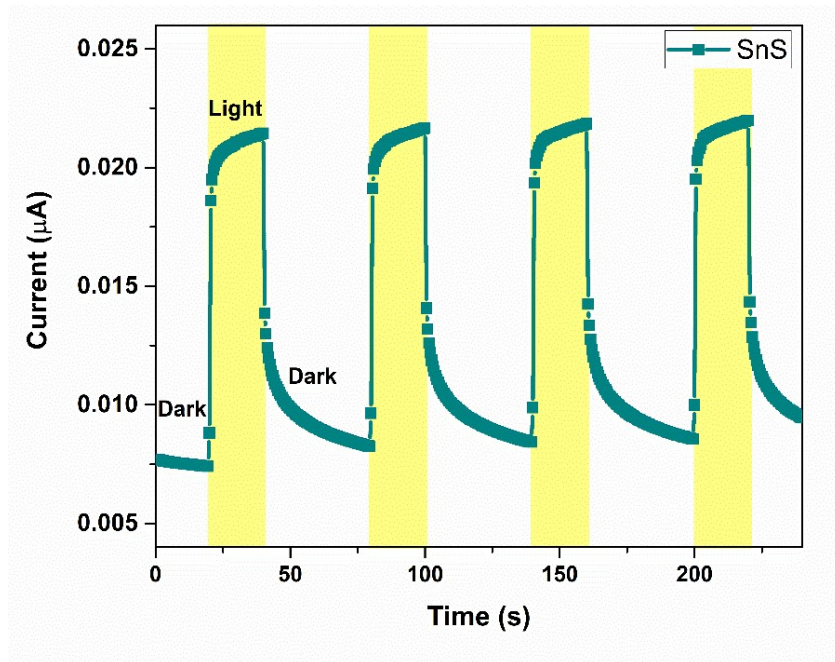


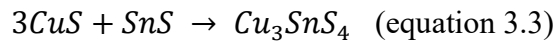
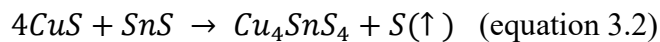
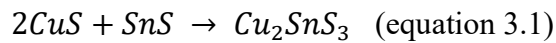
Figure 3.7 Cyclic photoresponse of SnS thin films under a bias voltage of 10 V.

This SnS precursor layer deposited via chemical bath deposition was used to synthesize Cu-Sn-S thin films.

3.2 Role of Cu precursor layer thickness on the formation and the properties of Cu₄SnS₄ thin films

This section demonstrates the effect of Cu precursor layer thickness on the formation and the properties of Cu₄SnS₄ thin films. The thin films were fabricated by the sulfurization of stacked layers of thermally evaporated copper layer on SnS thin film.

Different phases of Cu-Sn-S thin films are formed by the reactions as follows, Cu reacts under a sulfur atmosphere forming CuS. This reacts with SnS to form different stoichiometries of Cu-Sn-S thin films [54,68].



The structure, morphology, composition, optical properties, and electrical characteristics of Cu₄SnS₄ thin films were investigated using a variety of characterization methods. Copper layers of thicknesses 150, 175, 185, and 200 nm were deposited on SnS precursor thin film of 200 nm (chemical bath deposition for 6 h). Stacked Cu/SnS layers were sulfurized at 500 and 550 °C for 1 h using 20 mg of sulfur powder. A photovoltaic architecture of FTO/Cu₄SnS₄/CdS/Ag was fabricated, and photovoltaic parameters were evaluated.

3.2.1 X-ray diffraction analysis

Preliminary studies were conducted by annealing Cu/SnS thin film layers under a sulfur atmosphere at 500 °C temperature for 1 h. XRD patterns of samples annealed at 500 °C confirm the formation of Cu₄SnS₄ with impurities and are presented in figure 3.8. Deposited films show poor crystallinity and the presence of binary sulfides of copper and tin. As copper layer thickness increases, the peak intensity of secondary phases of copper also increases. This preliminary experiment led to the assumption that annealing at higher temperatures is essential for the conversion of Cu/SnS stacks completely into the ternary phase and the minimization of secondary phases.

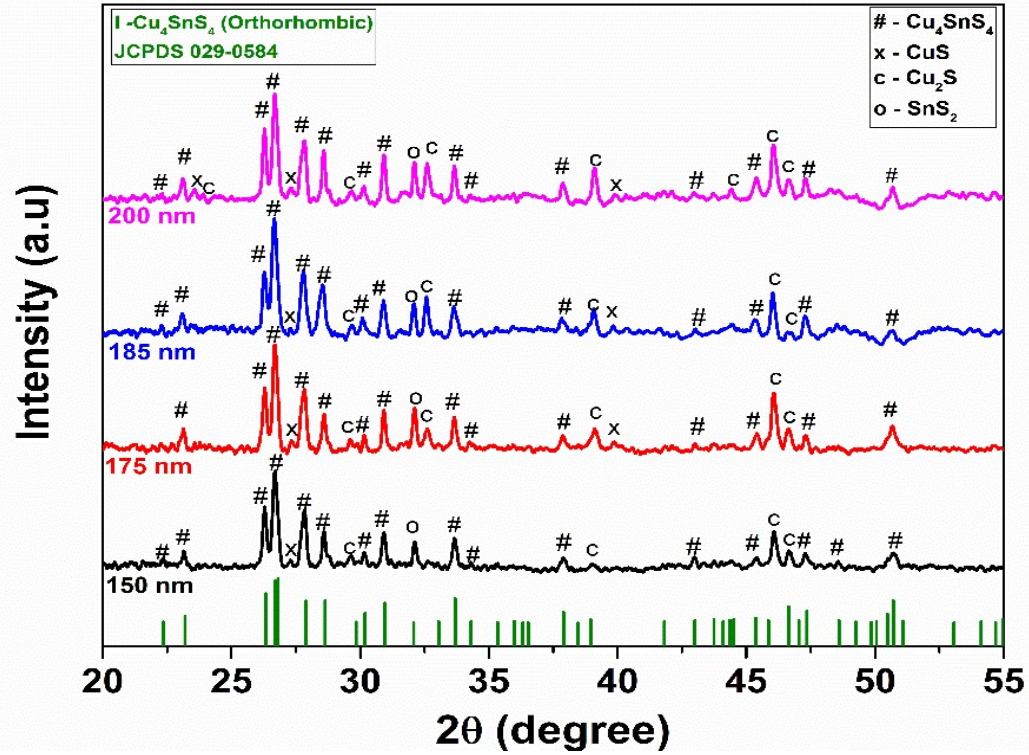


Figure 3.8 XRD patterns (relative intensity) of Cu_4SnS_4 samples with copper thicknesses of 150, 175, 185, and 200 nm sulfurized at 500 °C for 1 h.

XRD patterns (relative intensity) of the Cu_4SnS_4 films prepared by the sulfurization of stacked SnS/Cu layers at 550 °C for 1 h are shown in figure 3.9. Characteristic peaks of Cu_4SnS_4 are found at 26.27, 26.65, 26.75, 27.84, 28.58, 30.9, and 33.64°, which corresponds to reflection from (400), (220), (311), (121), (102), (112), and (321) planes, respectively (JCPDS #00-029-0584). Samples with lower thickness of Cu show binary sulfide of tin and samples with higher Cu thickness exhibit binary sulfide of copper. SnS_2 peaks in the 150 and 175 nm samples agree with JCPDS #00-900-0613 whereas those in 185 and 200 nm samples show peaks related to CuS (JCPDS #00-900-8371) and Cu_2S (JCPDS #01-072-1071). Significant crystal growth along the (102) plane (peak at 28.58°) is visible with increasing thickness of the copper layer from 150 to 185 nm. The film with a copper layer thickness of 200 nm, exhibits a characteristic peak at 27.31° which is accounted to the reflection from the (200) plane of Cu_3SnS_4 (JCPDS #00-036-0217). An increase in copper layer thickness from 150 to 185 nm led to the conversion of binary sulfides into the Cu_4SnS_4 phase and ultimately to the Cu_3SnS_4 phase. This is due to an increase in the reactivity of the copper by the

participation of a greater proportion in the reaction as reported by Wang et. al. [109]. When copper layer thickness is increased, more copper atoms react under sulfur atmosphere to form crystalline ternary phase. This increase in the crystallinity is also visible in the improvement of the peak intensity of the (102) plane.

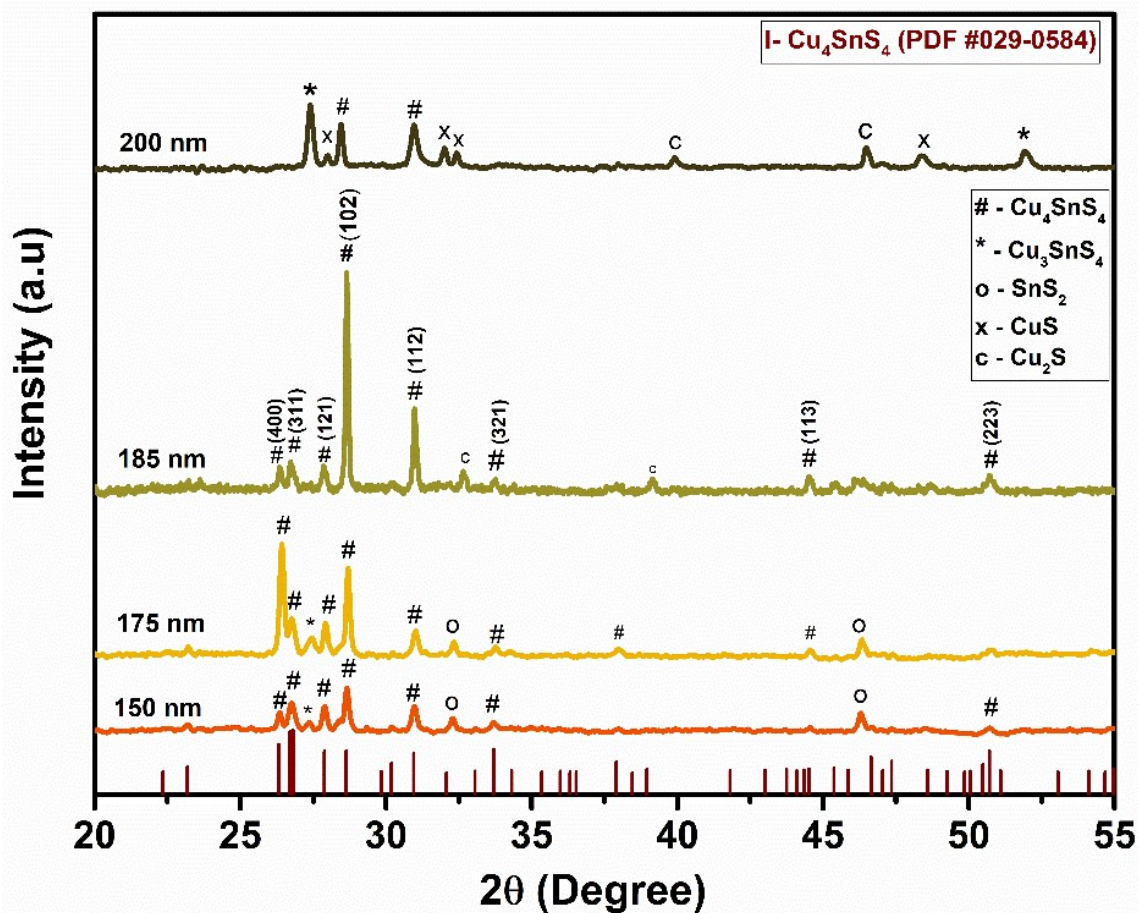


Figure 3.9 XRD patterns of Cu₄SnS₄ samples of Cu thicknesses of 150,175,185 and 200 nm sulfurized at 550 °C for 1 h along with Cu₄SnS₄ (JCPDS #029-0584) standard pattern.

3.2.2 Raman analysis

The thin films were characterized using Raman spectroscopy for the confirmation of the phases (Figure 3.10). 150, 175, and 200 nm samples exhibit an intense peak at 315 cm⁻¹ whereas highly oriented 185 nm sample display an intense peak at 316 cm⁻¹. The sample with a Cu layer of 150 nm shows a low intense peak at 287 cm⁻¹ and the 200 nm sample shows a small peak at 470 cm⁻¹. The intense peak of the 185 nm sample at 316 cm⁻¹ is close to the

values reported for Cu_4SnS_4 by different research groups [110–112]. According to previous reports, a small peak at 287 cm^{-1} accounted for SnS vibrations [113] and a peak at 470 cm^{-1} to that of the binary phase of copper [53,114]. Raman peaks within $310\text{--}320\text{ cm}^{-1}$ are also assigned to SnS_2 , Cu_2SnS_3 (Wurtzite), Cu_2SnS_3 (Monoclinic), Cu_2SnS_3 (Triclinic), Cu_3SnS_4 (Orthorhombic), $\text{Cu}_2\text{Sn}_3\text{S}_7$ (Monoclinic), and Cu_4SnS_4 (Orthorhombic) phases [40,115,116]. By combining the observations from XRD and Raman analysis, it could be concluded that there exists an optimum value for copper precursor layer thickness for the formation of preferentially orientation Cu_4SnS_4 . In this work, 185 nm film exhibited the highest intense diffraction peaks and better preferential crystalline orientation along (102) and (112) planes with negligible presence of secondary phases.

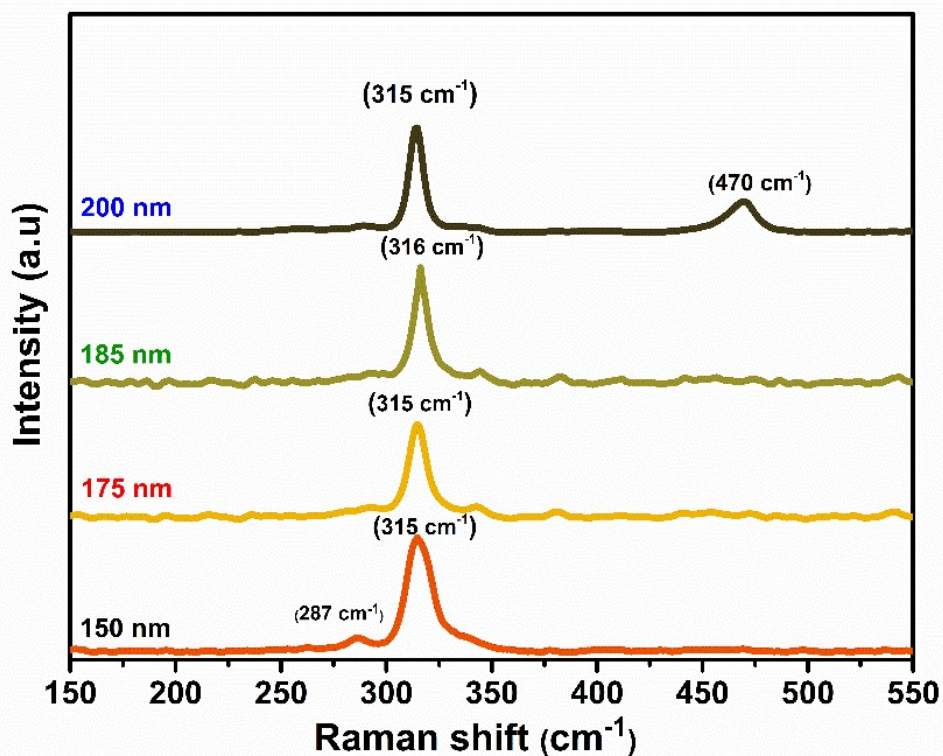


Figure 3.10 Raman spectra of the 150, 175, 185, and 200 nm samples.

3.2.3 Compositional analysis - XPS

The chemical environment of Cu, Sn, and S in the synthesized Cu_4SnS_4 thin films was analyzed using XPS. Figure 3.10(a) shows the XPS survey spectrum of the 185 nm sample sulfurized at $550\text{ }^\circ\text{C}$ for 1 h and the high-resolution spectra for the elements Cu, Sn, and S

are presented in Figure 3.11(b-d). The XPS survey shows peaks corresponding to the elements: Cu, Sn, S, C, and O. Surface contamination due to oxidation of the film is responsible for the presence of oxygen in the survey spectrum [69]. The core level spectrum of Cu consists of (Figure 3.11(b)) doublets at 932.11 and 951.94 eV with an energy separation of 19.8 eV. These values are consistent with spin-orbit coupling doublet states of Cu and confirm the presence of the Cu^{1+} state. The core level spectrum of Sn (Figure 3.11(c)) shows doublets at 486.01 and 494.41 eV with an energy difference of 8.4 eV. These peaks are associated with Sn $3d_{5/2}$ and Sn $3d_{3/2}$ states and confirm the presence of Sn in the Sn^{4+} state. Deconvoluted peaks at 161.45 eV and 162.63 eV with charge splitting of 1.18 eV in the core level spectrum of S (Figure 3.11(d)) can be associated with S $2p_{3/2}$ and S $2p_{1/2}$ states, which indicates the presence of S in -2 oxidation state [69]. Elements Cu, Sn, and S with +1, +4, and -2 oxidation states confirm the formation of the Cu_4SnS_4 phase.

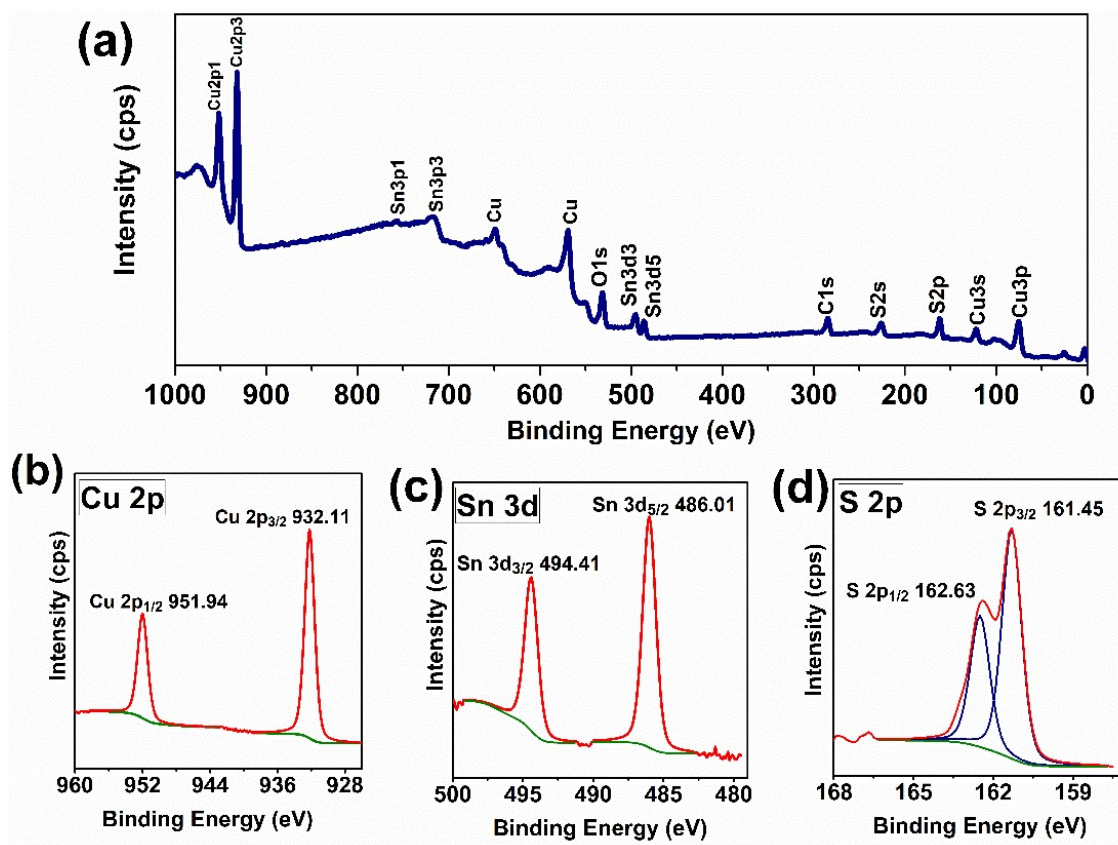


Figure 3.11 XPS (a) survey scan, and core level spectra of (b) Cu, (c) Sn, and (d) S of 185 nm sample.

3.2.4 EDX analysis

The elemental composition of the Cu_4SnS_4 thin films was evaluated using EDX analysis. The obtained chemical composition results are tabulated in Table 3.1 along with the corresponding Cu/Sn ratio.

Table 3.1 Elemental composition from EDX analysis and Cu/Sn ratio of Cu_4SnS_4 films with different copper layer thicknesses.

Sample	Cu	Sn	S	Cu/Sn
150 nm	40.9	9.55	49.47	4.2
175 nm	46.37	7.98	45.6	5.8
185 nm	41.78	9.26	48.8	4.5
200 nm	50.93	3.35	45.72	15.2

The 200 nm sample with a higher content of binary sulfides of copper shows a higher Cu/Sn ratio as expected. Phase pure 185 nm sample exhibits slightly higher copper and sulfur stoichiometry. Unfortunately, copper-deficient Cu-Sn-S thin films are predicted to have better properties for photovoltaic applications [117]. Shallow acceptor vacancies formed upon copper-deficient conditions are projected to be beneficial for enhancing photovoltaic parameters [51]. The formation of copper-rich and sulfur-rich thin films might be caused by the evaporation of tin at higher temperatures. The elemental composition of thin films has to be controlled by further iterations in sulfurization parameters.

3.2.5 Surface morphology-SEM

SEM images of films with a copper layer thickness of 150 to 200 nm are presented in Figure 3.12(a-d). Surface morphology analysis reveals bigger spherical particles on the top and a smooth compact layer underneath for 150 to 185 nm thin films. 200 nm sample shows a

microstructure comprised of coral-like fused grains of tiny flakes. The increase in copper layer thickness significantly affects the surface morphology of the films. The grain size of the films was augmented with the copper layer thickness until a phase change occurred in the sample with 200 nm copper thickness. This trend of increase in grain growth and surface modification is also reflected in crystalline size values estimated using the Debye-Scherrer formula (equation 2.2). Crystallite size values are 43.9, 45.4, 52.7, and 33.6 nm for the 150, 175, 185, and 200 nm samples, respectively.

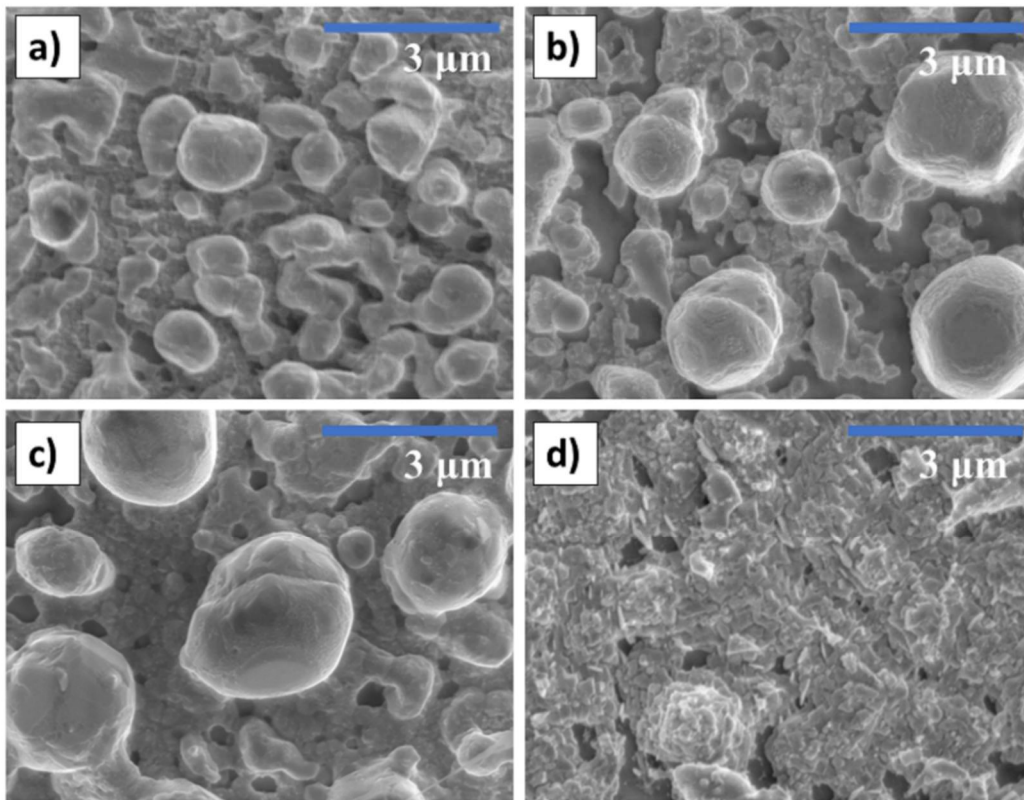


Figure 3.12 SEM images (a) 150, (b) 175, (c) 185, and (d) 200 nm samples, respectively.

3.2.6 Surface topography - AFM

The surface topography of films was studied using AFM for a three-dimensional understanding of the surface. 3-D images of films sulfurized at 550 °C for 1 h with a copper layer thickness of 150, 175, 185, and 200 nm are presented in Figure 3.13(a-d). Average

roughness values of Cu_4SnS_4 films are 52, 61, 63, and 47 nm for 150, 175, 185, and 200 nm samples, respectively. This increase in roughness might be due to the growth of preferentially oriented grains perpendicular to the surface. These bigger grains observed from the topographical analysis are consistent with SEM images.

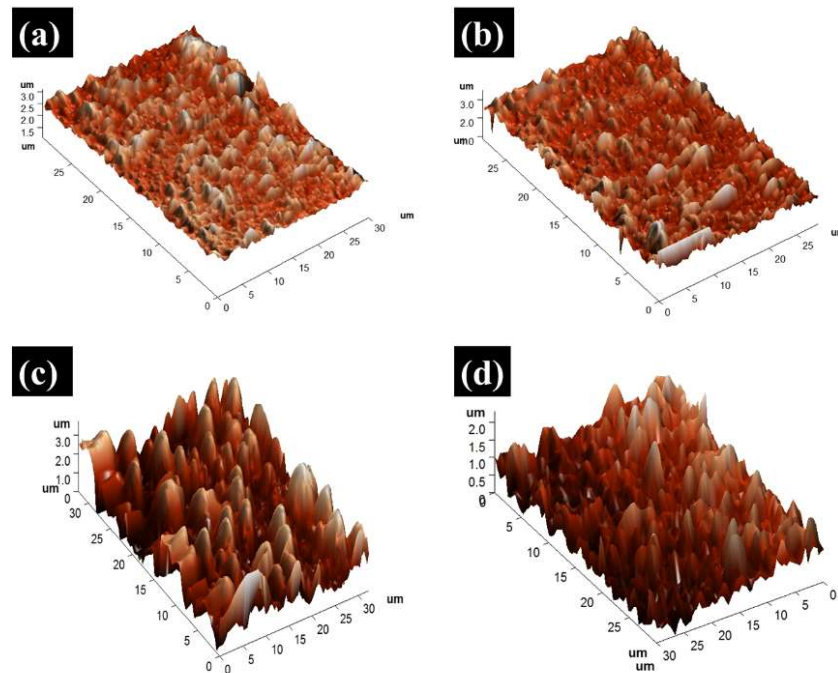


Figure 3.13 AFM images of (a) 150, (b) 175, (c) 185, and (d) 200 nm thin films

3.2.7 Optical characterization

The optical absorption of Cu_4SnS_4 thin films (wavelength range 350-2500 nm) is represented in Figure 3.14. The thin films show high absorption in the visible region in the order of 150, 175, 200, and 185 nm. The preferentially oriented 185 nm sample exhibits the highest absorption. The transmittance and reflectance spectra of Cu_4SnS_4 films are given in Figure 3.15(a-b). The thin films display poor transmittance and reflectance due to the presence of binary and ternary impurity phases. The metallic nature of Cu_4SnS_4 thin films may further contribute to their poor transmittance in the visible spectrum [69]. Zhao et. al. have reported the impact of binary sulfides of copper and tin on the optical characteristics of Cu-Sn-S thin

films. They proposed that binary phases act as defects and trap centers which consequently affect the optical properties of the films [118].

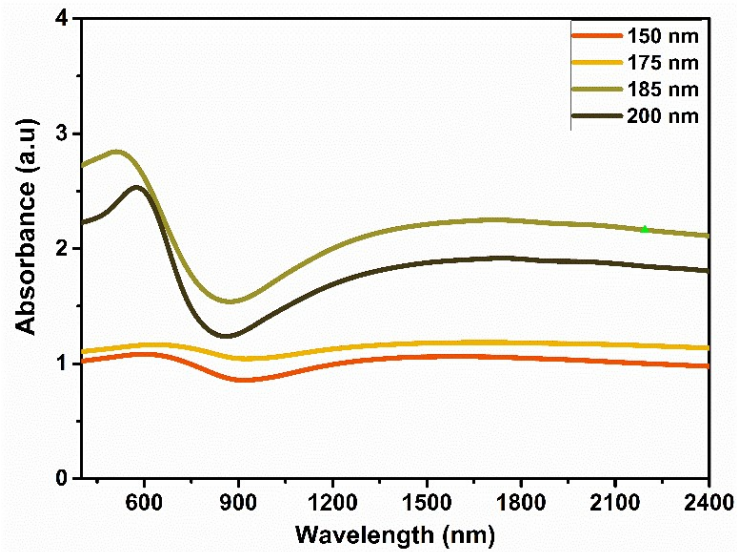


Figure 3.14 Absorbance spectra of Cu_4SnS_4 samples with copper thickness 150 to 200 nm sulfurized at 550 °C for 1 h.

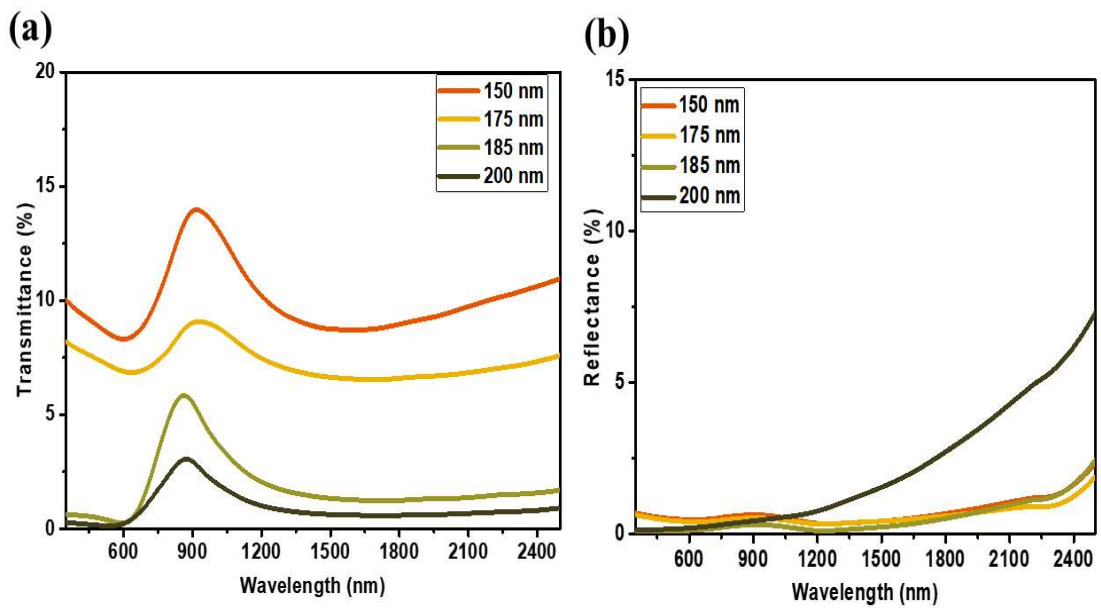


Figure 3.15 (a) Transmittance and (b) reflectance spectra of Cu_4SnS_4 samples with copper thickness 150 to 200 nm sulfurized at 550 °C for 1 h.

Using equation 2.4, the absorption coefficient was computed. According to the calculations, Cu_4SnS_4 thin films do have high optical absorption in the visible region ($\alpha \sim 10^5 \text{ cm}^{-1}$). The optical band gap (E_g) of the films was calculated using the Tauc relation (equation 2.5) and the Tauc plots of Cu_4SnS_4 films are presented in Figure 3.16. The bandgap energies of the synthesized films were 1.18, 1.05, 1.43, and 1.62 eV for 150, 175, 185, and 200 nm samples, respectively. Similar bandgap values are reported for Cu_4SnS_4 and Cu_3SnS_4 in the literature [54,68,69,73,112]. Preferentially oriented 185 nm film shows a suitable bandgap of 1.43 eV, whereas 150 and 175 nm films display lower optical bandgap due to the presence of binary phases. This phenomenon has already been reported for the Cu-Sn-S thin films synthesized by chemical methods [119]. The sample with 200 nm thickness exhibits a direct bandgap of 1.62 eV and comparable values are reported for Cu_3SnS_4 by various research groups [120,121]. Preferentially oriented 185 nm film with a high absorption coefficient and optimum bandgap of 1.43 eV is proposed as a promising candidate for photovoltaic applications.

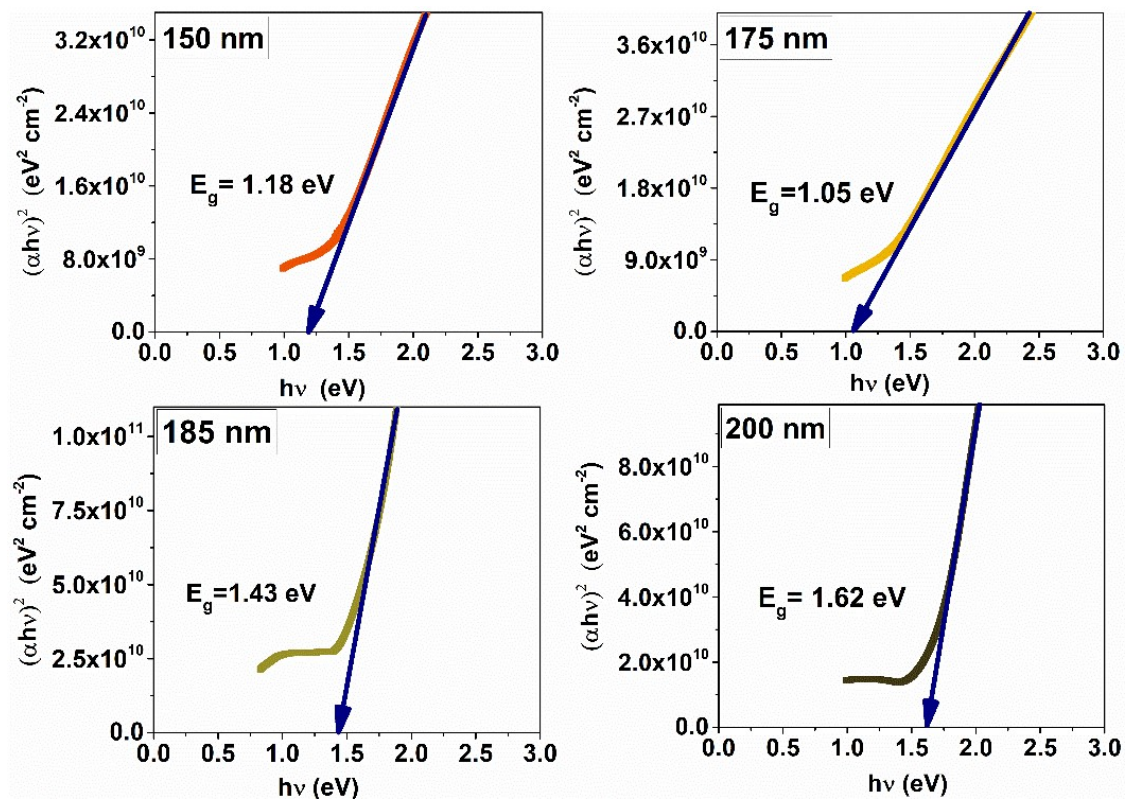


Figure 3.16 Tauc plots of Cu_4SnS_4 thin films with different copper thickness sulfurized at 550 °C for 1 h.

3.2.8 Electrical characterization

The electrical conductivity of the deposited films varies with the concentration of copper. Thin films with copper thicknesses 150, 175, and 185 nm show photoconductivity response. First, the current values were measured without light for 30 s, then 20 s under a halogen light source (50 W), and finally 50 s dark (Figure 3.17). Conductivity values of the Cu_4SnS_4 thin films were 17.69, 43.34, 0.59, and 5×10^3 $(\Omega\text{cm})^{-1}$ for 150, 175, 185, and 200 nm samples, respectively.

Table 3.2 Bandgap and conductivity values of samples with different copper layer thicknesses.

Copper layer thickness (nm)	Bandgap (eV)	Conductivity (dark) $(\Omega\text{cm})^{-1}$
150	1.18	17.69
175	1.05	43.34
185	1.43	0.59
200	1.62	5000

Samples with Cu thicknesses of 150 and 175 nm show higher conductivity values owing to the existence of binary phases and impurity phases. 200 nm sample does not show any photoconductive response due to the metallic nature of Cu_3SnS_4 . Preferentially oriented 185 nm film shows conductivity values suitable for photovoltaic applications. The presence of binary sulfides of copper (CuS or Cu_{2-x}S) and tin (Sn_2S_3 or SnS_2) affect the electrical and optical properties of Cu-Sn-S thin films.

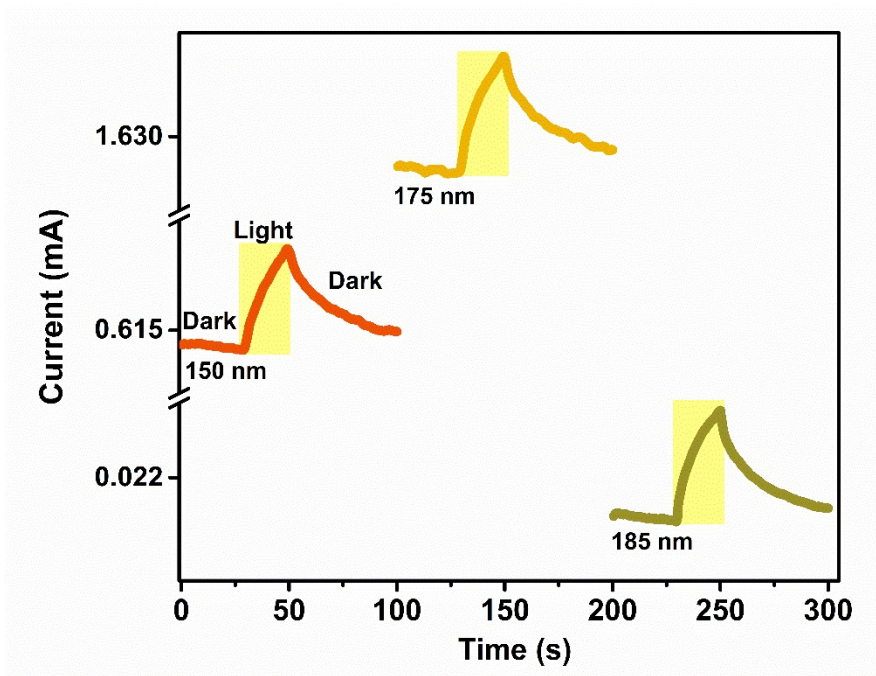


Figure 3.17 Photoconductive response of Cu_4SnS_4 thin films with a bias voltage of 1 V.

3.2.9 Photovoltaic device

Photovoltaic configuration: $\text{FTO}/\text{Cu}_4\text{SnS}_4/\text{CdS}/\text{C}/\text{Ag}$ was fabricated using Cu_4SnS_4 thin film as absorber material. J-V analysis of the device results in the photovoltaic parameters: $V_{oc}=370$ mV, $J_{sc}=0.41 \mu\text{Acm}^{-2}$, and $\text{FF}=20\%$ (figure 3.18). This is the highest open circuit voltage reported for Cu_4SnS_4 -based solar cells to date. Short circuit current and fill factor values are inferior to the previous reports of this phase [71]. Diffusion of Cu into the window layer (CdS) and Cd diffusion into the absorber layer (Cu_4SnS_4) might have occurred. These diffusions greatly affect the photovoltaic performance due to the increased electron-hole recombination [4]. Sulfur contamination on FTO due to high-temperature sulfurization might also affect the current density values of the Cu_4SnS_4 solar cell [122].

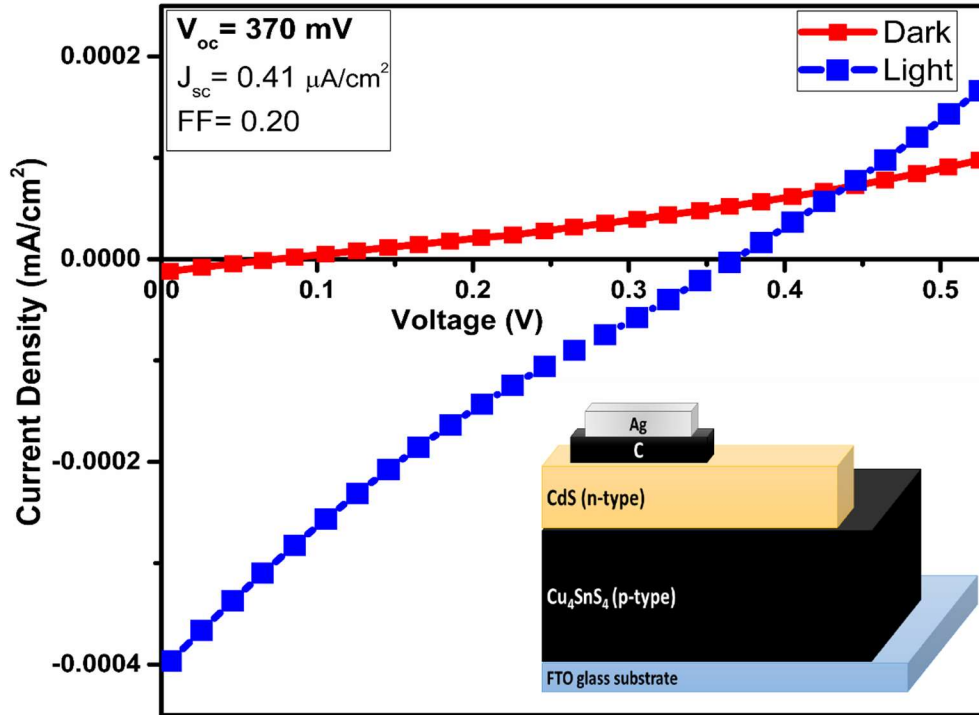


Figure 3.18 Current density vs voltage curves of FTO/Cu₄SnS₄/CdS/C/Ag.

Further optimization of the device structure is needed to improve photovoltaic parameters. The optimization of sulfurization parameters (time, temperature, quantity of sulfur used, etc.) [110], variations in device structure (transparent conductive oxide layers, window layers, buffer layers, hole transport layers electrodes) as well as post-deposition treatments (annealing, rapid thermal processing, plasma annealing, pulsed laser irradiation) [51,123,124] can enhance photovoltaic performance. Since photovoltaic parameters are inferior to the previous reports, further research is necessary to improve the photovoltaic performance of Cu₄SnS₄ thin film solar cells.

CHAPTER 4

INFLUENCE OF SULFURIZATION PARAMETERS ON THE SYNTHESIS AND PROPERTIES OF Cu_2SnS_3 THIN FILMS

In this chapter, the influence of sulfurization parameters on the properties of Cu_2SnS_3 films is described. Extensive preliminary studies were conducted before the selection of varying parameters and their values. The quantity of sulfur used for sulfurization, sulfurization temperature, and sulfurization time for the synthesis process was optimized. Optimal surface morphology and optoelectrical properties were obtained for Cu_2SnS_3 thin films via this three-stage deposition method.

4.1 Influence of sulfur quantity on the deposition and properties of Cu-Sn-S thin films

This section describes the alteration of properties of Cu-Sn-S thin films upon varying sulfur quantities used for sulfurization. Precursor SnS thin films were deposited on the glass slides by CBD at 40 °C for 16 h (~450 nm). A copper precursor layer of 100 nm thickness was deposited on the SnS layer using thermal evaporation and these stacked layers were subjected to sulfurization. Sulfurization temperature and time were kept constant at 500 °C and 1 hour, respectively. The quantity of sulfur powder used for the sulfurization process varied from 10 to 300 mg. The different sulfur quantities on the formation of ternary phases and the properties of Cu-Sn-S thin films were studied. The influence of sulfur quantity on the structure, chemical environment, microstructure, and optical and electrical properties was evaluated using XRD, Raman, XPS, EDX, SEM, and optical and electrical measurements.

4.1.1 X-ray diffraction analysis

XRD analysis was employed to determine the crystal structure and phases present in the Cu-Sn-S films. Diffraction patterns corresponding to the films sulfurized using different quantities of sulfur powder are presented in Figure 4.1 along with standard patterns of

Cu_2SnS_3 (tetragonal) and Cu_4SnS_4 (orthorhombic). The sample with 10 mg of sulfur shows intense diffraction peaks at 28.4, 32.9, 47.2, and 56.1° which agree with the tetragonal Cu_2SnS_3 phase (JCPDS # 01-079-3648). These peaks correspond to the reflection from (1 1 2), (0 0 4), (2 0 4), and (3 1 2) planes, respectively. After increasing the sulfur quantity to 100 mg, new peaks corresponding to the orthorhombic Cu_4SnS_4 phase also emerged along with the characteristic peaks of Cu_2SnS_3 . According to JCPDS #00-029-0584, new Cu_4SnS_4 peaks at 26.2, 26.6, 27.8, 30.9, 33.6, and 46.6° are identified as reflections from (4 0 0), (2 2 0), (1 2 1), (1 1 2), (3 2 1) and (6 2 0) planes, respectively. These peaks confirm the coexistence of the sulfur-rich Cu_4SnS_4 phase along with Cu_2SnS_3 . As sulfur quantity increases to 300 mg, all diffraction peaks are found to be matching with the Cu_4SnS_4 phase. The formation mechanism of different phases Cu-Sn-S was described in section 3.2 (equations 3.1 to 3.3). The principal reflection peak of Cu_2SnS_3 at 28.3° is disappeared and the characteristic peak of Cu_4SnS_4 at 28.5° appeared. Sample sulfurized using 300 mg sulfur displays two new intense peaks at 28.5 and 50.7° corresponding to (1 0 2) and (2 2 3) reflection planes of orthorhombic Cu_4SnS_4 [41]. The crystallite sizes of the samples were 34.3, 29.8, 25.7, and 26.1 nm for samples using sulfur quantities of 10, 100, 200, and 300 mg, respectively (using equation 2.2). A gradual decrease in crystallite size with increasing sulfur quantity used for the annealing process, was observed. This decrease might be due to the formation of the Cu_4SnS_4 phase in a sulfur-rich atmosphere.

Furthermore, the dislocation density values (δ) of the samples calculated using equation 2.3 were 8.49×10^{-4} , 1.12×10^{-3} , 1.51×10^{-3} , and 1.46×10^{-3} lines nm^{-2} for the samples using sulfur quantities of 10, 100, 200, and 300 mg, respectively. Dislocation density represents the amount of defects in the sample which is defined as the dislocation lines per unit volume of the crystal and found to be increasing with the quantity of sulfur used for sulfurization.

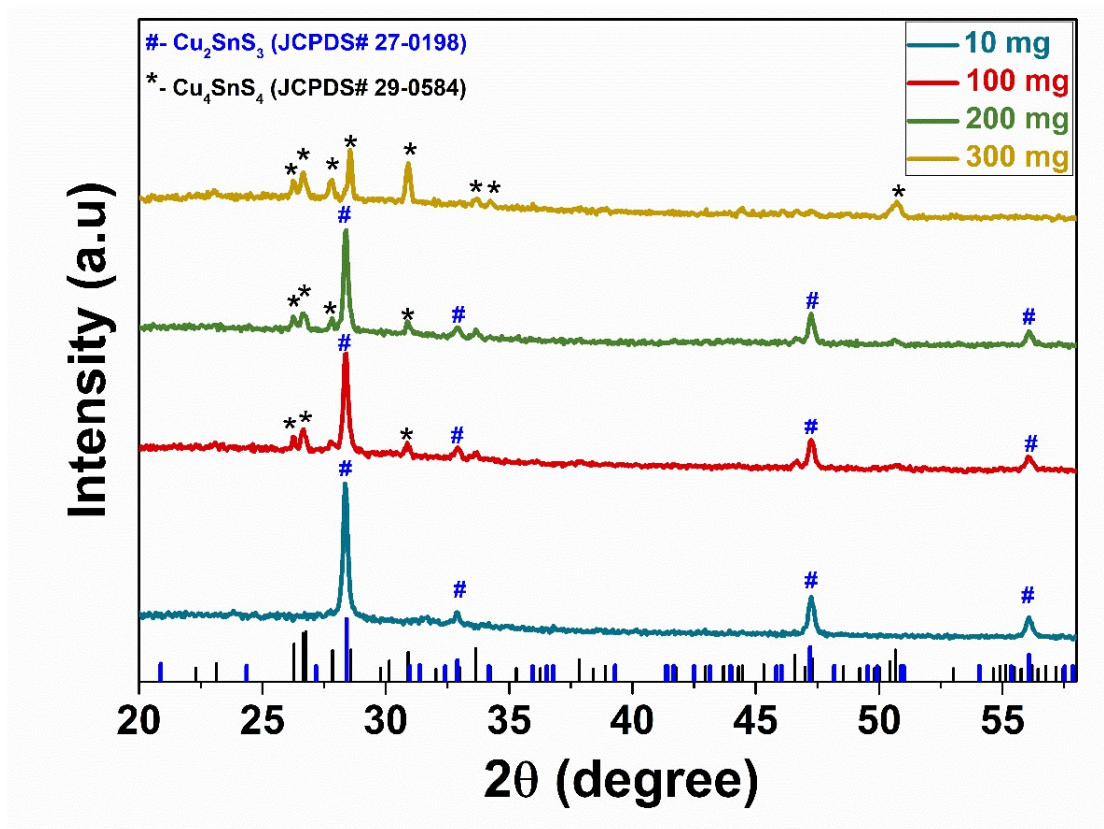


Figure 4.1 XRD patterns of Cu-Sn-S films sulfurized using 10, 100, 200, and 300 mg of sulfur powder along with standard JCPDS patterns of Cu_2SnS_3 and Cu_4SnS_4 .

Further iterations in sulfurization temperature might help to avoid the formation of binary and impurity phases. Owing to the close positioning of diffraction peaks of Cu_2SnS_3 and Cu_4SnS_4 phases leads to perplexity in the assignment of peaks. Raman analysis is widely used in complementary to XRD analysis to resolve this confusion and confirm phases accurately.

4.1.2 Raman Analysis

Raman spectroscopy is considered as a suitable characterization method to find different structures and phases present in Cu-Sn-S thin films [46]. Figure 4.2 represents the Raman spectra of Cu-Sn-S films sulfurized using different quantities of sulfur powder. Samples using 10, 100, and 200 mg of sulfur show peaks at 283, 299, 310, 325, and 344 cm^{-1} whereas sample sulfurized using 300 mg exhibits two peaks at 315 and 475 cm^{-1} . Raman peaks at

283, 325, and 344 cm^{-1} are attributed to the formation of the tetragonal Cu_2SnS_3 phase [125]. All films except the 300 mg sample show small peaks at 299 and 310 cm^{-1} , which are attributed to Cu_2SnS_3 polymorphs in the literature [115]. The intense peaks in the sample sulfurized using 300 mg of sulfur at 315 and 475 cm^{-1} are correlated to the characteristic Raman peak of Cu_4SnS_4 [115,126] and the binary phase of copper (Cu_{2-x}S), respectively [49]. Complete conversion of Cu_2SnS_3 to Cu_4SnS_4 phase was revealed by Raman analysis which was also consistent with XRD analysis.

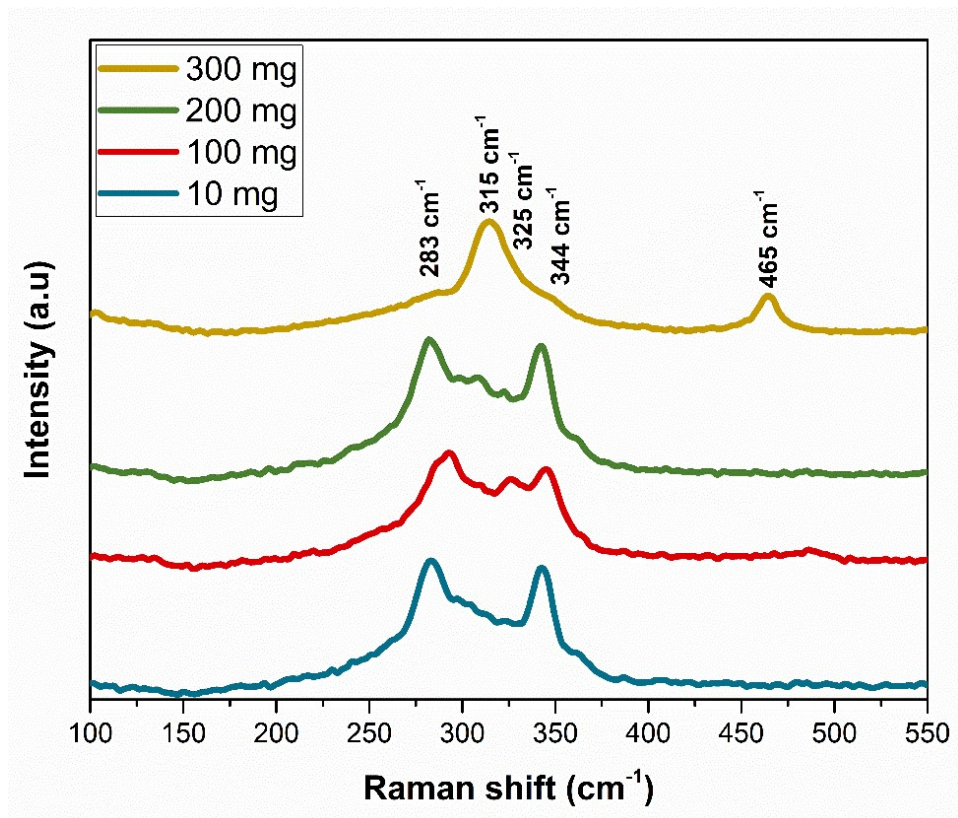


Figure 4.2 Raman spectra of Cu-Sn-S samples sulfurized using 10, 100, 200, and 300 mg of sulfur.

4.1.3 Chemical composition -XPS

X-ray photoelectron spectroscopy was used to evaluate the chemical composition and oxidation states of elements. Oxidation states were verified using core-level electron spectra of constituting elements. The chemical state of elements was estimated by assessing the binding energy peak values and energy separation of doublet peaks.

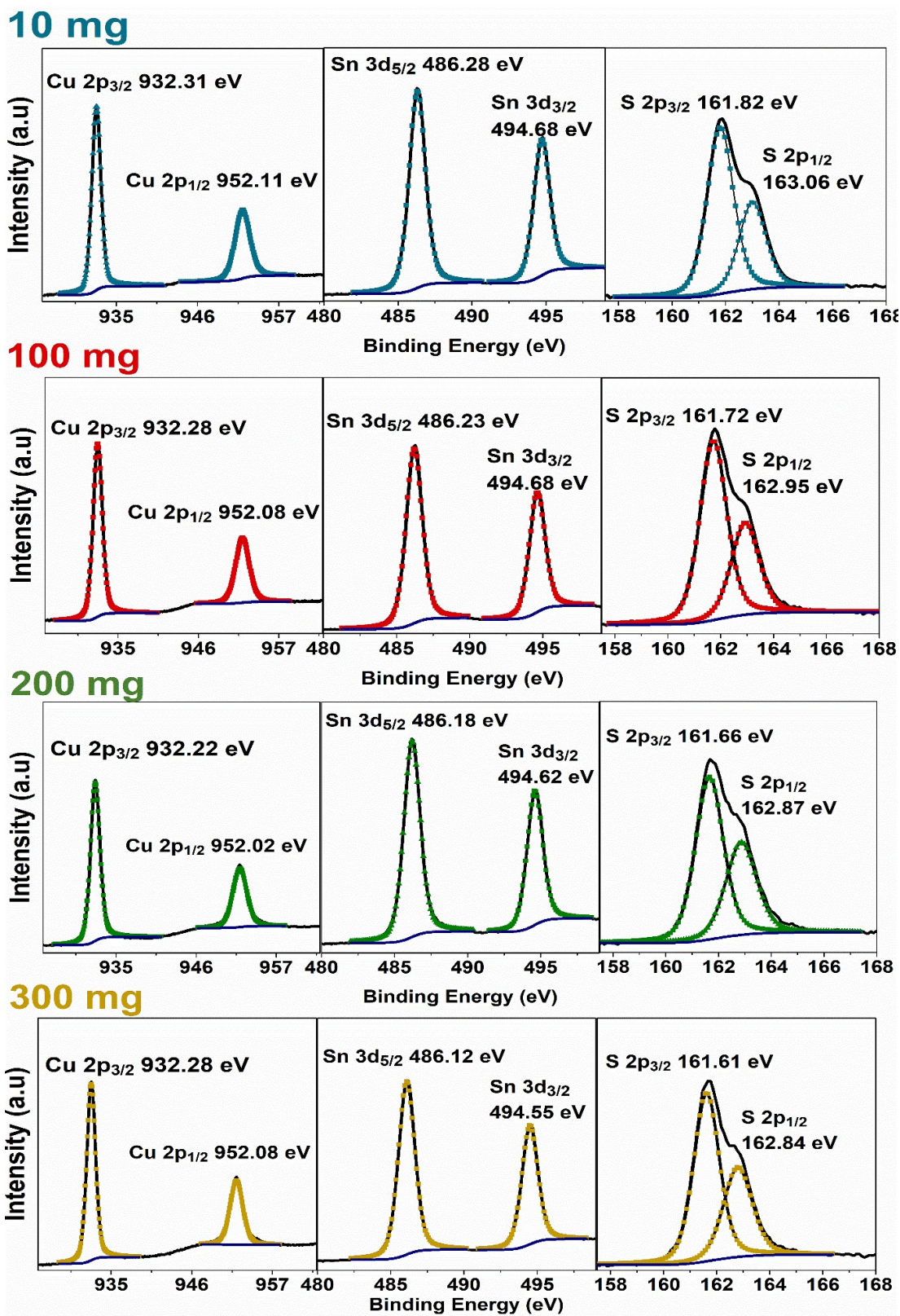


Figure 4.3 XPS spectra of Cu, Sn, and S for samples sulfurized using 10, 100, 200, and 300 mg of sulfur.

All samples show the presence of characteristic spin orbit coupled peaks corresponding to Cu, Sn, and S, and core level electron spectra for samples sulfurized using 10, 100, 200, and 300 mg of sulfur are given in figure 4.3. Core level spectra of all samples show similar peak positions and energy separation for each element and those were consistent with previous reports [40]. Cu 2p core level spectrum shows doublet peaks around 932 and 952 eV with an energy separation of 19.8 eV. Thus, Cu in the Cu¹⁺ oxidation state in all films was confirmed by correlating these peaks to spin-orbit coupled peaks of Cu 2p_{3/2} and Cu 2p_{1/2} [127]. Similarly, the Sn core level spectrum exhibits two peaks around 486 and 494 eV with an energy separation of 8.4 eV. These peaks are linked to Sn 3d_{5/2} and Sn 3d_{3/2} doublet peaks and confirm the occurrence of Sn in the Sn⁴⁺ oxidation state [128]. The deconvoluted core level electron spectrum of S shows two peaks around 161 and 162 eV with energy separation of ~ 1.2 eV for every sample. These peaks are correlated to spin-orbit coupled peaks of S 2p_{3/2} and S 2p_{1/2} and indicate the presence of S in the S²⁻ state in all samples [88]. Cu, Sn, and S were found to be in +1, +4, and -2 oxidation states for all the samples.

4.1.4 Elemental composition-EDX

The elemental composition of thin films sulfurized using different sulfur quantities was estimated using EDX analysis and is given in Table 4.1. Sample sulfurized with 10 mg indicates the formation of copper and sulfur-deficient Cu₂SnS₃ phase. Whereas samples sulfurized using 100, 200, and 300 mg of sulfur show an increase in sulfur and copper content in the films. The S/Sn ratio rises from 2.81 to 3.91 while increasing the sulfur quantity from 10 to 300 mg. Also, the Cu/Sn ratio increases from 2.28 to 3.67 while increasing the sulfur quantity from 10 to 300 mg. These augmentations are accounted for the formation of sulfur-rich Cu₄SnS₄ phase along with Cu₂SnS₃ when annealed with sufficient sulfur supply. Sulfurization using 300 mg of sulfur results in a composition comparable to the Cu₄SnS₄ phase which is also consistent with the findings of structural analysis.

Table 4.1 EDX elemental composition of samples sulfurized using 10, 100, 200, and 300 mg of sulfur.

Sample	Cu (%)	Sn (%)	S (%)	Cu/Sn	S/Sn	Composition
10 mg	37.5	16.4	46.1	2.28	2.81	$\text{Cu}_{2.28}\text{SnS}_{2.81}$
100 mg	35.5	15.4	49.1	2.31	3.18	$\text{Cu}_{2.31}\text{SnS}_{3.18}$
200 mg	38.1	14.5	47.4	2.63	3.28	$\text{Cu}_{2.63}\text{SnS}_{3.28}$
300 mg	42.8	11.6	45.6	3.67	3.91	$\text{Cu}_{3.67}\text{SnS}_{3.91}$

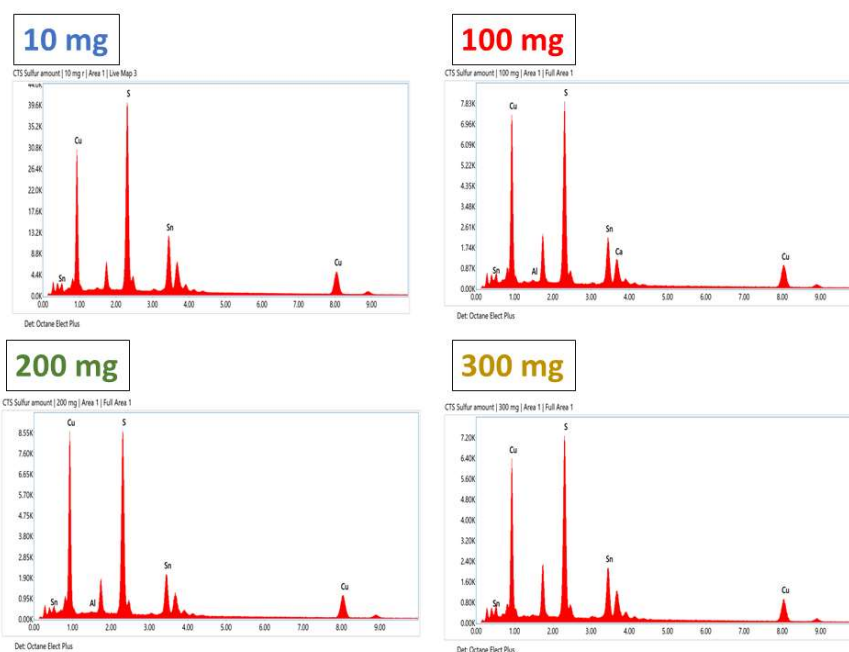


Figure 4.4 EDX spectra of samples sulfurized using 10, 100, 200, and 300 mg of sulfur.

4.1.5 Surface morphology-SEM

The surface morphology of the synthesized Cu-Sn-S thin films is presented in Figure 4.5. Samples sulfurized using 100, 200, and 300 mg of sulfur display relatively rougher surfaces than the 10 mg sample. When the sulfur quantity is higher than 10 mg, non-uniform spherical grains are encountered on the surface. Interestingly, high-resolution images of the 100 mg sample display moderately bigger grains with scattered spherical particles. 300 mg sample exhibits agglomerated bigger spherical particles on the surface. Similar bigger spherical grains were observed for the Cu_4SnS_4 phase in the previous investigation which is consistent with XRD results (section 3.2) [41]. Cu-Sn-S films synthesized using lower quantities of sulfur displayed relatively more compact and uniform grain growth. This type of uniform

microstructure of bigger grains has already been reported for Cu-Sn-S thin films [129]. Morphological studies suggest that a lower quantity of sulfur will be appropriate for the formation of uniform bigger grains without spherical growths on the surface.

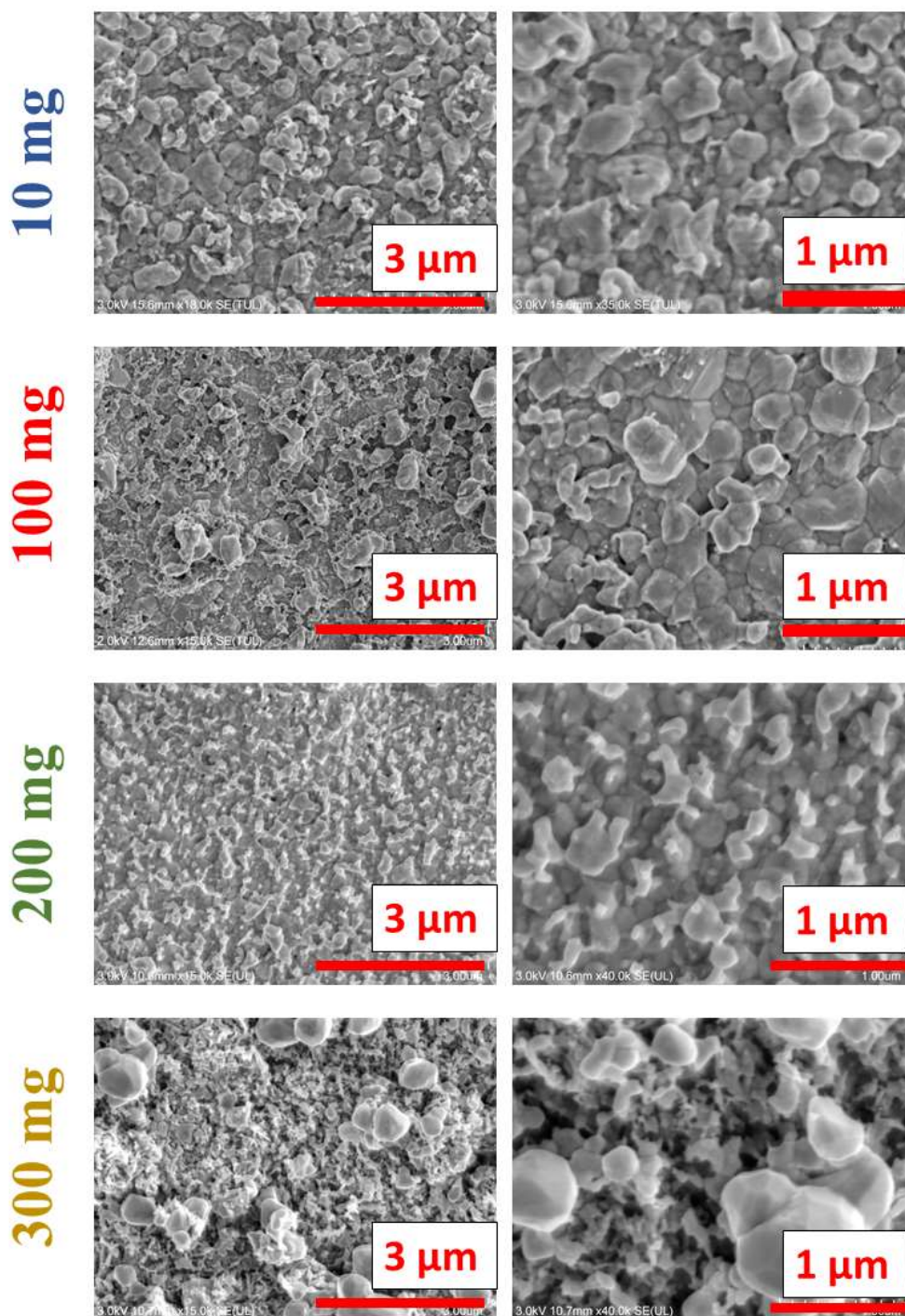


Figure 4.5 SEM images of Cu-Sn-S samples sulfurized using 10, 100, 200, and 300 mg of sulfur powder.

4.1.6 Optical characterization

Optical transmittance and reflectance of Cu-Sn-S samples sulfurized using 10 to 300 mg of sulfur were measured using a UV-Vis-NIR spectrophotometer (Figure 4.6(a-b)). All samples show an absorption near 1100 nm and very low reflectance in all wavelength ranges. To estimate the absorption coefficient, equation 2.4 was utilized and the Cu-Sn-S thin films show strong optical absorption ($\alpha > 10^5 \text{ cm}^{-1}$) in the visible region, which is advantageous for photovoltaic applications.

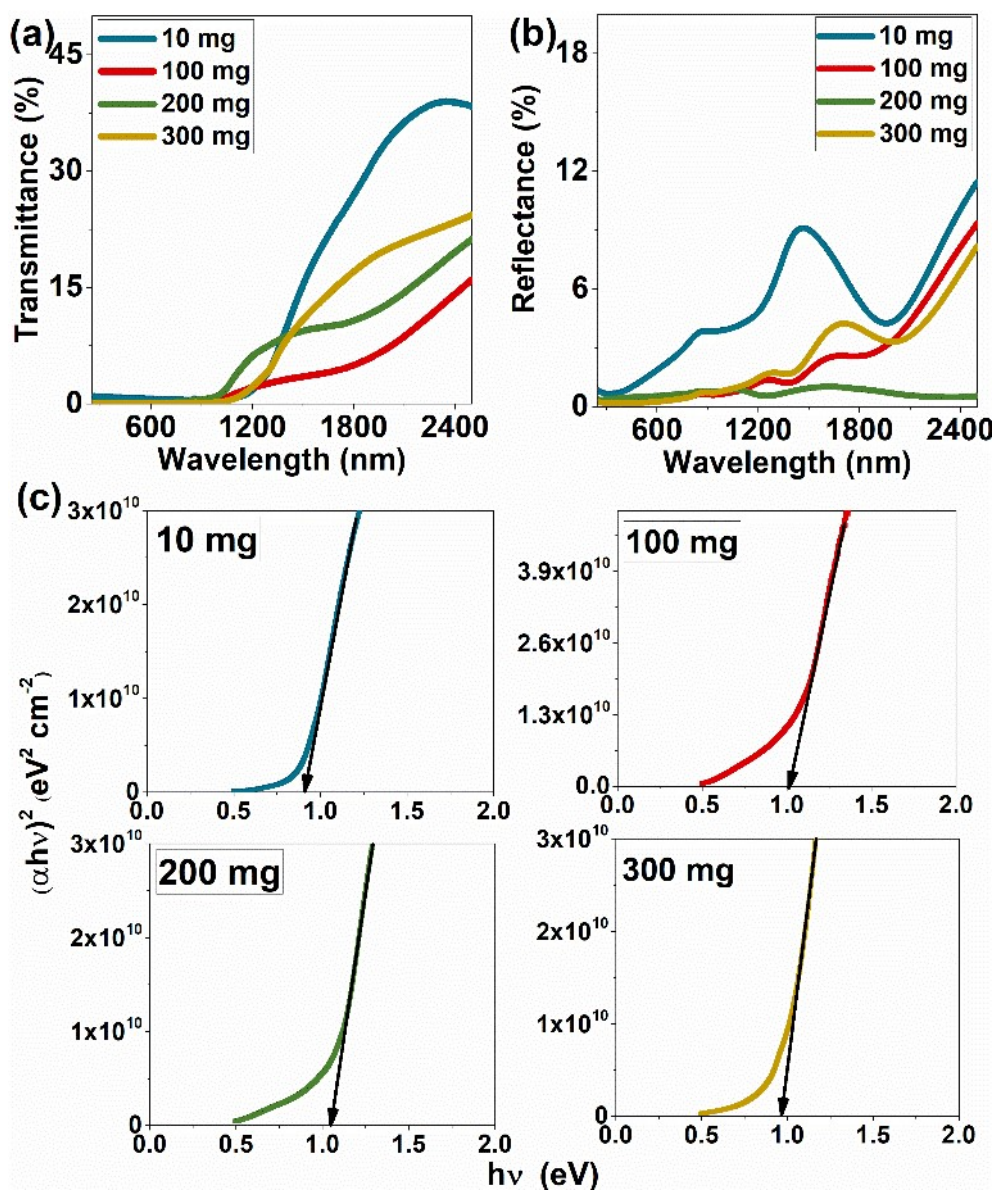


Figure 4.6 a) Transmittance b) reflectance and c) Tauc plots (bandgap) of Cu-Sn-S films sulfurized using different quantities of sulfur powder.

Tauc plots of Cu-Sn-S thin films sulfurized using different sulfur quantities are presented in Figure 4.5(c). The bandgap energies of Cu-Sn-S samples for direct transitions are 0.91, 1.01, 1.04, and 0.96 eV for 10, 100, 200, and 300 mg samples, respectively. Optical bandgaps of Cu-Sn-S thin films have been reported in between a wide range of 0.9 to 1.7 eV [46].

4.1.7 Electrical characterization

Photoconductivity response (PR) measurements were employed to evaluate the electrical characteristics of Cu-Sn-S films. The photocurrent was measured for the first 30 s in the dark, then 20 s under illumination from a halogen source, and finally 50 s in dark conditions. The photoconductivity response of samples under a 50 W halogen source using an applied voltage of 1 V is presented in Figure 4.7. The electrical conductivities of the samples in dark conditions are 11.2, 5.2, 9.4, and 30.7 (Ωcm)⁻¹ for 10, 100, 200, and 300 mg samples, respectively. All samples exhibit transient photoresponse behavior due to the higher conductivity of the films and defect levels inside the material which are widely reported for Cu-Sn-S thin films [42,130].

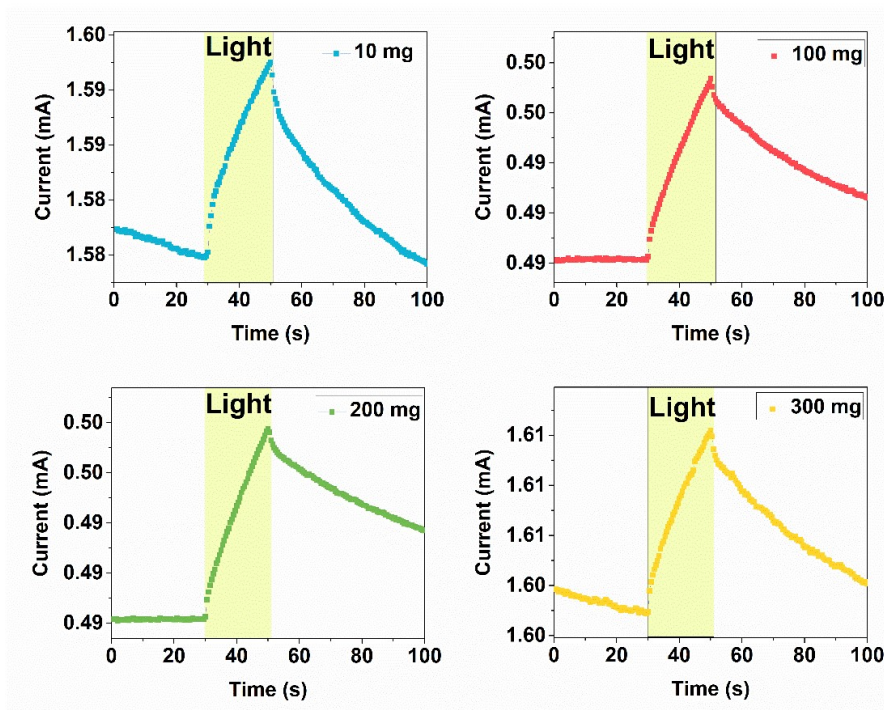


Figure 4.7 Photoconductive response of Cu-Sn-S films sulfurized using different quantities of sulfur powder

Cu-Sn-S thin films were synthesized using different quantities of sulfur and the outcomes were carefully analyzed. 10 mg sulfur powder was sufficient for the formation of the ternary phase and the chance of the formation of other impurity phases increased after increasing the sulfur quantity. We also probed the surface morphology of Cu_2SnS_3 thin films sulfurized using 20 to 80 mg and found minimal agglomerated spherical grains for 20 mg.

4.2 Influence of sulfurization time on the properties of Cu_2SnS_3 thin films

This section describes the influence of sulfurization time on the properties of Cu_2SnS_3 thin films. A copper precursor layer of 100 nm thickness was deposited on SnS thin films (~ 450 nm) by a chemical bath deposition of 17 h. Sulfurization time was varied from 30 to 120 min while sulfurization temperature and quantity of sulfur used were kept at 500 °C and 20 mg, respectively. These values were chosen according to the outcomes of the previous study (section 4.1).

4.2.1 X-ray diffraction analysis

The crystal structure of Cu_2SnS_3 thin films was studied using XRD analysis and the obtained diffraction patterns of films sulfurized for different durations are presented in Figure 4.8 along with the standard pattern of Cu_2SnS_3 . XRD patterns of films exhibit intense diffraction peaks of Cu_2SnS_3 polymorphs. Diffraction peaks at 28.5, 32.9, 47.3, and 56.2° are accounted to the reflections from (002), (131), ($3\bar{3}\bar{1}$), and ($40\bar{2}$) planes of monoclinic Cu_2SnS_3 . Samples annealed for 30, 90, and 120 min show the presence of a conductive impurity phase Cu_4SnS_4 . Small diffraction peaks visible at 26.7 and 30.9° are accounted for the reflections from (3 1 1) and (1 1 2) planes of orthorhombic Cu_4SnS_4 thin films [73]. The formation of impurity Cu_4SnS_4 phase along with the Cu_2SnS_3 phase at higher temperatures has already been reported in the literature [131]. Crystallite sizes were estimated using the Debye Scherrer formula (equation 2.2) and values are 31, 37, 33, and 21 nm for samples annealed for 30, 60, 90, and 120 min, respectively. It is noteworthy that different polymorphs of Cu_2SnS_3 have similar diffraction patterns and different polymorphs of Cu_2SnS_3 exhibit

different optical and electrical properties [46]. The similarity of diffraction peak positions and peak intensities makes the identification process using only XRD leading to perplexity. Raman analysis has been widely employed for the identification of different phases of Cu-Sn-S thin films.

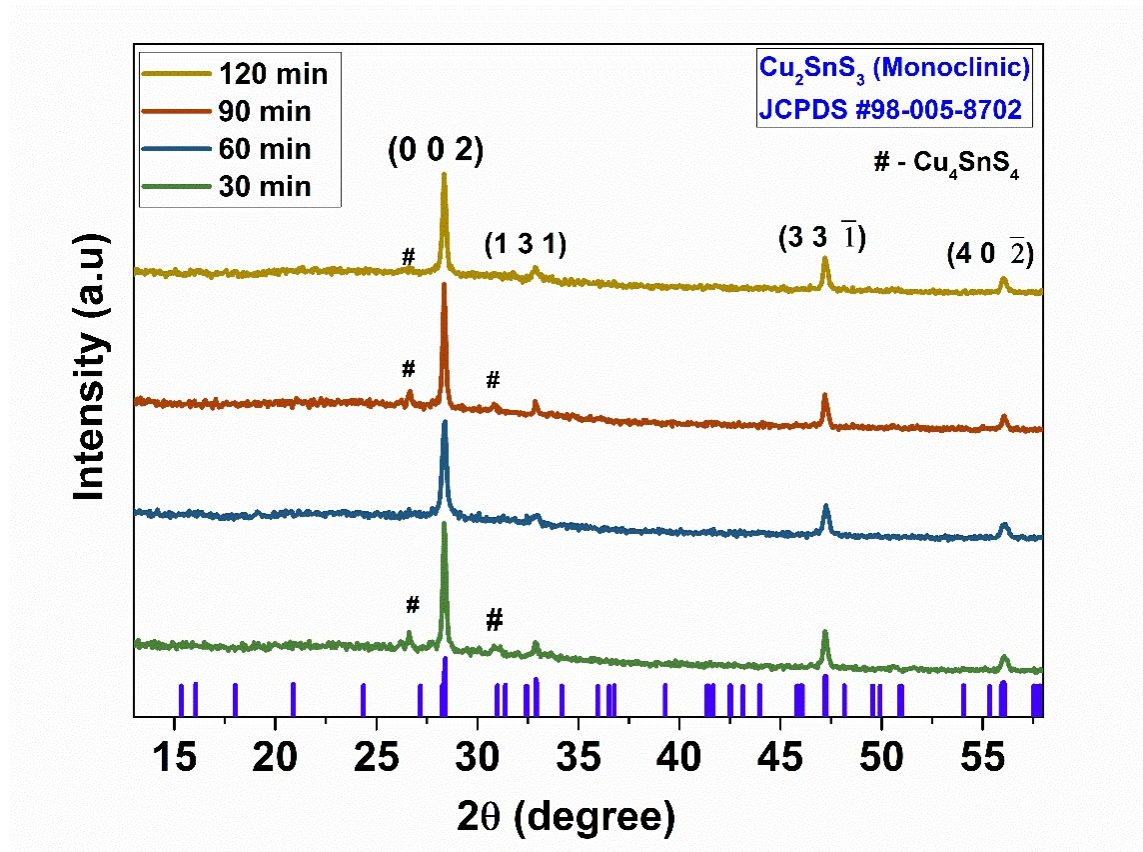


Figure 4.8 XRD patterns of Cu_2SnS_3 samples sulfurized for 30, 60, 90, and 120 min with monoclinic Cu_2SnS_3 (JCPDS#98-005-8702) pattern.

4.2.2 Raman analysis

Raman spectroscopy is a widespread practice for distinguishing different polymorphs of Cu_2SnS_3 . Raman spectra of Cu_2SnS_3 thin films sulfurized for 30, 60, 90, and 120 minutes are presented in figure 4.9. Raman spectra show peaks at 290, 318, 350, and 487 cm^{-1} . All films display intense peaks near 290 and 350 cm^{-1} which are correlated to monoclinic Cu_2SnS_3 in literature [132,133]. The samples annealed for 30 and 90 min exhibit an intense peak at 318 cm^{-1} which is accounted for the characteristic Raman peak of Cu_4SnS_4 [134,135]. The trivial

peak that appears at 487 cm^{-1} is associated with the negligible presence of binary sulfide of copper [136]. The commonly observed Raman peaks for cubic phase are at 303 and 355 cm^{-1} , for monoclinic at 290 and 352 cm^{-1} , and for tetragonal at 336 and 351 cm^{-1} [137]. Raman spectroscopy analysis confirms the formation of Cu_2SnS_3 along with Cu_4SnS_4 in Cu-Sn-S thin films sulfurized for different durations.

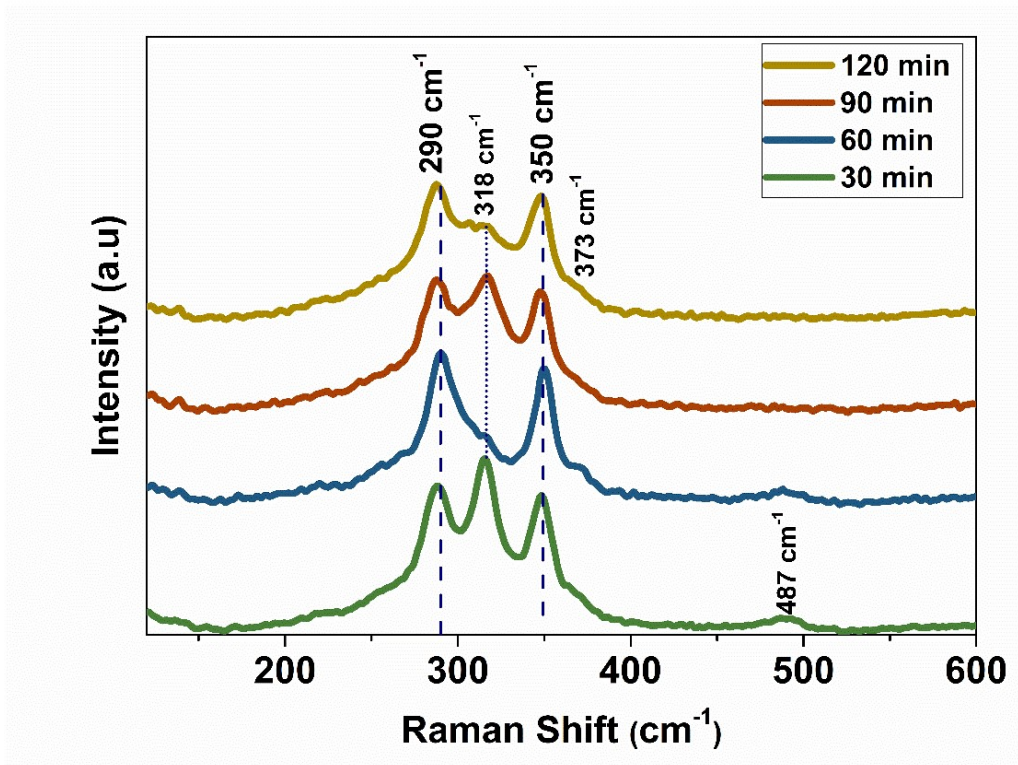


Figure 4.9 Raman spectra of Cu_2SnS_3 samples sulfurized for 30, 60, 90, and 120 min.

4.2.3 Chemical composition -XPS

X-ray photoelectron spectroscopy was employed to gain insights into the oxidation states of the constituent elements of Cu_2SnS_3 thin films. XPS core electron spectra of Cu, Sn, and S for different sulfurization durations are plotted and presented in Figure 4.10(a-c). Samples annealed for 30, 60, 90, and 120 min show two intense characteristic spin orbit coupled peaks for Cu, Sn, and S. Peak positions and energy differences between peaks for each element are consistent in all the samples. Furthermore, the deconvolution of Cu 2p, Sn 3d, and S 2p core electron high-resolution spectrum of the 60 min sample was assessed and given in Figure 4.10(d-f). The high-resolution scan of Cu 2p consists of a doublet at 932.15 eV (Cu $2p_{3/2}$)

and 951.95 eV (Cu 2p_{1/2}) with an energy separation of 19.8 eV. The energy separation and peak positions confirm the presence of Cu in the +1 oxidation state [69]. The core level spectrum of Sn comprises two peaks at 486.18 and 494.58 eV with an energy separation of 8.4 eV, which corroborates the presence of Sn in the +4 oxidation state [107]. In the core level spectrum of sulfur, deconvoluted peaks at 161.79 and 162.98 eV with 1.18 eV separation confirm the presence of S in the -2 oxidation state [107]. XPS analysis confirmed the presence of Cu, Sn, and S in +1, +4, and -2 oxidation states, respectively for all the samples.

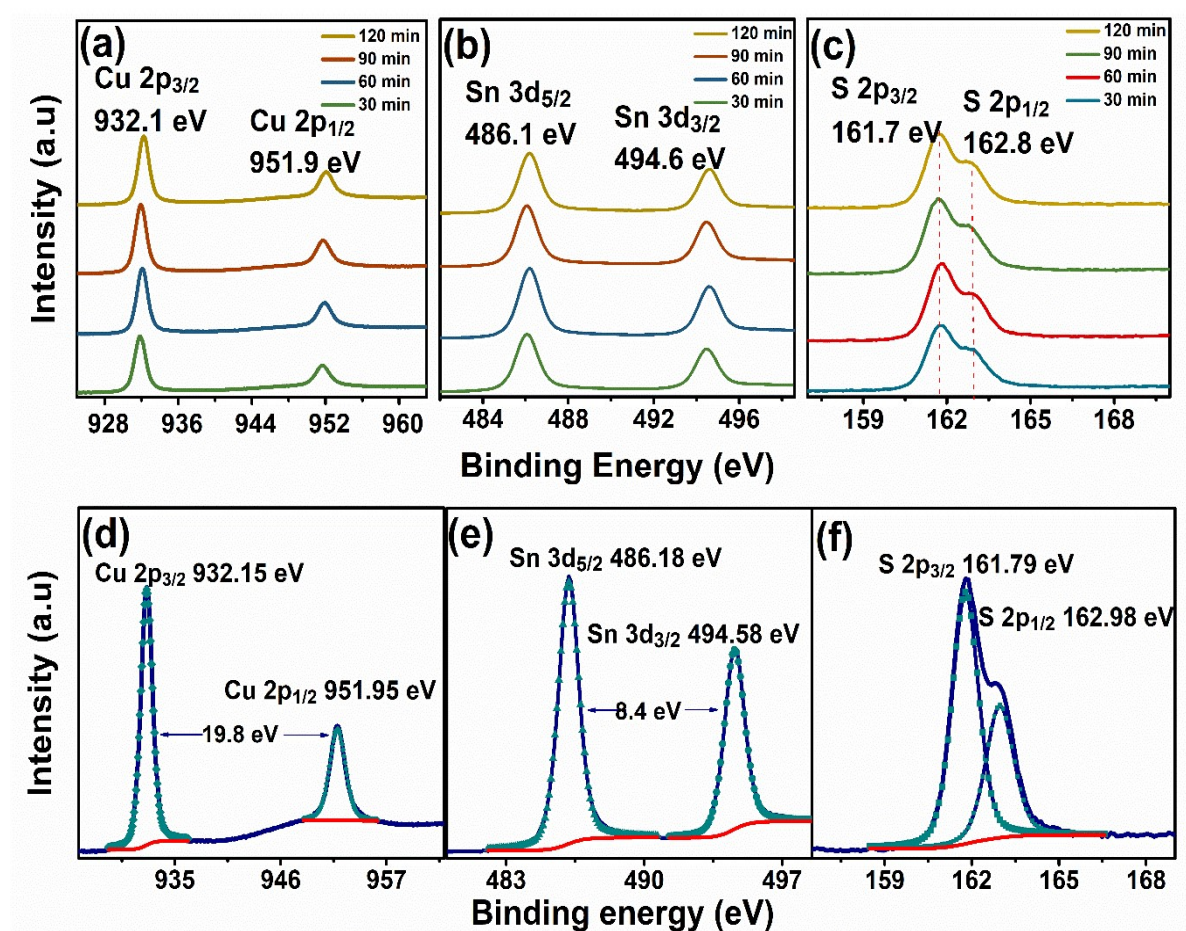


Figure 4.10 XPS core electron spectra of (a) Cu, (b) Sn, and (c) S of samples sulfurized for different durations. Deconvoluted core electron spectra of (d) Cu, (e) Sn, and (f) S of 60 min sample.

4.2.4 Elemental composition-EDX

Elemental composition was determined using EDX analysis and the composition of individual elements is tabulated in Table 4.2. All samples show sulfur-deficient composition with similar copper content. The sample sulfurized for 60 min exhibits the lowest Cu/Sn and S/Sn ratios which are proposed as appropriate for photovoltaic applications. From observing the Sn content in films, it is understood that sulfurization promotes the formation of the ternary phase until 60 min, whereas sulfurization for longer durations (90 and 120 min) experiences a Sn loss. This might be due to the evaporation of Sn from the surface of the film. This deficiency can result in the formation of binary sulfides of copper and impurity ternary phases. The copper-deficient composition is predicted to be beneficial for solar cell applications. The presence of a trivial amount of Cu_4SnS_4 phase might also have affected the final composition. Sulfurization for 60 min was found to be suitable for achieving desirable composition without impurities.

Table 4.2 Elemental composition of Cu_2SnS_3 thin films sulfurized for 30, 60, 90, and 120 min duration.

Sample	Cu (%)	Sn (%)	S (%)	Composition
30 min	35.8	16.5	47.6	$\text{Cu}_{2.2}\text{SnS}_{2.9}$
60 min	36.5	17.6	45.9	$\text{Cu}_{2.1}\text{SnS}_{2.6}$
90 min	36.4	17.0	46.6	$\text{Cu}_{2.1}\text{SnS}_{2.7}$
120 min	36.9	16.9	46.2	$\text{Cu}_{2.2}\text{SnS}_{2.7}$

EDX mapping was utilized to study the distribution of elements of the film. Elemental mapping of Cu, Sn, and S corresponding to the samples sulfurized for 30, 60, 90, and 120 min are presented in Figure 4.11. SnS and Cu precursor layers were stacked before the sulfurization process. The copper diffuses into the SnS and reacts under a sulfur atmosphere to form ternary phases and this reaction needs to be homogeneous throughout the surface of the films. Thus, the uniform distribution of Cu, Sn, and S elements at the microscale from

EDX mapping analysis underlines the formation of the ternary Cu-Sn-S phase. These compositions by EDX agree with the identification of phases obtained from XRD and Raman spectroscopy analysis.

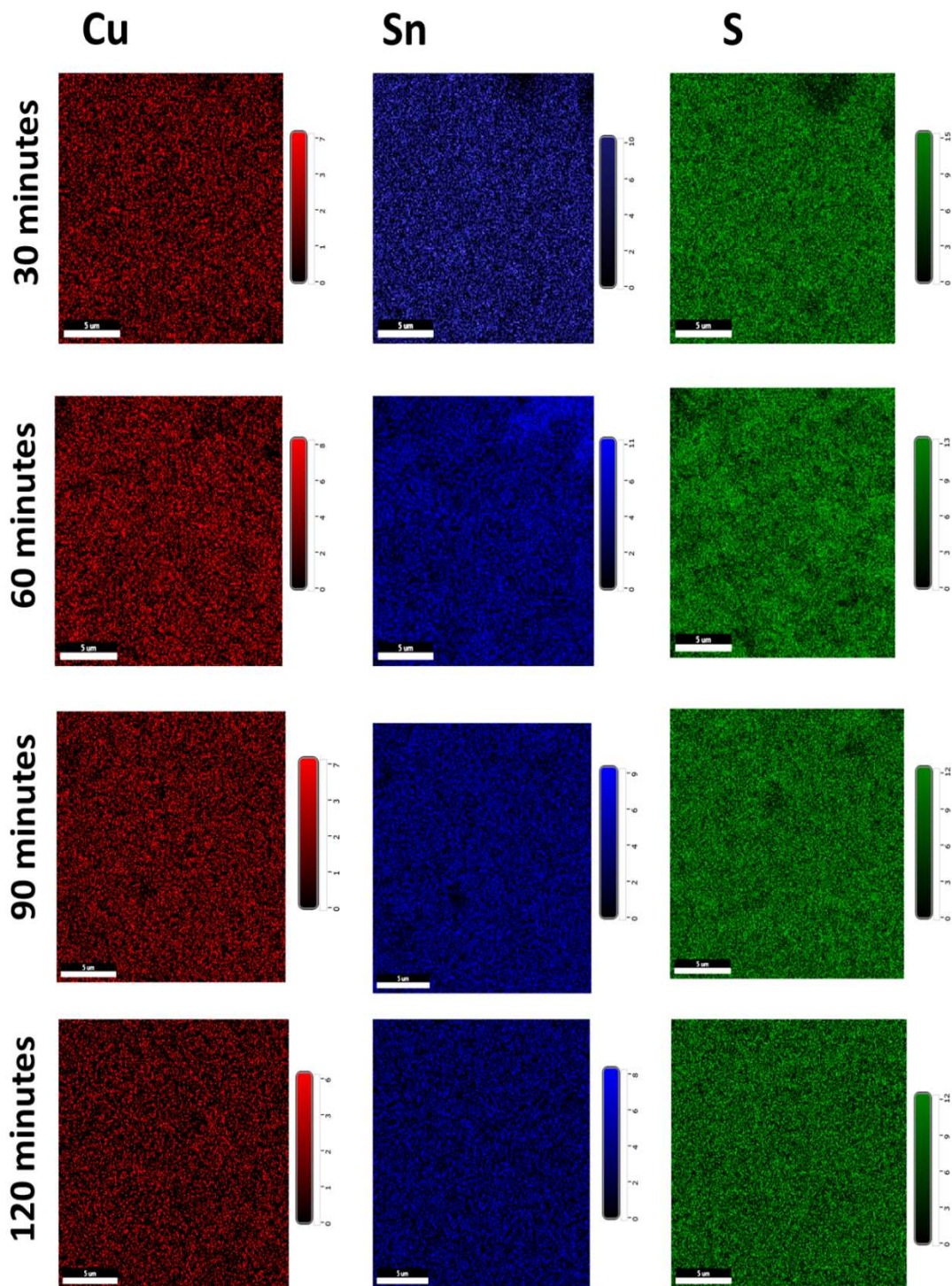


Figure 4.11 EDX elemental mapping of Cu, Sn, and S for different sulfurization durations.

4.2.5 Surface morphology - SEM

Scanning electron microscopy images of the samples sulfurized for 30, 60, 90, and 120 min are given in Figure 4.12. The sample sulfurized for 30 min shows relatively smaller grains with scattered, agglomerated shapes on the surface. These might be due to incomplete diffusion of the copper into the SnS thin film. The samples sulfurized for 60 and 90 minutes exhibit a network of bigger grains. This type of compact larger grain structure is advisable for better carrier transport in photovoltaic applications. After increasing the sulfurization time to 120 min, the surface deteriorated with the presence of voids and a significant reduction in grain size. SEM images revealed the importance of sulfurization time for the formation of uniformly distributed bigger grains.

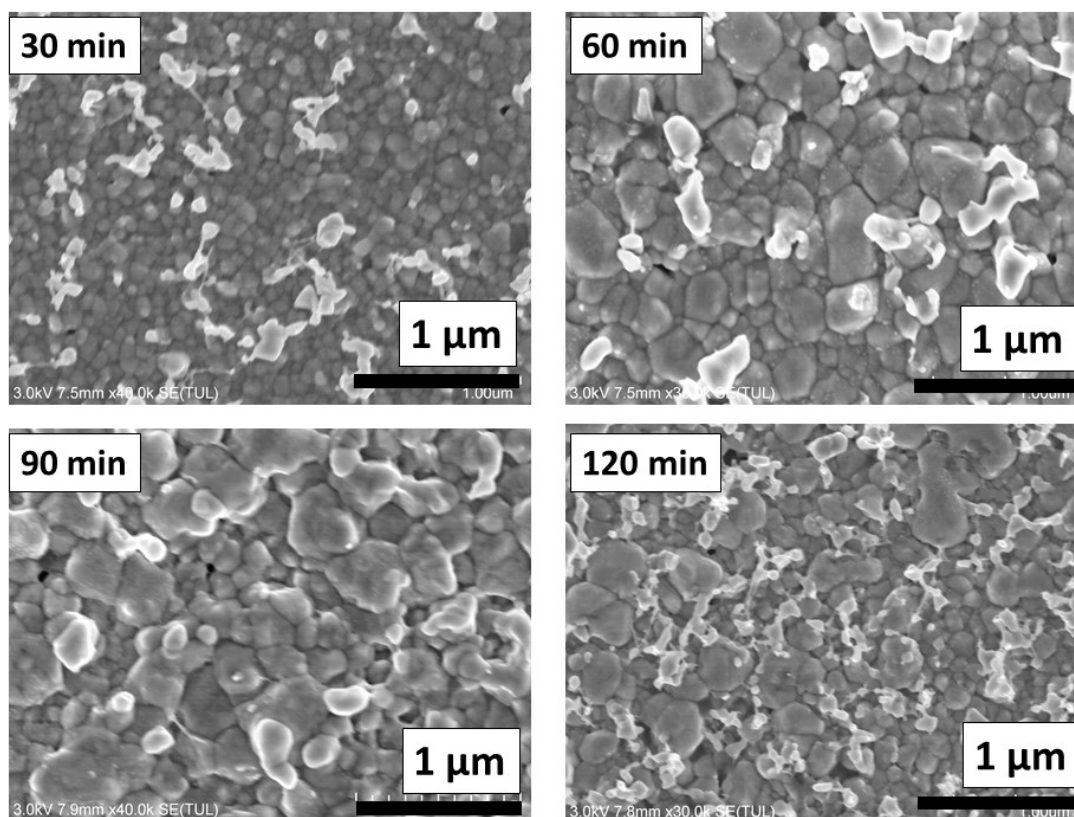


Figure 4.12 SEM images of samples sulfurized for 30, 60, 90, and 120 min.

4.2.6 Optical characterization

The optical transmittance and reflectance spectra of films sulfurized for 30 to 120 min are presented in figure 4.13(a,b). The thin films show high transmittance and low reflectance values. The 30 and 90 min films exhibit a weak absorption in the NIR region and multiple absorptions in the visible region due to the presence of the Cu_4SnS_4 phase [69]. The existence of Cu_4SnS_4 has already been proven by Raman spectroscopy and XRD. The film sulfurized for 120 min shows transmittance in all regions due to the presence of voids on the surface caused by partial removal of the film. The optical absorption coefficient was estimated utilizing equation 2.4 for which all films showed high values of $\sim 10^5 \text{ cm}^{-1}$.

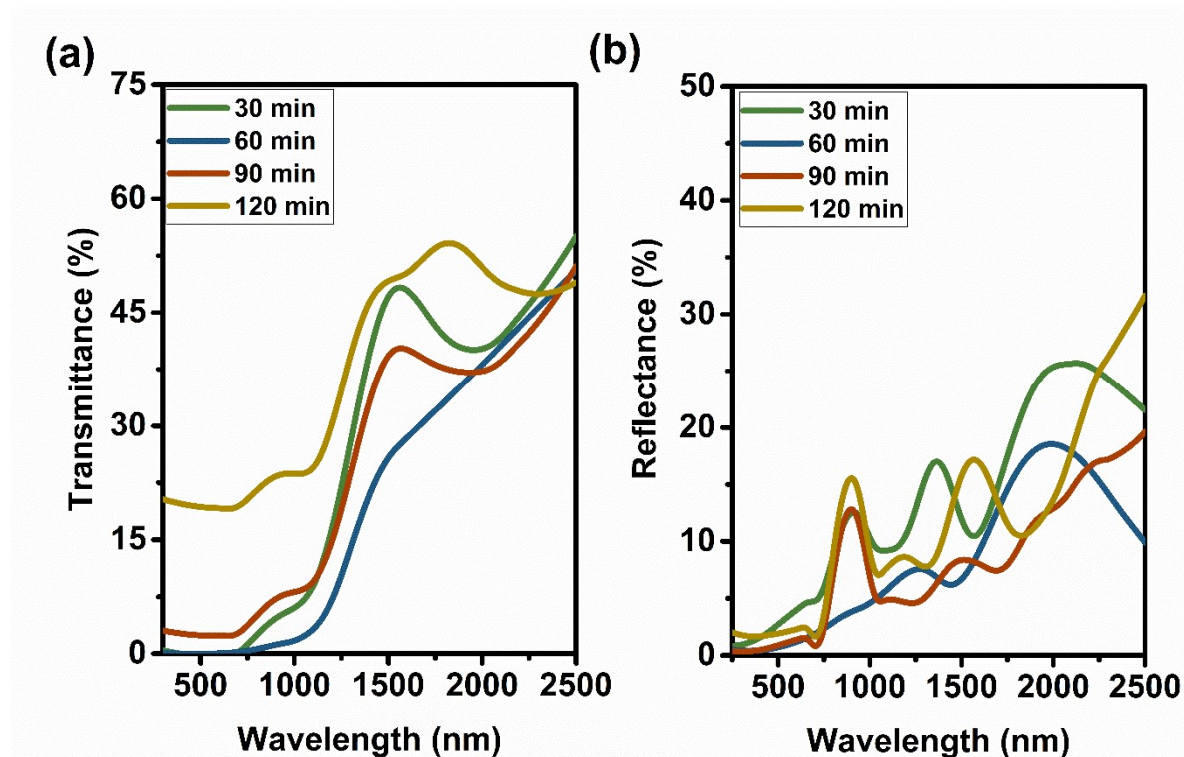


Figure 4.13 (a) Transmittance and (b) reflectance of samples sulfurized for 30, 60, 90, and 120 min.

Figure 4.14 shows the bandgap diagrams for the films, which were computed using the Tauc relation (equation 2.5). The optical bandgap of films sulfurized for 30, 60, 90, and 120 min are 0.96, 0.96, 0.94, and 0.91 eV, respectively. These values are consistent with previous

reports for Cu_2SnS_3 thin films [138]. The slight deviation in optical bandgap values can be accounted for the difference in elemental composition and the presence of the Cu_4SnS_4 phase [131].

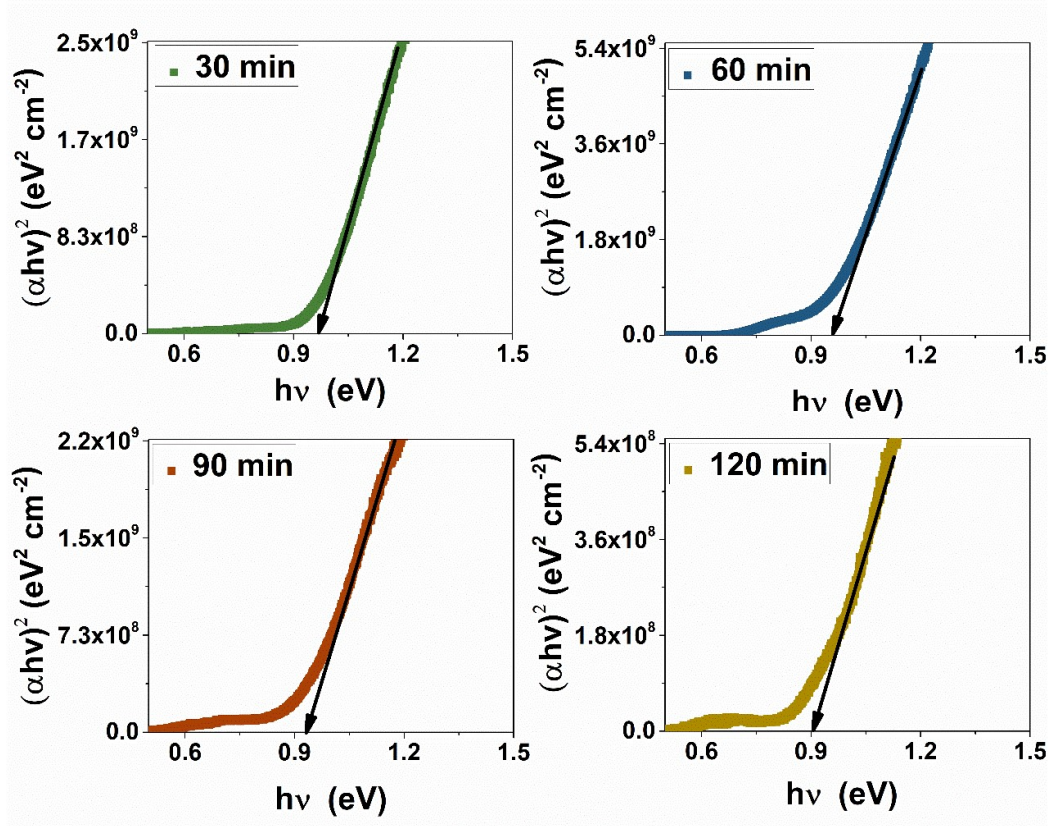


Figure 4.14 Tauc plots of films sulfurized for 30, 60, 90, and 120 min.

4.2.7 Electrical characterization

The electrical properties of films were evaluated using I-V measurements under dark conditions and are given in figure 4.15. The electrical conductivity of films sulfurized for 30, 60, 90, and 120 min are 32.6 , 1.78 , 2.7 , and 1.1 $(\Omega\cdot\text{m})^{-1}$, respectively. The sample sulfurized for 30 min shows higher conductivity than those of all other conditions owing to the existence of unreacted binary phases (CuS) and copper-rich composition. The presence of binary phases in the 30 min sample was previously deduced from the Raman spectrum.

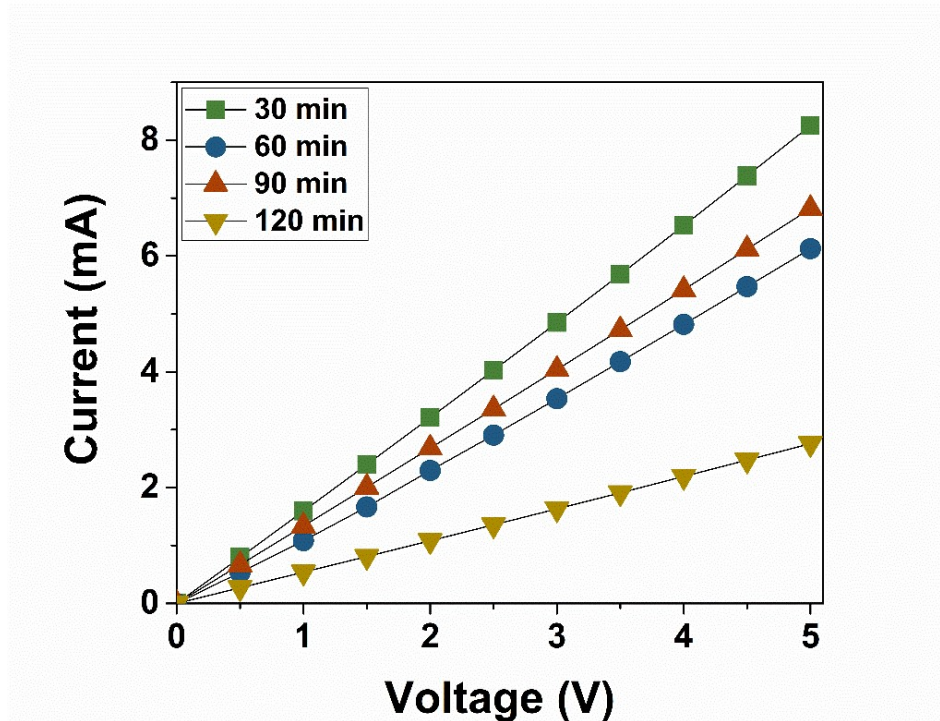


Figure 4.15 Current-voltage curve of films sulfurized for 30, 60, 90, and 120 min.

After analyzing the outcomes, a sulfurization time of 60 minutes and a sulfur quantity of 20 mg is used for further investigations. The quantity of copper was found to be sufficient for the formation of nearly stoichiometric Cu_2SnS_3 thin films.

4.3 Effect of sulfurization temperature on the properties of Cu_2SnS_3 thin films

This section discusses the optimization of sulfurization temperature and the formation of Cu_2SnS_3 thin films with optimal properties. The thickness of the copper precursor layer was reduced to 80 nm for the formation of copper-deficient films while that of the SnS layer was maintained at 450 nm. The sulfurization temperature was varied from 350 to 550 °C and the role of sulfur annealing temperature on the optoelectronic characteristics of Cu_2SnS_3 thin films was studied.

4.3.1 X-ray diffraction analysis

XRD analysis was used to assess how the sulfurization temperature affected the structure of the formed Cu_2SnS_3 thin films.

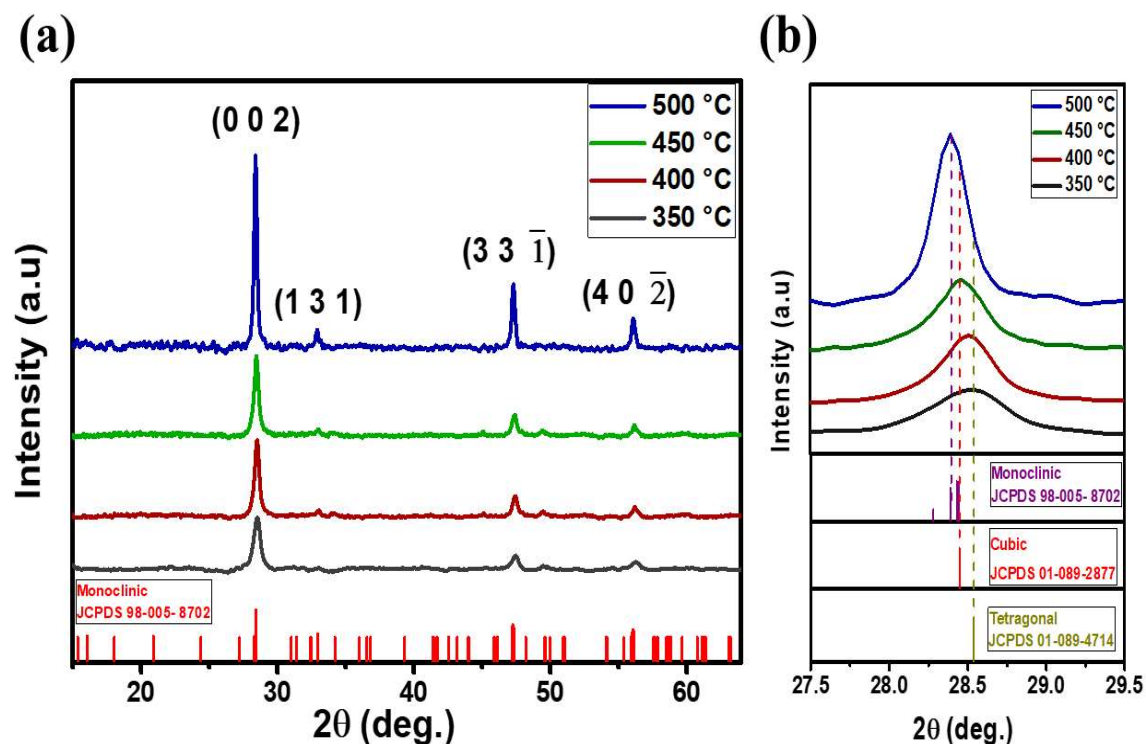


Figure 4.16 (a) XRD patterns of Cu_2SnS_3 samples sulfurized at 350 to 500 °C along with standard monoclinic Cu_2SnS_3 pattern and (b) magnified principal peak of XRD patterns along with the standard pattern of monoclinic, cubic, and tetragonal Cu_2SnS_3 .

The XRD patterns of Cu-Sn-S thin films sulfurized at different temperatures are presented in Figure 4.16(a) along with the standard pattern of monoclinic Cu_2SnS_3 . All thin films exhibit intense characteristic diffraction peaks at 28.5, 32.9, 47.3, and 56.2° which are accounted for cubic, tetragonal, and monoclinic polymorphs of Cu_2SnS_3 . Figure 4.16(b) represents the magnified principal peak of Cu_2SnS_3 samples along with the standard pattern of monoclinic, cubic, and tetragonal Cu_2SnS_3 . The shift of the principal peak towards the standard peak of monoclinic Cu_2SnS_3 indicates the formation of a pure monoclinic phase at 500 °C. The thin film sulfurized at 500 °C displays intense characteristic diffraction peaks at 28.4, 32.9, 47.3,

and 56.2° which are attributed to the reflections from (002) , (131) , $(33\bar{1})$, and $(40\bar{2})$ planes of monoclinic Cu_2SnS_3 . It is noteworthy that the coexistence of polymorphs at lower temperatures has been reported [51]. Improved crystalline quality and phase purity of films as a result of increasing the sulfurization temperature is evident from the diffraction peak intensities. Further increasing the temperature to 550°C , the diffraction pattern contains an intense peak corresponding to the impurity Cu_4SnS_4 phase. This also results in the formation of voids on the surface and the film was partially removed from the substrate (inset of Figure 4.17). Higher temperature annealing of Cu_2SnS_3 thin films causes evaporation of Sn which triggers the formation of impurity phases. Growth of conductive impurities such as CuS , Cu_3SnS_4 , and Cu_4SnS_4 above 500°C and their detracting impact on the properties of Cu_2SnS_3 thin films have been vastly reported in the literature [139].

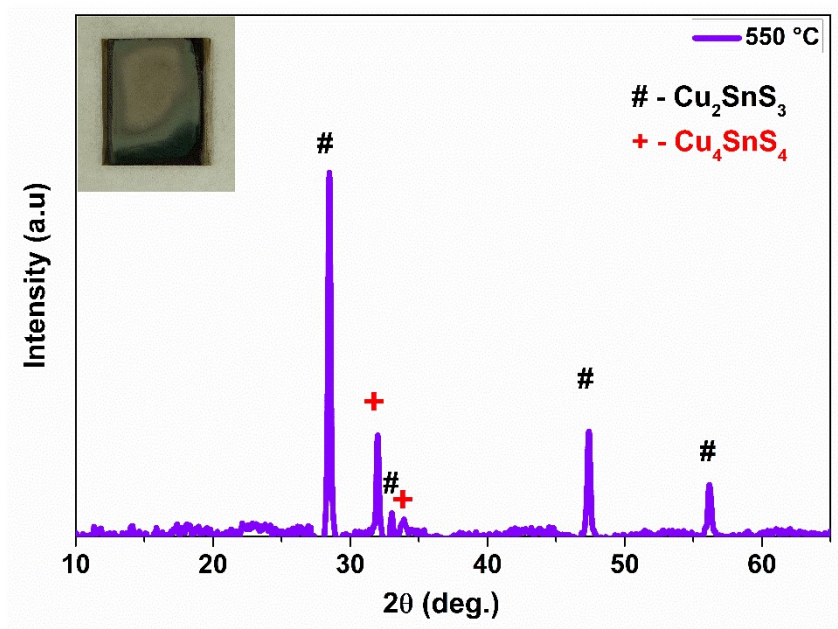


Figure 4.17 XRD pattern of sample sulfurized at 550°C along with sample photo as inset.

The average crystallite size was estimated using the Scherrer equation (equation 2.2), from which the values are 14.0, 19.2, 22.8, and 39.1 nm for 350, 400, 450, and 500°C samples, respectively. The uncertainty in identifying the structure of films persists due to similar diffraction peaks, which leads to the use of Raman spectroscopy to assign the crystal structure of Cu_2SnS_3 accurately (section 4.3.3).

4.3.2 Rietveld refinement

The Rietveld refinement of the diffraction data of the 500 °C sample was carried out using GSAS-II (General Structure Analysis System-II) and is given in figure 4.18 [140]. Cu_2SnS_3 monoclinic structure reported by Onoda et. al. was used as the base crystal structure for the refinement process [141]. In the Rietveld refined pattern, Bragg's peak positions are plotted as blue vertical lines. The background of the pattern was corrected by the Chebyshev function provided by the software. Rietveld refinement with the goodness of fit (GOF=1.19) value near unity and the extremely low residual value (R_w) of 2.74 % reinforces the formation of the monoclinic Cu_2SnS_3 phase. The refined unit cell parameters: $a = 6.65129 \text{ \AA}$, $b = 11.52083 \text{ \AA}$, $c = 6.65621 \text{ \AA}$, $\alpha(\alpha) = 90.0$, $\beta(\beta) = 109.241$, $\gamma(\gamma) = 90.0$, volume = 481.563 \AA^3 , and density = 4.706 g/cm^3 . The R_{exp} value and GOF are significantly lower than the previous reports on the refinement of monoclinic Cu_2SnS_3 thin films [142].

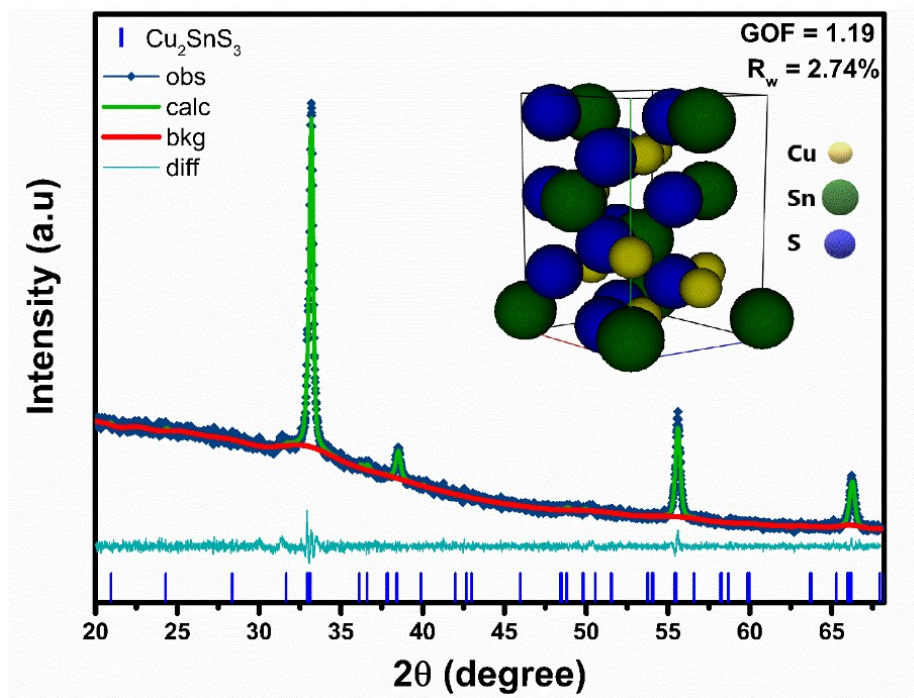


Figure 4.18 Rietveld refinement results of 500 °C sample with a graphical representation of refined unit cell as inset.

4.3.3 Raman analysis

Raman spectroscopy is useful for identifying the structure of Cu_2SnS_3 polymorphs owing to their distinct vibration peaks. Raman spectra obtained for Cu_2SnS_3 thin films formed at different sulfurization temperatures are presented in Figure 4.19. Samples annealed at 350 and 400 °C have vibrational peaks at 296, 334, 350, and 475 cm^{-1} whereas 450 and 500 °C samples show peaks at 290, 316, 350, and 372 cm^{-1} . According to previous reports, the peaks exhibited by the 500 °C sample accounted for the characteristic vibrational modes of monoclinic structure: 290 (A' symmetry mode), 316 (A' symmetry mode), 350 (A' symmetry mode), and 372 cm^{-1} (A'' symmetry mode) [42,143]. Raman peaks at 296 and 334 cm^{-1} agree with values reported for tetragonal structures of Cu_2SnS_3 thin films [42]. This suggests the coexistence of monoclinic and tetragonal structures in the 350 and 400 °C samples. A similar coexistence of polymorphs of the Cu-Sn-S phase was reported in the investigations of Yang et. al. and Zhao et. al. [51,144]. A trivial peak at 475 cm^{-1} due to the presence of binary phases of copper (Cu_{2-x}S) was also reported [145]. From the assessment of numerous investigations, distinct vibrational modes for polymorphs of Cu_2SnS_3 are accepted as follows: 303 and 355 cm^{-1} for cubic, 296 and 336 cm^{-1} for tetragonal, and 290 and 352 cm^{-1} for monoclinic phase [42]. The disappearance of the peak corresponding to the secondary phase of copper after 400 °C indicates the importance of sulfurization at higher temperatures for the complete conversion into the ternary phase. A shift of the vibrational peak at 295 cm^{-1} to lower frequencies is accounted for the formation of pure monoclinic Cu_2SnS_3 by different investigations [51,146]. Accordingly, a gradual shift of the first intense peak from 296 to 290 cm^{-1} when temperature increased from 350 to 500 °C confirms the formation of monoclinic structured films. In addition, the absence of vibrational peaks corresponding to cubic and tetragonal phases and the growth of all four characteristic vibrational modes of the monoclinic phase validate the formation of monoclinic Cu_2SnS_3 films at 500 °C. This study reports the formation of the monoclinic phase pure at relatively lower temperatures (<550 °C) using this method that combines chemical and physical deposition techniques [51].

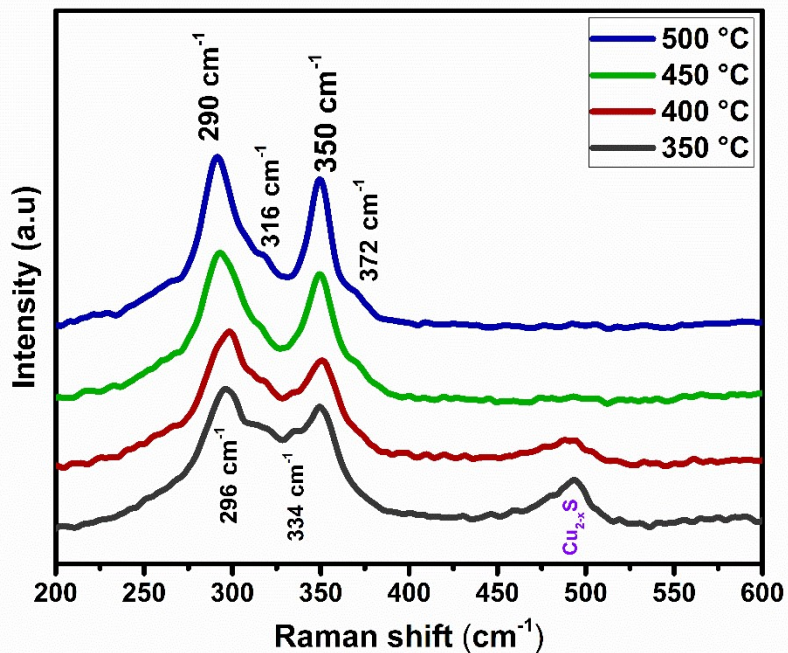


Figure 4.19 Raman spectra of Cu_2SnS_3 samples sulfurized at 350, 400, 450, and 500 °C.

4.3.4 Chemical composition - XPS

XPS was employed to study the chemical environment and oxidation state of elements in the films. Figure 4.20 represents the survey spectrum and core level electron spectra of Cu, Sn, and S of the 500 °C sample. The XPS survey shows the peaks corresponding to elements: Cu, Sn, S, C, and O on the surface. Surface contamination on the film surface was responsible for the presence of trivial peaks of oxygen (O) and carbon (C) in the survey spectrum which was further removed by etching using Ar^+ ions. The core level spectrum of Cu comprises two peaks at 932.7 and 952.5 eV which are associated with spin-orbit doublets of Cu with an energy separation of 19.8 eV. The presence of the Cu^{1+} oxidation state is confirmed by these peaks which are associated with Cu $2p_{3/2}$ and Cu $2p_{1/2}$ singlet states [42]. The core level spectrum of Sn consists of doublets at 486.4 and 494.8 eV with an energy separation of 8.4 eV. These peaks correspond to Sn $3d_{5/2}$ and Sn $3d_{3/2}$ singlet states which further confirm the presence of Sn in the Sn^{4+} oxidation state [110]. The deconvoluted core level spectrum of S shows two peaks at 162.08 and 163.26 eV with an energy gap of 1.18 eV. These peaks are associated with S $2p_{3/2}$ and S $2p_{1/2}$ spin orbit coupled peaks of S and confirm the presence of

sulfur in of S^{2-} oxidation state. No satellite or shake-up peaks related to the Cu^{2+} state are observed around 942 eV, which further endorses the phase purity of the best condition sample (500 °C) [137].

A depth profile study was utilized to assess the distribution of constituent elements and composition at each level. X-ray photoelectron depth profile analysis of Cu, Sn, and S of 500 °C sample is presented in Figure 4.21. The consistent presence of Cu, Sn, and S throughout the samples was corroborated by well-defined characteristic peaks in the depth profile analysis. The complete conversion of stacked layers into ternary phases by diffusion and reaction at higher temperatures was confirmed by depth profile analysis.

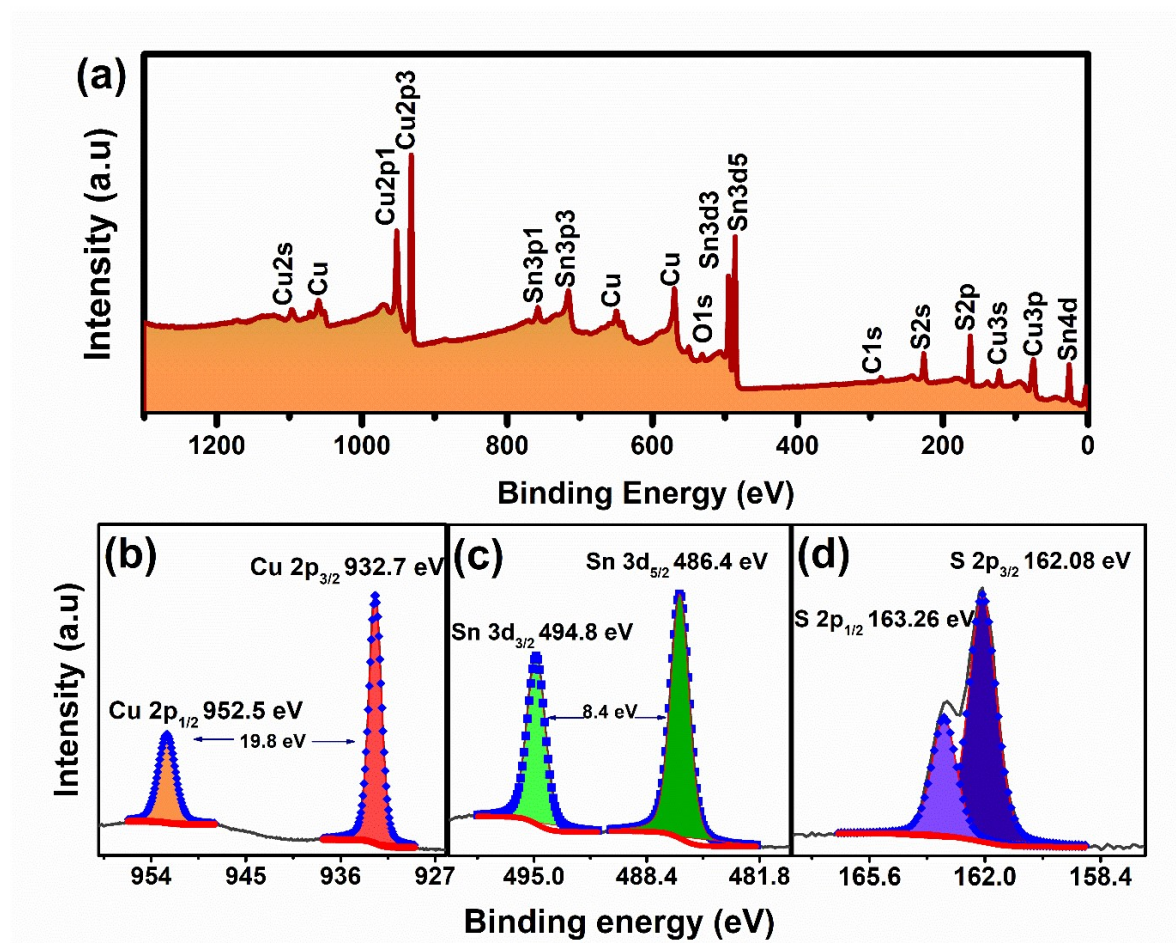


Figure 4.20 XPS a) survey, core electron spectrum of b) Cu, c) Sn, and d) S of sample sulfurized at 500 °C.

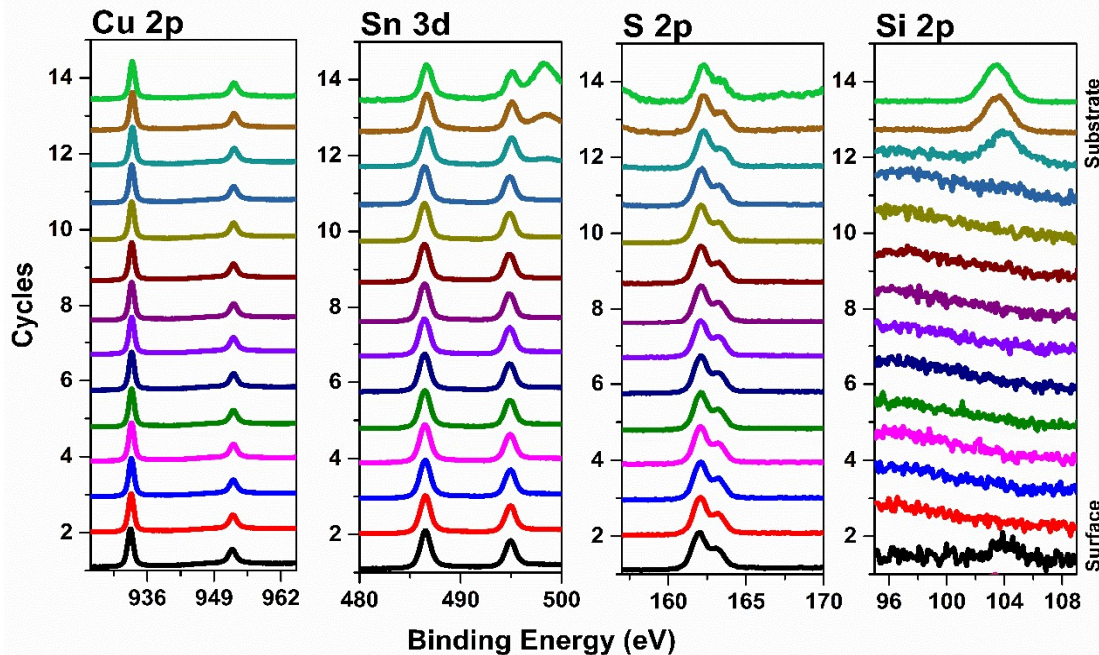


Figure 4.21 XPS depth profile analysis of 500 °C sample.

4.3.5 Elemental composition - EDX

Elemental composition was estimated using EDX analysis and is given in Table 4.3 (EDX spectra of all samples are presented in Figure 4.22). The 350 and 400 °C samples exhibit Cu-rich composition whereas the 450 and 500 °C samples reveal Cu-poor composition. Even though T400 samples have near stoichiometric composition, previous studies found that Cu and S-poor Cu_2SnS_3 are expected to deliver improved photovoltaic conversion efficiency [117]. Guan et. al. studied defect energetics of Cu_2SnS_3 using hybrid functional theory and found that the usual experimental conditions can lead to abundant deep centers consequently deteriorating solar cell performance [147]. They proposed that Sn-rich and S-poor conditions should be attempted to reduce the carrier recombination caused by the deep centers [148]. According to theoretical calculations supported by experimental studies of Baranowski et al., the Cu_2SnS_3 phase synthesized with both Cu- and S-poor conditions can give optimum carrier concentrations for device integration [117]. It is noteworthy that many researchers have demonstrated better photovoltaic performance for Cu and S-poor Cu_2SnS_3 [46,149]. In this

work, the phase pure sample that was sulfurized at 500 °C showed Cu and S-poor composition which is predicted as favorable for photovoltaic applications.

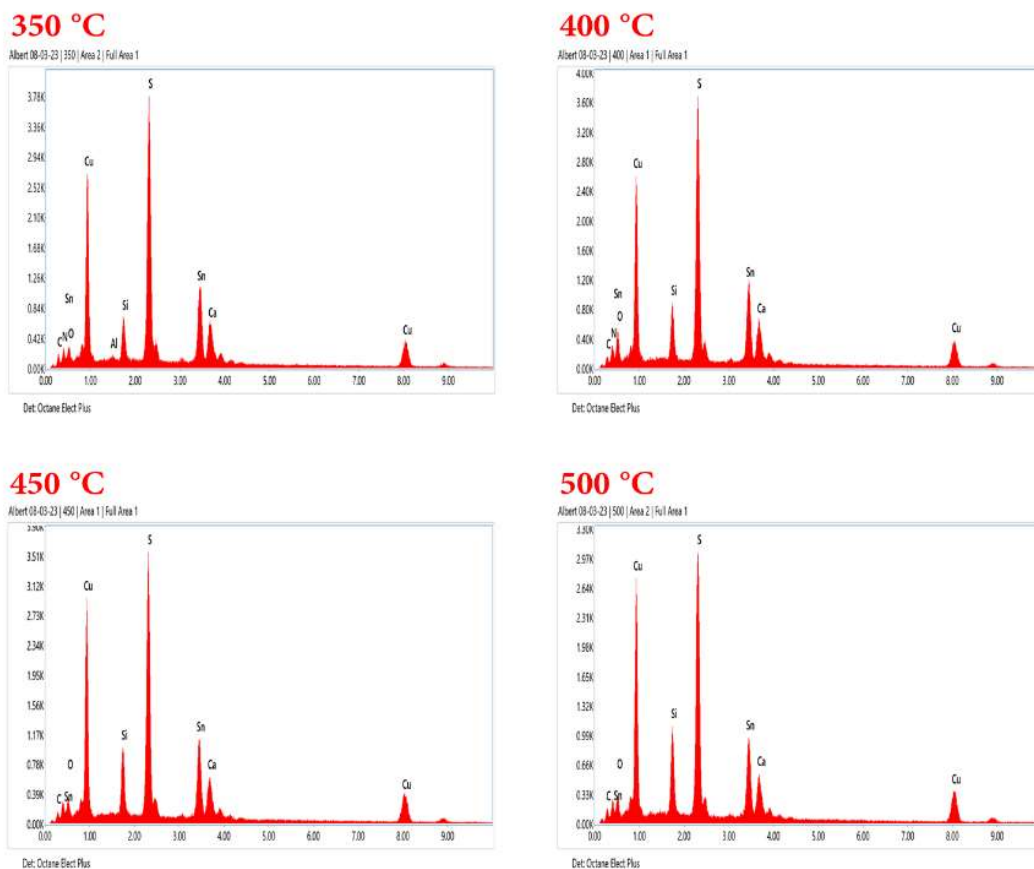


Figure 4.22 EDX spectra of Cu_2SnS_3 films sulfurized at 350 to 500 °C.

Table 4.3 Elemental composition of samples sulfurized at 350 to 500 °C

Sample	Cu (%)	Sn (%)	S (%)	Composition
350 °C	35.82	16.56	47.62	$\text{Cu}_{2.16} \text{Sn S}_{2.88}$
400 °C	33.64	16.65	49.81	$\text{Cu}_{2.02} \text{Sn S}_{2.99}$
450 °C	33.34	17.89	48.77	$\text{Cu}_{1.86} \text{Sn S}_{2.73}$
500 °C	31.8	19.45	48.75	$\text{Cu}_{1.63} \text{Sn S}_{2.51}$

EDX mapping of samples was utilized to evaluate the uniform distribution and homogeneity of the constituent elements of the ternary phase which are presented in Figure 4.23. EDX elemental mapping of samples shows a uniform distribution of Cu, Sn, and S.

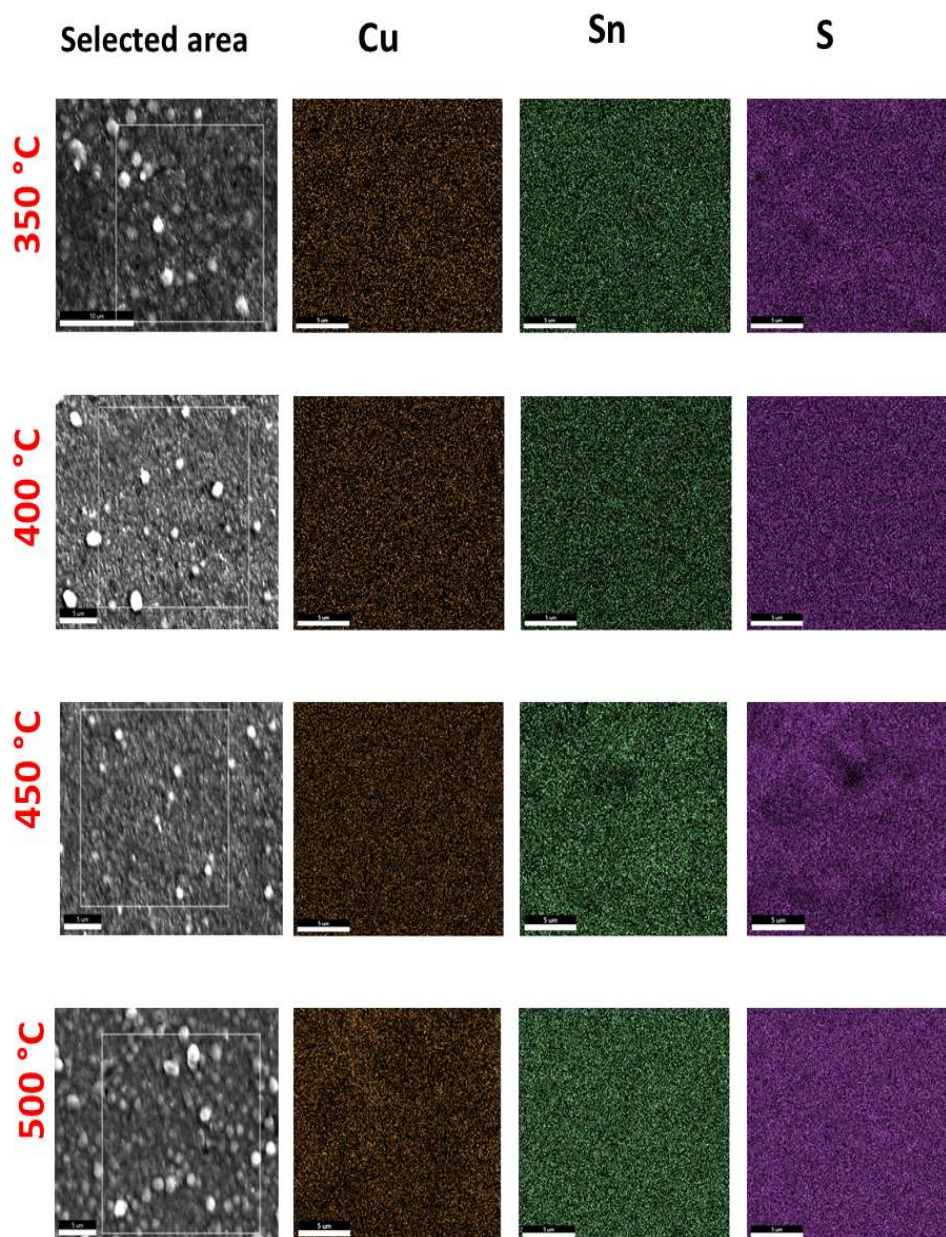
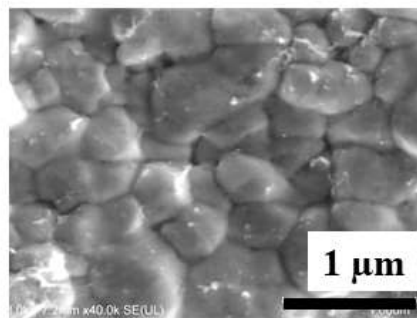
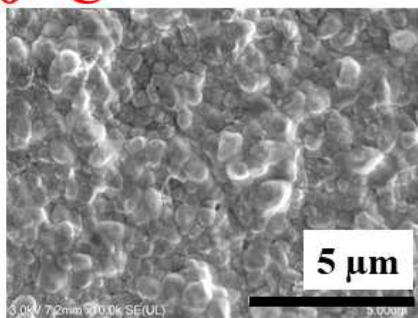


Figure 4.23 EDX elemental mapping of Cu_2SnS_3 samples sulfurized at 350 to 500 °C.

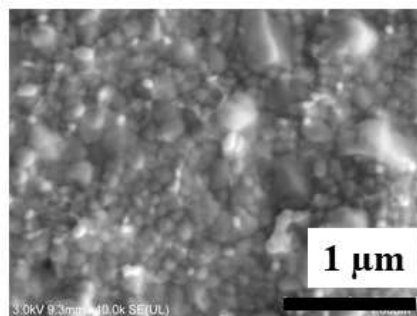
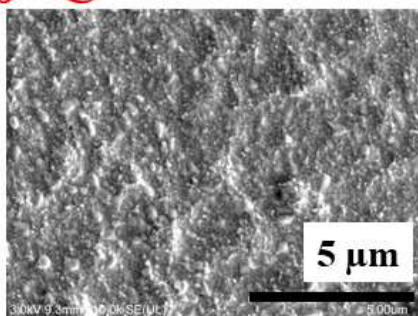
4.3.6 Surface morphology- SEM

The surface morphology of films was analyzed using scanning electron microscopy and images are given in Figure 4.24. The 350 °C sample shows a network morphology of randomly distributed flakes resembling SnS petal-like morphology. The 400 °C sample displays a reduction of these nonuniformly distributed flakes and the starting of the formation of smaller spherical grains on the surface. Some of the grains are fused and moderately bigger grains appear on certain parts of the 450 °C sample. Uniformly distributed bigger grains are observed on the surface after increasing the temperature to 500 °C. Similarly, a significant improvement in grain size by increasing the annealing temperature from 470 to 560 °C was reported by Yang et. al. for Cu_2SnS_3 thin films deposited via spin coating [51]. The formation of long flakes on the surface of samples sulfurized at 350 and 400 °C is due to the agglomeration and diffusion of the copper into the SnS. This diffusion of the copper into the SnS layer might be incomplete until 400 °C. As the temperature increased, more copper diffused into the structure and reacted with SnS under the sulfur atmosphere. Subsequently, the fusion of smaller grains led to the formation of larger grains on the surface. The pure ternary compound was formed at 450 °C and any additional temperature applied was used for the fusion of smaller grains to form bigger, uniform, and compact grains. The 500 °C sample exhibited an interconnected bigger grain microstructure that is suitable for photovoltaic applications. The bigger grains can minimize the recombination of charge carriers due to scattering at grain boundaries which can facilitate better carrier mobility [142]. This trend in grain size is also consistent with the crystallite size values estimated using X-ray diffraction patterns. By this method, compact larger grain morphology for Cu_2SnS_3 thin films was attained at relatively lower sulfurization temperatures than in previous reports [51,138]. Sulfurization temperature was found to have a great role in the surface morphology and grain development of Cu_2SnS_3 thin films.

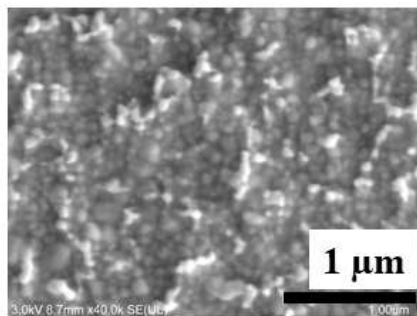
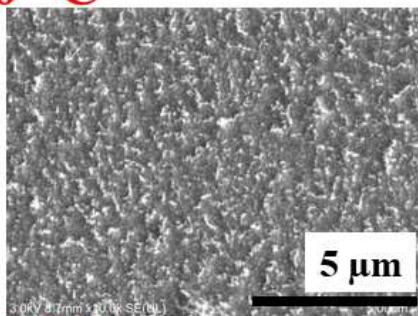
500 °C



450 °C



400 °C



350 °C

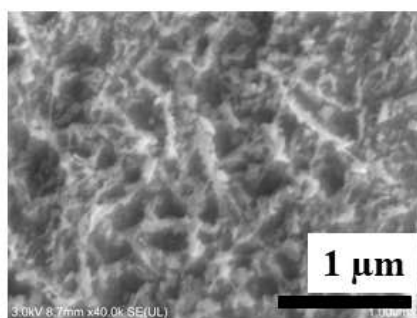
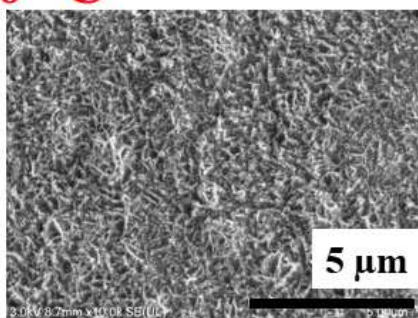


Figure 4.24 SEM images of Cu_2SnS_3 samples sulfurized at 350 to 500 °C.

4.3.7 Surface topography -AFM

The surface topography of films studied using AFM and the corresponding 2D and 3D images of the samples annealed at different sulfurization temperatures are presented in Figure 4.25. AFM images are consistent with SEM images and the improvement in grain growth is also visible in the AFM images.

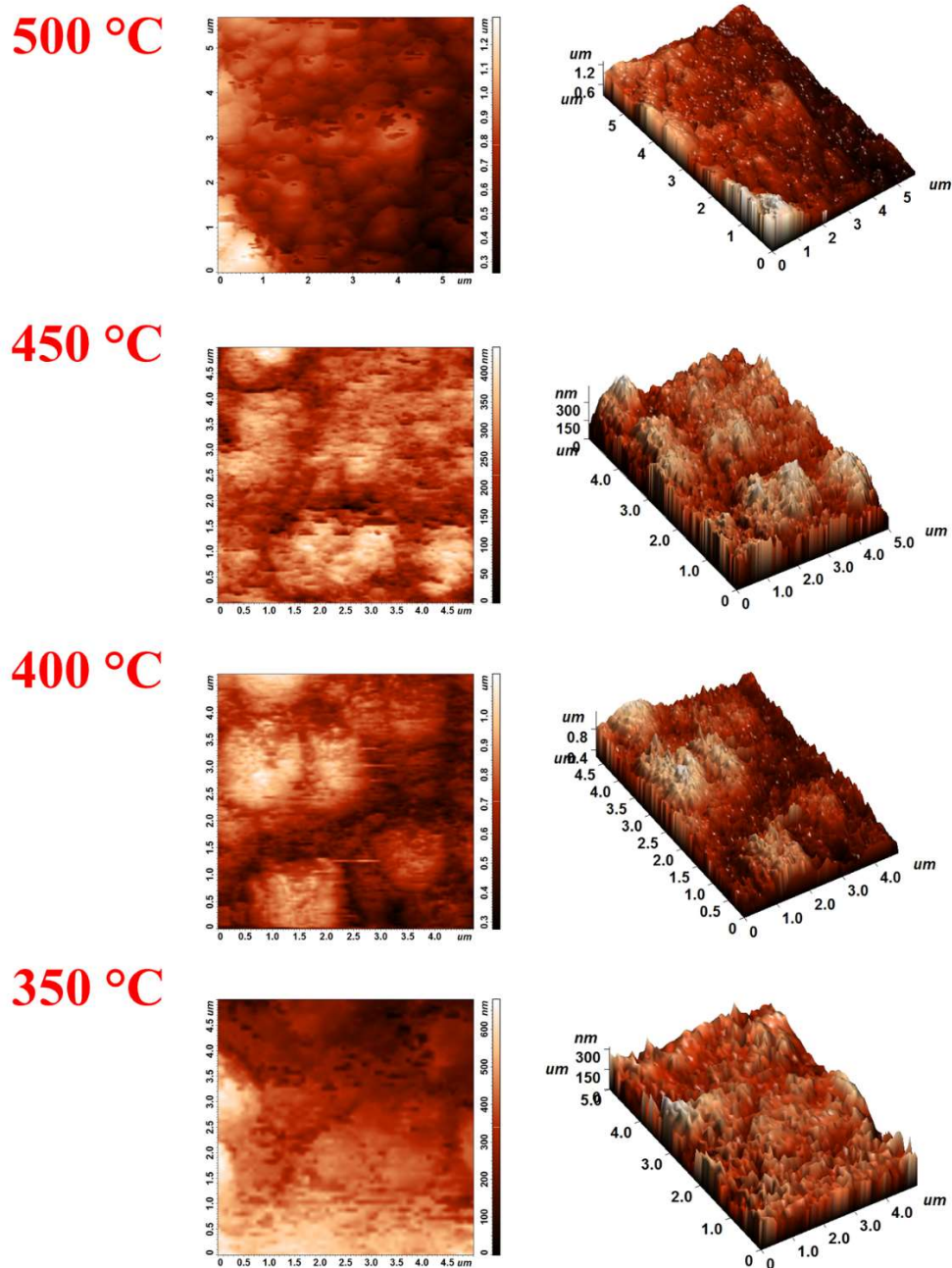


Figure 4.25 AFM 2D and 3D images of samples sulfurized at 350 to 500 °C

4.3.8 Optical characterization

A UV-Vis-NIR spectrophotometer was used to analyze the transmittance and reflectance of films in the range of 250 to 2500 nm presented in figure 4.26) All films show very low transmittance and reflectance in the visible light region. Phase pure monoclinic structured 500 °C sample exhibits characteristic double absorption of monoclinic Cu_2SnS_3 thin films in the 1100 to 1300 nm region [150,151].

The absorption coefficient was computed using equation 2.4. From the calculations, it was found that the Cu_2SnS_3 thin films possess a large optical absorption coefficient $>10^5 \text{ cm}^{-1}$ in the visible region.

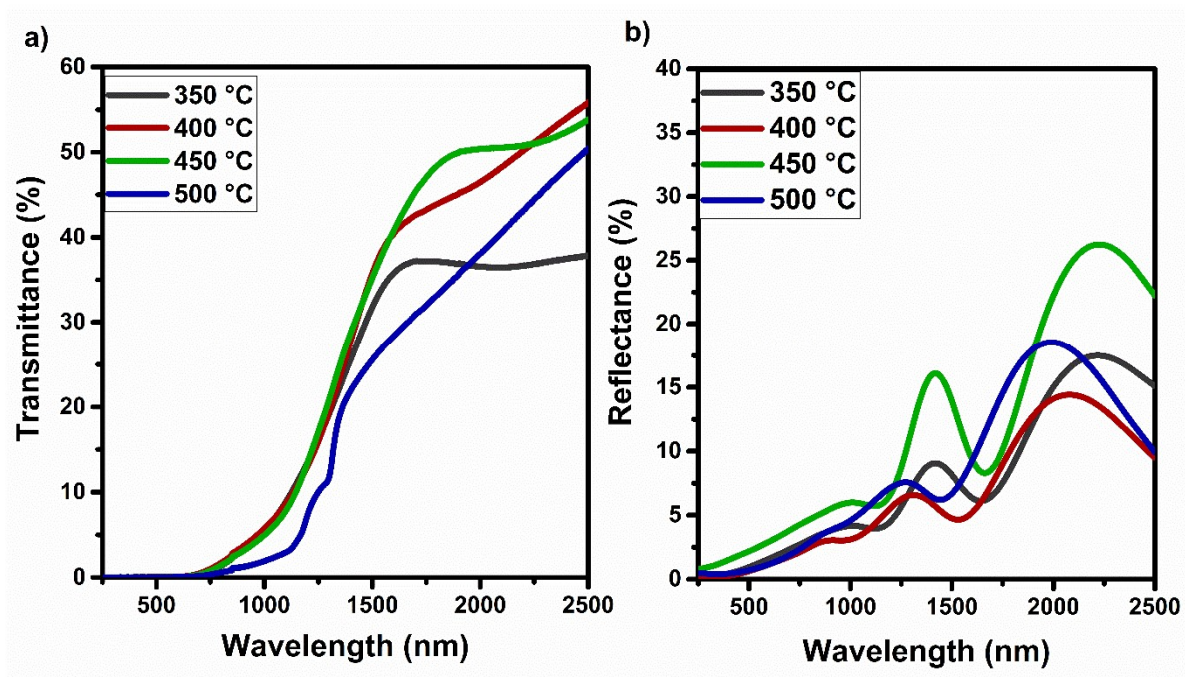


Figure 4.26 Optical (a) transmittance and (b) reflectance of Cu_2SnS_3 thin films sulfurized at 350, 400, 450, and 500 °C.

The bandgap (E_g) values of the samples were determined using equation 2.5 [119]:

The direct bandgap can be determined by extrapolating the linear portion of the plot into the photon energy axis. The bandgap values of thin films are 1.13, 1.11, 1.03, and 0.97 eV for the 350, 400, 450, and 500 °C, respectively (Figure 4.27). The 350 and 400 °C samples

possess slightly higher band gap values than the reported value for the monoclinic phase due to the presence of cubic and tetragonal Cu_2SnS_3 . Monoclinic Cu_2SnS_3 film (500 °C) shows two optical absorptions at 0.9 and 0.97 eV. Several experimental studies have shown evidence of two optical absorption edges in monoclinic Cu_2SnS_3 between 0.91–0.94 eV and 0.97–1.04 eV [42]. This phenomenon originates from direct optical transitions at the Γ -point from three energetically closely spaced valence bands to a single conduction band in perfectly crystalline monoclinic Cu_2SnS_3 [150]. Theoretical studies on monoclinic structured Cu_2SnS_3 using VASP revealed that the conduction band consists of contribution from Cu 3d and S 3p states whereas the valance band was found to be comprised of S 3p and Sn 5s states [152].

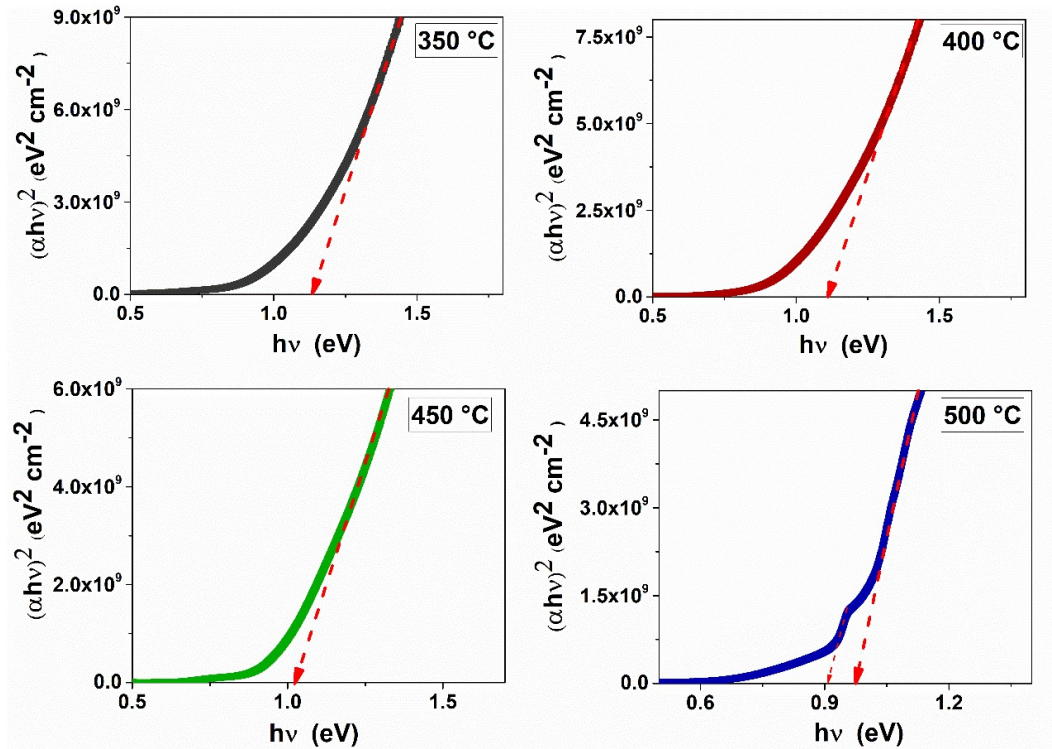


Figure 4.27 Tauc plots of Cu_2SnS_3 films sulfurized at 350, 400, 450, and 500 °C.

The refractive index (n) of Cu_2SnS_3 films at the band edges was calculated using the Herve and Vandamme relation as follows [153]:

$$n = \sqrt{1 + \left[\frac{A}{B + E_g} \right]^2} \quad (\text{equation 4.1})$$

where $A=13.6$ eV and $B=3.47$ eV are constants.

The values of refractive index for Cu_2SnS_3 determined by applying the Herve and Vandamme relation were found to be 3.12, 3.13, 3.18, and 3.22 for 350, 400, 450, and 500 °C samples, respectively. Estimated values were found to be similar to the values reported by Guddeti et. al. and Reddy et. al. for Cu_2SnS_3 thin films [154,155].

4.3.9 Electrical characterization

The electrical properties of Cu_2SnS_3 thin films were examined employing photoconductive measurements under a bias voltage of 1 V (Figure 4.28). All samples showed a p-type conducting nature (by hot probe method) and electrical conductivity (σ) in the dark for the 350, 400, 450, and 500 °C samples were found to be 60, 12.3, 12.2, and 0.2 $\Omega^{-1}\text{cm}^{-1}$, respectively. Cu vacancies in the Cu_2SnS_3 films are responsible for p-type conductivity due to the presence of hole carriers by the formation of an acceptor level just above the valance band maximum [156]. The conductivity value of the 500 °C sample was found to be suitable for photovoltaic applications. The highly conductive 350 °C sample did not show any photoresponse whereas the 400 and 450 °C samples showed a transient photo-responsive behavior due to the thermoelectric effects and defect levels within the material. Different research groups reported similar persistent photoconductive behavior for Cu_2SnS_3 thin films and accounted for charge carrier trap levels in the material [42]. Cu_2SnS_3 is also explored widely for its impressive thermoelectric applications [157]. The 500 °C sample demonstrated better photo-responsive behavior due to the formation of copper-deficient phase pure monoclinic Cu_2SnS_3 [145].

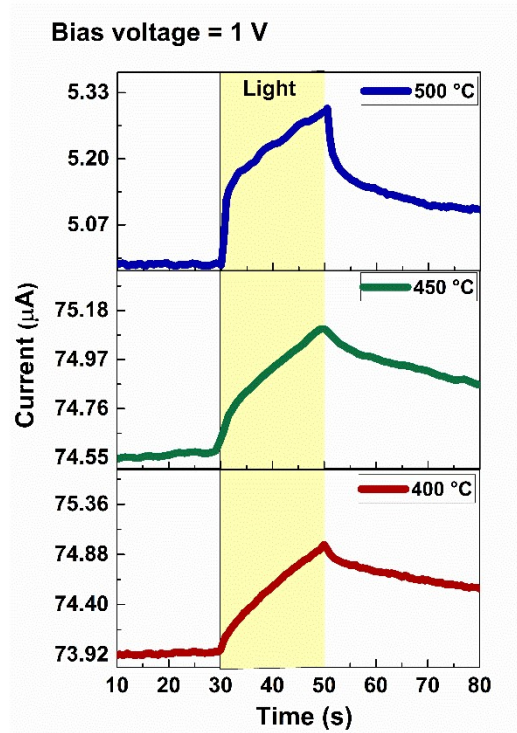


Figure 4.28 Photoresponse measurements of samples sulfurized at 400, 450, and 500 °C.

Copper and sulfur deficient monoclinic Cu_2SnS_3 thin films were synthesized by the sulfurization of stacked Cu (80 nm)/SnS (450 nm) precursors at 500 °C using 20 mg of sulfur for 1 h. These optimized monoclinic Cu_2SnS_3 thin films are used for the fabrication of photovoltaic and photodetector devices.

CHAPTER 5

PHOTOVOLTAIC AND PHOTODETECTION APPLICATIONS USING OPTIMIZED Cu_2SnS_3 THIN FILMS

This chapter demonstrates photovoltaic and photodetection applications with the optimized Cu_2SnS_3 layer. The photovoltaic structure was fabricated with monoclinic Cu_2SnS_3 (M- Cu_2SnS_3) as the absorber layer and CdS as the window layer. The effect of vacuum annealing temperature on the photovoltaic performance of the device was evaluated. Furthermore, the performance of the same structure with a thin p-SnS absorber layer was theoretically studied and the device was fabricated. The photodetection abilities of these photovoltaic structures were evaluated under the illumination of laser sources of different wavelengths.

5.1 CdS/CTS photovoltaic device

5.1.1 CdS/CTS thin film solar cell

The photovoltaic architecture was fabricated with optimized M- Cu_2SnS_3 thin films as the absorber layer. CdS was used as the window layer which was deposited on FTO substrates (front electrode) and conductive silver paint was used for painting the back electrodes. FTO/CdS/ Cu_2SnS_3 /Ag structure was fabricated, and the J-V curve is presented in Figure 5.1. The photovoltaic device structure resulted in photovoltaic parameters of V_{oc} = 174 mV, J_{sc} = 9.4 mAcm^{-2} , FF= 25 %, and PCE= 0.41 %. This low V_{oc} value accounted for the undesirable band alignment at the interface of the p-n junction, the presence of interface defects, band tail formation, and defects within the material [158]. The band alignment engineering at the heterojunction interface is critical to obtain high-performance solar cells. A spike-like or positive conduction band alignment (conduction band minimum (CBM) of the n-type semiconductor must be slightly higher than that of the p-type semiconductor) at the interface or at least a flat-band is favorable for a high efficiency device. The spike-like barrier minimize recombination losses by acting as a notch against photo-generated carriers in the

absorber layer. Spike barriers up to 0.4 eV are suitable for better charge transport, while larger conduction band offset values will lead to lower short-circuit current (J_{sc}) and efficiency. On the other side, cliff-like or negative conduction band offset (position of the CBM of the n-type semiconductor is lower than that of the p-type semiconductor) causes enhanced carrier recombination at trap states near the interface and poor cell performance. Consequently, V_{oc} decreases with increasing the absolute value of the conduction band offset [159]. The existence of lower shunt resistance paths in the circuit causes low V_{oc} due to the recombination of carriers at deep traps in the band gap [45]. Still, this open circuit voltage value is higher than some previous reports of Cu_2SnS_3 -based solar cells [60,160–162].

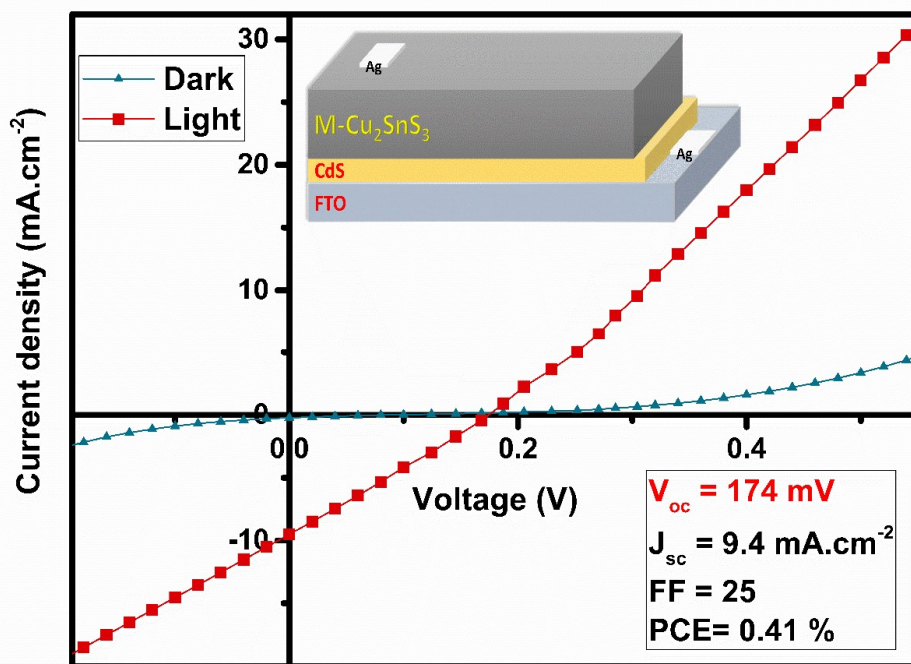


Figure 5.1 Current density vs voltage characteristics of the CdS/CTS photovoltaic cell.

Optimization of the device structure by incorporation of more layers, and evaluation of the impact of various transparent conductive oxide layers, buffer layers, hole transport layers, and electrodes can help to attain the maximum potential of this thin film solar cell. The optimization of the absorber layer/electron transport layer interface is considered the most effective approach to achieving higher open circuit voltages and efficiencies.

5.1.2 Effect of vacuum annealing on CdS/CTS thin film solar cell

The solar cell structure was annealed at different temperatures (100, 200, 300, and 400 °C) for 30 min in vacuum (1.5×10^{-2} Torr) and the J-V characteristics are given in Figure 5.2. The photovoltaic parameters obtained after annealing at 100 - 400 °C are tabulated in Table 5.1. The structure annealed at 100 °C resulted in photovoltaic parameters of: $V_{oc} = 212$ mV, $J_{sc} = 8.51$ mAcm⁻², FF = 25 %, and PCE = 0.35%. After increasing the temperature to 200 °C, an increase in open circuit voltage and FF was observed while the current density value decreased. The device annealed at 200 °C demonstrated $V_{oc} = 245$ mV, $J_{sc} = 5.72$ mAcm⁻², FF = 26 %, and PCE = 0.36%. This increase in V_{oc} resulted in a slight improvement in the power conversion efficiency. The photovoltaic structure annealed at 300 °C revealed the highest open circuit voltage of 310 mV, FF of 26 %, and a current density of 7.45 mAcm⁻². The photovoltaic device exhibited a low V_{oc} after increasing the annealing temperature to 400 °C. The photovoltaic parameters were: $V_{oc} = 151$ mV, $J_{sc} = 1.58$ mAcm⁻², FF = 24 %, and PCE = 0.06%. These inferior values might be due to the breakdown or decomposition of layers which subsequently leads to drastic diffusion at the interfaces. An improvement in open circuit voltage was registered along with the increase of annealing temperature up to 300 °C. This improvement can be accounted for reduced band-tailing states or the extended minority carrier lifetime [163]. The vacuum annealing at suitable temperatures causes a reduction of the deep-level defects and interface traps which aid in significantly decreasing nonradiative recombination [164]. Enhancement of V_{oc} can also be attributed to proper bandgap matching attained by minor alteration of band structure due to the inter-layer diffusion between the absorber and window layers [165]. CZTS solar cells have also reported similar enhancement of open circuit voltage by thermal annealing [166]. A decrease in current density values by annealing photovoltaic structures was observed. Grain boundary density was found to be increased by increasing the annealing duration while studying the impact of annealing time on the properties of Cu₂SnS₃ (section 4.2). Additional annealing after the sulfurization process might have also increased the grain boundary density in the absorber layer and equivalently recombination loss due to scattering at the grain boundaries [167]. Annealing of the absorber layer at higher temperatures results in the evaporation of volatile Sn and S from the surface. In addition, the diffusion of elements into the next layers

can cause an inhomogeneous distribution of elements which leads to the formation of binary phases [168]. These binary phases initiate a severe decrease in the J_{sc} and ultimately damage the photovoltaic structure [165]. The vacuum annealing studies revealed that careful optimization of thermal treatment parameters can aid in effectively improving the built-in voltage at the contact between the absorber and window layer. These enhanced open circuit voltages can improve hole mobility and cause extended lifetime for the electrons, ultimately improving the photovoltaic performance [166]. Other post-deposition thermal/surface treatments such as air annealing, rapid thermal processing, plasma thermal treatment, and pulsed laser treatment are also proposed for improved photovoltaic performance [51,123,124].

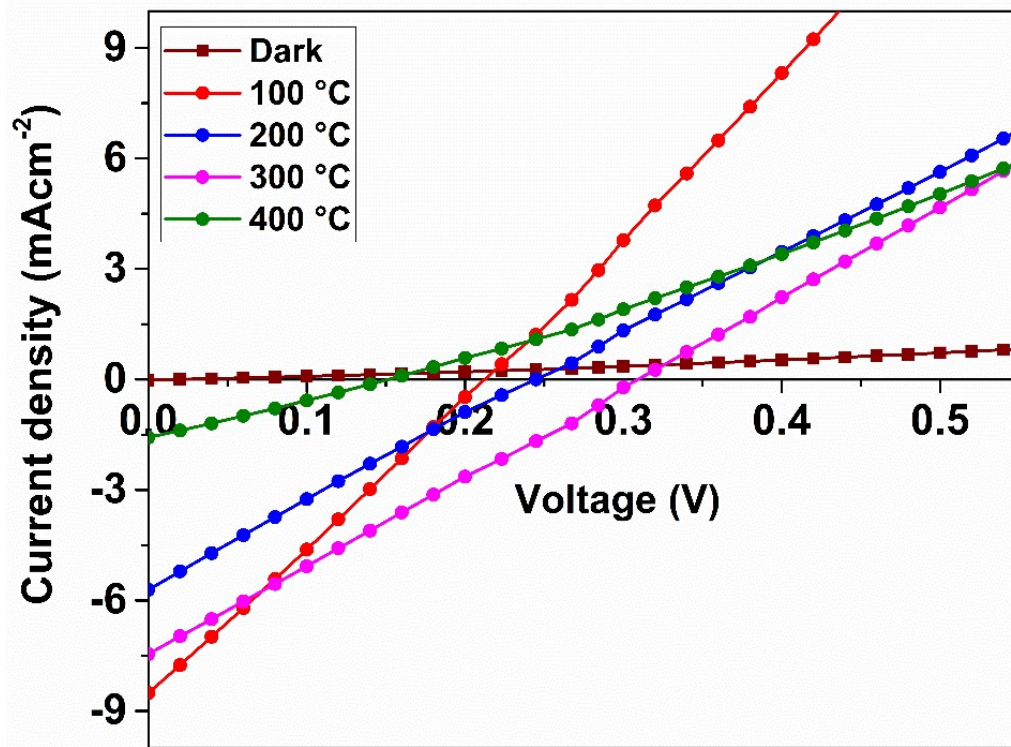


Figure 5.2 Current density vs voltage plot of CdS/CTS device annealed at different temperatures (100 - 400 °C)

Table 5.1 V_{oc} , J_{sc} , FF, and efficiency of CdS/CTS device annealed at different temperatures (100 - 400 °C)

Annealing temperature (°C)	V_{oc} (mV)	J_{sc} (mA.cm ⁻²)	FF (%)	Efficiency (%)
100	212	8.51	25	0.35
200	245	5.72	26	0.36
300	310	7.45	26	0.60
400	151	1.58	24	0.06

5.1.3 Self powered CTS/CdS photodetector

Conventional photodetector devices that operate under external power sources demand complex circuit configurations. This also causes an increase in production cost and limits their application in different environmental circumstances. The invention of self-powered photodetectors that work without an external power supply aroused as a prominent research topic in optoelectronics. The built-in electric field at the p-n junction aids in the suppression of carrier recombination by serving as the driving force for charge carriers [76]. Chalcogenide-based self-powered photodetectors have shown prodigious potential due to their cost efficiency and energy savings [75]. Cu_2SnS_3 -based self-powered photodetectors consisting of earth-abundant and low-cost materials can contribute greatly to sustainable and stable photodetection. The photodetection ability of the heterojunction of CdS and optimized Cu_2SnS_3 (photoconductive mode) was evaluated and the schematic diagram is given in Figure 5.3. The photovoltaic structure displayed excellent stability in cyclic photodetection over 20 cycles (10 s dark -10 s light -10 s dark) under zero bias. The response time of the photovoltaic structure was determined using photoresponse measurements with a data interval of 12 ms. The rise time of the device was found to be 99 ms and a decay time of 10 ms. Imperfection in the shape of photoresponse is due to the thermoelectric property of Cu_2SnS_3 that causes higher rise time than decay time.

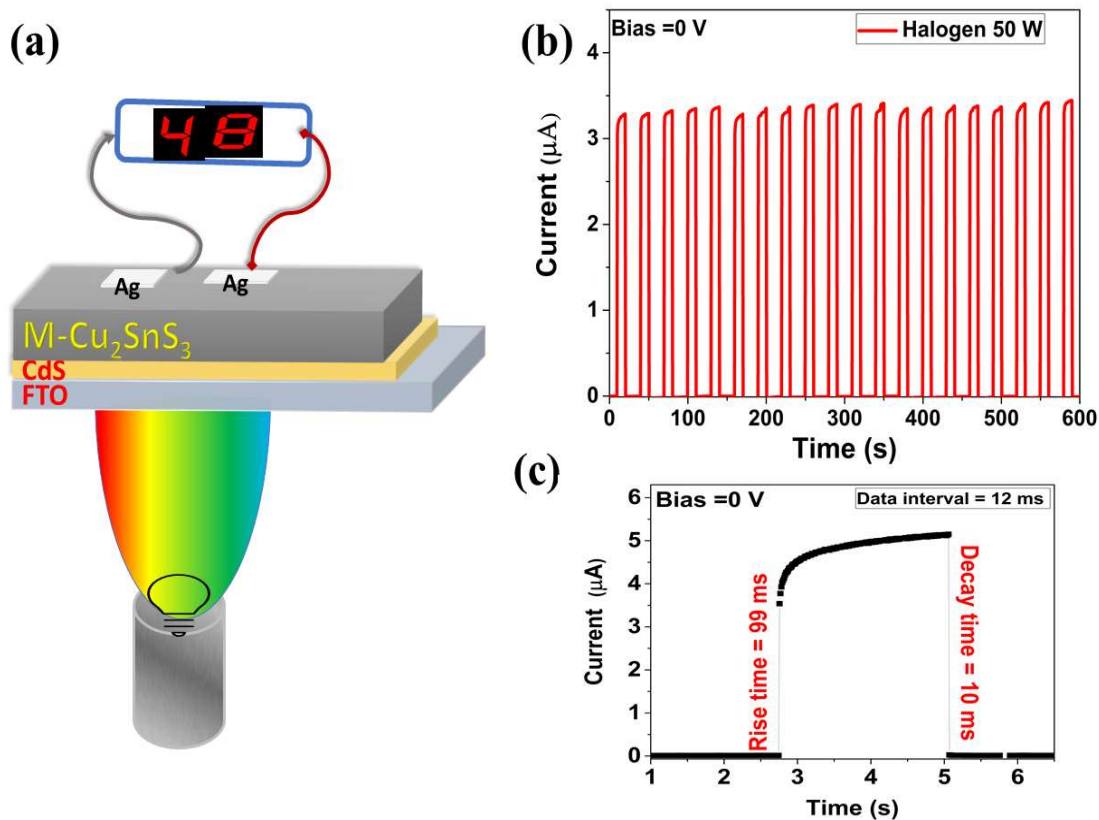


Figure 5.3 a) Photovoltaic device structure of CdS/CTS photodetector, b) photoresponse for 20 cyclic illuminations under 50 W halogen source illumination, c) photoresponse for one cycle of illumination for rise/decay time evaluation (data interval of 12 ms).

The cyclic photoresponse of the CdS/CTS device was measured under the illumination of LEDs of different wavelengths and given in Figure 5.4. Under LED illumination, the self-powered CdS/CTS photodetector demonstrated excellent responsiveness (current in the order of 10^{-6} A). The photocurrent increased in the order of UV to IR LEDs due to the increased absorption near the bandgap of the absorber layer and efficient transportation of charge carriers without thermal effect confrontations under NIR illumination.

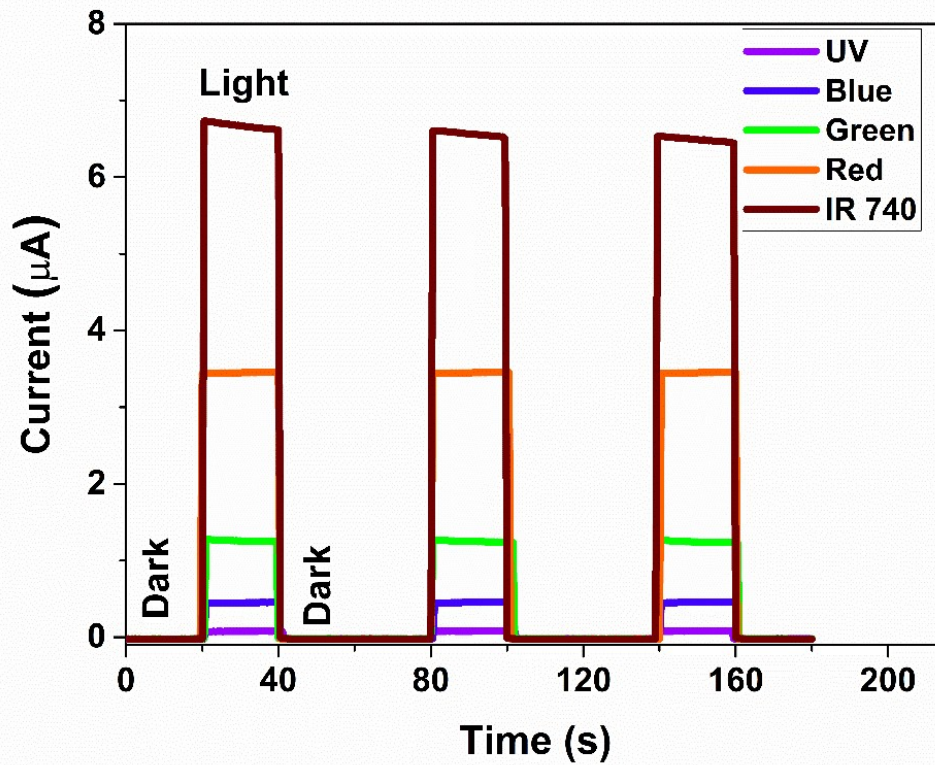


Figure 5.4 Cyclic photoresponse of the device illuminated with LEDs of different wavelengths.

The photodetection capabilities of a CdS/CTS self-powered device were explored utilizing laser sources of different wavelengths 532, 785, 840, and 1064 nm and a halogen source. Self-driven cyclic photoresponse of the CdS/CTS photovoltaic structure under different illuminations is given in Figure 5.5. Cyclic photoresponse measurements demonstrated high stability and reproducibility over broad UV-Vis-NIR regions. The device showed photocurrent in the order of 10^{-6} A for the 532, 785, and 840 nm laser illumination whereas 10^{-8} A for the 1064 nm laser. The responsivity and detectivity of the device under different sources of illumination were calculated using equations 1.6 and 1.7.

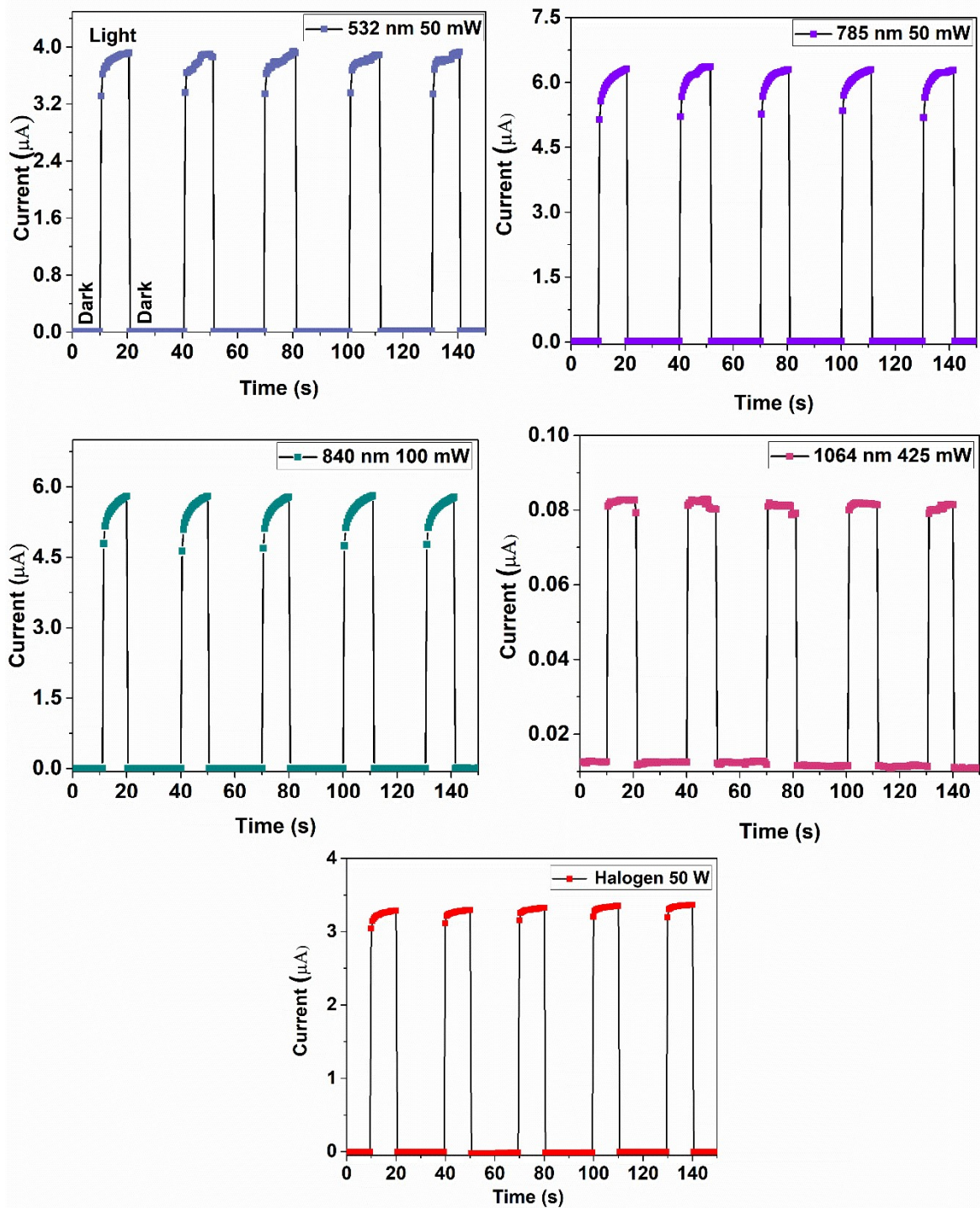


Figure 5.5 Cyclic photoresponse under illumination using different laser sources of wavelengths (532, 785, 840, and 1064 nm) and halogen 50 W lamp (bias voltage = 0 V).

Figure 5.6 represents the power density vs photocurrent (a-c) and power density vs responsivity (d-f) plots for 532, 785, and 1064 nm lasers at zero bias of the CdS/CTS device. The photocurrent was increased with the incident power density due to increased carrier generation. The responsivity was found to be decreasing with the rise in power density due to increased recombination rates at higher incident powers [169].

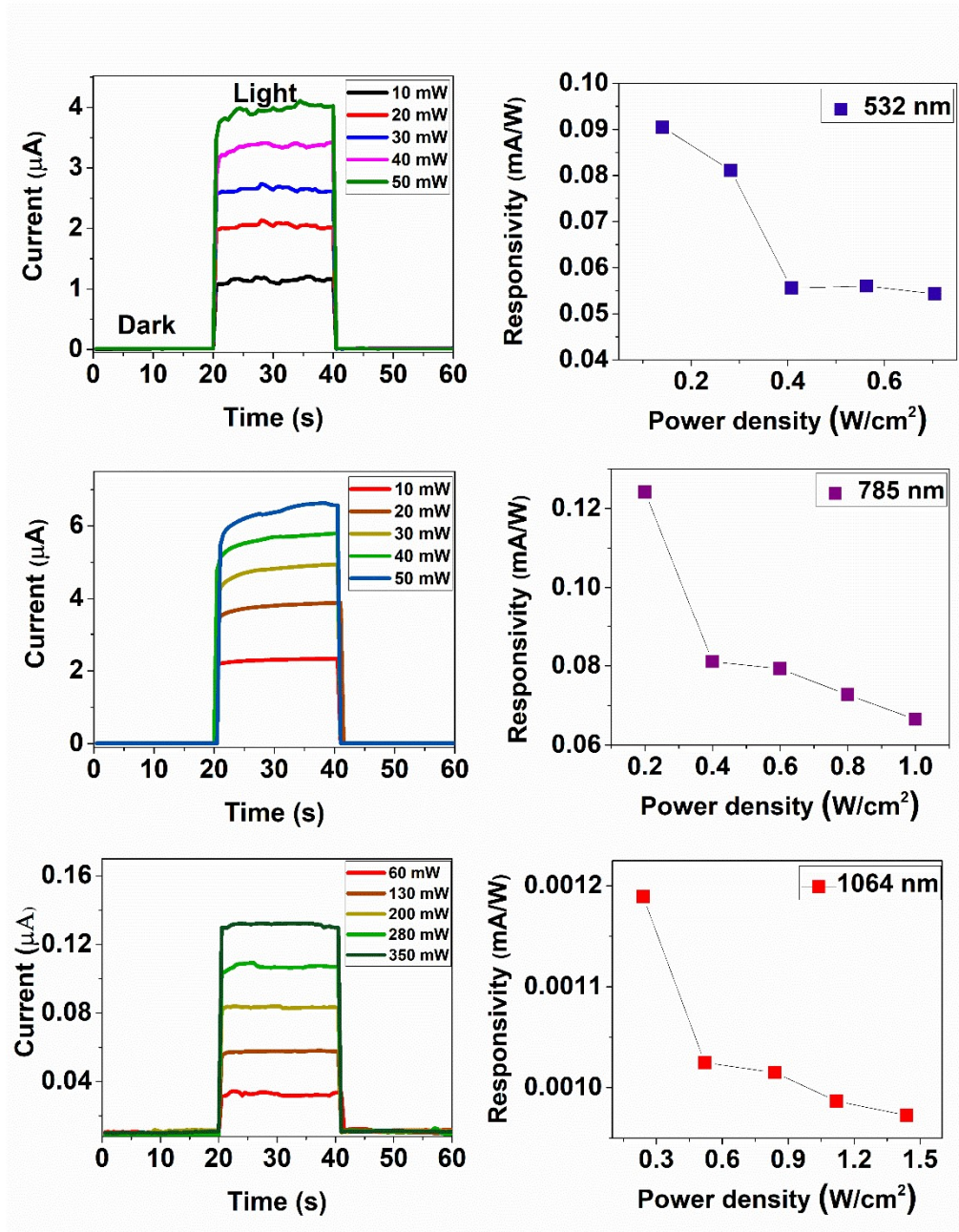


Figure 5.6 Power density vs photocurrent (a-c) and power density vs responsivity (d-f) for 532, 785, and 1064 nm lasers at zero bias of CdS/CTS device.

The power law fitting of photocurrent vs. power density for various wavelength illuminations is shown in Figure 5.7. The power law relationship is expressed as (equation 5.1).

$$I_{ph} = KP^\theta \quad (\text{Equation 5.1})$$

Where I_{ph} is the photogenerated current, K is a constant, P represents the incident power density and θ describes the response of the photocurrent to incident power. The determined exponent θ values of 532, 785, and 1064 nm laser illuminations are 0.63, 0.68, and 0.88, respectively where unity is considered as the ideal value. By Rose-Bube theory, unity is the ideal value and lower exponent values denote the occurrence of defect states inside a material, which subsequently increases the trapping and recombination of created carriers. [170].

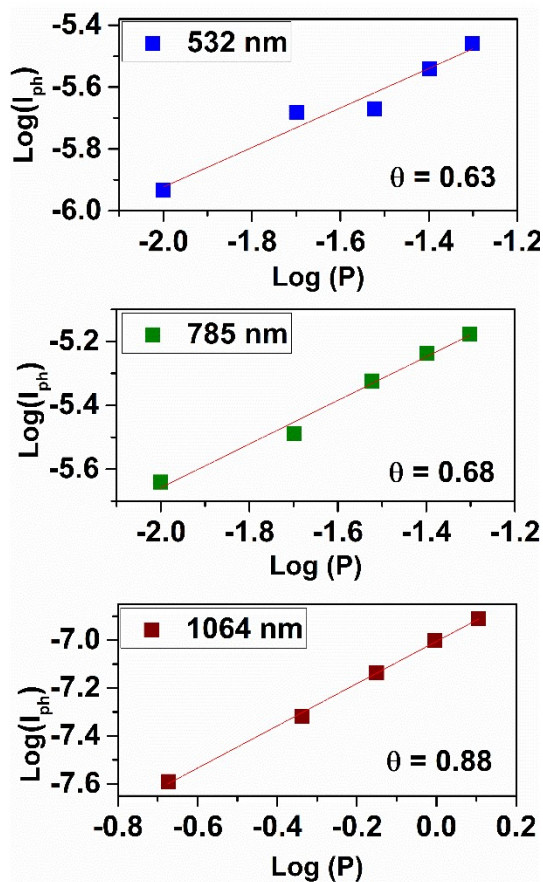


Figure 5.7 Power law fitting of photocurrent vs incident power density for different lasers (532, 785, and 1064 nm)

The variation of detectivity and responsivity vs wavelength of CdS/CTS photodetector under illumination using different laser sources is presented in Figure 5.8(a-b). The responsivity

values were 9.05×10^{-2} , 12.0×10^{-2} , 8.47×10^{-2} , and 1.19×10^{-3} mA/W^{-1} for illumination under laser of wavelength 532 (10 mW), 785 (10 mW), 840 (100 mW), and 1064 nm (60 mW), respectively. Detectivity values were found to be increasing from 532 to 840 nm wavelength illumination and decreasing towards 1064 nm laser.

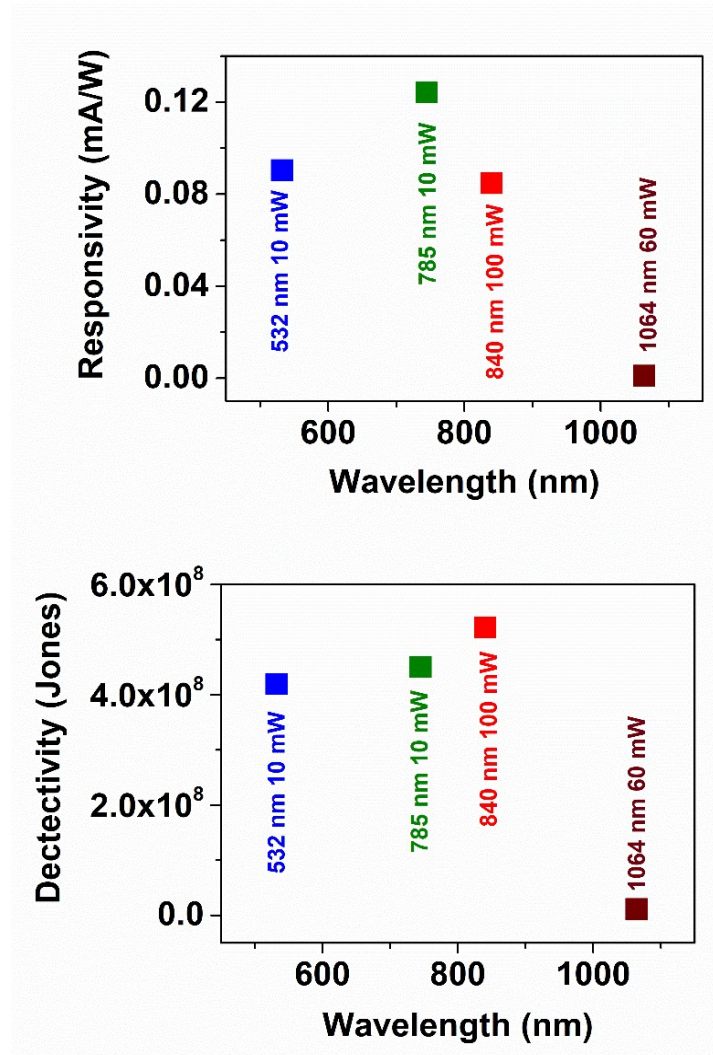


Figure 5.8 Variation of a) detectivity and b) responsivity vs wavelength of CdS/CTS photodetector under illumination using different laser sources.

This work calls for further research on CTS-based self-powered photodetectors for broad-band detection with improved performance.

5.2 CdS/SnS/CTS photovoltaic structure

5.2.1 SCAPS 1D simulation

Numerical simulation is essential to understand the operation of the solar cells and predict output photovoltaic parameters. We can obtain a preliminary estimation of the effect of different parameters on the device's performance. SCAPS 1D (version 3.3.10), a one-dimensional solar cell simulation program developed by the Department of Electronics and Information Systems (ELIS) of the University of Gent, Belgium was used for the simulation of thin film solar cell structure. Numerical simulation using SCAPS 1D software possesses several advantages as described below [171].

- 1) Estimation of photovoltaic parameters before the experimental process
- 2) Calculation of the inner electronic parameters which are unable to be measured directly
- 3) Ability to forecast faults in the photovoltaic device structure
- 4) Save time and production cost by the optimization of parameters [172].

It can support the configurations of up to 7 semiconductor layers and almost all parameters can be graded. It allows for the integration of recombination mechanisms and interface defect levels (single level, uniform, Gauss, tail, and user-defined). Optimization of back contact parameters: work function or flat-band; optical property (reflection of transmission filter) filter and various illuminations: (AM0, AM1.5D, AM1.5G, AM1.5G, monochromatic, and white). This program simulates thin film solar cell devices by solving basic semiconductor equations such as the Poisson equation, relating the charge to the electrostatic potential F , and the continuity equations for electrons and holes[173]. Moreover, the results obtained from SCAPS-1D simulation have been showing good agreement with experimental results in the literature [174].

Table 5.2 Material parameters used for various materials for the SCAPS-1D program

Material parameter	FTO [175]	CdS [176]	SnS [177,178]	CTS [176]
Thickness(nm)	300	250	180	600

Bandgap(eV)	3.5	2.42	1.46	0.97
Electron affinity (eV)	4	4.2	4.35	4.72
Relative dielectric permittivity	9	10	13	10
C.B density of states (cm ⁻³)	2.2×10 ¹⁸	1.8×10 ¹⁸	1.18×10 ¹⁸	2.2×10 ¹⁸
V.B density of states (cm ⁻³)	1.8×10 ¹⁹	2.4×10 ¹⁹	4.76×10 ¹⁸	1.8×10 ¹⁹
Electron thermal velocity (cms ⁻¹)	1.0×10 ⁷	1.0×10 ⁷	1.0×10 ⁷	1.0×10 ⁷
Hole thermal velocity (cms ⁻¹)	1.0×10 ⁷	1.0×10 ⁷	1.0×10 ⁷	1.0×10 ⁷
Electron mobility (cm ² V ⁻¹ s ⁻¹)	20	100	130	100
Hole mobility (cm ² V ⁻¹ s ⁻¹)	10	25	4.3	80
N _d (cm ⁻³)	1.0×10 ¹⁸	1.0×10 ¹⁸	0	0
N _a (cm ⁻³)	0	0	1.0×10 ¹⁵	1.0×10 ¹⁸
Neutral defect density (cm ⁻³)	0	1.0×10 ¹⁴	1.0×10 ¹⁴	1.0×10 ¹⁴
Single acceptor defect density (cm ⁻³)	0	0	0	1.0×10 ¹⁴

Table 5.3 Parameters used for defects at interfaces of the layers

Interface layer	CdS/CTS	CdS/SnS	SnS/CTS
Type of defect	neutral	neutral	neutral

Electrons Capture cross-section (cm ²)	1.0×10 ⁻¹⁹	1.0×10 ⁻¹⁹	1.0×10 ⁻¹⁹
Holes Capture cross-section (cm ²)	1.0×10 ⁻¹⁹	1.0×10 ⁻¹⁹	1.0×10 ⁻¹⁹
Distribution of energy	single	single	single
Reference for defect energy level (E _t)	Above the highest E _v	Above the highest E _v	Above the highest E _v
Energy to a reference (eV)	0.6	0.6	0.6
Total defect density (cm ⁻³)	1.0×10 ¹⁴	1.0×10 ¹⁴	1.0×10 ¹⁴

SCAPS-1D software was employed for simulating the photovoltaic performance and parameters (type of defect, total defect density concentration, shunt resistance, and series resistance) were adjusted to match the simulated J-V curve with experimentally obtained CdS/CTS solar cell parameters. The theoretical cell resulted in photovoltaic parameters of V_{oc}= 174.1 mV, J_{sc}= 9.46 mA.cm⁻², FF = 26, and power conversion efficiency = 0.42 %. The adjusted parameters were kept constant for the following simulations.

Many researchers have reported significant improvement in photovoltaic parameters by introducing an intrinsic layer in the photovoltaic structure [179,180]. The presence of a suitable intrinsic layer can drive excellent interface properties by suppressing tunneling produced by localized states in the doped layer. Recently, Ahmed et. al. proposed a double absorber photovoltaic structure with a PCE of 34 % [181]. They numerically modeled the feasibility of thin film solar cells with 300 nm thick CIGS and 870 nm thick CZTSSe absorber layers which revealed higher photovoltaic performance than cells with one absorber layer. CdS/SnS junction with an open circuit voltage of 330 mV was already reported in the literature [182].

In light of this, this study proposes a new photovoltaic cell design that incorporates a small layer of p-SnS in between the window and absorber layers. It will be interesting to explore the capabilities of this novel photovoltaic structure because of the addition of an extra p-type

SnS layer with a high absorption coefficient. Moreover, using the SnS layer makes this structure more feasible because it is a precursor layer as well.

A thin layer of SnS (180 nm) was added into the theoretical cell and the photovoltaic performance of the newly proposed FTO/CdS/SnS/CTS/Ag photovoltaic structure was evaluated. The simulation projected a significant improvement in the open circuit voltage for the SnS-incorporated photovoltaic structure. Theoretically predicted photovoltaic parameters were found to be: $V_{oc} = 419$ mV, $J_{sc} = 17.5$ mA.cm⁻², FF = 34, and PCE = 2.52 %. The simulation results of the device with and without the SnS layer have been compared and plotted in Figure 5.9.

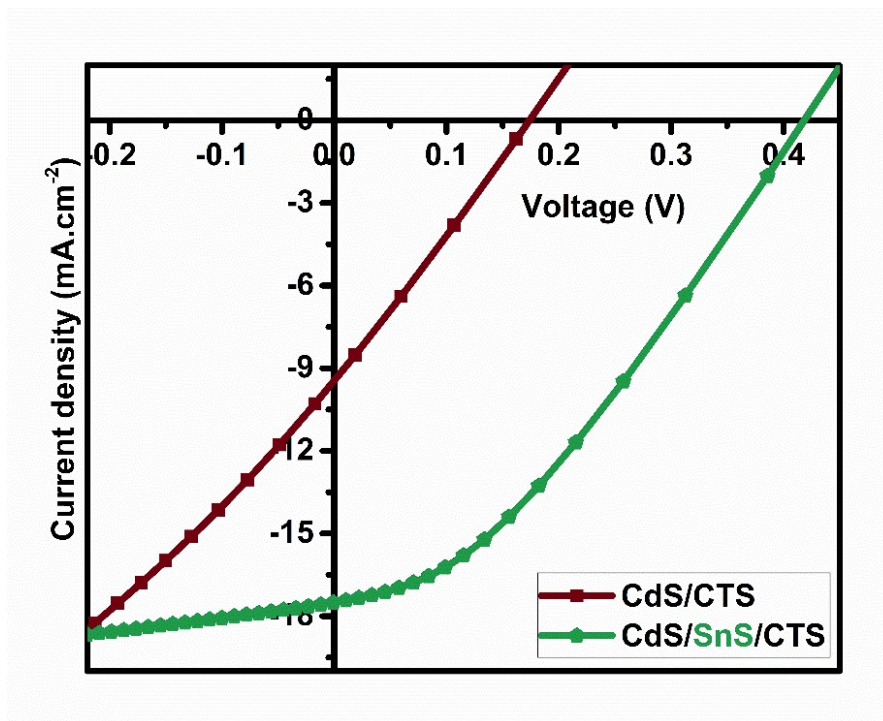


Figure 5.9. Simulated current density vs voltage curve of FTO/CdS/CTS/Ag and FTO/CdS/SnS/CTS/Ag photovoltaic structures using SCAPS-1D software.

This device configuration with the same thickness of individual layers (FTO-300 nm, CdS-250 nm, SnS-180 nm, and CTS-600 nm) is expected to deliver a maximum power conversion efficiency of 9.7 % at ideal conditions with optimized material parameters. A theoretically predicted device under ideal conditions can result in photovoltaic parameters of $V_{oc} = 0.501$ V, $J_{sc} = 24.4$ mA.cm⁻², FF = 79 %, and a simulated J-V plot is given in Figure 5.10. This structure can achieve higher efficiencies by increasing the thickness of individual layers. Also

optimizing the optical properties such as bandgap, carrier concentration, and defect density of individual layers can result in higher efficiency values for this structure.

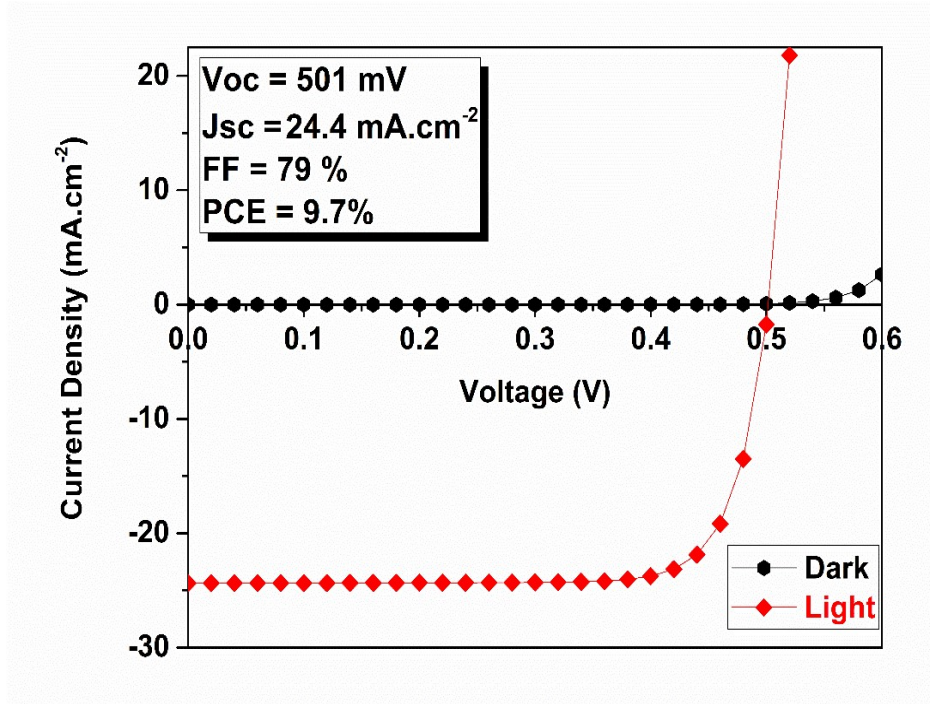


Figure 5.10 Maximum simulated current density vs voltage curve of FTO/n-CdS/p-SnS/p-CTS/Ag photovoltaic structures using SCAPS-1D software

5.2.2 CdS/SnS/CTS thin film solar cell

PV device with configuration: FTO/CdS/SnS/Cu₂SnS₃/Ag was fabricated and experimental details of the synthesis of different layers are explained in the experimental section 2.3. The thickness of individual layers was kept the same as per the previous study and optimized monoclinic Cu₂SnS₃ synthesized by sulfurization of Cu(80 nm)/SnS(450 nm) stacked layers for 1 h at 500 °C with 20 mg of sulfur was used. The thin film solar cell fabricated using Cu₂SnS₃ thin film (600 nm) and a thin SnS (180 nm) layer on n-CdS (250 nm) results in photovoltaic parameters of $V_{oc}=415$ mV, $J_{sc}=17.2$ mA.cm⁻², FF=30 %, and PCE=2.12 % (Figure 5.11).

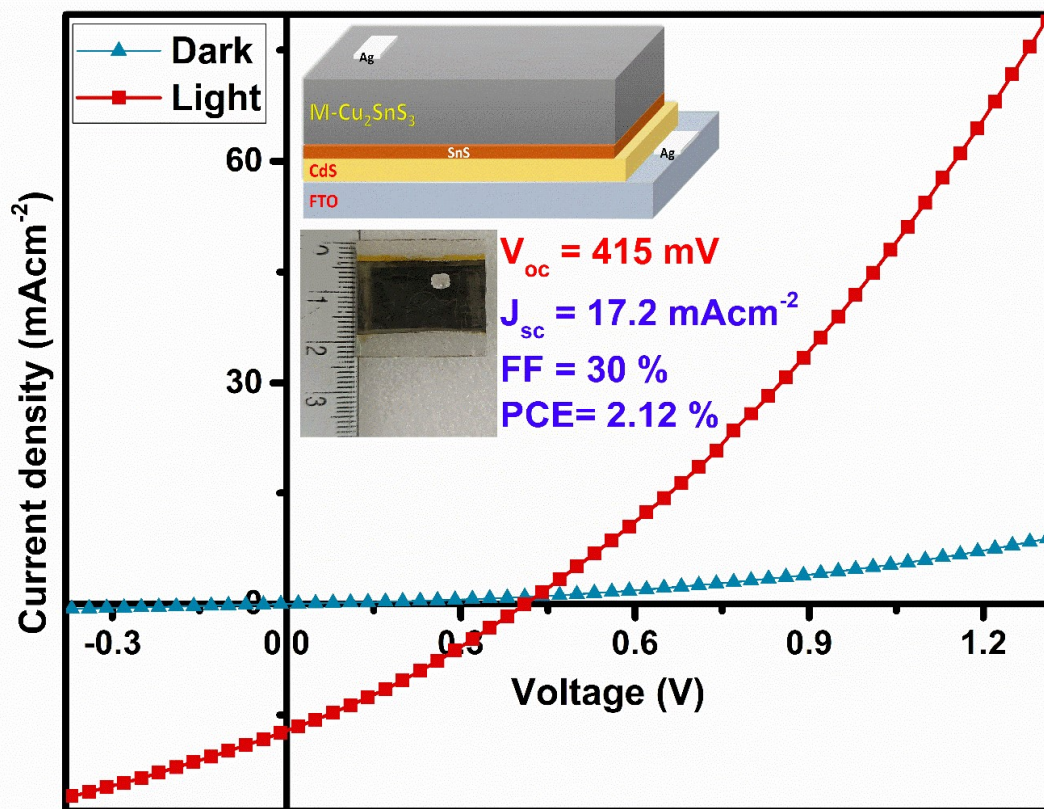


Figure 5.11 Current density vs voltage curve of FTO/CdS/SnS/Cu₂SnS₃/Ag photovoltaic structure (schematic structure and image of cell in the inset).

A large improvement in the open circuit voltage for Cu₂SnS₃ photovoltaic cells was achieved by integrating a thin SnS layer along with a monoclinic Cu₂SnS₃ layer. The improved V_{oc} is accounted to the bandgap gradient provided by the SnS layer which can cause a small spike in the band alignment and efficient suppression of the non-radiative recombination at the interface [183]. The spike band type I alignment (CBO < 0.4 eV) between CdS and SnS has already reported in the literature [184]. Surface morphology with large interconnected grains of optimized Cu₂SnS₃ thin films also significantly contributed to reducing the carrier recombination at the grain boundaries. The high grain boundary density of absorber layers and charge recombination at the interface of the absorber and window layers seriously affect the photovoltaic performance of Cu₂SnS₃ thin film solar cells [139]. The optical bandgap of SnS thin films deposited via chemical bath deposition was found to be 1.46 eV, which aids to create a better carrier transport between window layer CdS (2.4 eV) and absorber layer Cu₂SnS₃ (1.0 eV). An additional p-type layer can generate better electric charge separation

and subsequently result in improved carrier collection [185]. Most of the reports on Cu_2SnS_3 -based photovoltaic devices are based on Mo glass substrates whereas cost-effective FTO substrates were utilized in this study (Table 5.4). Improved performance on economical FTO substrate can make industrial manufacture one step closer. Further studies on post-thermal treatment parameters will be beneficial to improve photovoltaic parameters to the next level and this research inspires extensive studies in the future.

Table 5.4 Photovoltaic devices reported using monoclinic Cu_2SnS_3 thin films.

Photovoltaic device structure	V_{oc} (mV)	J_{sc} (mAcm^{-2})	FF (%)	PCE (%)	Reference
Mo/CTS/CdS/i-ZnO/AZO/Ni: Al	104	17.1	30	0.54	2012 [60]
Mo/CTS/CdS/i-ZnO/AZO/Ag	215	13.8	25	0.76	2016 [186]
Mo/CTS/CdS/i-ZnO/AZO/Ni: Al	147	23.6	32	1.10	2016 [161]
Mo/CTS/CdS/i-ZnO/AZO/Al.	148	28.3	32	1.35	2016 [160]
Mo/CTS/CdS/i-ZnO/AZO/Al	87	19.2	31	0.52	2017 [162]
Mo/CTS/CdS/i-ZnO/AZO/Al	179	29.7	41	2.21	2017 [187]
Mo/CTS/CdS/i-ZnO/AZO/Ni/Ag	184	12.6	27	0.64	2021 [142]
FTO/CdS/SnS/CTS/C/Ag	415	17.2	30	2.12	This work

5.2.3 Self powered CdS/SnS/CTS photodetector

The photodetection abilities of the CTS/SnS/CTS heterojunction device were probed under different wavelengths of light illumination in self-powered mode (bias voltage =0) and the photovoltaic device structure is represented in Figure 5.12(a). Figure 5.12(b) represents the I-t curve of the device utilizing 20 periodical light illuminations under a 50 W halogen source (10 s dark -10 s light -10 s dark) which demonstrates the rapid response and excellent stability of the device. The response speed of the photodetection device is demonstrated via photoresponse measurement of one cycle using a data interval of 12 ms and is given in Figure 5.12(c). A significant decrease in the rise time was observed after incorporating the SnS layer, which might be due to the contribution of more photoelectrons by the SnS layer than the

thermal electrons produced by Cu_2SnS_3 . The p-p+ junction between SnS and Cu_2SnS_3 might have also boosted the efficient separation of photogenerated carriers.

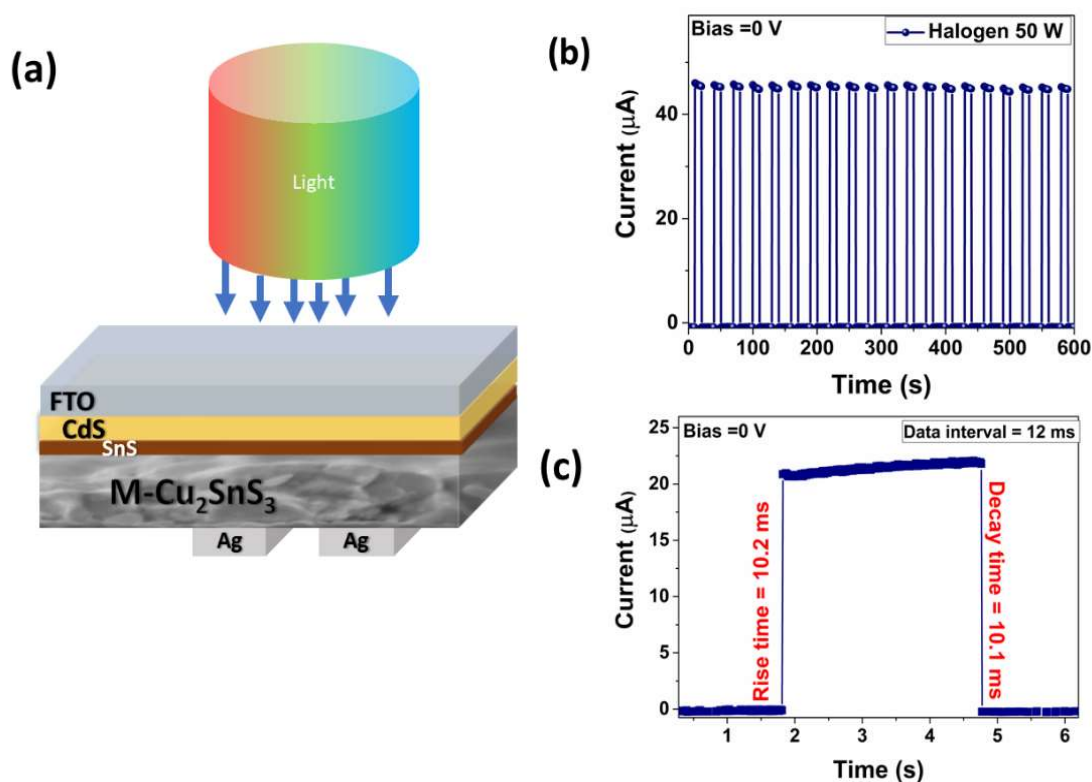


Figure 5.12 a) Photovoltaic device structure of FTO/CdS/SnS/ Cu_2SnS_3 photodetector, b) photoresponse for 20 cyclic illuminations under 50 W halogen source illumination, and c) photoresponse for one cycle of illumination for rise/decay time evaluation (data interval of 12 ms).

Furthermore, the cyclic photoresponse of the photovoltaic structure was measured under the illumination of 30 W LED sources as given in Figure 5.13. The photocurrent was higher for IR illuminations while relatively lower for illumination under UV LED. Moreover, different laser sources (532, 785, 840, 980, and 1064 nm) and solar AM 1.5G spectrum were utilized to demonstrate stable detection for broad regions over cyclic measurements and are given in Figure 5.14.

Three important photodetection parameters: responsivity (R), detectivity (D^*), and linear dynamic range of photodetector were evaluated using equations 1.6 to 1.8 [75,76]. The photovoltaic structure exhibited a maximum responsivity of 15.56 mA W^{-1} and a specific

detectivity of 1.41×10^{11} Jones under the illumination of an 840 nm laser. The linear dynamic range of the photodetector could achieve up to 93.2 dB indicating a very large ratio of photocurrent to dark current and thus an excellent signal-to-noise ratio in the NIR range. Rise and decay times are also important deciding factors in the detection capabilities of a photodetector. The rise and decay time of the photovoltaic structure was found to be 10.2 and 10.1 ms, respectively. This is one of the fastest rise and decay times reported for a chalcogenide heterojunction photodetector and is comparable to ultra-performing perovskite materials [76]. Rise and decay time in the order of milliseconds demonstrates the spontaneous response of this photovoltaic structure. The superior photoresponse time is attributed to the built-in electric field of the SnS/Cu₂SnS₃ films interface and high carrier mobility [188].

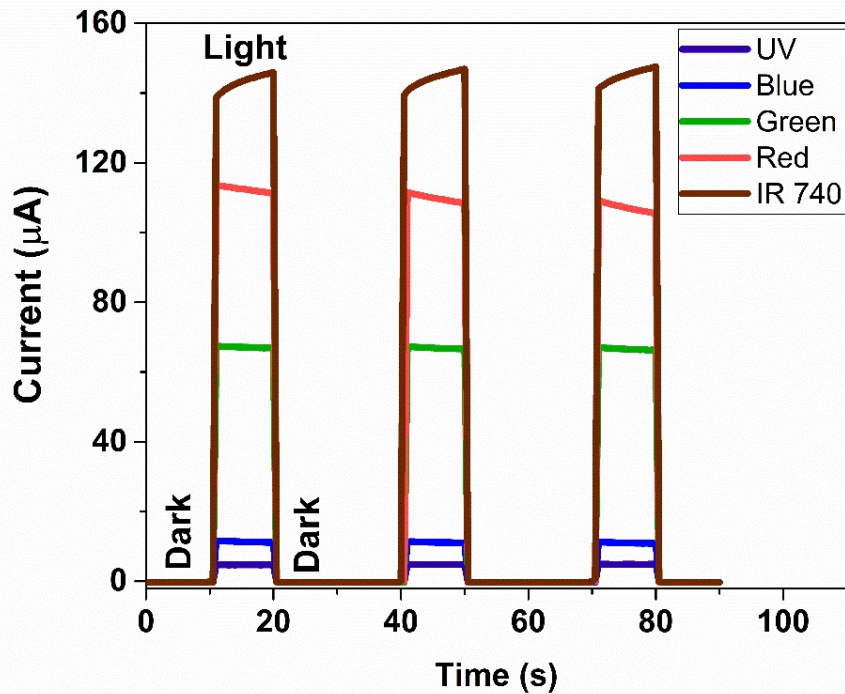


Figure 5.13 Cyclic photoresponse under illumination using 30 W LED sources of different wavelengths.

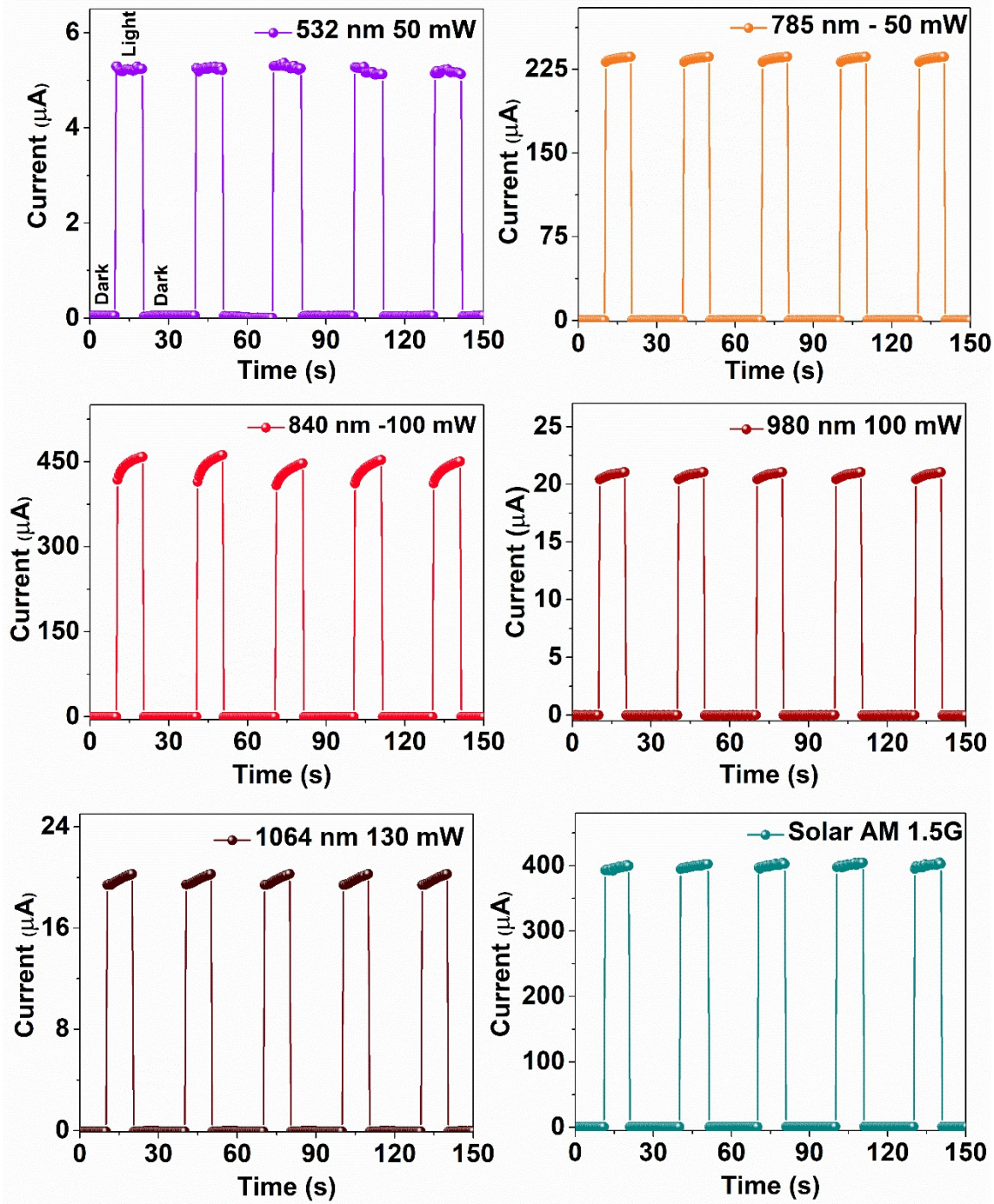


Figure 5.14 Cyclic photoresponse under illumination using different laser sources of wavelengths (532, 785, 840, 980, and 1064 nm) and solar AM 1.5G simulator illumination (bias voltage = 0 V).

The effect of power density on the photocurrent and responsivity of the device was studied using varying power lasers of wavelength 532 (10-50 mW), 785 (10-50 mW), and 1064 nm (60-350 mW) while 840 and 980 nm laser was fixed power of 100 mW. Figure 5.15(a-c) depicts a graph of photocurrent against incident power density and Figure 5.15(e-f) represents the variation of responsivity with incident power density for different laser sources with wavelengths 532, 785, and 1064 nm. Photocurrent increases with incident power and responsivity decreases with the increase of power density in all wavelength regions. The rise in photocurrent with increased incident power density is related to the improved electron-hole pair generation. Whereas higher carrier recombination and scattering rates compared to effective transportation of generated carriers cause a reduction in responsivity at higher power densities [169]. Photocurrent generation under 1064 nm laser was mostly contributed from the narrow bandgap absorption of Cu_2SnS_3 . Relatively the decrease in responsivity was lower in the case of 1064 nm laser illumination. This phenomenon reinforces the efficient charge separation and carrier transport due to compact monoclinic Cu_2SnS_3 with larger grains. These properties facilitate the enhanced photodetection in the NIR region and encourage prospective investigations for highly efficient IR photodetection based on Cu_2SnS_3 thin films.

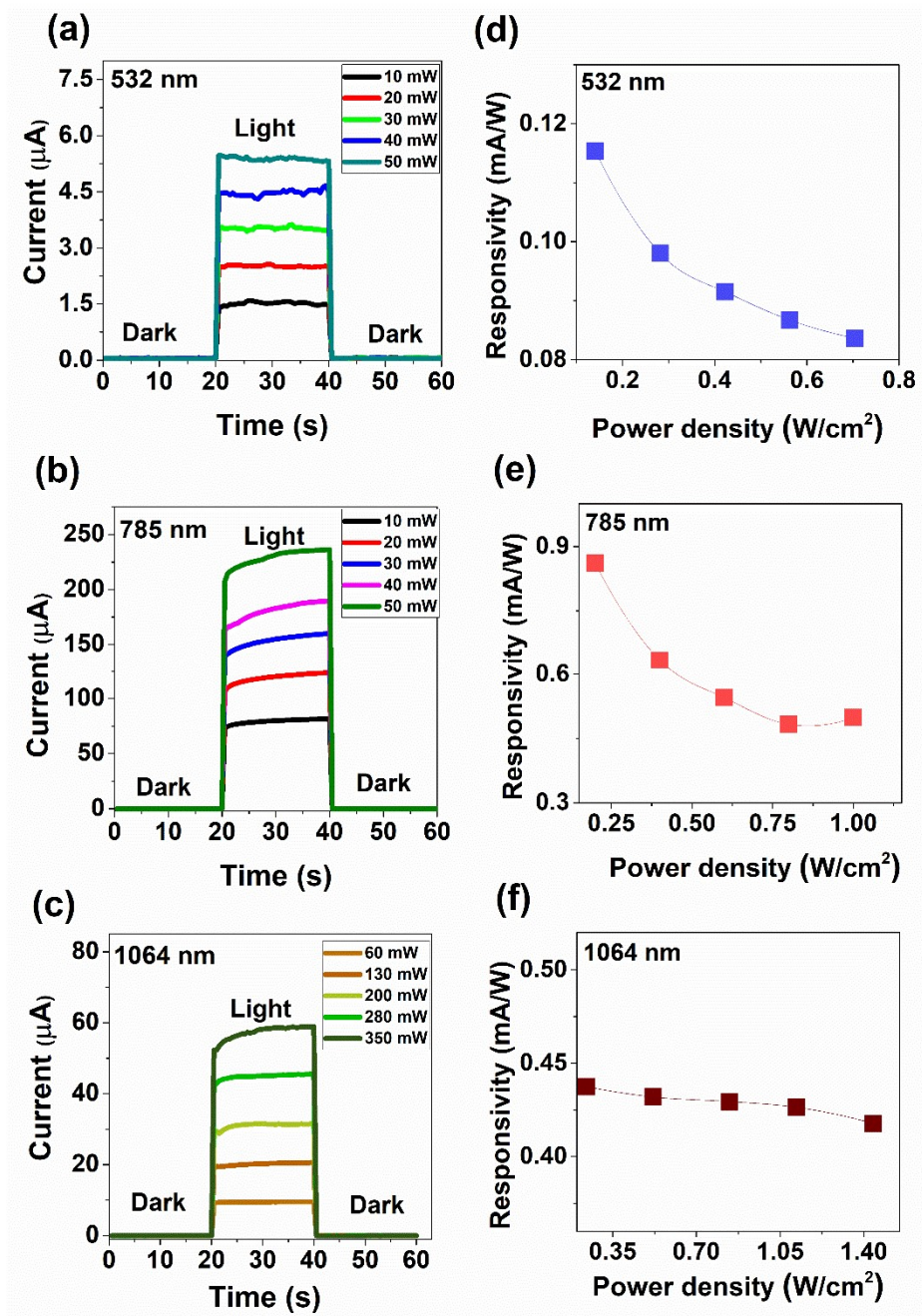


Figure 5.15 Power density vs photocurrent (a-c) and power density vs responsivity (d-f) for 532, 785, and 1064 nm lasers at zero bias.

Power law fitting was employed to study the efficiency of photogenerated carriers by determining the θ value (equation 5.1). Figure 5.16 represents the power law fitting of photocurrent vs incident power density for different lasers (532, 785, and 1064 nm). The fitting curve with $\theta = 0.75, 0.83,$ and 0.97 is obtained for 532, 785, and 1064 nm, respectively.

The value closer to unity for 1064 nm laser illumination indicates efficient carrier transport with minimum recombination. These values suggest the possibility of higher quality CdS/SnS/CTS self-powered photodiodes for future NIR photodetection.

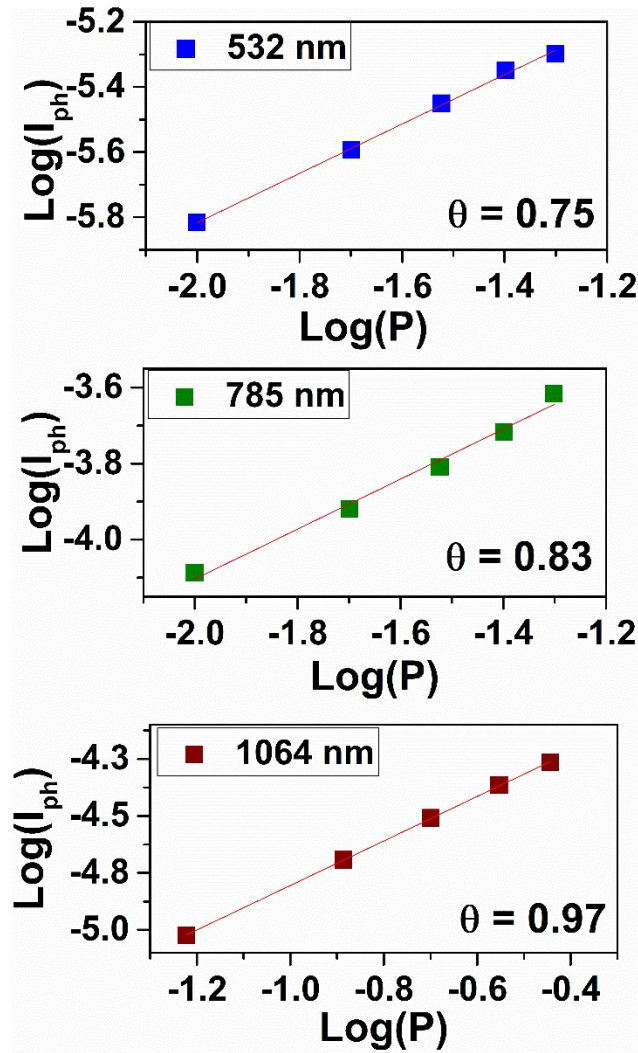


Figure 5.16 Power law fitting of photogenerated current vs incident power density for different lasers (532, 785, and 1064 nm)

Variation of detectivity and responsivity vs wavelength of CdS/SnS/CTS photodetector under illumination using different laser sources is presented in Figure 5.17(a-b). The responsivity values were found to be 0.06, 0.49, 15.56, 0.66, and 0.44 mA W^{-1} for illumination wavelengths of 532, 785, 840, 980, and 1064 nm, respectively. The responsivity and detectivity values were increased up to the wavelength of 840 nm and found to be falling

towards the IR region. The photodetection device shows excellent responsivity and detectivity near 840 nm which accounted for the increased absorption at the bandgap edge of SnS (840 nm \sim 1.47 eV). The combined carrier generation of SnS and Cu₂SnS₃ layers resulted in the highest photocurrent near the bandgap edge of SnS [189]. This narrowband absorption is due to the absorption of shorter wavelength radiations (energy less than the bandgap of absorber layer) near the surface and they experience massive recombination due to higher local carrier concentration and imbalanced transit times for the electron and holes before being collected in the electrodes [190]. Radiations with energy values near the optical bandgap of the absorber layer can penetrate through the photoactive layer and electron-hole pairs generated with the influence of optical interference get transported to electrodes efficiently. In brief, shorter wavelength generates electron-hole pairs near the surface and loses most of the part by recombination whereas longer wavelengths of light penetrate the structure and facilitate narrow-band responsivity [191]. This spectral selective NIR detection using tuned electro-optical properties of broadband absorbing semiconductors is referred to as a charge collection narrowing mechanism [192]. High specific detectivities can be attained by the use of thicker junctions which significantly reduce defect densities and subsequently result in suppressing dark current. Improvement in responsivity and response time values compared to earlier reports on CdS/SnS photodetectors emphasize the positive effect of the Cu₂SnS₃ layer in this novel photovoltaic structure [84,193]. Moreover, the extended photodetection due to the Cu₂SnS₃ layer was demonstrated using a 1064 nm laser source and expected detection abilities beyond this wavelength. Due to the stronger photovoltaic effect induced by the longer wavelength radiations, incident photons get closer to the p-n junction interface and enable better carrier collection. In this study, the optimized Cu₂SnS₃ layer facilitates efficient charge transport to the electrodes through bigger grains with minimal scattering. This is the highest specific detectivity and response time reported for Cu₂SnS₃ based photodetector. For future applications, it is possible to engineer response peak wavelength and selective detection band by tuning the thickness of different layers [192,194].

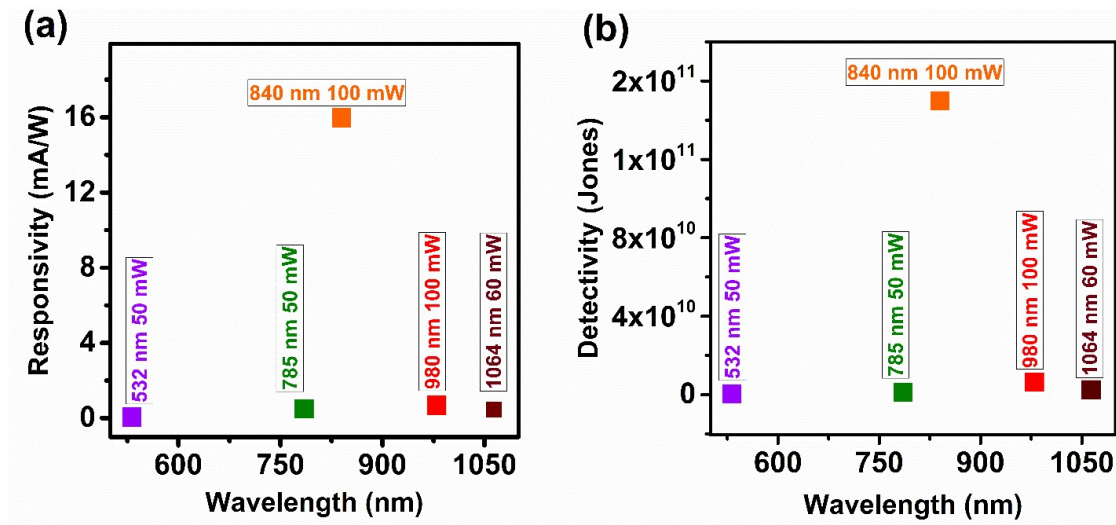


Figure 5.17 Variation of a) detectivity and b) responsivity vs wavelength of CdS/SnS/CTS photodetector under illumination using different laser sources.

These findings pave prodigious contributions for the synthesis of stable self-driven NIR photodetectors using Cu_2SnS_3 thin film heterojunction consisting of low-cost and earth-abundant elements.

CHAPTER 6

CONCLUSIONS AND OUTLOOK

In summary, this work demonstrates the optimization of different deposition parameters to achieve suitable optoelectronic properties for different phases of Cu-Sn-S thin films synthesized via sulfurization of stacked layers of SnS and Cu by chemical bath deposition and thermal evaporation. Furthermore, the incorporation of these optimized phases into thin film solar cells and heterojunction photodetection devices.

- ✓ (102) preferentially oriented Cu_4SnS_4 thin films were synthesized for the first time by varying Cu precursor layer thickness and subsequent sulfurization at 550 °C for 1 h. Their structure, chemical composition, morphology, and optical and electrical properties were altered significantly with copper precursor layer thickness. Cu_4SnS_4 thin films with a preferred orientation (Cu-185 nm) and an ideal bandgap of 1.42 eV are found to be suitable absorber material for thin film solar cells (SnS-200 nm, Cu-185 nm, and sulfur-20 mg).
- ✓ The effect of sulfurization parameters on the structure, chemical composition, surface morphology, and optoelectronic properties of Cu_2SnS_3 thin films was studied. Cu and S deficient monoclinic Cu_2SnS_3 thin films were synthesized via this three-step method (SnS- 450 nm, Cu- 80 nm, sulfurization time- 1 h, quantity of sulfur-20 mg, and temperature - 500 °C).
- ✓ Optimized monoclinic Cu_2SnS_3 thin film was incorporated in the thin film solar cell structure of FTO/CdS/ Cu_2SnS_3 /Ag and photovoltaic parameters of $V_{oc}= 174 \text{ mV}$, $J_{sc}= 9.4 \text{ mAcm}^{-2}$, $\text{FF}= 25 \%$ and a power conversion efficiency of 0.41 % were obtained.
- ✓ Vacuum annealing of CTS/CdS photovoltaic structure up to 300 °C for 30 minutes was found to be beneficial to increase open circuit voltage by proper bandgap matching due to the weakening of band tail and interface traps which further aid in the efficient reduction of nonradiative recombination.
- ✓ The effect of a thin SnS layer along with a Cu_2SnS_3 layer was studied by numerical simulation (SCAPS-1D) and predicted an enhancement of photovoltaic performance.

- ✓ The photovoltaic structure fabricated using optimized Cu_2SnS_3 thin film with a thin SnS absorber layer resulted in photovoltaic parameters of $V_{oc} = 415$ mV, $J_{sc} = 17.2$ mAcm^{-2} , FF= 30 %, and PCE = 2.12 %. This improved photovoltaic performance is accounted to the proper bandgap gradient provided by the SnS layer and subsequent efficient suppression of the non-radiative recombination at the interface.
- ✓ Photodetection measurements using different laser sources revealed the applicability of FTO/CdS/SnS/ Cu_2SnS_3 /Ag photovoltaic structure for self-powered enhanced NIR photodetection with high specific detectivity of 1.46×10^{11} Jones and a quick response time of 10.2 ms.

In condense, Cu_2SnS_3 thin films were applied to the photovoltaic and photodetection applications. This thesis reveals great advancement in the development of earth-abundant, nontoxic, and cost-effective Cu-Sn-S thin films for photovoltaic and photodetection applications. The investigation also proposes further possibilities for the optimization of Cu-Sn-S thin films for better photovoltaic performance and enhanced spectral selective self-powered photodetection.

REFERENCES

- [1] B.W. G A, V. The action of light on selenium, *Proc. R. Soc. London.* 25 (1877) 113–117. <https://doi.org/10.1098/RSPL.1876.0024>.
- [2] D.M. Chapin, C.S. Fuller, G.L. Pearson, A New Silicon p-n Junction Photocell for Converting Solar Radiation into Electrical Power, *J. Appl. Phys.* 25 (2004) 676. <https://doi.org/10.1063/1.1721711>.
- [3] M.A. Green, E.D. Dunlop, J. Hohl-Ebinger, M. Yoshita, N. Kopidakis, K. Bothe, D. Hinken, M. Rauer, X. Hao, Solar cell efficiency tables (Version 60), *Prog. Photovoltaics Res. Appl.* 30 (2022) 687–701. <https://doi.org/10.1002/PIP.3595>.
- [4] A. Le Donne, V. Trifiletti, S. Binetti, New Earth-Abundant Thin Film Solar Cells Based on Chalcogenides, *Front. Chem.* 7 (2019) 297. <https://doi.org/10.3389/fchem.2019.00297>.
- [5] L.C. Andreani, A. Bozzola, P. Kowalczewski, M. Liscidini, L. Redorici, Silicon solar cells: Toward the efficiency limits, *Adv. Phys. X.* 4 (2019) 125–148. <https://doi.org/10.1080/23746149.2018.1548305>.
- [6] I. Massiot, A. Cattoni, S. Collin, Progress and prospects for ultrathin solar cells, *Nat. Energy.* 5 (2020) 959–972. <https://doi.org/10.1038/s41560-020-00714-4>.
- [7] S. Kasap, C. Koughia, H.E. Ruda, Electrical Conduction in Metals and Semiconductors, *Springer Handbooks.* 1 (2017) 1. https://doi.org/10.1007/978-3-319-48933-9_2.
- [8] R.N. Hall, Electron-Hole Recombination in Germanium, *Phys. Rev.* 87 (1952) 387. <https://doi.org/10.1103/PhysRev.87.387>.
- [9] J. Ramanujam, U.P. Singh, Copper indium gallium selenide based solar cells - A review, *Energy Environ. Sci.* 10 (2017) 1306–1319. <https://doi.org/10.1039/C7EE00826K>.
- [10] A. Izadian, A. Pourtaherian, S. Motahari, Basic model and governing equation of solar cells used in power and control applications, *IEEE Energy Convers. Congr. Expo.* (2012) 1483–1488. <https://doi.org/10.1109/ECCE.2012.6342639>.
- [11] M.T. Boyd, S.A. Klein, D.T. Reindl, B.P. Dougherty, Evaluation and validation of equivalent circuit photovoltaic solar cell performance models, *J. Sol. Energy Eng.*

- Trans. ASME. 133 (2011) 021005. <https://doi.org/10.1115/1.4003584>.
- [12] S. Bana, R.P. Saini, A mathematical modeling framework to evaluate the performance of single diode and double diode based SPV systems, *Energy Reports*. 2 (2016) 171–187. <https://doi.org/10.1016/J.EGYR.2016.06.004>.
- [13] P. Würfel, *Physics of Solar Cells*, Wiley, 2005. <https://doi.org/10.1002/9783527618545>.
- [14] M. Powalla, S. Paetel, E. Ahlswede, R. Wuerz, C.D. Wessendorf, T. Magorian Friedlmeier, Thin-film solar cells exceeding 22% solar cell efficiency: An overview on CdTe-, Cu(In,Ga)Se₂ -, and perovskite-based materials, *Appl. Phys. Rev.* 5 (2018) 041602. <https://doi.org/10.1063/1.5061809>.
- [15] K.L. Chopra, P.D. Paulson, V. Dutta, Thin-film solar cells: an overview, *Prog. Photovoltaics Res. Appl.* 12 (2004) 69–92. <https://doi.org/10.1002/PIP.541>.
- [16] G. Regmi, A. Ashok, P. Chawla, P. Semalti, S. Velumani, S.N. Sharma, H. Castaneda, Perspectives of chalcopyrite-based CIGSe thin-film solar cell: a review, *J. Mater. Sci. Mater. Electron.* 31 (2020) 7286–7314. <https://doi.org/10.1007/s10854-020-03338-2>.
- [17] S. Guha, Thin-film photovoltaics: Buffer against degradation, *Nat. Energy*. 2 (2017) 17057. <https://doi.org/10.1038/nenergy.2017.57>.
- [18] I. Sharma, P.S. Pawar, R. Kumar Yadav, R. Nandi, J. Heo, Review on bandgap engineering in metal-chalcogenide absorber layer via grading: A trend in thin-film solar cells, *Sol. Energy*. 246 (2022) 152–180. <https://doi.org/10.1016/J.SOLENER.2022.09.046>.
- [19] H. Soonmin, Hardani, P. Nandi, B.S. Mwankemwa, T.D. Malevu, M.I. Malik, Overview on Different Types of Solar Cells: An Update, *Appl. Sci.* 13 (2023) 2051. <https://doi.org/10.3390/app13042051>.
- [20] M.A. Green, E.D. Dunlop, G. Siefer, M. Yoshita, N. Kopidakis, K. Bothe, X. Hao, Solar cell efficiency tables (Version 61), *Prog. Photovoltaics Res. Appl.* 31 (2023) 3–16. <https://doi.org/10.1002/PIP.3646>.
- [21] D.E. Carlson, C.R. Wronski, Amorphous silicon solar cell, *Appl. Phys. Lett.* 28 (1976) 671–673. <https://doi.org/10.1063/1.88617>.
- [22] S. Guha, ; J Yang, ; A Banerjee, ; Al, J. Yang, A. Banerjee, T. Glaffelter, X. Xu,

- Advances in amorphous silicon alloy-based multijunction cells and modules, AIP Conf. Proc. 268 (1992) 64–71. <https://doi.org/10.1063/1.42943>.
- [23] H. Lin, M. Yang, X. Ru, G. Wang, S. Yin, F. Peng, C. Hong, M. Qu, J. Lu, L. Fang, C. Han, P. Procel, O. Isabella, P. Gao, Z. Li, X. Xu, Silicon heterojunction solar cells with up to 26.81% efficiency achieved by electrically optimized nanocrystalline-silicon hole contact layers, *Nat. Energy*. 8 (2023) 789–799. <https://doi.org/10.1038/s41560-023-01255-2>.
- [24] J. Zhou, Q. Huang, Y. Ding, G. Hou, Y. Zhao, Passivating contacts for high-efficiency silicon-based solar cells: From single-junction to tandem architecture, *Nano Energy*. 92 (2022) 106712. <https://doi.org/10.1016/J.NANOEN.2021.106712>.
- [25] T. Matsui, H. Sai, A. Bidiville, H.-J. Hsu, K. Matsubara, Progress and limitations of thin-film silicon solar cells, *Sol. Energy*. 170 (2018) 486–498. <https://doi.org/10.1016/j.solener.2018.05.077>.
- [26] A. Romeo, E. Artegiani, CdTe-Based Thin Film Solar Cells: Past, Present and Future, *Energies*. 14 (2021) 1684. <https://doi.org/10.3390/en14061684>.
- [27] S. Rühle, Tabulated values of the Shockley–Queisser limit for single junction solar cells, *Sol. Energy*. 130 (2016) 139–147. <https://doi.org/10.1016/J.SOLENER.2016.02.015>.
- [28] W.K. Metzger, S. Grover, D. Lu, E. Colegrove, J. Moseley, C.L. Perkins, X. Li, R. Mallick, W. Zhang, R. Malik, J. Kephart, C.-S. Jiang, D. Kuciauskas, D.S. Albin, M.M. Al-Jassim, G. Xiong, M. Gloeckler, Exceeding 20% efficiency with in situ group V doping in polycrystalline CdTe solar cells, *Nat. Energy*. 4 (2019) 837–845. <https://doi.org/10.1038/s41560-019-0446-7>.
- [29] N. Mufti, T. Amrillah, A. Taufiq, Sunaryono, Aripriharta, M. Diantoro, Zulhadjri, H. Nur, Review of CIGS-based solar cells manufacturing by structural engineering, *Sol. Energy*. 207 (2020) 1146–1157. <https://doi.org/10.1016/j.solener.2020.07.065>.
- [30] M. Nakamura, K. Yamaguchi, Y. Kimoto, Y. Yasaki, T. Kato, H. Sugimoto, Cd-Free Cu(In,Ga)(Se,S)₂ thin-film solar cell with record efficiency of 23.35%, *IEEE J. Photovoltaics*. 9 (2019) 1863–1867. <https://doi.org/10.1109/JPHOTOV.2019.2937218>.
- [31] E. Rezaee, W. Zhang, S.R.P. Silva, Solvent Engineering as a Vehicle for High

- Quality Thin Films of Perovskites and Their Device Fabrication, *Small*. 17 (2021) 2008145. <https://doi.org/10.1002/SMLL.202008145>.
- [32] H. Sun, P. Dai, X. Li, J. Ning, S. Wang, Y. Qi, Strategies and methods for fabricating high quality metal halide perovskite thin films for solar cells, *J. Energy Chem.* 60 (2021) 300–333. <https://doi.org/10.1016/J.JECHEM.2021.01.001>.
- [33] J. Park, J. Kim, H.-S. Yun, M.J. Paik, E. Noh, H.J. Mun, M.G. Kim, T.J. Shin, S. Il Seok, Controlled growth of perovskite layers with volatile alkylammonium chlorides, *Nature*. 616 (2023) 724–730. <https://doi.org/10.1038/s41586-023-05825-y>.
- [34] L. Wang, Y. Wang, Z. Zhou, W. Zhou, D. Kou, Y. Meng, Y. Qi, S. Yuan, L. Han, S. Wu, Progress and perspectives of solution-processed kesterite absorbers for photovoltaic applications, *Nanoscale*. 15 (2023) 8900–8924. <https://doi.org/10.1039/D3NR00218G>.
- [35] Y. Gong, Q. Zhu, B. Li, S. Wang, B. Duan, L. Lou, C. Xiang, E. Jedlicka, R. Giridharagopal, Y. Zhou, Q. Dai, W. Yan, S. Chen, Q. Meng, H. Xin, Elemental demixing-induced epitaxial kesterite/CdS interface enabling 13%-efficiency kesterite solar cells, *Nat. Energy*. 7 (2022) 966–977. <https://doi.org/10.1038/s41560-022-01132-4>.
- [36] D. Zhang, B. Yao, Y. Li, Z. Ding, C. Wang, J. Zhang, T. Wang, D. Ma, Y. Liu, Insight into the role of air-annealing $\text{Cu}_2\text{ZnSnS}_4$ precursor films in improving efficiency of $\text{Cu}_2\text{ZnSn}(\text{S},\text{Se})_4$ solar cells, *J. Alloys Compd.* 929 (2022) 167308. <https://doi.org/10.1016/J.JALLCOM.2022.167308>.
- [37] M. He, C. Yan, J. Li, M.P. Suryawanshi, J. Kim, M.A. Green, X. Hao, Kesterite Solar Cells: Insights into Current Strategies and Challenges, *Adv. Sci.* 8 (2021) 2004313. <https://doi.org/10.1002/ADVS.202004313>.
- [38] U. Chalapathi, Y.B. Kishore Kumar, S. Uthanna, V.S. Raja, Growth and characterization of Cu_3SnS_4 thin films by spray pyrolysis, *AIP Conf. Proc.* 1447 (2012) 649–650. <https://doi.org/10.1063/1.4710170>.
- [39] H. Guan, H. Shen, C. Gao, X. He, Structural and optical properties of Cu_2SnS_3 and Cu_3SnS_4 thin films by successive ionic layer adsorption and reaction, *J. Mater. Sci. Mater. Electron.* 24 (2013) 1490–1494. <https://doi.org/10.1007/s10854-012-0960-x>.
- [40] V.R. Minnam Reddy, M.R. Pallavolu, P.R. Guddeti, S. Gedi, K.K. Yarragudi Bathal

- Reddy, B. Pejjai, W.K. Kim, T.R.R. Kotte, C. Park, Review on Cu_2SnS_3 , Cu_3SnS_4 , and Cu_4SnS_4 thin films and their photovoltaic performance, *J. Ind. Eng. Chem.* 76 (2019) 39–74. <https://doi.org/10.1016/j.jiec.2019.03.035>.
- [41] A. Paul, S. Shaji, B. Krishnan, D.A. Avellaneda, Effect of copper precursor layer thickness on the properties of preferentially oriented Cu_4SnS_4 thin films for photovoltaic applications, *Opt. Mater. (Amst)*. 120 (2021) 111423. <https://doi.org/10.1016/j.optmat.2021.111423>.
- [42] R. Garza-Hernández, H.J. Edwards, J.T. Gibbon, M.R. Alfaro-Cruz, V.R. Dhanak, F.S. Aguirre-Tostado, Tunable crystal structure of Cu_2SnS_3 deposited by spray pyrolysis and its impact on the chemistry and electronic structure, *J. Alloys Compd.* 881 (2021) 160552. <https://doi.org/10.1016/J.JALLCOM.2021.160552>.
- [43] H.D. Shelke, A.C. Lokhande, J.H. Kim, C.D. Lokhande, Photoelectrochemical (PEC) studies on Cu_2SnS_3 (CTS) thin films deposited by chemical bath deposition method, *J. Colloid Interface Sci.* 506 (2017) 144–153. <https://doi.org/10.1016/J.JCIS.2017.07.032>.
- [44] M. He, A.C. Lokhande, I.Y. Kim, U. V. Ghorpade, M.P. Suryawanshi, J.H. Kim, Fabrication of sputtered deposited Cu_2SnS_3 (CTS) thin film solar cell with power conversion efficiency of 2.39 %, *J. Alloys Compd.* 701 (2017) 901–908. <https://doi.org/10.1016/j.jallcom.2017.01.191>.
- [45] S.A. Vanalakar, G.L. Agawane, A.S. Kamble, C.W. Hong, P.S. Patil, J.H. Kim, Fabrication of Cu_2SnS_3 thin film solar cells using pulsed laser deposition technique, *Sol. Energy Mater. Sol. Cells.* 138 (2015) 1–8. <https://doi.org/10.1016/j.solmat.2015.02.031>.
- [46] M. Heidariramsheh, S. Gharabeiki, S.M. Mahdavi, N. Taghavinia, Optoelectrical and structural characterization of Cu_2SnS_3 thin films grown via spray pyrolysis using stable molecular ink, *Sol. Energy.* 224 (2021) 218–229. <https://doi.org/10.1016/J.SOLENER.2021.05.088>.
- [47] R.E. Agbenyeke, S. Song, H. Choi, B.K. Park, J.H. Yun, T.-M. Chung, Y.K. Lee, C.G. Kim, J.H. Han, Atomic Layer Deposition of Cu_2SnS_3 Thin Films: Effects of Composition and Heat Treatment on Phase Transformation, *Chem. Mater.* 33 (2021) 8112–8123. <https://doi.org/10.1021/acs.chemmater.1c02982>.

- [48] A. Basak, H. Deka, A. Mondal, U.P. Singh, Impact of post-deposition annealing in Cu_2SnS_3 thin film solar cells prepared by doctor blade method, *Vacuum*. 156 (2018) 298–301. <https://doi.org/10.1016/j.vacuum.2018.07.049>.
- [49] D. Avellaneda, A. Paul, S. Shaji, B. Krishnan, Synthesis of Cu_2SnS_3 , Cu_3SnS_4 , and Cu_4SnS_4 thin films by sulfurization of SnS-Cu layers at a selected temperature and /or Cu layers thickness, *J. Solid State Chem.* 306 (2022) 122711. <https://doi.org/10.1016/j.jssc.2021.122711>.
- [50] X. Liu, X. Li, X. Li, Q. Li, D. Zhang, N. Yu, S. Wang, Fabrication of Cu_2SnS_3 thin film solar cells via a sol-gel technique in air, *Phys. B Condens. Matter*. 627 (2022) 413613. <https://doi.org/10.1016/J.PHYSB.2021.413613>.
- [51] G. Yang, X. Li, X. Ji, X. Xu, A. Wang, J. Huang, Y. Zhu, G. Pan, S. Cui, Phase composition of the earth-abundant Cu_2SnS_3 thin films with different annealing temperature and its effects on the performance of the related solar cells, *Sol. Energy*. 208 (2020) 206–211. <https://doi.org/10.1016/J.SOLENER.2020.07.090>.
- [52] E. Jo, S.G. Kim, K.S. Gour, S. Jang, J.S. Jang, J.H. Kim, Improved Jsc by Increasing the Absorber Layer Thickness of Monoclinic-Dominated Cu_2SnS_3 Thin Film Solar Cells Fabricated on Flexible Mo Foil, *Sol. RRL*. 6 (2022) 2100743. <https://doi.org/10.1002/SOLR.202100743>.
- [53] P.R. Guddeti, S. Gedi, K.T. Ramakrishna Reddy, Sulfurization temperature dependent physical properties of Cu_2SnS_3 films grown by a two-stage process, *Mater. Sci. Semicond. Process.* 86 (2018) 164–172. <https://doi.org/10.1016/j.mssp.2018.06.021>.
- [54] D. Avellaneda, M.T.S. Nair, P.K. Nair, Cu_2SnS_3 and Cu_4SnS_4 Thin Films via Chemical Deposition for Photovoltaic Application, *J. Electrochem. Soc.* 157 (2010) D346. <https://doi.org/10.1149/1.3384660>.
- [55] A. Kanai, K. Toyonaga, K. Chino, H. Katagiri, H. Araki, Fabrication of Cu_2SnS_3 thin-film solar cells with power conversion efficiency of over 4%, *Jpn. J. Appl. Phys.* 54 (2015) 3–7. <https://doi.org/10.7567/JJAP.54.08KC06>.
- [56] Y. Zhao, L. Chang, X.F. Dong, H.X. Zhang, Y. Li, J.B. Chen, Effect of Ag doping on the performance of Cu_2SnS_3 thin-film solar cells, *Sol. Energy*. 201 (2020) 190–194. <https://doi.org/10.1016/j.solener.2020.03.006>.

- [57] J. Chantana, K. Tai, H. Hayashi, T. Nishimura, Y. Kawano, T. Minemoto, Investigation of carrier recombination of Na-doped Cu_2SnS_3 solar cell for its improved conversion efficiency of 5.1%, *Sol. Energy Mater. Sol. Cells.* 206 (2020) 110261. <https://doi.org/10.1016/j.solmat.2019.110261>.
- [58] M. Umehara, S. Tajima, Y. Aoki, Y. Takeda, T. Motohiro, $\text{Cu}_2\text{Sn}_{1-x}\text{Ge}_x\text{S}_3$ solar cells fabricated with a graded bandgap structure, *Appl. Phys. Express.* 9 (2016) 3–7. <https://doi.org/10.7567/APEX.9.072301>.
- [59] T.A. Kuku, O.A. Fakolujo, Photovoltaic characteristics of thin films of Cu_2SnS_3 , *Sol. Energy Mater.* 16 (1987) 199–204. [https://doi.org/10.1016/0165-1633\(87\)90019-0](https://doi.org/10.1016/0165-1633(87)90019-0).
- [60] D.M. Berg, R. Djemour, L. Gütay, G. Zoppi, S. Siebentritt, P.J. Dale, Thin film solar cells based on the ternary compound Cu_2SnS_3 , *Thin Solid Films.* 520 (2012) 6291–6294. <https://doi.org/10.1016/j.tsf.2012.05.085>.
- [61] K. Chino, J. Koike, S. Eguchi, H. Araki, R. Nakamura, K. Jimbo, H. Katagiri, Preparation of Cu_2SnS_3 thin films by sulfurization of Cu/Sn stacked precursors, *Jpn. J. Appl. Phys.* 51 (2012) 10NC35. <https://doi.org/10.1143/JJAP.51.10NC35>.
- [62] A. Kanai, H. Araki, A. Takeuchi, H. Katagiri, Annealing temperature dependence of photovoltaic properties of solar cells containing Cu_2SnS_3 thin films produced by co-evaporation, *Phys. Status Solidi.* 252 (2015) 1239–1243. <https://doi.org/10.1002/PSSB.201400297>.
- [63] Q. Zhang, H. Deng, J. Yu, B. Xu, J. Tao, P. Yang, L. Sun, J. Chu, Effect of sulfurization temperature of solution-processed Cu_2SnS_3 absorber for low cost photovoltaic cells, *Mater. Lett.* 228 (2018) 447–449. <https://doi.org/10.1016/j.matlet.2018.06.083>.
- [64] S. Jaulmes, J. Rivet, P. Laruelle, Cuivre–étain–soufre Cu_4SnS_4 , *Acta Crystallogr. Sect. B Struct. Crystallogr. Cryst. Chem.* 33 (1977) 540–542. <https://doi.org/10.1107/s0567740877004002>.
- [65] A. Suzumura, N. Nagasako, Y. Kinoshita, M. Watanabe, T. Kita, R. Asahi, Presence of a Doubly-Splitting Site and Its Effect on Thermoelectric Properties of Cu_4SnS_4 , *Mater. Trans.* 56 (2015) 858–863. <https://doi.org/10.2320/matertrans.E-M2015804>.
- [66] J. Mahy, J. Van Landuyt, S. Amelinckx, The phase transition at -41°C in Cu_4SnS_4 as observed in electron microscopy, *Solid State Commun.* 54 (1985) 621–624.

[https://doi.org/10.1016/0038-1098\(85\)90091-2](https://doi.org/10.1016/0038-1098(85)90091-2).

- [67] A. Choudhury, S. Mohapatra, H. Yaghoobnejad Asl, S.H. Lee, Y.S. Hor, J.E. Medvedeva, D.L. McClane, G.E. Hilmas, M.A. McGuire, A.F. May, H. Wang, S. Dash, A. Welton, P. Boolchand, K.P. Devlin, J. Aitken, R. Herbst-Irmer, V. Petříček, New insights into the structure, chemistry, and properties of Cu_4SnS_4 , *J. Solid State Chem.* 253 (2017) 192–201. <https://doi.org/10.1016/j.jssc.2017.05.033>.
- [68] M.T.S. Nair, C. Lopéz-Mata, O. GomezDaza, P.K. Nair, Copper tin sulfide semiconductor thin films produced by heating SnS-CuS layers deposited from chemical bath, *Semicond. Sci. Technol.* 18 (2003) 755–759. <https://doi.org/10.1088/0268-1242/18/8/306>.
- [69] U. Chalapathi, B. Poornaprakash, S.H. Park, Two-stage processed Cu_4SnS_4 thin films for photovoltaics - Effect of ($\text{N}_2 + \text{S}_2$) pressure during annealing, *Thin Solid Films.* 660 (2018) 236–241. <https://doi.org/10.1016/j.tsf.2018.06.008>.
- [70] V.P.G. Vani, M.R.V. Reddy, K.T.R. Reddy, Influence of source - Substrate distance of Cu_4SnS_4 thin films grown by co-evaporation, *Adv. Mater. Res.* 768 (2013) 103–108. <https://doi.org/10.4028/www.scientific.net/AMR.768.103>.
- [71] Q. Chen, X. Dou, Z. Li, Y. Ni, J. Chen, F. Zhou, Y. Yamaguchi, S. Zhuang, Study on the photovoltaic property of Cu_4SnS_4 synthesized by mechanochemical process, *Optik (Stuttg).* 125 (2014) 3217–3220. <https://doi.org/10.1016/j.ijleo.2013.12.023>.
- [72] H. Guan, H. Shen, C. Gao, X. He, The influence of annealing atmosphere on the phase formation of Cu-Sn-S ternary compound by SILAR method, *J. Mater. Sci. Mater. Electron.* 24 (2013) 3195–3198. <https://doi.org/10.1007/s10854-013-1227-x>.
- [73] U. Chalapathi, B. Poornaprakash, S.H. Park, Enhanced mobility of Cu_4SnS_4 films prepared by annealing SnS-CuS stacks in a graphite box, *Sol. Energy.* 155 (2017) 336–341. <https://doi.org/10.1016/j.solener.2017.06.051>.
- [74] Y. Yu, Y. Hu, J. Yang, Z. Wei, Recent advances in wide-spectrum photodetectors based on low-dimensional semiconductors, *Mater. Today Electron.* 2 (2022) 100013. <https://doi.org/10.1016/j.mtelec.2022.100013>.
- [75] Y. Zhang, W. Song, High performance self-powered CuZnS/GaN UV photodetectors with ultrahigh on/off ratio (3×10^8), *J. Mater. Chem. C.* 9 (2021) 4799–4807. <https://doi.org/10.1039/D1TC00137J>.

- [76] Z. Li, H. Li, K. Jiang, D. Ding, J. Li, C. Ma, S. Jiang, Y. Wang, T.D. Anthopoulos, Y. Shi, Self-Powered Perovskite/CdS Heterostructure Photodetectors, *ACS Appl. Mater. Interfaces*. 11 (2019) 40204–40213. <https://doi.org/10.1021/acsami.9b11835>.
- [77] X. Wang, K. Xu, X. Yan, X. Xiao, C. Aruta, V. Foglietti, Z. Ning, N. Yang, Amorphous ZnO/PbS Quantum Dots Heterojunction for Efficient Responsivity Broadband Photodetectors, *ACS Appl. Mater. Interfaces*. 12 (2020) 8403–8410. <https://doi.org/10.1021/acsami.9b19486>.
- [78] A. Parameswaran Sreekala, B. Krishnan, R. Fabian Cienfuegos Pelaes, D. Avellaneda Avellaneda, J. Amilcar Aguilar-Martínez, S. Shaji, Ultraviolet to near infrared wavelength independent SnS-graphene hybrid thin film photodetector from nanocolloids, *Appl. Surf. Sci.* 609 (2023) 155277. <https://doi.org/10.1016/J.APSUSC.2022.155277>.
- [79] J. Yu, L. Dong, B. Peng, L. Yuan, Y. Huang, L. Zhang, Y. Zhang, R. Jia, Self-powered photodetectors based on β -Ga₂O₃/4H-SiC heterojunction with ultrahigh current on/off ratio and fast response, *J. Alloys Compd.* 821 (2020) 153532. <https://doi.org/10.1016/J.JALLCOM.2019.153532>.
- [80] J. Jiang, J. Huang, Z. Ye, S. Ruan, Y.J. Zeng, Self-Powered and Broadband Photodetector Based on SnS₂/ZnO_{1-x}S_x Heterojunction, *Adv. Mater. Interfaces*. 7 (2020) 2000882. <https://doi.org/10.1002/ADMI.202000882>.
- [81] A.A. Ahmed, M.R. Hashim, T.F. Qahtan, M. Rashid, Preparation and characteristics study of self-powered and fast response p-NiO/n-Si heterojunction photodetector, *Ceram. Int.* 48 (2022) 20078–20089. <https://doi.org/10.1016/J.CERAMINT.2022.03.285>.
- [82] B. Sun, W. Sun, S. Li, G. Ma, W. Jiang, Z. Yan, X. Wang, Y. An, P. Li, Z. Liu, W. Tang, High-sensitive, self-powered deep UV photodetector based on p-CuSCN/n-Ga₂O₃ thin film heterojunction, *Opt. Commun.* 504 (2022) 127483. <https://doi.org/10.1016/J.OPTCOM.2021.127483>.
- [83] P. Salunkhe, P. Bhat, D. Kekuda, Performance evaluation of transparent self-powered n-ZnO/p-NiO heterojunction ultraviolet photosensors, *Sensors Actuators A Phys.* 345 (2022) 113799. <https://doi.org/10.1016/J.SNA.2022.113799>.
- [84] Y. Chang, J.Y. Wang, F.L. Wu, W. Tian, W. Zhai, Y. Chang, J.Y. Wang, F.L. Wu,

- W. Zhai, W. Tian, Structural Design and Pyroelectric Property of SnS/CdS Heterojunctions Contrived for Low-Temperature Visible Photodetectors, *Adv. Funct. Mater.* 30 (2020) 2001450. <https://doi.org/10.1002/ADFM.202001450>.
- [85] S. Dias, K.L. Kumawat, S. Biswas, S.B. Krupanidhi, Heat-up synthesis of Cu₂SnS₃ quantum dots for near infrared photodetection, *RSC Adv.* 7 (2017) 23301–23308. <https://doi.org/10.1039/C7RA02485A>.
- [86] S. Dias, K. Kumawat, S. Biswas, S.B. Krupanidhi, Solvothermal Synthesis of Cu₂SnS₃ Quantum Dots and Their Application in Near-Infrared Photodetectors, *Inorg. Chem.* 56 (2017) 2198–2203. <https://doi.org/10.1021/ACS.INORGCHEM.6B02832>.
- [87] Z. Lv, S. Yan, W. Mu, Y. Liu, Q. Xin, Y. Liu, Z. Jia, X. Tao, A High Responsivity and Photosensitivity Self-Powered UV Photodetector Constructed by the CuZnS/Ga₂O₃ Heterojunction, *Adv. Mater. Interfaces.* 10 (2023) 2202130. <https://doi.org/10.1002/ADMI.202202130>.
- [88] A. Nadukkandy, S. Shaji, D.A. Avellaneda, J.A. Aguilar-Martínez, B. Krishnan, Cubic structured silver antimony sulfide-selenide solid solution thin films for sustainable photodetection and photovoltaic application, *J. Alloys Compd.* 942 (2023) 169072. <https://doi.org/10.1016/J.JALLCOM.2023.169072>.
- [89] D. Avellaneda, M.T.S.S. Nair, P.K. Nair, Polymorphic tin sulfide thin films of zinc blende and orthorhombic structures by chemical deposition, *J. Electrochem. Soc.* 155 (2008) 517–525. <https://doi.org/10.1149/1.2917198>.
- [90] P. Pramanik, P.K. Basu, S. Biswas, Preparation and characterization of chemically deposited tin(II) sulphide thin films, *Thin Solid Films.* 150 (1987) 269–276. [https://doi.org/10.1016/0040-6090\(87\)90099-X](https://doi.org/10.1016/0040-6090(87)90099-X).
- [91] M.T.S. Nair, P.K. Nair, Simplified chemical deposition technique for good quality SnS thin films, *Semicond. Sci. Technol.* 6 (1991) 132–134. <https://doi.org/10.1088/0268-1242/6/2/014>.
- [92] L. V. Garcia, M.I. Mendivil, G. Garcia Guillen, J.A. Aguilar Martinez, B. Krishnan, D. Avellaneda, G.A. Castillo, T.K. Das Roy, S. Shaji, CdS thin films prepared by laser assisted chemical bath deposition, *Appl. Surf. Sci.* 336 (2015) 329–334. <https://doi.org/10.1016/j.apsusc.2014.12.122>.

- [93] U. Holzwarth, N. Gibson, The Scherrer equation versus the “Debye-Scherrer equation,” *Nat. Nanotechnol.* 6 (2011) 534–534.
<https://doi.org/10.1038/nnano.2011.145>.
- [94] N.A. Khan, K.S. Rahman, K.A. Aris, A.M. Ali, H. Misran, M. Akhtaruzzaman, S.K. Tiong, N. Amin, Effect of laser annealing on thermally evaporated CdTe thin films for photovoltaic absorber application, *Sol. Energy.* 173 (2018) 1051–1057.
<https://doi.org/10.1016/J.SOLENER.2018.08.023>.
- [95] L.A. Bulla, G. Julian, C.W. Hesseltine, F.L. Baker, Chapter I Scanning Electron Microscopy, *Methods Microbiol.* 8 (1973) 1–33. [https://doi.org/10.1016/S0580-9517\(08\)70158-2](https://doi.org/10.1016/S0580-9517(08)70158-2).
- [96] P. Agarwal, M. V. Salapaka, Control and Systems Approaches to Atomic Force Microscopy, *IFAC Proc. Vol.* 41 (2008) 10456–10467.
<https://doi.org/10.3182/20080706-5-KR-1001.01772>.
- [97] G. Greczynski, L. Hultman, X-ray photoelectron spectroscopy: Towards reliable binding energy referencing, *Prog. Mater. Sci.* 107 (2020) 100591.
<https://doi.org/10.1016/J.PMATSCI.2019.100591>.
- [98] R.K. Mishra, A.K. Zachariah, S. Thomas, Energy-Dispersive X-ray Spectroscopy Techniques for Nanomaterial, *Microsc. Methods Nanomater. Charact.* 2017 (2017) 383–405. <https://doi.org/10.1016/B978-0-323-46141-2.00012-2>.
- [99] J. Tauc, A. Menth, States in the gap, *J. Non. Cryst. Solids.* 10 (1972) 569–585.
[https://doi.org/10.1016/0022-3093\(72\)90194-9](https://doi.org/10.1016/0022-3093(72)90194-9).
- [100] S.K. Suram, P.F. Newhouse, J.M. Gregoire, High Throughput Light Absorber Discovery, Part 1: An Algorithm for Automated Tauc Analysis, *ACS Comb. Sci.* 18 (2016) 673–681. <https://doi.org/10.1021/acscombsci.6b00053>.
- [101] D. Alagarasan, S. Varadharajaperumal, K.D.A. Kumar, R. Naik, S. Umrao, M. Shkir, S. AIFaify, R. Ganesan, Influence of nanostructured SnS thin films for visible light photo detection, *Opt. Mater. (Amst).* 121 (2021) 111489.
<https://doi.org/10.1016/J.OPTMAT.2021.111489>.
- [102] A. Bhorde, A. Pawbake, P. Sharma, S. Nair, A. Funde, P. Bankar, M. More, S. Jadkar, Solvothermal synthesis of tin sulfide (SnS) nanorods and investigation of its field emission properties, *Appl. Phys. A.* 124 (2018) 133.

<https://doi.org/10.1007/s00339-017-1529-6>.

- [103] S.I. Son, D. Shin, Y.G. Son, C.S. Son, D.R. Kim, J.H. Park, S. Kim, D. Hwang, P. Song, Effect of working pressure on the properties of RF sputtered SnS thin films and photovoltaic performance of SnS-based solar cells, *J. Alloys Compd.* 831 (2020) 154626. <https://doi.org/10.1016/J.JALLCOM.2020.154626>.
- [104] F. Ballipinar, A.C. Rastogi, Tin sulfide (SnS) semiconductor photo-absorber thin films for solar cells by vapor phase sulfurization of Sn metallic layers using organic sulfur source, *J. Alloys Compd.* 728 (2017) 179–188. <https://doi.org/10.1016/J.JALLCOM.2017.08.295>.
- [105] M.S. Mahdi, K. Ibrahim, A. Hmood, N.M. Ahmed, S.A. Azzez, F.I. Mustafa, A highly sensitive flexible SnS thin film photodetector in the ultraviolet to near infrared prepared by chemical bath deposition, *RSC Adv.* 6 (2016) 114980–114988. <https://doi.org/10.1039/C6RA24491B>.
- [106] D. Sharma, N. Kamboj, K. Agarwal, B.R. Mehta, Structural, optical and photoelectrochemical properties of phase pure SnS and SnS₂ thin films prepared by vacuum evaporation method, *J. Alloys Compd.* 822 (2020) 153653. <https://doi.org/10.1016/J.JALLCOM.2020.153653>.
- [107] Y. Chen, L. Ma, Y. Yin, X. Qian, G. Zhou, X. Gu, W. Liu, X. Wu, F. Zhang, Strong quantum confinement effect in Cu₄SnS₄ quantum dots synthesized via an improved hydrothermal approach, *J. Alloys Compd.* 672 (2016) 204–211. <https://doi.org/10.1016/j.jallcom.2016.02.135>.
- [108] L.V.A. Scalvi, C.F. Bueno, Transient decay of photoinduced current in semiconductors and heterostructures, *J. Phys. D. Appl. Phys.* 53 (2019) 033001. <https://doi.org/10.1088/1361-6463/AB495A>.
- [109] C.J. Wang, S.C. Shei, S.C. Chang, S.J. Chang, Fabrication and sulfurization of Cu₂SnS₃ thin films with tuning the concentration of Cu-Sn-S precursor ink, *Appl. Surf. Sci.* 388 (2016) 71–76. <https://doi.org/10.1016/j.apsusc.2016.03.154>.
- [110] M.R. Pallavolu, C.D. Kim, V.R. Minnam Reddy, S. Gedi, C. Park, Effect of sulfurization time on the performance of monoclinic Cu₂SnS₃ solar cells, *Sol. Energy.* 188 (2019) 209–217. <https://doi.org/10.1016/j.solener.2019.06.004>.
- [111] U. Chalapathi, B. Poornaprakash, S.-H. Park, Fabrication of Cu₂SnS₃ films by

- annealing chemically deposited SnS–CuS precursors in a graphite box, *J. Mater. Sci. Mater. Electron.* 29 (2018) 1451–1462. <https://doi.org/10.1007/s10854-017-8053-5>.
- [112] V.P.G. Vani, M.V. Reddy, K.T.R. Reddy, Thickness-Dependent Physical Properties of Coevaporated Cu₄SnS₄ Films, *ISRN Condens. Matter Phys.* 2013 (2013) 1–6. <https://doi.org/10.1155/2013/142029>.
- [113] L.T. Yarce, E.R. Andres, R.R. Trujillo, C.M. Ruiz, T.D. Becerril, R.S. Gonzalez, R.G. Isasmendi, A.C. Solis, G.G. Salgado, The Morphological Changes of SnS Thin Films Deposited on Stainless-Steel Substrates at Low Temperatures, *Eur. J. Eng. Res. Sci.* 4 (2019) 1–4. <https://doi.org/10.24018/ejers.2019.4.1.980>.
- [114] L.A. Isac, A. Duta, A. Kriza, I.A. Enesca, M. Nanu, The growth of CuS thin films by Spray Pyrolysis, *J. Phys. Conf. Ser.* 61 (2007) 477–481. <https://doi.org/10.1088/1742-6596/61/1/096>.
- [115] M. Guc, F. Oliva, A. Fairbrother, T. Jawhari, X. Alcobe, M. Placidi, A. Pérez-Rodríguez, E. Saucedo, V. Izquierdo-Roca, Cu-Sn-S system: Vibrational properties and coexistence of the Cu₂SnS₃, Cu₃SnS₄ and Cu₄SnS₄ compounds, *Scr. Mater.* 186 (2020) 180–184. <https://doi.org/10.1016/j.scriptamat.2020.05.050>.
- [116] Y. Gong, H. Yuan, C.L. Wu, P. Tang, S.Z. Yang, A. Yang, G. Li, B. Liu, J. Van De Groep, M.L. Brongersma, M.F. Chisholm, S.C. Zhang, W. Zhou, Y. Cui, Spatially controlled doping of two-dimensional SnS₂ through intercalation for electronics, *Nat. Nanotechnol.* 13 (2018) 294–299. <https://doi.org/10.1038/s41565-018-0069-3>.
- [117] L.L. Baranowski, P. Zawadzki, S. Christensen, D. Nordlund, S. Lany, A.C. Tamboli, L. Gedvilas, D.S. Ginley, W. Tumas, E.S. Toberer, A. Zakutayev, Control of Doping in Cu₂SnS₃ through Defects and Alloying, *Chem. Mater.* 26 (2014) 4951–4959. <https://doi.org/10.1021/cm501339v>.
- [118] P. Zhao, S. Cheng, Influence of Sulfurization Temperature on Photoelectric Properties Cu₂SnS₃ Thin Films Deposited by Magnetron Sputtering, *Adv. Mater. Sci. Eng.* 2013 (2013) 1–4. <https://doi.org/10.1155/2013/726080>.
- [119] H.D. Shelke, A.C. Lokhande, J.H. Kim, C.D. Lokhande, Influence of deposition temperature on the structural, morphological, optical and photoelectrochemical properties of CBD deposited Cu₂SnS₃ thin films, *J. Alloys Compd.* 831 (2020) 154768. <https://doi.org/10.1016/j.jallcom.2020.154768>.

- [120] U. Chalapathi, Y.B.K. Kumar, S. Uthanna, V.S. Raja, Investigations on Cu_3SnS_4 thin films prepared by spray pyrolysis, *Thin Solid Films*. 556 (2014) 61–67. <https://doi.org/10.1016/j.tsf.2014.01.005>.
- [121] P.A. Fernandes, P.M.P. Salomé, A.F. da Cunha, $\text{Cu}_x\text{SnS}_{x+1}$ ($x = 2, 3$) thin films grown by sulfurization of metallic precursors deposited by dc magnetron sputtering, *Phys. Status Solidi C*. 7 (2010) 901–904. <https://doi.org/10.1002/pssc.200982746>.
- [122] S. Devasia, S. Shaji, D.A. Avellaneda, J.A. Aguilar Martinez, B. Krishnan, Tin antimony sulfide ($\text{Sn}_6\text{Sb}_{10}\text{S}_{21}$) thin films by heating chemically deposited $\text{Sb}_2\text{S}_3/\text{SnS}$ layers: Studies on the structure and their optoelectronic properties, *J. Alloys Compd.* 827 (2020) 154256. <https://doi.org/10.1016/j.jallcom.2020.154256>.
- [123] V. Vinayakumar, C.R.O. Hernández, S. Shaji, D.A. Avellaneda, J.A.A. Martínez, B. Krishnan, Effects of rapid thermal processing on chemically deposited antimony sulfide thin films, *Mater. Sci. Semicond. Process.* 80 (2018) 9–17. <https://doi.org/10.1016/j.mssp.2018.02.011>.
- [124] D. Avellaneda, B. Krishnan, T.K. Das Roy, G.A. Castillo, S. Shaji, Modification of structure, morphology and physical properties of tin sulfide thin films by pulsed laser irradiation, *Appl. Phys. A Mater. Sci. Process.* 110 (2013) 667–672. <https://doi.org/10.1007/s00339-012-7148-3>.
- [125] V. V. Brus, I.S. Babichuk, I.G. Orletskyi, P.D. Maryanchuk, V.O. Yukhymchuk, V.M. Dzhagan, I.B. Yanchuk, M.M. Solovan, I. V. Babichuk, Raman spectroscopy of Cu-Sn-S ternary compound thin films prepared by the low-cost spray-pyrolysis technique, *Appl. Opt.* 55 (2016) B158. <https://doi.org/10.1364/AO.55.00B158>.
- [126] K. Hamamura, J. Chantana, K. Suzuki, T. Minemoto, Influence of Cu/(Ge + Sn) composition ratio on photovoltaic performances of $\text{Cu}_2\text{Sn}_{1-x}\text{Ge}_x\text{S}_3$ solar cell, *Sol. Energy*. 149 (2017) 341–346. <https://doi.org/10.1016/J.SOLENER.2017.04.025>.
- [127] V. Vinayakumar, S. Shaji, D. Avellaneda, J.A. Aguilar-Martínez, B. Krishnan, Copper antimony sulfide thin films for visible to near infrared photodetector applications, *RSC Adv.* 8 (2018) 31055–31065. <https://doi.org/10.1039/C8RA05662E>.
- [128] U. Chalapathi, B. Poornaprakash, S.H. Park, Chemically deposited cubic SnS thin films for solar cell applications, *Sol. Energy*. 139 (2016) 238–248.

<https://doi.org/10.1016/J.SOLENER.2016.09.046>.

- [129] M.R. Pallavolu, V.R. Minnam Reddy, B. Pejjai, D. Jeong, C. Park, Effect of sulfurization temperature on the phase purity of Cu_2SnS_3 thin films deposited via high vacuum sulfurization, *Appl. Surf. Sci.* 462 (2018) 641–648.
<https://doi.org/10.1016/j.apsusc.2018.08.112>.
- [130] S. Dias, S.B. Krupanidhi, Solution processed Cu_2SnS_3 thin films for visible and infrared photodetector applications, *AIP Adv.* 6 (2016) 025217.
<https://doi.org/10.1063/1.4942775>.
- [131] U. Chalapathi, Y. Jayasree, S. Uthanna, V. Sundara Raja, Effect of annealing on the structural, microstructural and optical properties of co-evaporated Cu_2SnS_3 thin films, *Vacuum.* 117 (2015) 121–126. <https://doi.org/10.1016/j.vacuum.2015.04.006>.
- [132] M.Y. Zaki, F. Sava, I.D. Simandan, A.T. Buruiana, C. Mihai, A. Velea, A.C. Galca, Effect of the stacking order, annealing temperature and atmosphere on crystal phase and optical properties of Cu_2SnS_3 , *Sci. Reports* 2022 121. 12 (2022) 1–18.
<https://doi.org/10.1038/s41598-022-12045-3>.
- [133] M.R. Pallavolu, S.W. Joo, C. Park, Significance of rapid thermal annealing and its ramp rate effect on the properties of monoclinic CTS thin films, *Micro and Nanostructures.* 166 (2022) 207234.
<https://doi.org/10.1016/J.MICRNA.2022.207234>.
- [134] A.C. Lokhande, A.A. Yadav, J.Y. Lee, M. He, S.J. Patil, V.C. Lokhande, C.D. Lokhande, J.H. Kim, Room temperature liquefied petroleum gas sensing using $\text{Cu}_2\text{SnS}_3/\text{CdS}$ heterojunction, *J. Alloys Compd.* 709 (2017) 92–103.
<https://doi.org/10.1016/J.JALLCOM.2017.03.135>.
- [135] A.-J. Cheng, M. Manno, A. Khare, C. Leighton, S.A. Campbell, E.S. Aydil, Imaging and phase identification of $\text{Cu}_2\text{ZnSnS}_4$ thin films using confocal Raman spectroscopy, *J. Vac. Sci. Technol. A Vacuum, Surfaces, Film.* 29 (2011) 051203.
<https://doi.org/10.1116/1.3625249>.
- [136] K.M. Koskela, C. Mora Perez, D.B. Eremin, J.M. Evans, M.J. Strumolo, N.S. Lewis, O. V. Prezhdo, R.L. Brutchey, Polymorphic Control of Solution-Processed Cu_2SnS_3 Films with Thiol–Amine Ink Formulation, *Chem. Mater.* 34 (2022) 8654–8663.
<https://doi.org/10.1021/acs.chemmater.2c01612>.

- [137] D. Tiwari, T. Koehler, R. Klenk, D.J. Fermin, Solution processed single-phase Cu_2SnS_3 films: structure and photovoltaic performance, *Sustain. Energy Fuels*. 1 (2017) 899–906. <https://doi.org/10.1039/C7SE00150A>.
- [138] J. Li, C. Xue, Y. Wang, G. Jiang, W. Liu, C. Zhu, Cu_2SnS_3 solar cells fabricated by chemical bath deposition-annealing of SnS/Cu stacked layers, *Sol. Energy Mater. Sol. Cells*. 144 (2016) 281–288. <https://doi.org/10.1016/j.solmat.2015.09.017>.
- [139] W. Wang, H. Cai, G. Chen, B. Chen, L. Yao, J. Dong, X. Yu, S. Chen, Z. Huang, Preparation of Sn loss-free Cu_2SnS_3 thin films by an oxide route for solar cell, *J. Alloys Compd.* 742 (2018) 860–867. <https://doi.org/10.1016/j.jallcom.2018.01.391>.
- [140] B.H. Toby, R.B. Von Dreele, GSAS-II: the genesis of a modern open-source all purpose crystallography software package, *Urn:Issn:0021-8898*. 46 (2013) 544–549. <https://doi.org/10.1107/S0021889813003531>.
- [141] M. Onoda, X.A. Chen, A. Sato, H. Wada, Crystal structure and twinning of monoclinic Cu_2SnS_3 , *Mater. Res. Bull.* 35 (2000) 1563–1570. [https://doi.org/10.1016/S0025-5408\(00\)00347-0](https://doi.org/10.1016/S0025-5408(00)00347-0).
- [142] M.R. Pallavolu, R.R. Nallapureddy, S.W. Joo, C. Park, Fabrication of monoclinic- Cu_2SnS_3 thin-film solar cell and its photovoltaic device performance, *Opt. Mater. (Amst)*. 111 (2021) 110668. <https://doi.org/10.1016/J.OPTMAT.2020.110668>.
- [143] D.M. Berg, R. Djemour, L. Gütay, S. Siebentritt, P.J. Dale, X. Fontane, V. Izquierdo-Roca, A. Pérez-Rodríguez, Raman analysis of monoclinic Cu_2SnS_3 thin films, *Appl. Phys. Lett.* 100 (2012) 192103. <https://doi.org/10.1063/1.4712623>.
- [144] Y. Zhao, X. Han, B. Xu, C. Dong, J. Li, X. Yan, Effect of sulfurization process on the properties of solution-processed Cu_2SnS_3 thin film solar cells, *J. Mater. Sci. Mater. Electron.* 30 (2019) 17947–17955. <https://doi.org/10.1007/s10854-019-02148-5>.
- [145] E. Ketenci Ozsoy, F. Atay, O. Buyukgungor, Production and characterization of Cu_2SnS_3 films for solar cell applications: The effect of the sulfurization temperature on CuS secondary phase, *Sol. Energy*. 214 (2021) 179–188. <https://doi.org/10.1016/j.solener.2020.11.068>.
- [146] F. Oliva, L. Arqués, L. Acebo, M. Guc, Y. Sánchez, X. Alcobé, A. Pérez-Rodríguez, E. Saucedo, V. Izquierdo-Roca, Characterization of Cu_2SnS_3 polymorphism and its

- impact on optoelectronic properties, *J. Mater. Chem. A*. 5 (2017) 23863–23871.
<https://doi.org/10.1039/c7ta08705e>.
- [147] P.-W. Guan, Z.-K. Liu, A hybrid functional study of native point defects in Cu_2SnS_3 : implications for reducing carrier recombination, *Phys. Chem. Chem. Phys.* 20 (2018) 256–261. <https://doi.org/10.1039/C7CP06891C>.
- [148] P.W. Guan, S.L. Shang, G. Lindwall, T. Anderson, Z.K. Liu, Phase stability of the Cu-Sn-S system and optimal growth conditions for earth-abundant Cu_2SnS_3 solar materials, *Sol. Energy*. 155 (2017) 745–757.
<https://doi.org/10.1016/j.solener.2017.07.017>.
- [149] Y. Dong, J. He, L. Sun, Y. Chen, P. Yang, J. Chu, Effect of sulfurization temperature on properties of Cu_2SnS_3 thin films and solar cells prepared by sulfurization of stacked metallic precursors, *Mater. Sci. Semicond. Process.* 38 (2015) 171–176.
<https://doi.org/10.1016/j.mssp.2015.04.026>.
- [150] A. Crovetto, R. Chen, R.B. Ettliger, A.C. Cazzaniga, J. Schou, C. Persson, O. Hansen, Dielectric function and double absorption onset of monoclinic Cu_2SnS_3 : Origin of experimental features explained by first-principles calculations, *Sol. Energy Mater. Sol. Cells*. 154 (2016) 121–129.
<https://doi.org/10.1016/J.SOLMAT.2016.04.028>.
- [151] J. De Wild, E.V.C. Robert, B.E.L. Adib, P.J. Dale, Optical characterization of solution prepared Cu_2SnS_3 for photovoltaic applications, *MRS Online Proc. Libr.* 2015 17711. 1771 (2015) 151–156. <https://doi.org/10.1557/OPL.2015.624>.
- [152] R. Dahule, A. Raghav, A.T. Hanindriyo, K. Hongo, R. Maezono, E. Panda, Surface Study of Cu_2SnS_3 Using First-Principles Density Functional Theory, *Adv. Theory Simulations*. 4 (2021) 2000315. <https://doi.org/10.1002/ADTS.202000315>.
- [153] P. Hervé, L.K.J. Vandamme, General relation between refractive index and energy gap in semiconductors, *Infrared Phys. Technol.* 35 (1994) 609–615.
[https://doi.org/10.1016/1350-4495\(94\)90026-4](https://doi.org/10.1016/1350-4495(94)90026-4).
- [154] P.R. Guddeti, P.M.B. Devi, K.T.R. Reddy, Optical and electrical investigations on Cu_2SnS_3 layers prepared by two-stage process, *Chinese J. Phys.* 67 (2020) 458–472.
<https://doi.org/10.1016/J.CJPH.2020.08.003>.
- [155] T. Srinivasa Reddy, R. Amiruddin, M.C. Santhosh Kumar, Deposition and

- characterization of Cu_2SnS_3 thin films by co-evaporation for photovoltaic application, *Sol. Energy Mater. Sol. Cells*. 143 (2015) 128–134.
<https://doi.org/10.1016/j.solmat.2015.06.049>.
- [156] M. Cota-Leal, D. Cabrera-German, M. Sotelo-Lerma, M. Martínez-Gil, J.A. García-Valenzuela, Highly-transparent and conductive CuI films obtained by a redirected low-cost and electroless two-step route: Chemical solution deposition of CuS_2 and subsequent iodination, *Mater. Sci. Semicond. Process.* 95 (2019) 59–67.
<https://doi.org/10.1016/J.MSSP.2019.02.016>.
- [157] K. Lohani, H. Nautiyal, N. Ataollahi, C. Fanciulli, I. Sergueev, M. Etter, P. Scardi, Experimental and Ab Initio Study of Cu_2SnS_3 (CTS) Polymorphs for Thermoelectric Applications, *J. Phys. Chem. C*. 125 (2021) 178–188.
<https://doi.org/10.1021/acs.jpcc.0c09139>.
- [158] T. Gershon, Y.S. Lee, P. Antunez, R. Mankad, S. Singh, D. Bishop, O. Gunawan, M. Hopstaken, R. Haight, Photovoltaic Materials and Devices Based on the Alloyed Kesterite Absorber $(\text{Ag}_x\text{Cu}_{1-x})_2\text{ZnSnSe}_4$, *Adv. Energy Mater.* 6 (2016) 1502468.
<https://doi.org/10.1002/aenm.201502468>.
- [159] M. Gansukh, Z. Li, M.E. Rodriguez, S. Engberg, F.M.A. Martinho, S.L. Mariño, E. Stamate, J. Schou, O. Hansen, S. Canulescu, Energy band alignment at the heterointerface between CdS and Ag-alloyed CZTS, *Sci. Rep.* 10 (2020) 18388.
<https://doi.org/10.1038/s41598-020-73828-0>.
- [160] I.Y. Kim, J.Y. Lee, U. V. Ghorpade, M.P. Suryawanshi, D.S. Lee, J.H. Kim, Influence of annealing temperature on the properties and solar cell performance of Cu_2SnS_3 (CTS) thin film prepared using sputtering method, *J. Alloys Compd.* 688 (2016) 12–17. <https://doi.org/10.1016/J.JALLCOM.2016.06.264>.
- [161] J. De Wild, E.V.C. Robert, B. El Adib, D. Abou-Ras, P.J. Dale, Secondary phase formation during monoclinic Cu_2SnS_3 growth for solar cell application, *Sol. Energy Mater. Sol. Cells*. 157 (2016) 259–265. <https://doi.org/10.1016/j.solmat.2016.04.039>.
- [162] Y.M. Ko, R.B.V. Chalapathy, L. Larina, B.T. Ahn, Growth of a void-free Cu_2SnS_3 thin film using a Cu/SnS₂ precursor through an intermediate-temperature pre-annealing and sulfurization process, *CrystEngComm*. 19 (2017) 5764–5773.
<https://doi.org/10.1039/C7CE01261F>.

- [163] J. Chantana, Y. Kawano, T. Nishimura, A. Mavlonov, T. Minemoto, Impact of Urbach energy on open-circuit voltage deficit of thin-film solar cells, *Sol. Energy Mater. Sol. Cells*. 210 (2020) 110502.
<https://doi.org/10.1016/J.SOLMAT.2020.110502>.
- [164] Z. Su, G. Liang, P. Fan, J. Luo, Z. Zheng, Z. Xie, W. Wang, S. Chen, J. Hu, Y. Wei, C. Yan, J. Huang, X. Hao, F. Liu, Device Postannealing Enabling over 12% Efficient Solution-Processed $\text{Cu}_2\text{ZnSnS}_4$ Solar Cells with Cd^{2+} Substitution, *Adv. Mater.* 32 (2020) 2000121. <https://doi.org/10.1002/adma.202000121>.
- [165] C. Zeng, Y. Liang, L. Zeng, L. Zhang, J. Zhou, P. Huang, R. Hong, Effect of S/(S+Se) ratio during the annealing process on the performance of $\text{Cu}_2\text{ZnSn}(\text{S},\text{Se})_4$ solar cells prepared by sputtering from a quaternary target, *Sol. Energy Mater. Sol. Cells*. 203 (2019) 110167. <https://doi.org/10.1016/J.SOLMAT.2019.110167>.
- [166] T. Zheng, X. Dong, F. Yang, L. Yu, X. Sun, J. Chen, C. Wang, Y. Zhao, Y. Li, An effective air heat-treatment strategy of precursor films in search of high open-circuit voltage for efficient CZTSSe cells, *Sol. Energy Mater. Sol. Cells*. 239 (2022) 111662. <https://doi.org/10.1016/J.SOLMAT.2022.111662>.
- [167] H. Nazem, H.P. Dizaj, N.E. Gorji, Modeling of J_{sc} and V_{oc} versus the grain size in CdTe, CZTS and Perovskite thin film solar cells, *Superlattices Microstruct.* 128 (2019) 421–427. <https://doi.org/10.1016/J.SPML.2019.02.002>.
- [168] Y.C. Kim, H.J. Jeong, S.K. Lee, S.T. Kim, J.H. Jang, The effect of S/(S+Se) ratios on the formation of secondary phases in the band gap graded $\text{Cu}_2\text{ZnSn}(\text{S},\text{Se})_4$ thin film solar cells, *J. Alloys Compd.* 793 (2019) 289–294.
<https://doi.org/10.1016/J.JALLCOM.2019.04.118>.
- [169] K. Kumar, R. Yadav, S. Devi, P. Singh, S. Husale, S. Tyagi, D. Kaur, Effective ways to enhance the performance of n-MoS₂/p-CuO heterojunction based self-powered photodetectors, *Sol. Energy Mater. Sol. Cells*. 255 (2023) 112285.
<https://doi.org/10.1016/J.SOLMAT.2023.112285>.
- [170] V.H. Vuong, S.V.N. Pammi, S. Ippili, V. Jella, T. Nguyen Thi, K. Sairam Pasupuleti, M.D. Kim, M. Ji Jeong, J.R. Jeong, H. Sik Chang, S.G. Yoon, Flexible, stable, and self-powered photodetectors embedded with chemical vapor deposited lead-free bismuth mixed halide perovskite films, *Chem. Eng. J.* 458 (2023) 141473.

<https://doi.org/10.1016/J.CEJ.2023.141473>.

- [171] D. Jayan K, V. Sebastian, J. Kurian, Simulation and optimization studies on CsPbI₃ based inorganic perovskite solar cells, *Sol. Energy*. 221 (2021) 99–108.
<https://doi.org/10.1016/J.SOLENER.2021.04.030>.
- [172] D. Mora-Herrera, M. Pal, J. Santos-Cruz, Theoretical modelling and device structure engineering of kesterite solar cells to boost the conversion efficiency over 20%, *Sol. Energy*. 220 (2021) 316–330. <https://doi.org/10.1016/J.SOLENER.2021.03.056>.
- [173] M. Burgelman, P. Nollet, S. Degrave, Modelling polycrystalline semiconductor solar cells, *Thin Solid Films*. 361–362 (2000) 527–532. [https://doi.org/10.1016/S0040-6090\(99\)00825-1](https://doi.org/10.1016/S0040-6090(99)00825-1).
- [174] A. Basak, U.P. Singh, Numerical modelling and analysis of earth abundant Sb₂S₃ and Sb₂Se₃ based solar cells using SCAPS-1D, *Sol. Energy Mater. Sol. Cells*. 230 (2021) 111184. <https://doi.org/10.1016/J.SOLMAT.2021.111184>.
- [175] N. Singh, A. Agarwal, M. Agarwal, Numerical simulation of highly efficient lead-free perovskite layers for the application of all-perovskite multi-junction solar cell, *Superlattices Microstruct.* 149 (2021) 106750.
<https://doi.org/10.1016/J.SPMI.2020.106750>.
- [176] J. Jiang, S. Yang, Y. Shi, R. Shan, X. Tian, H. Li, J. Yi, J. Zhong, Optimization bandgap gradation structure simulation of Cu₂Sn_{1-x}Ge_xS₃ solar cells by SCAPS, *Sol. Energy*. 194 (2019) 986–994. <https://doi.org/10.1016/J.SOLENER.2019.11.014>.
- [177] S. Lin, X. Li, H. Pan, H. Chen, X. Li, Y. Li, J. Zhou, Numerical analysis of In_xGa_{1-x}N/SnS and Al_xGa_{1-x}N/SnS heterojunction solar cells, *Energy Convers. Manag.* 119 (2016) 361–367. <https://doi.org/10.1016/J.ENCONMAN.2016.04.059>.
- [178] P. Tiwari, M.F. Alotaibi, Y. Al-Hadeethi, V. Srivastava, B. Arkook, S. Sadanand, P. Lohia, D.K. Dwivedi, A. Umar, H. Algadi, S. Baskoutas, Design and Simulation of Efficient SnS-Based Solar Cell Using Spiro-OMeTAD as Hole Transport Layer, *Nanomaterials*. 12 (2022) 2506. <https://doi.org/10.3390/nano12142506>.
- [179] F. Tahvilzadeh, N. Rezaie, Optimization of the CIGS solar cell by adding a heavily doped layer and an intrinsic layer at absorber layer, *Opt. Quantum Electron.* 48 (2016) 104. <https://doi.org/10.1007/s11082-016-0380-x>.
- [180] Y. Tsunomura, Y. Yoshimine, M. Taguchi, T. Baba, T. Kinoshita, H. Kanno, H.

- Sakata, E. Maruyama, M. Tanaka, Twenty-two percent efficiency HIT solar cell, *Sol. Energy Mater. Sol. Cells.* 93 (2009) 670–673.
<https://doi.org/10.1016/J.SOLMAT.2008.02.037>.
- [181] F. Ahmad, A. Lakhtakia, P.B. Monk, Double-absorber thin-film solar cell with 34% efficiency, *Appl. Phys. Lett.* 117 (2020). <https://doi.org/10.1063/5.0017916>.
- [182] D. Avellaneda, B. Krishnan, A.C. Rodriguez, T.K. Das Roy, S. Shaji, Heat treatments in chemically deposited SnS thin films and their influence in CdS/SnS photovoltaic structures, *J. Mater. Sci. Mater. Electron.* 26 (2015) 5585–5592.
<https://doi.org/10.1007/S10854-014-2295-2>.
- [183] D.-B. Li, S.S. Bista, R.A. Awni, S. Neupane, A. Abudulimu, X. Wang, K.K. Subedi, M.K. Jamarkattel, A.B. Phillips, M.J. Heben, J.D. Poplawsky, D.A. Cullen, R.J. Ellingson, Y. Yan, 20%-efficient polycrystalline Cd(Se,Te) thin-film solar cells with compositional gradient near the front junction, *Nat. Commun.* 13 (2022) 7849.
<https://doi.org/10.1038/s41467-022-35442-8>.
- [184] A. Abadi, M.T. Htay, Y. Hashimoto, K. Ito, N. Momose, Annealing effect of absorber layer on SnS/CdS heterojunction band alignments, *Jpn. J. Appl. Phys.* 61 (2022) 1042. <https://doi.org/10.35848/1347-4065/ac3a8f>.
- [185] T.D. Lee, A.U. Ebong, A review of thin film solar cell technologies and challenges, *Renew. Sustain. Energy Rev.* 70 (2017) 1286–1297.
<https://doi.org/10.1016/j.rser.2016.12.028>.
- [186] Y. Dong, J. He, X. Li, Y. Chen, L. Sun, P. Yang, J. Chu, Study on the preheating duration of Cu₂SnS₃ thin films using RF magnetron sputtering technique for photovoltaics, *J. Alloys Compd.* 665 (2016) 69–75.
<https://doi.org/10.1016/j.jallcom.2016.01.078>.
- [187] J.Y. Lee, I.Y. Kim, M.P. Surywanshi, U. V. Ghorpade, D.S. Lee, J.H. Kim, Fabrication of Cu₂SnS₃ thin film solar cells using Cu/Sn layered metallic precursors prepared by a sputtering process, *Sol. Energy.* 145 (2017) 27–32.
<https://doi.org/10.1016/j.solener.2016.09.041>.
- [188] L. Xiao, Z. Liu, W. Feng, Self-powered photodetector with fast response based on Sb₂Se₃/Cu₂S/Si heterojunction, *Opt. Mater. (Amst).* 137 (2023) 113512.
<https://doi.org/10.1016/J.OPTMAT.2023.113512>.

- [189] A. V. Agrawal, K. Kaur, M. Kumar, Interfacial study of vertically aligned n-type MoS₂ flakes heterojunction with p-type Cu-Zn-Sn-S for self-powered, fast and high performance broadband photodetector, *Appl. Surf. Sci.* 514 (2020) 145901. <https://doi.org/10.1016/J.APSUSC.2020.145901>.
- [190] Q. Lin, A. Armin, P.L. Burn, P. Meredith, Filterless narrowband visible photodetectors, *Nat. Photonics.* 9 (2015) 687–694. <https://doi.org/10.1038/nphoton.2015.175>.
- [191] X. Feng, Y. He, W. Qu, J. Song, W. Pan, M. Tan, B. Yang, H. Wei, Spray-coated perovskite hemispherical photodetector featuring narrow-band and wide-angle imaging, *Nat. Commun.* 13 (2022) 6106. <https://doi.org/10.1038/s41467-022-33934-1>.
- [192] A. Armin, R.D. Jansen-van Vuuren, N. Kopidakis, P.L. Burn, P. Meredith, Narrowband light detection via internal quantum efficiency manipulation of organic photodiodes, *Nat. Commun.* 6 (2015) 6343. <https://doi.org/10.1038/ncomms7343>.
- [193] H. Öztürk, F. Aslan, Preparation of high-quality SnS thin films for self-powered photodetectors and solar cells using a low-temperature powder technique, *Opt. Mater. (Amst).* 131 (2022) 112755. <https://doi.org/10.1016/J.OPTMAT.2022.112755>.
- [194] B. Xu, H. Shen, Y. Xu, J. Ge, S. Wang, Q. Zhao, B. Lai, ZnO/Al₂O₃/p-Si/Al₂O₃/CuO heterojunction NIR photodetector with inverted-pyramid light-trapping structure, *J. Alloys Compd.* 874 (2021) 159864. <https://doi.org/10.1016/J.JALLCOM.2021.159864>.
- [195] A. Paul, S. Shaji, B. Krishnan, D.A. Avellaneda, Novel low-cost synthesis of crystalline SnI₄ thin films via anionic replacement: Effect of iodization time on properties, *Opt. Mater. (Amst).* 133 (2022) 112982. <https://doi.org/10.1016/J.OPTMAT.2022.112982>.

ANNEXURE

Annexure A

Novel low-cost synthesis of crystalline SnI₄ thin films via anionic replacement: Effect of iodization time on properties

Albert Paul, Sadasivan Shaji, Bindu Krishnan, David Avellaneda Avellaneda *

<https://doi.org/10.1016/j.optmat.2022.112982> [195]

Abstract

SnI₄ thin films were deposited for the first time via a novel low-cost route employing rapid iodization of SnS thin films at relatively low temperatures in atmospheric conditions. This is the first report on SnI₄ thin films obtained via the anionic replacement of sulfur in SnS thin films. The effect of iodization time on the structure, morphology, optical, and electrical properties of SnI₄ thin films was studied. XRD analysis revealed the formation of SnI₄ thin films which crystallized in cubic Pa-3 structure and all samples were preferentially oriented along the (222) plane. The diffraction pattern of SnI₄ thin film was subjected to Rietveld refinement and obtained excellent goodness of fit value of 1.19. The formation of SnI₄ was further verified using Raman spectroscopy and intense peaks of SnI₄ at 43, 56, 101, and 140 cm⁻¹ are reported. X-ray photoelectron spectroscopy analysis was employed for the determination of chemical composition and the presence of tin and iodine in the Sn⁴⁺ and I⁻ states were verified throughout the depth of the sample using depth profiling analysis. Elemental mapping from the Energy-dispersive X-ray spectroscopy confirmed uniform distribution of elements (tin and iodine). Surface morphology was modified after iodization and the optical bandgap was shifted from 1.7 to 2.7 eV on the transition of as prepared SnS to SnI₄. The best condition SnI₄ thin films exhibited crystallite size, refractive index, and resistivity values of 63 nm, 2.46, and 3.1×10⁵ Ω.cm, respectively. SnI₄ films obtained by the rapid iodization of SnS films can be used as precursor layers in the two-step deposition of lead-free tin iodide perovskite solar cells for better photovoltaic performance. The obtained results validate the key role of iodization time on the properties of SnI₄ films.

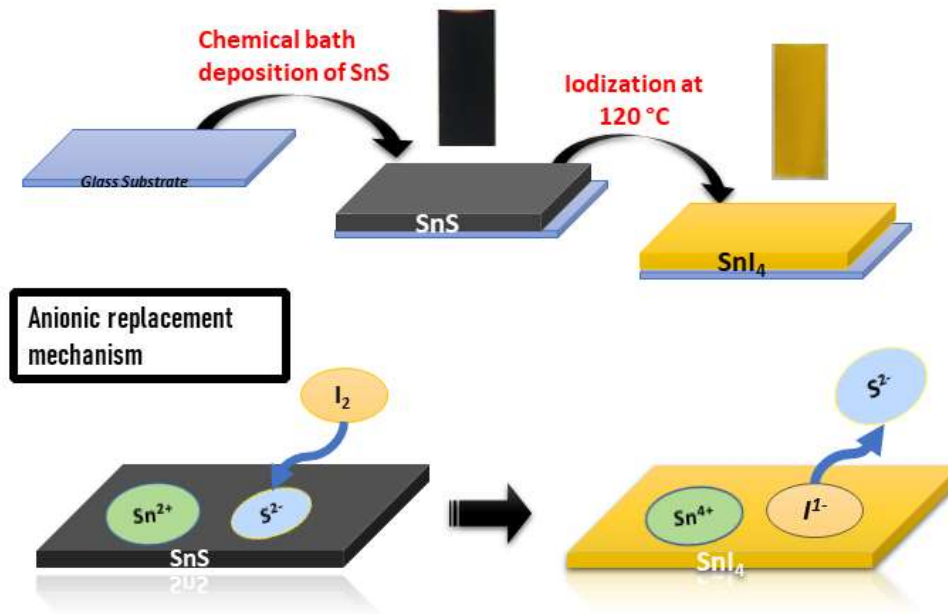


Figure 7.1 Experimental procedure of the two-stage deposition of SnI₄ thin films using anionic replacement mechanism.

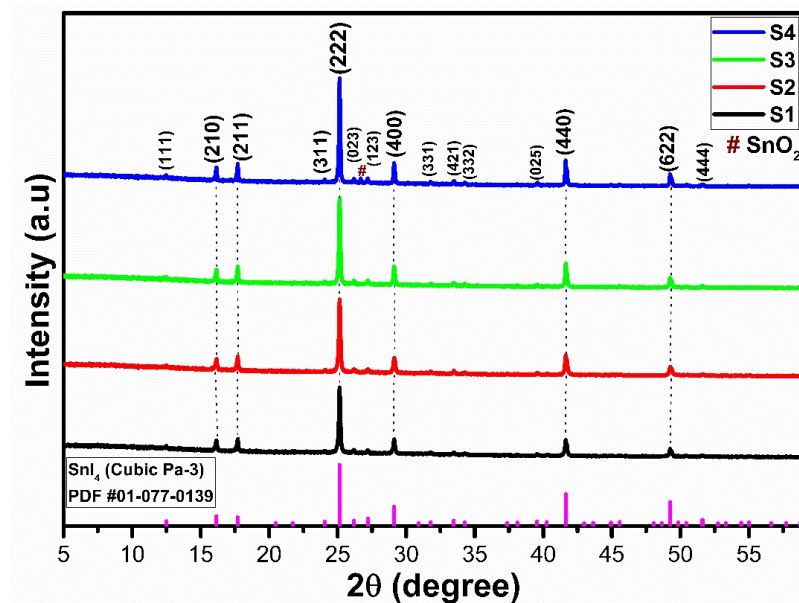


Figure 7.2 XRD patterns of the S1 (30 s), S2 (60 s), S3 (90 s), and S4 (120 s) SnI₄ thin films along with the standard pattern of SnI₄ (JCPDS 01-077-0139).

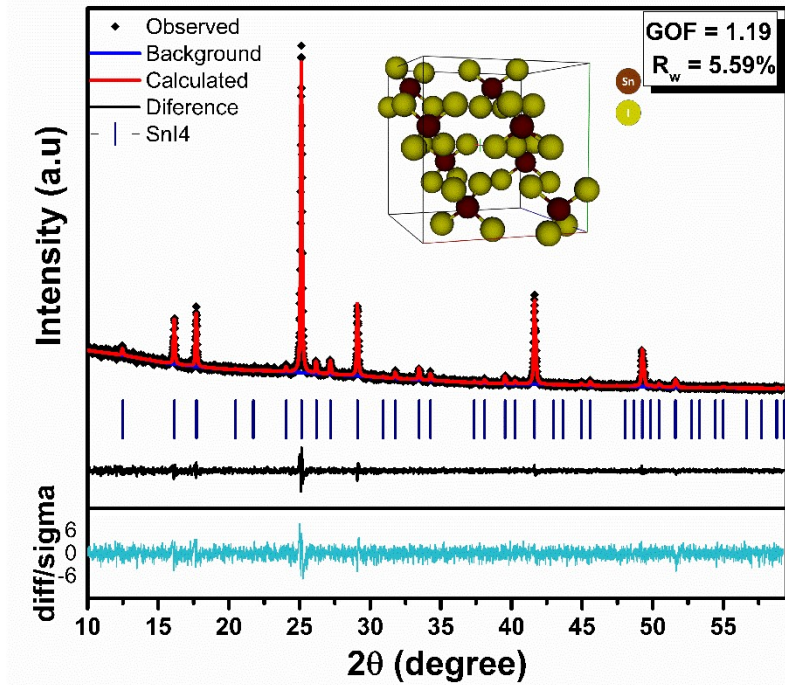


Figure 7.3 Rietveld refinement result of S3 SnI₄ sample and graphical representation of refined unit cell.

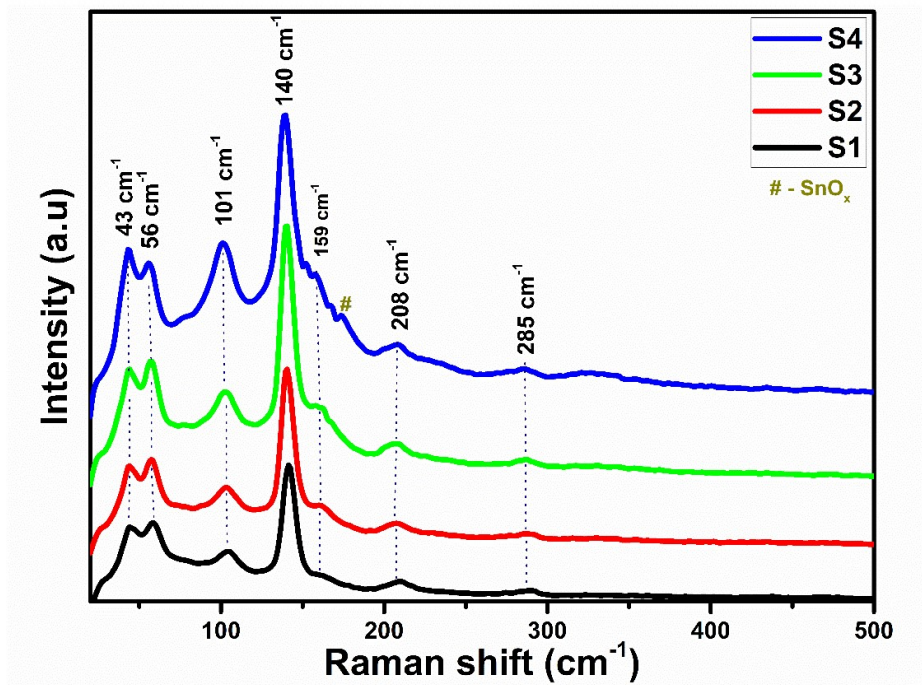


Figure 7.4 Raman spectra of the S1, S2, S3, and S4 SnI₄ samples.

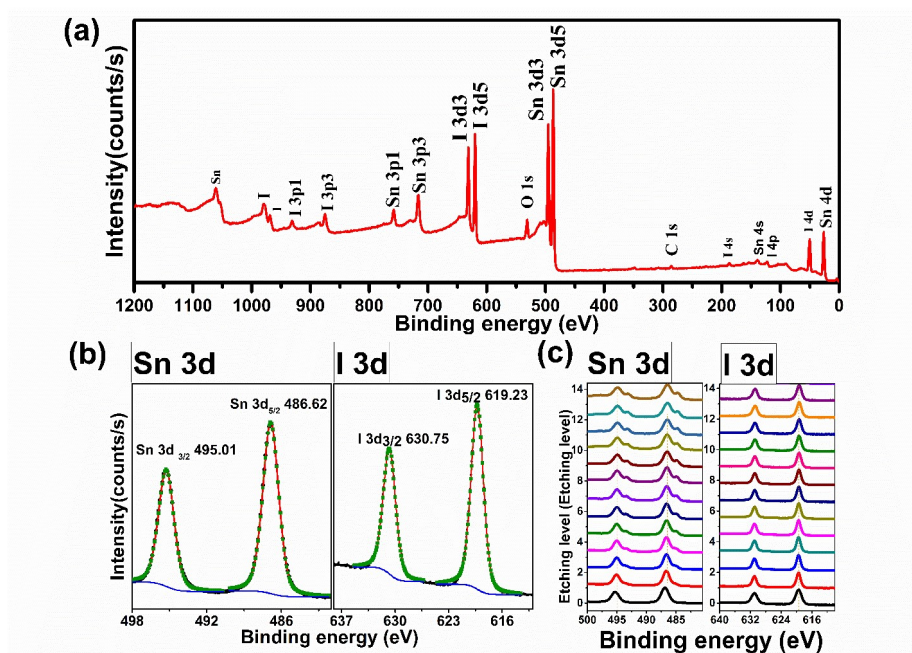


Figure 7.5 XPS (a) survey spectrum (b) core level spectrum of Sn and I (c) depth profile of S3 SnI₄ (90 s iodinated) sample showing Sn and I core level spectrum.

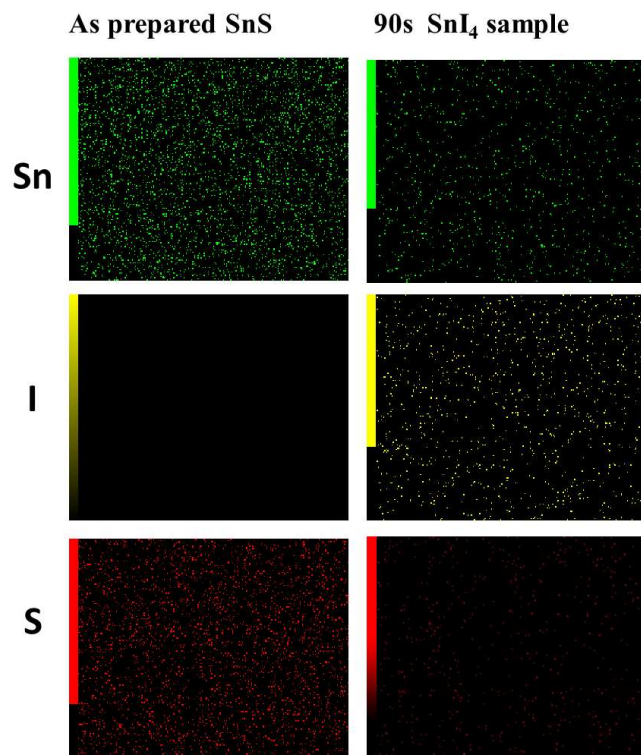


Figure 7.6 Elemental mapping of as prepared SnS and S3 SnI₄ thin films.

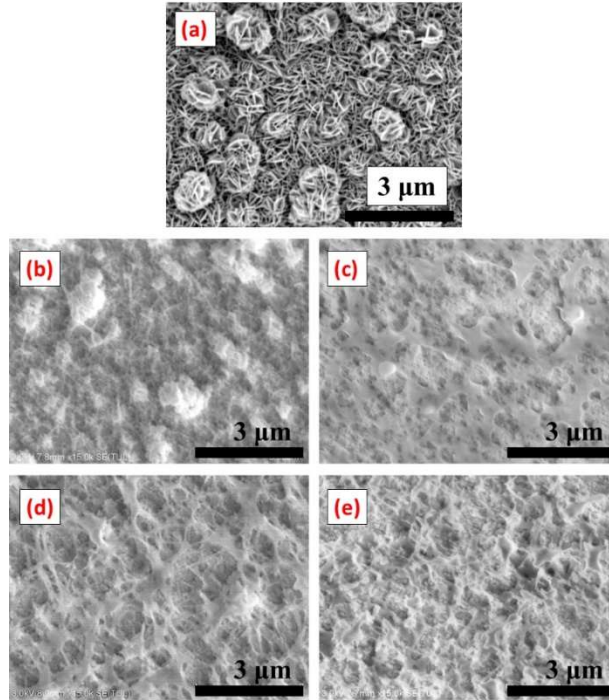


Figure 7.7 SEM images of (a) SnS, (b) S1, (c) S2, (d) S3, and (e) S4 SnI₄ thin films, respectively.

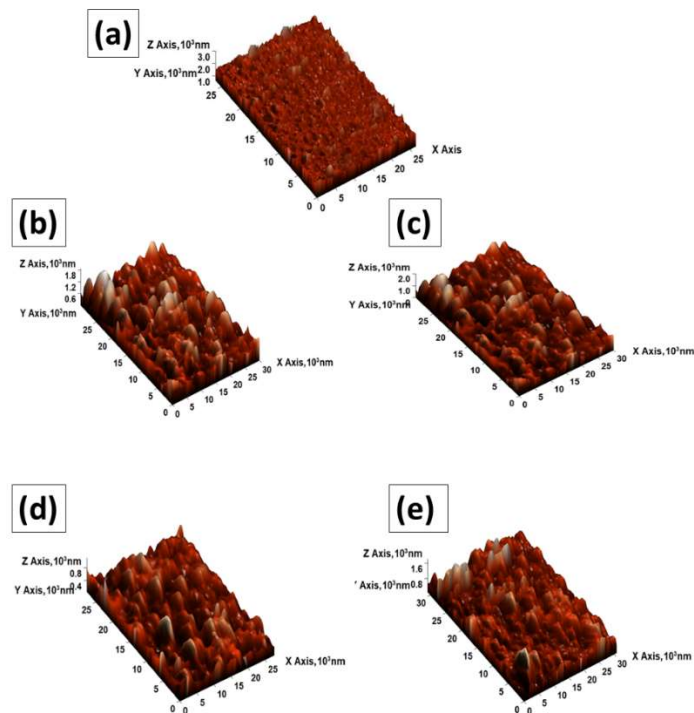


Figure 7.8 AFM images of (a) as prepared SnS, (b) S1, (c) S2, (d) S3, and (e) S4 SnI₄ thin films, respectively.

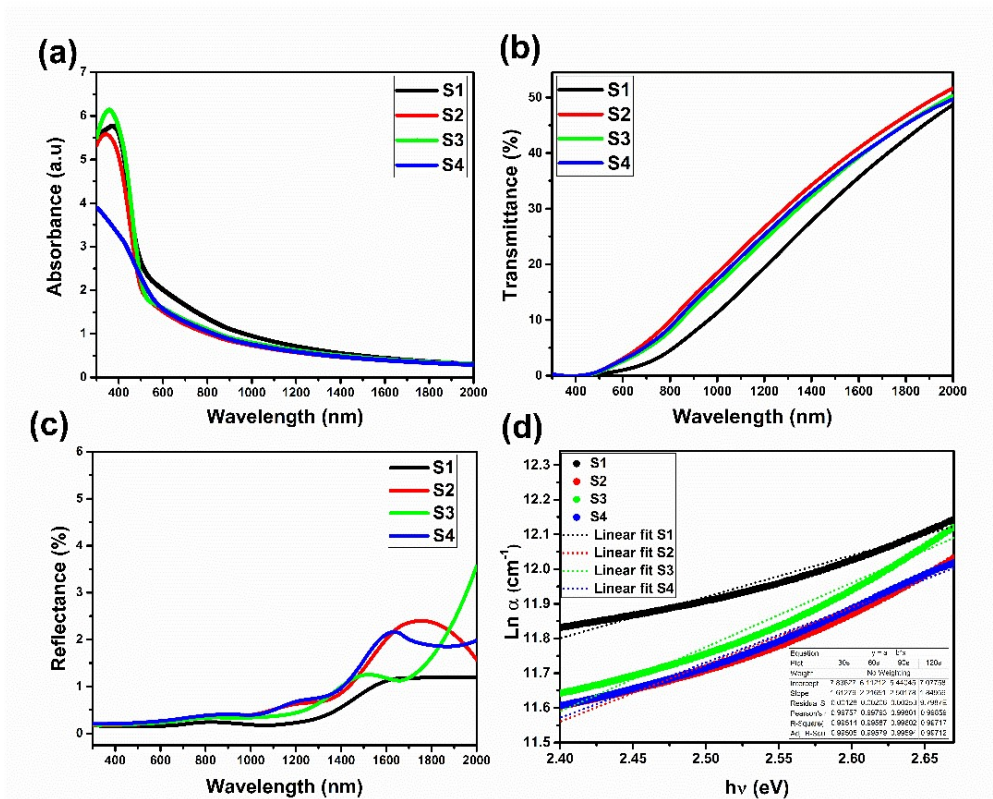


Figure 7.9 (a) Absorbance, (b) transmittance, (c) reflectance spectra, and (d) Urbach energy plots for different SnI₄ samples.

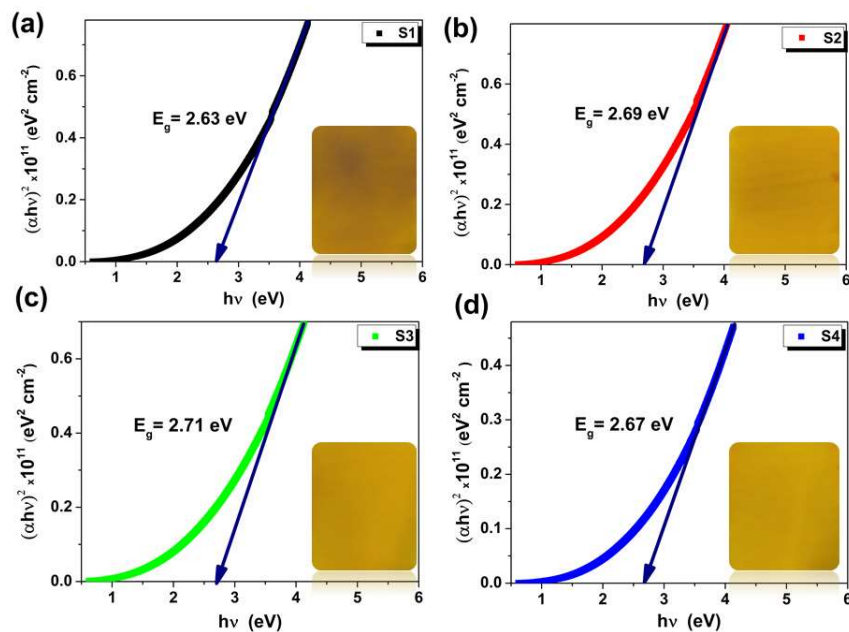


Figure 7.10 Tauc plots of (a) S1, (b) S2, (c) S3, and (d) S4 SnI₄ thin films along with photographs of film in the inset.

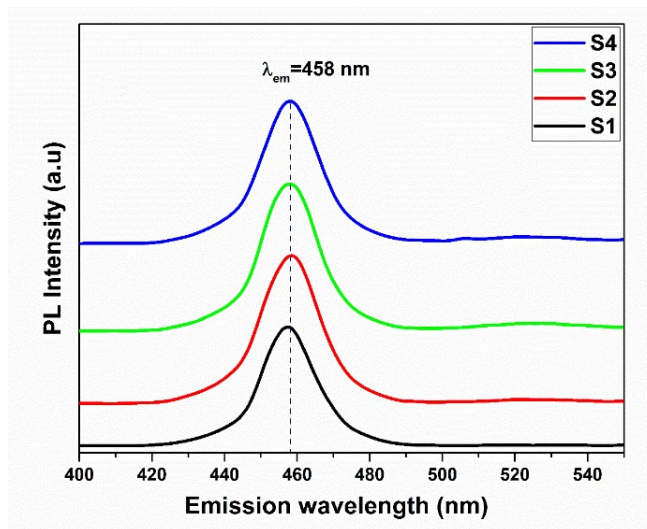


Figure 7.11 Photoluminescence spectra of SnI₄ samples excited with a wavelength of 227 nm.

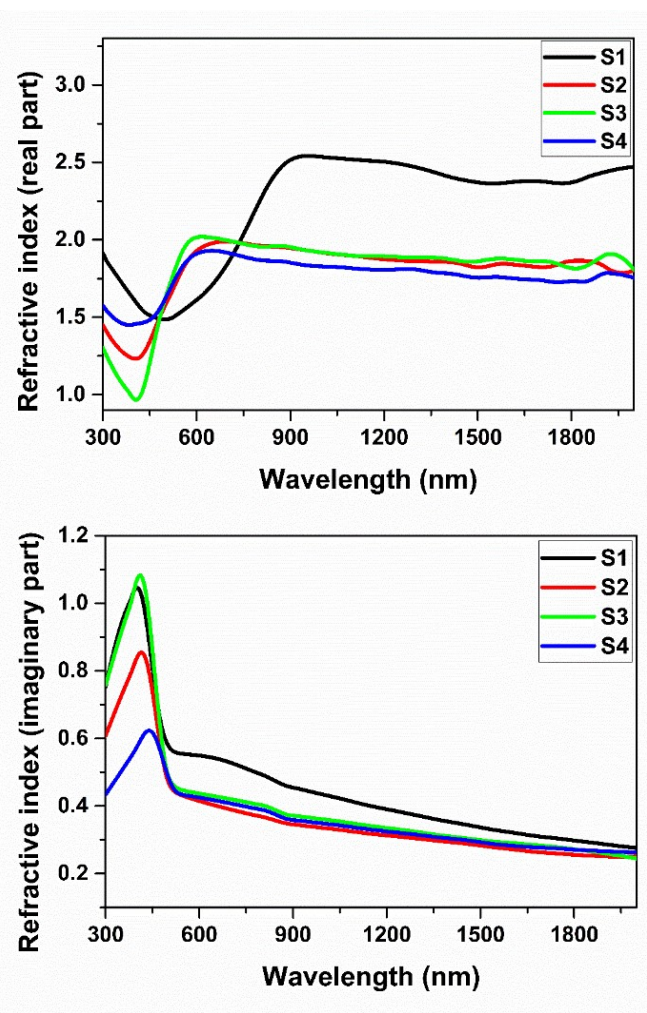


Figure 7.12 Variation of the real and imaginary part of complex refractive index with wavelength.

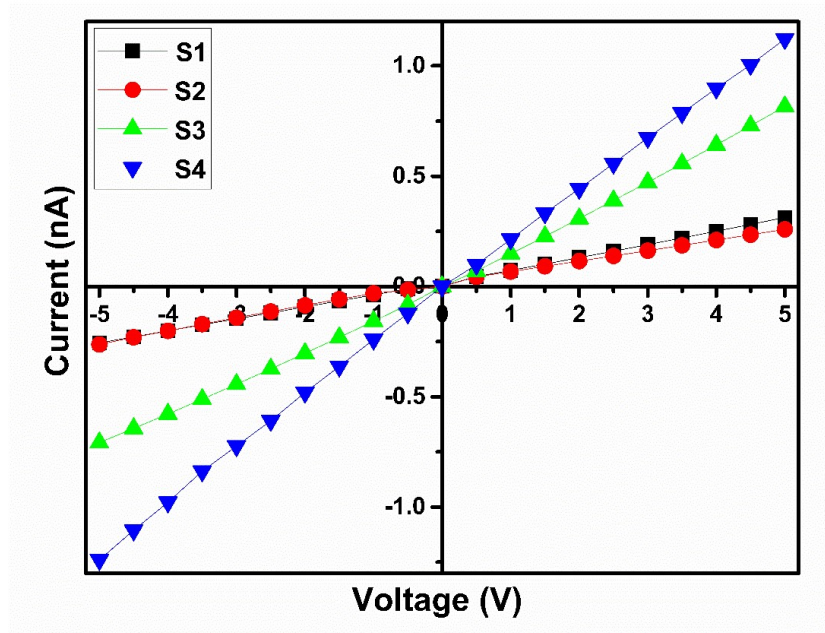


Figure 7.13 I-V characteristics of SnI₄ thin films iodinated for different time durations.

Conclusions

Crystalline SnI₄ thin films were successfully deposited via an inexpensive, non-vacuum, facile method (anionic replacement reaction) at a relatively low temperature. The effect of iodization time on structure, morphology, composition, and optoelectronic properties was studied. The thin films crystallized in cubic Pa-3 structure and exhibited an increase in crystallinity, grain size, and electrical conductivity with the increase in iodization time. The refractive index and dielectric properties of SnI₄ thin film were evaluated. The best condition of the 90 s sample resulted in SnI₄ thin films with crystallite size, bandgap, and resistivity values of 63.3 nm, 2.71 eV, and $3.1 \times 10^5 \Omega \cdot \text{cm}^{-1}$, respectively. Authors firmly believe that crystalline SnI₄ thin films obtained with facile non-vacuum deposition methods will provide a potential strategy to further enhance the optoelectronic properties and power conversion efficiencies of low-cost, lead-free, and stable tin iodide perovskite solar cells.

LIST OF PUBLICATIONS

1) **A. Paul**, B. Krishnan, S. Shaji, D.A. Avellaneda, Cu₂SnS₃ based photovoltaic structure with improved open circuit voltage for air stable self-driven enhanced NIR photodetection, Appl. Surf. Sci. 639 (2023) 158181.

<https://doi.org/10.1016/j.apsusc.2023.158181>.

2) **A. Paul**, S. Shaji, B. Krishnan, D.A. Avellaneda, Effect of copper precursor layer thickness on the properties of preferentially oriented Cu₄SnS₄ thin films for photovoltaic applications, Opt. Mater. 120 (2021) 111423.

<https://doi.org/10.1016/j.optmat.2021.111423>.

3) D.A. Avellaneda, **A. Paul**, S. Shaji, B. Krishnan, Synthesis of Cu₂SnS₃, Cu₃SnS₄, and Cu₄SnS₄ thin films by sulfurization of SnS-Cu layers at a selected temperature and /or Cu layers thickness, J. Solid State Chem. 306 (2022) 122711.

<https://doi.org/10.1016/j.jssc.2021.122711>

4) **A. Paul**, S. Shaji, B. Krishnan, D.A. Avellaneda, Novel low-cost synthesis of crystalline SnI₄ thin films via anionic replacement: Effect of iodization time on properties, Opt. Mater. 133 (2022) 112982.

<https://doi.org/10.1016/j.optmat.2022.112982>

PRESENTATIONS AT INTERNATIONAL CONFERENCES

1) Oral presentation at **XV International Conference on Surfaces, Materials, and Vacuum** 2022, Puerto Vallarta, Mexico.

2) Poster presentation at **XXX International Materials Research Congress & International Conference on Advanced Materials** 2022, Cancun, Mexico.

3) Poster presentation at **XXIX International Materials Research Congress** 2021, (Virtual), Cancun, Mexico.

4) Poster presentation at International Webinar Series, **Progress and Promises in Chemical Sciences 2021**, (Virtual) Christ University, Bengaluru, India.

5) Oral presentation at **International E-Symposium on Advanced Techniques for energy harvesting and storage applications** 2020, Facultad de Ciencias Químicas, UANL, Mexico.